Experiments and Numerical Simulation of Three-Dimensional Turbulence in Gravity Currents

Caroline Rosemary Marshall

The University of Leeds

School of Computing
EPSRC Centre for Doctoral Training in Fluid Dynamics

Submitted in accordance with the requirements for the degree of

Doctor of Philosophy

January 2021

Declaration

This copy has been supplied on the understanding that it is copyright material and that no quotation from the thesis may be published without proper acknowledgement.

The candidate confirms that the work submitted is his/her/their own, except where work which has formed part of jointly authored publications has been included. The contribution of the candidate and the other authors to this work has been explicitly indicated below. The candidate confirms that appropriate credit has been given within the thesis where reference has been made to the work of others.

A version of Chapter 4 has been submitted for publication in Experiments in Fluids with the preliminary title
'Internal gravity waves observed in the gravity current body', authors CR Marshall, RM Dorrell, GM Keevil, J Peakall, SM Tobias. Currently under review.
In this manuscript the work is the candidate's own, with the other authors having acted in a supervisory role, providing feedback and suggestions.

Acknowledgements

I would like to thank my supervisors Rob Dorrell, Gareth Keevil, Jeff Peakall, and Steve Tobias. Your seemingly endless patience, willingness to explain basic things, and excellent feedback made this project seem achievable and even fun (at least most of the time).

I am also very grateful to Helena Brown, for always being willing to help with preparing and running experiments as well as being a friendly ear when things were overwhelming. Additionally – Helena, Gareth, and Rob Thomas, you always quietly helped when I managed to flood the lab or clog a mixer with salt. Not once did any of you point out how much of an idiot I had been (at least not in front of me). Your restraint was greatly appreciated!

My thanks to the other CDT students for their support and friendship, but especially to Paul Allen and Charlie Lloyd. Before joining the CDT, I had never done any computational fluid dynamics. The two of you were never too busy to answer my questions (even when I'd asked the same questions the week before).

To Som Dutta, who provided invaluable support and advice regarding designing the numerical investigations – thank you for imparting some of your extensive Nek5000 knowledge to a complete novice. It was very much appreciated.

Finally a huge thanks to my husband, who spent many tedious hours proof reading, checking references, helping me with MATLAB and LaTeX, and calming me down. And for doing these things without complaint (or at least with vastly less complaint than there would have been if our positions were reversed).

This work was supported by the Engineering and Physical Sciences Research Council (EPSRC) Centre for Doctoral Training in Fluid Dynamics at the University of Leeds, grant number EP/L01615X/1.

Abstract

Gravity currents are a ubiquitous and crucial class of geophysical flow, being a key driver of sediment transport in rivers and oceans. The body typically forms the largest part of such flows, yet body structure remains poorly understood. Research into gravity current structure has primarily focused on the head of the flow in unsteady lock-exchange type currents (due to the highly turbulent nature of the head, and the simplicity of the lock-exchange setup).

The work presented consists of experimental and numerical investigations into the structure of constant-influx solute-based gravity currents. Particle image velocimetry, particle tracking velocimetry (Shake-the-Box), and direct numerical simulation are used to generate instantaneous whole-field two- and three-dimensional velocity measurements. These are used to discuss large-scale structures within the flow. Results question several common assumptions regarding gravity current dynamics.

Through application of Fourier transforms, wavelet transforms, and dynamic mode decomposition, empirical data (from both particle image velocimetry and Shake-the-Box) reveals internal waves, sometimes associated with three-dimensional motions, within the current body. These waves are shown to form a critical layer near the height of the velocity maximum. Wave breaking at this critical layer has the potential to limit dilution of the lower part of the flow, and accelerate the flow downstream at the height of the critical layer. The presence of these waves therefore questions the accuracy of extant models assuming a statistically steady body.

Existing numerical research concerning gravity currents has almost always assumed a Schmidt number of approximately unity. Using direct numerical simulation, it is shown that some flow features (such as the presence of structures in the upper part of the body) are highly Schmidt number dependent. Further, it is demonstrated that the difference in Schmidt number may explain the structural differences between the experimental and numerical components of this work.

Contents

List of Figures

List of Tables

Abbreviations

$\boldsymbol{A}$	Matrix representing linear transform of data between timesteps in DMD
$\boldsymbol{a}$	Dynamic mode amplitude, $\boldsymbol{a_j} = \frac{1}{\lvert\lvert \boldsymbol{G(:,j)} \rvert\rvert}$ where $\boldsymbol{G} = \boldsymbol{D\Lambda^{-1}\chi}$
(a, b, d, α)	Multiplication coefficients
BDFk/EXTk	k-th order backwards differencing and extrapolation time stepping scheme
$(\boldsymbol{C}, \boldsymbol{D})$	Unitary matrices in DMD
C	Courant number
c	Wave speed
Ca	Cauchy number, $Ca = \frac{U_c^2 \rho}{E_b}$
D	Mass diffusivity
d_p	Particle diameter (m)
DMD	Dynamic mode decomposition
DNS	Direct numerical simulation
E_b	Bulk modulus elasticity
Eu	Euler number, $Eu = \frac{\rho U_c^2}{\Delta p}$
F	Pump frequency (Hz)
F_e	Excess density flux estimated from data
F_I	Excess density flux at the inlet
f	Frequency (Hz)
FEM	Finite element method
FFT	Fast Fourier transform
Fl	Cospheric polyethylene microspheres UVPMS-BO-1.00 125-150µm
Fr	Froude number, $Fr = \frac{U_c}{\sqrt{g L_c}}$
Fr_d	Densimetric Froude number, $Fr = \frac{U_c}{\sqrt{g' L_c}}$
$\boldsymbol{g}$	Gravitational acceleration ($\mathrm{m\,s^{-2}}$), $\boldsymbol{g} = g\hat{\boldsymbol{g}}$
g'	Reduced gravity

GLL	Gauss-Legendre-Lobatto
GLY	Glycerol
h	Current height (m)
I_{orig}	Image recorded by camera in STB
I_{part}	Projection of particle in STB volume onto two-dimensional image in STB
I_{proj}	Projected two-dimensional image in STB
I_{res}	Residual image in STB
IA	Interrogation area
IPR	Iterative reconstruction of volumetric particle distribution
$\boldsymbol{k} = (k_x, k_y, k_z)$	Wavenumber
KDP	Potassium dihydrogen phosphate
k	Turbulent kinetic energy
L	Velocity gradient tensor
L_c	Characteristic length scale (m)
L_E	Large eddy length scale
LES	Large eddy simulation
M	Spatial mapping function
N	Brunt-Väisälä buoyancy frequency
N_{DS}	Doppler shifted Brunt-Väisälä buoyancy frequency
N_o	Number of operations
N_p	Number of points
N_t	Number of timesteps
n	Refractive index
OTF	Optical transfer function
P	Modified pressure, $P = p + \rho g h$
P_N	Legendre polynomials
p	Pressure
Pa	LaVision polyamide particles HQ, mean diameter 60 µm
Pe	Peclet number, $Pe = ReSc = \frac{U_c L_c}{D}$
PIV	Particle image velocimetry
PTV	Particle tracking velocimetry

Q	Influx ($\mathrm{m^3\,s^{-1}}$)
R	Residual
r	Radius (m)
RANS	Reynolds-averaged Navier-Stokes
Re	Reynolds number, $Re = \frac{\rho U_c L_c}{\eta}$
Re_T	Turbulent Reynolds number
RI	Refractive index
Ri	Gradient Richardson number, $Ri = \frac{g}{\rho_c}\frac{\partial\overline{\rho}/\partial Y}{(\partial\overline{U}/\partial Y)^2}$
Ri_B	Bulk Richardson number, $Ri_B = Fr_D^{-2}$
S	Salinity
S_x	Scalogram of signal $\boldsymbol{x}$
Sc	Schmidt number $Sc = \frac{\nu}{D}$
SGS	Subgrid-scale
STB	Shake-the-Box particle tracking velocimetry
t	Time (s)
t_c	Characteristic time scale (s)
$\boldsymbol{U} = (U, V, W)$	Velocity ($\mathrm{m\,s^{-1}}$)
U_c	Characteristic velocity scale ($\mathrm{m\,s^{-1}}$)
U_g	Stokes velocity ($\mathrm{m\,s^{-1}}$), $U_g = \frac{d_p^2(\rho_p - \rho)\boldsymbol{g}}{18\eta}$
U_{px}	Downstream particle displacement (pixel)
u_w	Friction velocity $u_w = \sqrt{\frac{\tau_w}{\rho}}$
u_η	Kolmogorov velocity scale
W_T	Width of tank
We	Weber number, $We = \frac{U_c}{\sqrt{\sigma/\rho L_c}}$
(X, Y, Z)	Position
(X_p, Y_p, Z_p, I_p)	Particle position and intensity
(X_p', Y_p', Z_p', I_p')	Updated particle position and intensity after a STB shaking step
(x^+, y^+, z^+)	Dimensionless wall distance, $y^+ = \frac{u_w y}{\nu}$
Δp	Pressure difference
ΔS	Difference between salinity and ambient salinity
ΔS_I	Difference between inlet and ambient salinities
Δt	Timestep

Δx	Grid spacing
$\Delta \tau$	Stress tensor
δ_S	Shift in particle position during STB shaking steps (voxel)
β	Coefficient of haline contraction
Γ	Eigenvectors
ϵ	Rate of kinetic energy dissipation
ζ	Eigenvalues
η	Dynamic viscosity (Pa s)
η_B	Batchelor length scale
η_K	Kolmogorov length scale
θ	Bed slope (°)
ϑ	Wavelet
κ	SGS flux term
Λ	Diagonal matrix
λ	Wavelength
ν	Kinematic viscosity
ξ	SGS stress
ϱ	Growth rate
ρ	Fluid density ($\mathrm{kg\,m^{-3}}$)
ρ_p	Particle density ($\mathrm{kg\,m^{-3}}$)
ρ_e	Excess density ($\mathrm{kg\,m^{-3}}$)
σ	Surface tension
ς	Data
τ	Reynolds stresses
τ_r	Relaxation time (s), $\tau_r = \frac{d_p^2 \rho_p}{18\eta}$
τ_w	Wall shear stress
τ_η	Kolmogorov time scale
ϕ	Basis function
φ	Dynamic mode
χ	Eigenvectors
ψ	Test function
$\mathbf{\Omega}$	Vorticity, $\mathbf{\Omega} = (\Omega_X, \Omega_Y, \Omega_Z)$

ω	Modal angular frequency
$\tilde{(\cdot)}$	Dimensionless variable
$\grave{(\cdot)}$	Similar matrix
$\breve{(\cdot)}$	Filtered variable
$\overline{(\cdot)}$	Averaged variable
$\overline{\overline{(\cdot)}}$	Mean relative to the ambient fluid
$\hat{(\cdot)}$	FFT of data
$\lvert(\cdot)\rvert$	Magnitude
$(\cdot)'$	Fluctuation from mean
$(\cdot)^*$	Dimensionless variable defined relative to mean flow
$(\cdot)^\dagger$	Complex conjugate
$(\cdot)_a$	A property of the ambient fluid
$(\cdot)_c$	A critical value
$(\cdot)^H$	Hermitian transpose
$(\cdot)_I$	A property of the inlet fluid
$(\cdot)_{RMS}$	Root mean square
$(\cdot)^T$	Transpose

Chapter 1

Introduction

1.1 Introduction

Gravity currents, also known as density currents, are a common and diverse class of geophysical flow with real-world examples ranging from thunderstorm outflows and haboobs to the flow resulting from opening the door to a heated house on a cold day. They are an important class of flow, often having a dramatic impact on their surroundings (such as the uprooting of trees (Feistl *et al.*, 2015) and the breaking of submarine cables (Simpson, 1997)) as well as being the primary source of transport in oceans. Their propagation is a result of a density difference between the current and surrounding ambient fluids. This could be a result of a temperature difference (e.g. atmospheric cold fronts), or the presence of a solute (e.g. salt wedge propagation) or suspended particulates (e.g. powder snow avalanches and sea floor turbidity currents) (Huppert, 2006; Simpson, 1997).

Due to their prevalence, the structure of gravity current flows has been extensively researched. However, despite the fact that the body often forms by far the largest part of the flow (Azpiroz-Zabala *et al.*, 2017), the existing work has primarily focused on the head. Further, much of the existing experimental research considers constant-volume

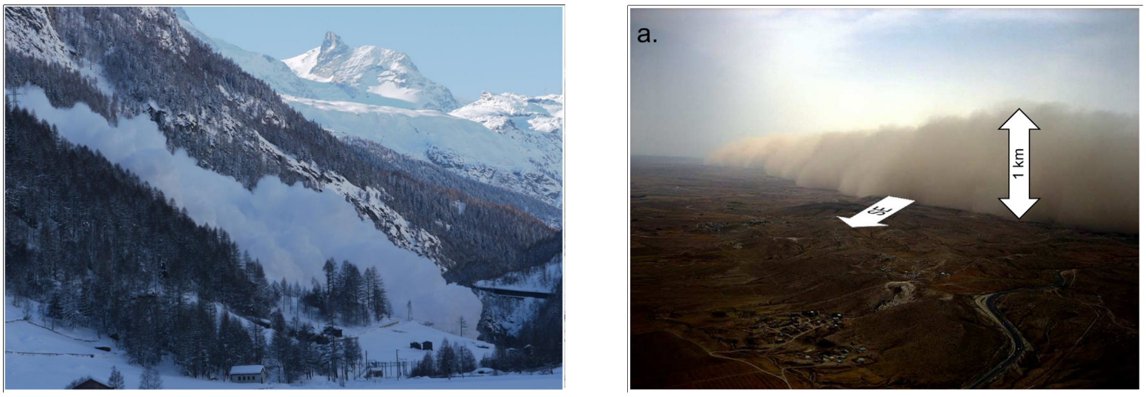

(a) (b)

Figure 1.1: Examples of real-world gravity current flows, (left) a powder snow avalanche (Feistl *et al.*, 2015), and (right) a haboob (Crouvi *et al.*, 2017).

lock-exchange type flows (Alahyari & Longmire, 1996; Cantero *et al.*, 2007; Hacker *et al.*, 1996; Hallworth *et al.*, 1996; Härtel *et al.*, 2000; Middleton, 1966; Nogueira *et al.*, 2014; Sher & Woods, 2015; Simpson, 1969; Thomas *et al.*, 2003) which have a more pronounced head region than constant-flux type flows and may not be an accurate representation of constant-flux flows (Peakall *et al.*, 2001). In general, the body is assumed to be statistically two-dimensional and statistically steady (Cantero *et al.*, 2007; Gerber *et al.*, 2010; Gray *et al.*, 2006; Kneller & Buckee, 2000; Meiburg *et al.*, 2015; Simpson, 1997). Those experimental studies that have considered the body have mostly done so using time-averaged statistics and at-a-point measurements (Buckee *et al.*, 2001; Cossu & Wells, 2012; Gray *et al.*, 2006; Kneller *et al.*, 1997, 1999). These are limiting in terms of understanding the turbulence structure of the flow.

More recent measurements, consisting of particle image velocimetry measurements of the body combined with simultaneous density measurements, have focused on entrainment and mixing without discussing large-scale structures within the flow (Krug *et al.*, 2013; Odier *et al.*, 2009, 2012). The only works presenting three-dimensional volumetric experimental measurements of the gravity current body are Krug *et al.* (2015) and Lefauve *et al.* (2018). The work of Krug *et al.* (2015) was restricted to a small area in the mixed region and again focused on entrainment and mixing, while Lefauve *et al.* (2018) considers a flow with equivalent downstream velocity magnitude in the dense and less-dense fluids (resulting in greater shear than in flows with small to no average downstream velocity in the ambient). Both works employed quasi-instantaneous scanning methods rather than fully instantaneous methods. Therefore, understanding of the structure of the body of gravity current flows, and in particular the three-dimensional structure, is currently very limited.

Numerical investigations have also largely considered constant-volume flows (Bhaganagar, 2017; Birman & Meiburg, 2006; Cantero *et al.*, 2007, 2008; Espath *et al.*, 2014; Härtel *et al.*, 2000; Necker *et al.*, 2002; Ooi *et al.*, 2009; Özgökmen *et al.*, 2004, 2006; Pelmard *et al.*, 2020). Additionally, despite Schmidt number (the ratio of momentum and mass diffusivities) effecting large-scale structural changes in other flows (Hanazaki *et al.*, 2009; Langham *et al.*, 2020; Rahmani *et al.*, 2016), numerical investigations of gravity current flows have typically assumed Schmidt number to have little impact on the flow. The only work to consider flows with Schmidt number greater than 1, Bonometti & Balachandar (2008), is largely based on two-dimensional simulations, which are known to exhibit unphysical vortices and incorrectly estimate the energy budget of the flow (Cantero *et al.*, 2007, 2008; Härtel *et al.*, 2000; Necker *et al.*, 2002).

The work presented in this thesis is a combined experimental and numerical investigation of constant-influx solute-based gravity current flows. Data is collected using planar particle image velocimetry, volumetric Shake-the-Box particle tracking velocimetry, and three-dimensional direct numerical simulation, to provide whole-field instantaneous velocity measurements. The data is used to address some of the unanswered questions regarding the structure of the gravity current body. In particular:

- What is the nature of large-scale structures within the gravity current body?
- How are these structures affected by the flow Reynolds number?
- What do these structures imply for the existing understanding of gravity currents and how they interact with the environment?
- How does Schmidt number affect the structure of the head and body of the flow?
- Which of the changes associated with increased Schmidt number are also seen with increased Reynolds number?
- Under what circumstances is assuming a low Schmidt number, in order to reduce computational cost, justified?

1.2 Thesis Outline

Chapter 2 provides a summary of the existing literature investigating gravity currents. The anatomy and structure of gravity currents is described, along with some of the ways in which the flows can be categorised. Current understanding of gravity current body structure is presented, with a description of the investigative approaches that have been applied to the body to date.

In Chapter 3, details of the experimental domain and the measurement techniques used to generate the data in this thesis are presented.

In Chapter 4, two-dimensional particle image velocimetry measurements in the cross-stream centre of the domain for a variety of Reynolds numbers are presented. This data is used to quantify the turbulence structure of the gravity current body, and how that structure is affected by increased Reynolds number, through a combination of Fourier transforms, wavelet transforms, and dynamic mode decomposition. This analysis demonstrates that internal waves are present in the body of the flow, that these waves are of the right frequency to be internal gravity waves, and that they may be forming a critical layer within the flow. This questions the general assumption of statistically steady flow. The implications of these waves for gravity current flows are discussed.

In Chapter 5, three-dimensional volumetric Shake-the-Box particle tracking velocimetry measurements are presented. Vertical and cross-stream velocities and velocity fluctuations within the current body are shown to be equivalent in magnitude. Using similar analysis to Chapter 4, internal gravity waves that may be forming a critical layer within the flow are again identified in the data. In one of the cases, the identified waves are shown to be associated with three-dimensional motions.

In Chapter 6, three-dimensional direct numerical simulation of the experimental domain is used to investigate the effect of Schmidt and Reynolds numbers on the structure of gravity current flows. Increasing Schmidt number is shown to cause large-scale structural changes in the flow, such as causing lobe-and-cleft structures within the head, and wave-like structures in the mixed layer behind the head. These changes are shown to be a result of sharpening of the density profile, which decreases the gradient Richardson number in the current-ambient interface behind the head from above to below the critical value. This suggests that Schmidt number affects the stability of stratification in the body. The effects of increased Reynolds number and increased Schmidt number are compared, and structural changes unique to increased Schmidt number identified. Recommendations are made regarding when assuming a low Schmidt number is justified for numerical investigations of gravity current flows.

In Chapter 7, the three methodologies are brought together and their comparability established. It is suggested that the difference in Schmidt number between the experimental and numerical components of the work may account for the differences in structure, and further that this may explain why existing numerical literature has not identified the presence of internal waves in the gravity current flow. Limitations of the presented work are discussed, and suggestions are made for the direction of future research.

Chapter 2

Background

Gravity currents are a common class of geophysical flow, with examples ranging from thunderstorm outflows and haboobs to the flow that forms when the door of a heated house is left open on a cold day (Simpson, 1997). Their ubiquitous nature has resulted in extensive research into their structure and dynamics. However this research has focused on the head of the flow through lock-exchange type flows, while the body remains comparatively poorly understood. In this chapter the existing literature considering gravity current flows will be summarised, with a focus on the structure of the body.

2.1 Gravity Current Anatomy

Gravity currents are primarily horizontal flows, driven by gravity, due to a density difference between the current and surrounding ambient fluids (Huppert, 2006; Simpson, 1997). Such a broad definition covers a wide range of real-world flows, and there are several ways in which gravity currents can be further categorised. For example, the density difference could be a result of the presence of a solute or suspended sediment, or a difference in temperature between the current and ambient fluids (Simpson, 1997). A conservative current is one in which density variations are only a result of mixing with the ambient fluid, while a non-conservative current also entrains bed particles or deposits suspended sediment (Kneller & Buckee, 2000; Nogueira *et al.*, 2014). Gravity current flows are often separated by mode of generation, into constant-volume and constant-flux flows (Hallworth *et al.*, 1996; Nogueira *et al.*, 2014; Ottolenghi *et al.*, 2016a). An unsteady (constant-volume) flow is one in which a fixed volume of fluid is abruptly released, comparable with the flows resulting from seismogenic slumping (Kneller & Buckee, 2000). In contrast, a steady (constant-flux) flow is generated by a constant influx of current fluid, comparable with quasi-permanent flows such as that in the Black Sea (Dorrell *et al.*, 2019).

The structure of gravity current flows, according to Kneller & Buckee (2000), is illustrated in Figure 2.1. At the front of the flow is a head region, with a raised nose at the

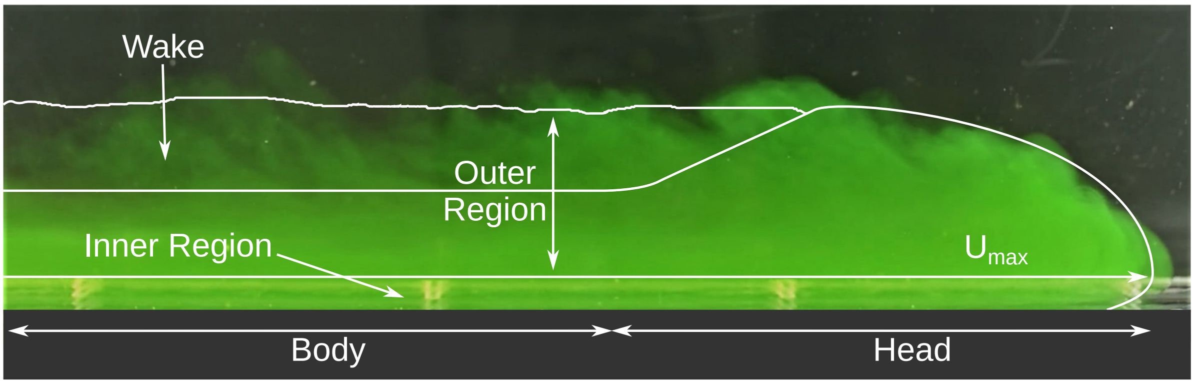

Figure 2.1: Flow visualisation from the work presented in this thesis, overlaid by the gravity current structure diagram of Kneller & Buckee (2000).

height of the downstream velocity maximum. The height of this velocity maximum is determined by the ratio of shear at the bed and at the current/ambient interface. High levels of drag at the bed raise the height of the velocity maximum, while high levels of drag at the current/ambient interface lower the height of the velocity maximum (Islam & Imran, 2010). Behind the head is the body, with a dense inner region and a less-dense outer region including a layer of mixed fluid. Typically, the inner region forms a smaller portion of the flow than the outer region (approximately 20% to 30% of the flow height (Kneller & Buckee, 2000)), but understanding the characteristics of this region (in particular the shear stress structure) is crucial to understanding the erosional/depositional capacity of the flow and thus the flow duration (Cossu & Wells, 2012). The relative importance of the head and body varies between flows, and is determined by factors such as mode of generation.

2.1.1 Differences Between Flow Types

The dynamics of different classes of gravity current flows vary significantly. A steady flow has a small head and prolonged body, that remain largely undiluted due to the constant replenishment of dense fluid (Gerber *et al.*, 2010; Hallworth *et al.*, 1996; Kneller & Buckee, 2000; Middleton, 1966; Sher & Woods, 2017). An unsteady flow has a better defined and more dominant head region compared with steady flows, a significantly shorter body section, and different sediment deposition characteristics (for example there is an area of low-sedimentation near the lock gate of a lock-exchange flow not present near the inlet of a constant-flux flow) (Hallworth *et al.*, 1996; Huang *et al.*, 2008). Peakall *et al.* (2001) suggest that steady currents may be better suited to modelling real-world flows, whether surge-type or continuous, and that the focus on lock-exchange type experimental flows has led to the importance of the current body being underestimated.

Additionally, a sediment-laden flow may not behave in the same way as a solute-based flow, though it is thought that nearly-conservative sedimented flows are comparable to solute-driven flows (Cossu & Wells, 2012; Gray *et al.*, 2006; Islam & Imran, 2010). Gray *et al.* (2006) considered constant-flux solute-based and sediment-laden flows with the same excess density and influx rate over a horizontal surface. They found that the sediment-laden flow will be thicker, with a larger head and a slower front velocity but faster averaged maximum velocities within the body. As a result, the solute-based flow has a smaller Reynolds number, larger Froude number, and smaller gradient Richardson number in the upper part of the flow. Gray *et al.* (2006) also demonstrated that bed slope has a smaller effect on sediment-laden compared with solute-based flows. Islam & Imran (2010) found no significant difference in the vertical structures of turbulent kinetic energy and Reynolds stress in sediment-laden and solute-based flows. While Gray *et al.* (2006) found that the magnitude of cross-stream and vertical contributions to turbulent kinetic energy is larger in sediment-laden flows compared with solute-based flows, Islam & Imran (2010) and Cossu & Wells (2012) found the opposite (possibly as a result of the low temporal frequency of Gray *et al.* (2005)).

Compared with flows on the flat, solute-based gravity currents flowing down a slope have higher maximum average downstream velocities and larger head volumes (Gray *et al.*, 2006; Simpson, 1997). On the other hand, if the slope is at least a few degrees the current front velocity is dependent on the influx of dense material but not on the slope (Simpson, 1997). Rates of entrainment and mixing also increase with bed slope in solute-based flows (Ellison & Turner, 1959; Gray *et al.*, 2006; Huang *et al.*, 2009; Kneller *et al.*, 2016; Stacey & Bowen, 1988), with increased slope associated with a reduction in the stability of the current-ambient interface (Kneller *et al.*, 2016). Gray *et al.* (2006) found that in sediment-laden flows the effect of slope is less pronounced, including a smaller velocity increase compared with equivalent solute-based flows and rates of mixing that are independent of slope, though Sequeiros *et al.* (2010) found that increasing bed slope increases the bed shear in turbidity currents and may change the character of the flow from depositional to erosional. An abrupt change in slope, such as flow over a ledge, can impact gravity current structure. Such slope changes often result in a hydraulic jump near to the ledge as a result of the internal Froude number being equal to 1 at the ledge and supercritical beyond it (see Section 2.1.2 below for a discussion of Froude number) (Armi, 1986; Negretti *et al.*, 2017; Simpson, 1997), and the fluid velocity may begin to increase a short distance before the drop (Negretti *et al.*, 2017). Despite this, many investigations include an abrupt drop above the outlet to prolong the duration of the flow (Buckee *et al.*, 2001; Cossu & Wells, 2012; Gray *et al.*, 2006; Islam & Imran, 2010; Lefauve *et al.*, 2018).

Some gravity current flows are laterally constrained, for example flow in submarine channels (Peakall & Sumner, 2015). The presence of side-walls can influence the dynamics of the flow, and has been investigated by considering channels of different aspect ratio, and by comparing numerical work using no slip and periodic boundary conditions (Chadha, 2015; Hallez & Magnaudet, 2009). In the initial stages, the front velocity of horizontal lock-exchange type flows is not thought to be affected by side-walls (Chadha, 2015; Hallez & Magnaudet, 2009), though when considering flows propagating down a slope the presence of side-walls results in a faster flow (Chadha, 2015). In the later stages of the flow Hallez & Magnaudet (2009) suggest that side-walls result in a slower travelling current, while Chadha (2015) suggests that side-walls result in a faster propagating flow. This discrepancy could be due to the difference in Reynolds number between the two works, or the sediment-laden nature of the flows in Chadha (2015). The presence of side-walls is found to produce a flatter head (Hallez & Magnaudet, 2009), which is further flattened by reducing the separation of the side-walls (Chadha, 2015), and a faster transition from the slumping regime to the viscous buoyant regime (Hallez & Magnaudet, 2009). In sediment-laden flows, side-walls increase the rate of sediment deposition (with the rate increased still further in a narrower channel), and three-dimensional instabilities originating with the side-walls result in faster breakdown of coherent structures (Chadha, 2015). Side-walls also lead to less pronounced lobe-and-cleft structures in the head of the flow (Chadha, 2015; Hallez & Magnaudet, 2009).

2.1.2 Dimensionless Parameters

Gravity current properties may be characterised using a small number of dimensionless parameters (Kneller & Buckee, 2000; Wells & Dorrell, 2021). In particular; Reynolds number, Froude number, gradient Richardson number, and Schmidt/Prandtl number.

The ratio of viscous and inertial forces captured in the Reynolds number,

$$Re = \frac{U_c L_c}{\nu}, \tag{2.1}$$

where U_c and L_c are some characteristic velocity and length scales, and ν is the kinematic viscosity of the fluid, is an indicator of flow turbulence. In gravity current flows, Reynolds number affects whether the primary mixing mechanism is Holmboe waves, Kelvin-Helmholtz vortices, or Kelvin-Helmholtz billows, and this has a substantial impact on mixing and entrainment (Balasubramanian & Zhong, 2018; Hogg *et al.*, 2015; Nogueira *et al.*, 2014). At high Reynolds number, over time the flow becomes three-dimensional and turbulent as instabilities in the head and body increase (Cantero *et al.*, 2007). It is thought that above some critical value of $Re_c \approx 1000$ (Parsons & García, 1998; Simpson, 1969, 1997) gravity current flow patterns are independent of Reynolds number (though a much higher value $\mathcal{O}(10^4)$ is needed for similar turbulent dynamics) (Simpson, 1997; Wells & Dorrell, 2021). When investigating real-world gravity current flows, where the Reynolds number is typically too large to investigate numerically or in a laboratory-based flow (e.g. $\mathcal{O}(10^8)$ for thunderstorm outflows (Simpson, 1997)), it is necessary to ensure the flow Reynolds number is beyond this critical value.

An appropriate choice of L_c is an area of debate, however the integral scale defined by Ellison & Turner (1959) is often chosen (Buckee *et al.*, 2001; Cossu & Wells, 2012),

$$L_c = \frac{\left(\int \bar{\bar{U}} dY\right)^2}{\int \bar{\bar{U}}^2 dY}, \tag{2.2}$$

where $\bar{\bar{U}}$ is the mean velocity relative to that in the ambient. In this thesis, X will refer to the downstream, Y to the vertical, and Z to the cross-stream directions (with corresponding velocities U, V, and W).

The ratio of inertial to buoyant forces captured in the densimetric Froude number,

$$Fr_D = \frac{U_c}{\sqrt{g' L_c}}, \tag{2.3}$$

(or similarly the bulk Richardson number $Ri_B = Fr_D^{-2}$) where g' is the reduced gravity, determines the propagation speed of the current (Wells & Dorrell, 2021), and is an indicator of stability. Turbulence is expected to be more damped in a low Froude number flow (Buckee *et al.*, 2001). The Froude number can be interpreted as the ratio of mean flow speed to the speed of a wave propagating along the flow surface (Hogg, 2006; Sumner *et al.*, 2013). In this case $Fr > Fr_c$ ($Fr < Fr_c$), where Fr_c is some critical Froude number, indicates that the wave speed is smaller (greater) than the mean flow speed and wave disturbances cannot (can) propagate upstream and affect the flow front. A current below/above Fr_c is called subcritical/supercritical. The commonly used critical value of $Fr_c = 1$ may not be applicable to gravity current flows as a result of their highly non-uniform velocity and density profiles coupled with their capacity for entrainment, erosion, and deposition (Huang *et al.*, 2009; Sumner *et al.*, 2013). Froude number is still considered to be an important parameter for the flow, with flows that transition from supercritical to subcritical experiencing hydraulic jumps (Sumner *et al.*, 2013).

The gradient Richardson number,

$$Ri = -\frac{g}{\rho_c} \frac{\partial \overline{\rho} / \partial Y}{(\partial \overline{U} / \partial Y)^2}, \tag{2.4}$$

where ρ_c is some characteristic density scale for the flow, is a measure of local density stratification stability. It is commonly quoted that above some critical value of $Ri_c = 0.25$, density stratification is sufficiently stable that energy generated through shear is dissipated and vertical mixing is suppressed (Buckee *et al.*, 2001; Kneller & Buckee, 2000). For small gradient Richardson numbers, the flow is unstable to Kelvin-Helmholtz instabilities as buoyancy effects are dominated by shear (Odier *et al.*, 2009).

The ratio of momentum and mass diffusivities is captured in the Schmidt number (or analogously the Prandtl number in temperature-driven flows) (Bonometti & Balachandar, 2008; Miller, 1991),

$$Sc = \frac{\nu}{D}, \tag{2.5}$$

where D is the mass diffusivity. The value of Schmidt number is highly fluid dependent, being $\mathcal{O}(1)$ for gases in air, $\mathcal{O}(1000)$ for solutes in water, and $\mathcal{O}(\infty)$ for oil in water (Andersson *et al.*, 2011; Bird *et al.*, 2007; Bonometti & Balachandar, 2008; Reynolds, 1974). This property indicates whether mass transfer is primarily a result of momentum, or of diffusion. It defines the size of the smallest length scales within the flow, reducing the smallest scales from the Kolmogorov scale (η_K) to the Batchelor scale ($\eta_B = \eta_K Sc^{-1/2}$) (Andersson *et al.*, 2011; Donzis *et al.*, 2014). Increasing Schmidt number is expected to decrease mixing (Miller, 1991; Rahmani *et al.*, 2016), and sharpen density profiles (increasing density gradients), which can cause large-scale structural changes such as stronger three-dimensional motions (Hanazaki *et al.*, 2009; Langham *et al.*, 2020; Rahmani *et al.*, 2016). The product of the Reynolds and Schmidt (or Prandtl) numbers is known as the Peclet number, $Pe = ReSc = LU/D$, and is the ratio of advection to solute (or thermal) diffusion (Chung, 2002; Johnson & Hogg, 2013).

2.2 The Structure of the Head

The structure of the head has been extensively researched, largely through measurements of unsteady, lock-exchange type flows (Alahyari & Longmire, 1996; Cantero *et al.*, 2007; Hacker *et al.*, 1996; Hallworth *et al.*, 1996; Härtel *et al.*, 2000; Middleton, 1966; Nogueira *et al.*, 2014; Sher & Woods, 2015; Simpson, 1969; Thomas *et al.*, 2003) and arrested head flows (Britter & Simpson, 1978; García & Parsons, 1996; Martin & García, 2009; Parsons & García, 1995, 1998; Simpson & Britter, 1979). The head is highly turbulent, three-dimensional, and is a region of intense mixing (Alahyari & Longmire, 1996; Cantero *et al.*, 2007; Hallworth *et al.*, 1996; Nogueira *et al.*, 2014). This highly turbulent head has a substantial effect on bed erosion, and is therefore critical for understanding the dynamics of the flow (Kneller & Buckee, 2000).

There are two primary mixing mechanisms in the head of the flow, illustrated by Simpson (1997) (shown in Figure 2.2). First, shear with the ambient fluid leads to Kelvin-Helmholtz billows that form at the top of the head and persist into the flow wake (Bhaganagar, 2017; García & Parsons, 1996; Nogueira *et al.*, 2014; Simpson, 1969, 1997; Simpson & Britter, 1979). Second, the raised nose at the head over-rides buoyant ambient fluid, which then rises and causes a three-dimensional lobe-and-cleft structure (Alahyari & Longmire, 1996; Bhaganagar, 2017; García & Parsons, 1996; Nogueira *et al.*, 2014; Simpson, 1969; Simpson & Britter, 1979). These mixing mechanisms are associated with areas of large negative Reynolds stress at the top of the head (associated with the Kelvin-Helmholtz billows) and under the nose (associated with the over-riding of buoyant

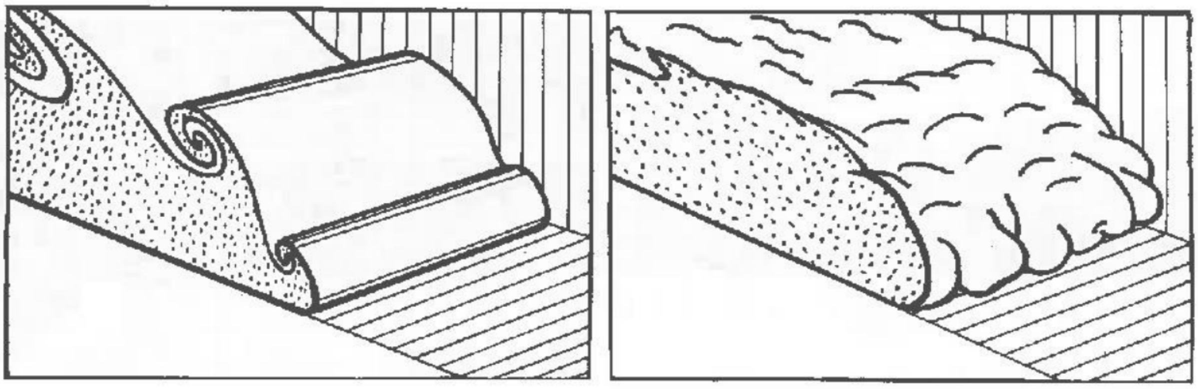

Figure 2.2: The two primary mixing mechanisms in the head of gravity current flows, specifically (left) Kelvin-Helmholtz billows and (right) lobe-and-cleft structures, as illustrated by Simpson (1997, p. 142).

ambient). While for a constant-volume flow, the strongest mixing is in the head (Sher & Woods, 2015), Sher & Woods (2017) observe that the location of greatest mixing in a constant-influx gravity current is dependent on the Froude number at the inlet. In a high source Froude number flow, mixing largely happens at the inlet, while if the source Froude number is low mixing is primarily at the head.

The turbulence structure is dominated by shear at the upper boundary (Martin & García, 2009), with corresponding peaks in turbulent kinetic energy. In high Reynolds number flows, entrainment is mostly a result of the breakdown of Kelvin-Helmholtz structures. In lower Reynolds number flows, this breakdown is less important relative to viscous effects and mixing rates are lower (Kneller & Buckee, 2000). The shape of the head is dependent on Schmidt number, with increased Schmidt number leading to a more defined head region with denser fluid reaching closer to the front of the flow, though front velocity and the formation of lobe-and-cleft structures are not thought to be affected (Bonometti & Balachandar, 2008).

2.3 The Structure of the Body

The body of gravity current flows often forms by far the largest part of the flow, persisting for hours or even days (see Figure 2.4) (Azpiroz-Zabala *et al.*, 2017). Despite this, the structure of the body remains poorly understood (Wells & Dorrell, 2021). The gravity current body is typically assumed to be statistically two-dimensional (Cantero *et al.*, 2007; Meiburg *et al.*, 2015; Simpson, 1997; Thomas *et al.*, 2003) and statistically steady (here meaning that when averaged over time, quantities such as downstream velocity and density appear constant though there are still fluctuations and instabilities) (Gerber *et al.*, 2010; Gray *et al.*, 2006; Kneller & Buckee, 2000; Simpson, 1997). Such flows are therefore frequently described using averaged velocity and density profiles such as those in Figure 2.3 (Abad *et al.*, 2011; Altinakar *et al.*, 1996; Davarpanah Jazi *et al.*, 2020; García, 1994; Gray *et al.*, 2006; Kneller & Buckee, 2000; Sequeiros *et al.*, 2010).

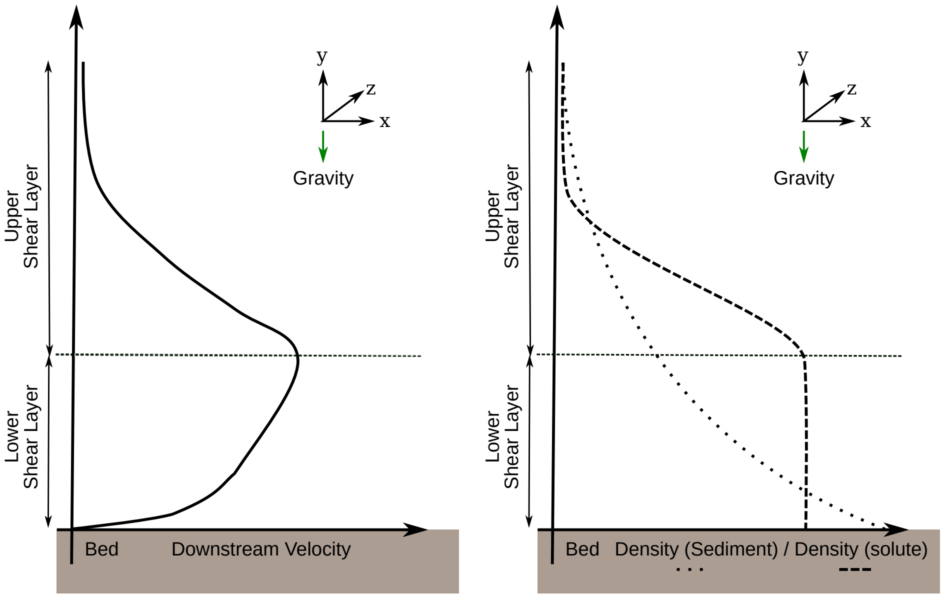

Figure 2.3: The currently accepted idealised structure of gravity current body (left) velocity and (right) density profiles (Abad *et al.*, 2011; Altinakar *et al.*, 1996; Davarpanah Jazi *et al.*, 2020; García, 1994; Kneller & Buckee, 2000; Sequeiros *et al.*, 2010).

The velocity profile can be divided into two layers by the height of the velocity maximum, the location of which is determined by the ratio of drag at the upper and lower boundaries and is dependent on the flow Reynolds number (Buckee *et al.*, 2001). Above the velocity maximum the shape of the velocity profile is similar to that of a turbulent wall-bounded jet (Dorrell *et al.*, 2019; Pelmard *et al.*, 2020), while below the velocity maximum the shape is closer to that of an open-channel flow (Dorrell *et al.*, 2019). While mean vertical velocities are thought to be small compared to mean downstream velocities (about 5% of the maximum mean downstream velocity), instantaneous vertical velocities may be an order of magnitude larger than the mean (Buckee *et al.*, 2001).

Depending on the flow type, the density profile may be stepped (in the case of low slope solute-based flows), or smooth (in the case of sediment-laden flows) (Gray *et al.*, 2006; Kneller & Buckee, 2000). In sediment-laden flows, coarse-grained material is concentrated in the lower part of the flow while fine-grained material is more evenly distributed vertically (Gray *et al.*, 2006; Kneller & Buckee, 2000). The thickness of the mixed layer, and thus the density profile, is strongly affected by Schmidt number, with a higher Schmidt number flow having a thinner mixed region and stronger density gradients (Bonometti & Balachandar, 2008).

There are significant velocity fluctuations in the body associated with the passage of coherent structures (Buckee *et al.*, 2001). The presence of these large instantaneous velocity fluctuations suggests that the body makes a substantial contribution to sediment entrainment in flows over an erodible bed (Kneller & Buckee, 2000; Kneller *et al.*, 1999). Instantaneous downstream velocities within the body can be as much as 40% greater than the mean value, and up to 50% greater than the current front velocity, and mean downstream velocities in the body can exceed current front velocity by 30% (Bhaganagar,

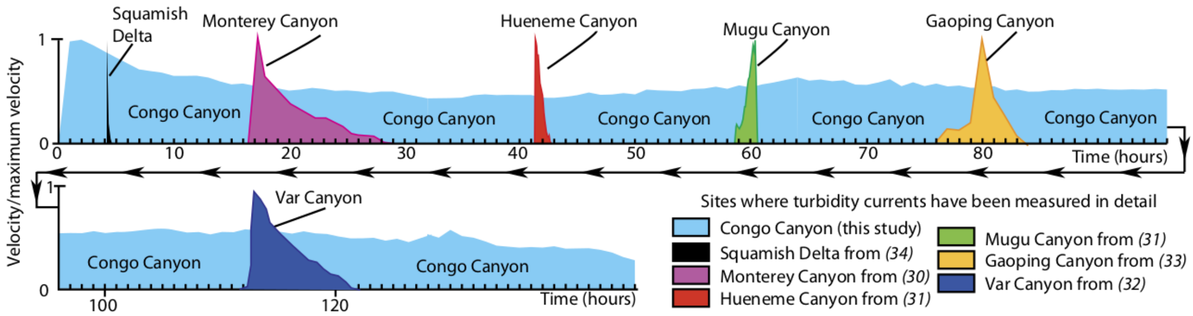

Figure 2.4: Comparison of flow durations based on real-world flow observations (Azpiroz-Zabala *et al.*, 2017).

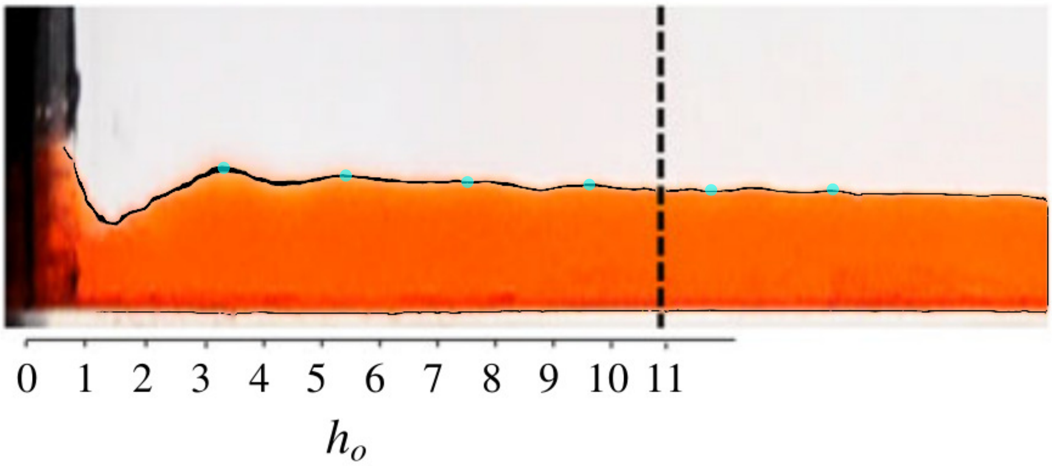

Figure 2.5: A snapshot taken of a dyed flow run from the work of Sher & Woods (2017), modified to include a black line showing the current-ambient interface (determined by choosing a pixel near the interface, and changing all pixels in the image that share that colour to black) and evenly spaced blue circles showing the wavelength of a possible wave (with spacing determined by the separation of the first two peaks).

2017; Kneller & Buckee, 2000; Kneller *et al.*, 1997; Sher & Woods, 2015). There are also significant fluctuations in density (and thus reduced gravity) sufficient to increase gravitational acceleration by up to 30% (Buckee *et al.*, 2001). Additionally, vortical Lagrangian coherent structures capable of affecting the height of the turbulent/non-turbulent interface (Neamtu-Halic *et al.*, 2019) and wave-like structures at the current-ambient interface (Gray *et al.*, 2006) have been identified. Though they are not addressed, evidence of such waves can be seen in flow visualisation images of a sub-critical flow with source Froude number 0.4 presented by Sher & Woods (2017) (Figure 2.5). As well as meaning that waves generated at the inlet may interact with the flow front, if the Froude number moves from sub- to super-critical at some distance from the inlet a hydraulic jump may occur causing an abrupt shift in flow thickness (Sumner *et al.*, 2013). Time-averaged profiles are therefore limiting when discussing the structure of the body.

It has recently been suggested that the current model of the gravity current body may need to be updated to a new and dynamic model. Measurements of a real-world flow in the Black Sea revealed a self-sharpened downstream velocity profile, with momentum

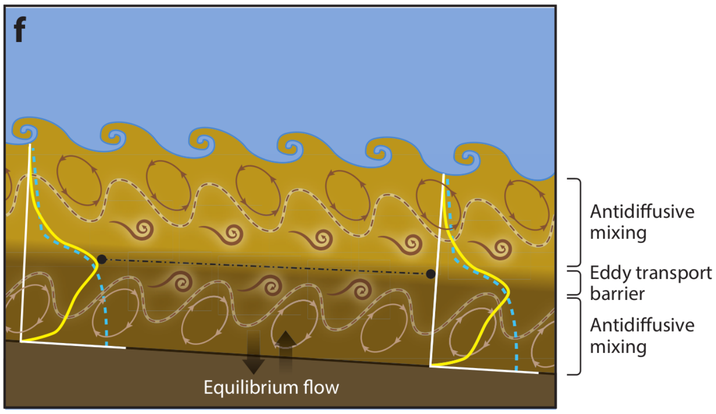

Figure 2.6: An illustration of internal gravity wave driven antidiffusive mixing from Wells & Dorrell (2021), as proposed by Dorrell *et al.* (2019) to explain the concentration of momentum at the height of the velocity maximum, and strongly stepped density profile, observed in measurements of flow in the Black Sea. The solid yellow and dashed blue lines illustrate the velocity and density fields respectively, the dot-dash black line the centre of mass of the flow, and the brown arrows/lines the incidence of turbulent mixing and internal waves.

concentrated towards the velocity maximum, and a highly stepped density profile featuring a sharp decrease above the velocity maximum (Dorrell *et al.*, 2019). To explain these observations, Dorrell *et al.* (2019) proposed internal gravity waves resulting from interfacial instabilities or bedforms. Irreversible wave breaking at some critical layer within the flow (see below) may cause local flow acceleration (Bühler, 2014), and result in the formation of an eddy transport barrier. This barrier is capable of maintaining the density difference within the body over larger distances than previously thought (Dorrell *et al.*, 2019; Wells & Dorrell, 2021). This mechanism is illustrated by Wells & Dorrell (2021) (see Figure 2.6). However, this explanation questions key assumptions about the gravity current body. An accelerating flow is inherently not statistically steady. Further, the presence of an eddy transport barrier requires a three-dimensional flow (Dorrell *et al.*, 2019; Wells & Dorrell, 2021).

Critical layers are of particular importance in the atmosphere and oceans (Booker & Bretherton, 1967; Bretherton, 1966; Hines, 1968). A critical layer is a region within the flow where the wave speed is close to the mean flow speed (Baines, 1998; Maslowe, 1986). When considering a density-stratified shear flow the importance of this region can be seen in the Taylor Goldstein equation that governs flow stability (Baines, 1998),

$$(\overline{U}-c)^2\left(\frac{d^2\hat{\phi}}{dY^2}+\left[\frac{N^2}{(\overline{U}-c)^2}-\frac{d^2\overline{U}/dY^2}{(\overline{U}-c)}-k^2\right]\hat{\phi}\right)=0, \tag{2.6}$$

where $\overline{U}$ is the local mean downstream velocity, $\phi=\hat{\phi}e^{ik(x-ct)}$ is a perturbation stream function, c is the wave speed, N the buoyancy frequency, and k the downstream wave number. A region with $\overline{U}=c$ constitutes a singularity in this equation, the presence of which suggests that a process assumed to be negligible during the derivation of the equation (e.g. dissipation or non-linearity) may be significant near the critical layer

(Baines, 1998; Booker & Bretherton, 1967). In order for this equation to hold, when the magnitude of the term multiplying ϕ becomes very large near the critical layer, the magnitude of $\partial\phi^2/\partial Y^2$ must also be very large. Therefore, ϕ may oscillate rapidly in Y, with the oscillations becoming infinitely rapid as the point where $\overline{U} = c$ is approached (Vallis, 2017). The transmission of wave energy across a critical layer is very small, with the critical layer reflecting or absorbing internal waves (Baines, 1998). Energy absorbed at a critical layer, as a result of wave breaking, is transferred to the mean flow causing acceleration local to the critical layer (Baines, 1998; Booker & Bretherton, 1967). Additionally critical layers can be a region of local mixing, resulting in a region of near-uniform velocity and density with wave breaking resulting in the homogenisation of potential vorticity either side of the critical layer (potential vorticity being a measure of circulation that is conserved in the absence of dissipation, defined as the product of density stratification and vorticity) (Baines, 1998; Dorrell *et al.*, 2019). This homogenisation produces strong potential vorticity gradients, which act as barriers to eddy transport and prevent mixing between regions above and below the critical layer (Dritschel & Scott, 2011). In a gravity current, this would maintain the density difference between the current and ambient fluids.

2.3.1 Turbulence in the Body

There are two mechanisms for turbulence generation in the body – shear, and buoyancy (Bhaganagar, 2017; Buckee *et al.*, 2001; Kneller & Buckee, 2000). If the gradient Richardson number is greater than the critical value, then energy produced by shear is dissipated (being insufficient to overcome the stability of the density stratification), while a low gradient Richardson number indicates unstable stratification (Buckee *et al.*, 2001). However, the gradient Richardson number may be below the critical value in the head of the flow, and above critical in the body. In this case, Kelvin-Helmholtz billows generated in the less stable head, and which significantly enhance mixing, dissipate some distance into the stable body (Pelmard *et al.*, 2020). Turbulence production by buoyancy is possible even in stable stratification, as turbulent kinetic energy may be generated by the conversion of potential energy if sections of fluid are displaced from their equilibrium positions (Buckee *et al.*, 2001). Interface stability is weakly dependent on Schmidt number, with the current-ambient interface becoming slightly more stable as Schmidt number increases (Bonometti & Balachandar, 2008).

Turbulence in the current is strongly linked to mixing (Bhaganagar, 2017). The strongest mixing in the gravity current body is a result of detrainment near the current-ambient interface (current fluid being lost to the ambient), while a smaller amount of mixing also occurs near the bed as a result of ambient entrainment (Odier *et al.*, 2012). For low Richardson numbers, turbulent mixing lengths scale with shear, not buoyancy.

However, at high Richardson number (e.g. in the ocean) the mixing length scale is determined by buoyancy (Odier *et al.*, 2009). Entrainment rates are reduced by increased density stratification (Krug *et al.*, 2015).

The highest levels of turbulence (turbulent velocities, Reynolds stresses, and turbulent kinetic energies) are a result of shear (Bhaganagar, 2017; Buckee *et al.*, 2001; Gray *et al.*, 2006; Islam & Imran, 2010; Kneller *et al.*, 1999). Instantaneous turbulent velocity calculations identify the movement of eddies through the flow with size comparable to the height of the lower layer of the body (Kneller *et al.*, 1999). Large eddies are generated through shear in the upper layer (Cantero *et al.*, 2008; Kneller *et al.*, 1999), while smaller eddies are generated through shear with the lower boundary (Kneller *et al.*, 1999). The formation of vortices on the current-ambient interface is highly Schmidt number dependent (Bonometti & Balachandar, 2008).

Reynolds stress, $\tau_R = -\rho(\overline{U'V'})$ where ρ is density, U' and V' are the downstream and vertical fluctuations from the mean velocity, and $\overline{(\cdot)}$ indicates an averaged property, gives an indication of turbulence in the flow (Buckee *et al.*, 2001) and contributes to mean momentum transfer by turbulent motion, as gradients in Reynolds stress lead to net acceleration (Gray *et al.*, 2006). The largest values of $U'V'$ within the body are associated with bed shear, while above the velocity maximum Reynolds stress associated with shear at the current-ambient interface is negative (indicating a downwards transfer of momentum) (Bhaganagar, 2017; Buckee *et al.*, 2001; Cossu & Wells, 2012; Kneller *et al.*, 1997). This may be a result of large-scale coherent structures (Buckee *et al.*, 2001).

Typical averaged turbulent kinetic energy profiles are shown in Figure 2.7 (Buckee *et al.*, 2001; Gray *et al.*, 2006). Turbulent kinetic energy is at a minimum at the height of minimum shear, around the same height as the velocity maximum, and with local maxima above and below this point within the body (Buckee *et al.*, 2001; Islam & Imran, 2010; Kneller *et al.*, 1999; Pelmard *et al.*, 2020). In flows with a stepped density profile (see Figure 2.3), the area of low turbulent kinetic energy at the velocity maximum may be a result of strong stratification at the step in the concentration profile (Buckee *et al.*, 2001). Further, the strength of stratification at this point could lead to low transport of mass between the lower and upper parts of the current, maintaining the density difference between current and ambient (Buckee *et al.*, 2001). However, Islam & Imran (2010) suggest that the turbulent kinetic energy at the height of the velocity maximum is large enough to allow transport across the velocity maximum, with diffusion increasing turbulence at the height of minimum shear and facilitating vertical redistribution of turbulence.

There is some dispute regarding the magnitude of cross-stream contributions to body flow. Islam & Imran (2010) conclude that the contribution of cross-stream flow to total turbulent kinetic energy is at least as large as that of vertical velocity and should be included in calculations of turbulent kinetic energy. Krug *et al.* (2015), on the other hand, conclude that cross-stream variations are small and can be neglected when considering

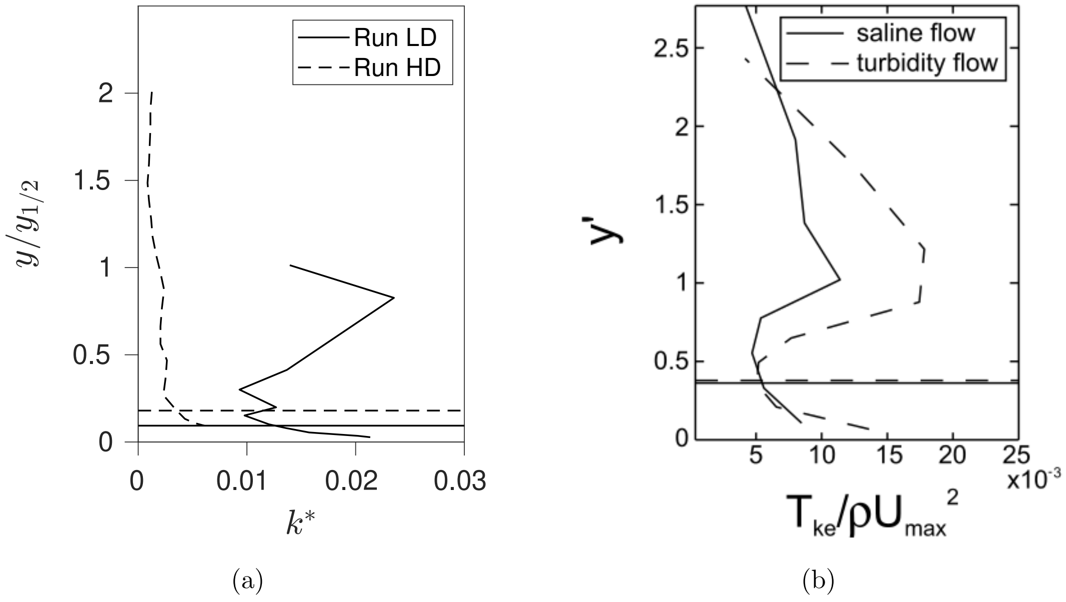

(a) (b)

Figure 2.7: Plots of turbulent kinetic energy for two flows from the work of (left) Buckee *et al.* (2001) (remade) and (right) Gray *et al.* (2006). The horizontal lines indicate the height of the average downstream velocity maximum.

entrainment of ambient fluid. Whether this apparent contradiction is attributable to the low spatial resolution of Islam & Imran (2010), the additional source of turbulence in Krug *et al.* (2015), or a difference in Reynolds or Richardson number between the two works is unclear. Pelmard *et al.* (2020) conclude that cross-stream velocity fluctuations are equivalent to vertical in an unsteady lock-exchange type flow.

2.4 Investigative Approaches

Direct measurements of real-world flows are challenging as a result of their often inaccessible location, their hazardous nature, their unpredictability, and the length and velocity scales involved (Azpiroz-Zabala *et al.*, 2017; Kneller & Buckee, 2000; Peakall & Sumner, 2015; Simpson, 1997; Wells & Dorrell, 2021). Therefore, many observations of field-scale flows have been indirect (Kneller & Buckee, 2000), for example estimates of gravity current front velocity based on the breaking of submarine cables 300 miles apart over 13 hours in Newfoundland in 1929 (Simpson, 1997). Recent technological advances (such as autonomous underwater vehicles) have allowed far more real-world measurements than previously possible and in far more detail (Azpiroz-Zabala *et al.*, 2017; Dorrell *et al.*, 2019; Sumner *et al.*, 2013), however to date laboratory-based and numerical investigations provide the highest resolution measurements of flow in the gravity current body.

2.4.1 Experimental Approaches

Experimental investigations into flow in the head have applied a wide variety of techniques to establish flow properties. Early works used shadowgraphs (Simpson, 1969), and tracked tracer particles and dye droplets across photographs (Britter & Simpson, 1978; Middleton, 1966; Simpson, 1969) to improve understanding of flow structure. Velocity structure has been investigated using hot film probe techniques (Britter & Simpson, 1978; Simpson & Britter, 1979), particle tracking velocimetry (Thomas *et al.*, 2003), and particle image velocimetry (Alahyari & Longmire, 1996; Martin & García, 2009). Density structure has been investigated using conductivity probes (Parsons & García, 1998; Simpson & Britter, 1979), laser induced fluorescence (Parsons & García, 1998), and planar laser induced fluorescence (Martin & García, 2009). Additionally, mixing in the head has been investigated using neutralisation (Hallworth *et al.*, 1996) and light attenuation (Nogueira *et al.*, 2014; Sher & Woods, 2015, 2017) techniques.

Fewer techniques have been applied to flow in the body. Kneller *et al.* (1997) and Kneller *et al.* (1999) used laser Doppler anemometry to measure the instantaneous two-dimensional velocity profile of an unsteady lock-exchange type current with a very short duration of body flow, $\mathcal{O}(5\,\mathrm{s})$. Buckee *et al.* (2001) applied the same technique to a constant-influx type flow, again with measurements limited to two components of velocity and with low spatial resolution. This work was extended by Gray *et al.* (2006) (with a low temporal sampling frequency) and Cossu & Wells (2012) to consider all three components of velocity using ultrasonic Doppler velocity profilers and acoustic Doppler velocity profilers. All of these works exclusively considered a cross-stream central location within the flow.

In recent years, the gravity current body has been investigated using techniques capable of producing whole-field data. High spatial resolution, whole-field, instantaneous particle image velocimetry measurements on a central plane, in some cases combined with simultaneous density measurements using laser induced fluorescence, have been used to discuss entrainment and mixing in constant-influx gravity currents (Krug *et al.*, 2013; Odier *et al.*, 2009, 2012). However, some of these measurements had low temporal resolution (Odier *et al.*, 2009, 2012), and all three investigations considered flows with a source of turbulence at the domain inlet, additional to the shear and buoyancy sources expected in such a flow. These flows are shown to be expanding downstream and have heights linked to the size of the domain outlet, despite being described as statistically steady gravity current bodies (Krug *et al.*, 2013; Odier *et al.*, 2009, 2012).

Sher & Woods (2017) used a light attenuation technique to investigate mixing in the constant-influx body, though as the focus was on concentration no instantaneous velocity measurements were presented. Krug *et al.* (2015) used simultaneous three-dimensional volumetric measurements of the velocity and density fields of a constant-influx flow using scanning particle tracking velocimetry and scanning laser induced fluorescence to consider entrainment in the gravity current body. The volume considered in this work was small (4 cm × 4 cm × 2 cm in a domain 200 cm × 50 cm × 50 cm). A larger measurement volume in the same experimental domain (four connected regions of 9 cm × 9 cm × 4 cm) was considered by Neamtu-Halic *et al.* (2019) to investigate vortical Lagrangian coherent structures at the turbulent/non-turbulent interface using three-dimensional particle tracking velocimetry. In both of these works, measurements were limited to the current-ambient interface, and the techniques were again applied to an expanding flow (as in (Krug *et al.*, 2013)).

Lefauve *et al.* (2018) investigated the formation of Holmboe waves in an exchange type flow, with equivalent downstream velocity magnitude in both fluids. This would increase the level of shear compared with other gravity current flows such as that in Krug *et al.* (2015) where average downstream velocity in the ambient is near 0. As in Krug *et al.* (2015), these measurements were taken using a scanning PIV technique so were not instantaneous. Experimental measurements in the existing literature have largely been limited planes at a single cross-stream location (the exceptions being volumetric measurements in Krug *et al.* (2015), Lefauve *et al.* (2018), Neamtu-Halic *et al.* (2019), and a single plane in Alahyari & Longmire (1996)), and the extent and nature of three-dimensional flow within the body remains unclear.

Laboratory-based flows are typically limited to much lower Reynolds numbers than real-world flows, and rely on dynamic similarity of the laboratory-based and real-world flows (Meiburg & Kneller, 2010). This is justified by similar values of the dimensionless parameters such as Froude and Reynolds numbers (see Chapter 3, (Heller, 2011; Rubinato, 2015)). Many experimental techniques have additional restrictions that limit the investigable parameter ranges. For instance, the available values of reduced gravity are limited in optical techniques requiring refractive index matching. There are also parameters that cannot typically be investigated through experimental methods, like the Schmidt number. These restrictions are reduced with numerical methods. Numerical work also typically has far fewer restrictions on available data, being capable of providing high-resolution, whole-domain, instantaneous velocity and density fields simultaneously.

2.4.2 Numerical Approaches

Numerical contributions to this chapter have come from direct numerical simulation (DNS) (Cantero *et al.*, 2008; Espath *et al.*, 2014; Necker *et al.*, 2002; Özgökmen *et al.*, 2006), and large eddy simulation (LES) (Bhaganagar, 2017; Ooi *et al.*, 2009; Pelmard *et al.*, 2020) of unsteady lock-exchange type gravity current flows. Direct numerical simulation is the more accurate method, but is extremely computationally expensive (with the cost scaling like Re^3Sc^2; see Chapter 3) (Meiburg & Kneller, 2010; Pope, 2001; Wilcox, 2006). It requires the resolution of all length scales down to the Kolmogorov scale (or the Batchelor scale when Schmidt number is above 1 (Andersson *et al.*, 2011; Donzis *et al.*, 2014)). Due to the high computational cost, three-dimensional direct numerical simulation has only become an option in recent years. Even with recent advances in computational power, three-dimensional simulations are limited to laboratory-scale flows.

LES does not require resolution of all turbulence scales, instead resolving the large eddy scales and modelling motions below some limit (Meiburg & Kneller, 2010; Pope, 2001; Wilcox, 2006). This is significantly less computationally expensive, and is therefore applicable to a wider range of flows, but has the additional complexity of requiring a subgrid-scale model such as an eddy-viscosity approximation (Meiburg & Kneller, 2010). LES can be applied to much higher Reynolds number flows (Ooi *et al.*, 2009; Pelmard *et al.*, 2020). However, even this method cannot yet be applied to gravity currents with field-scale Reynolds numbers as a result of the lower boundary, which introduces energy containing, small-scale eddies that must be captured (Meiburg & Kneller, 2010).

To overcome the high computational cost of numerical work, many investigations have relied on two-dimensional simulations (for example, Birman & Meiburg (2006); Bonometti & Balachandar (2008); Ooi *et al.* (2007)). Two-dimensional simulations allow investigation of a much wider range of Reynolds number flows, for example Härtel *et al.* (2000) were limited to $Re = 750$ for their three-dimensional simulations, but were able to achieve $Re = 30000$ in two-dimensions. However, the three-dimensional nature of gravity current flows means the reliability of such simulations is suspect.

While some characteristics of gravity current flows are captured well by two-dimensional numerics, for example the height of the over hanging nose and the Froude number, other characteristics such as the thickness of the mixed layer and the current front velocity are different between two- and three-dimensional simulations (Cantero *et al.*, 2007, 2008; Härtel *et al.*, 2000; Özgökmen *et al.*, 2004). Two-dimensional simulations are unable to capture edge effects in cross-stream constrained flows (Özgökmen *et al.*, 2004), and are known to exhibit large and unphysical vortices not present in three-dimensional work (illustrated in Figure 2.8) (Cantero *et al.*, 2007, 2008; Espath *et al.*, 2014; Härtel *et al.*, 2000; Necker *et al.*, 2002).

The effect of Kelvin-Helmholtz roll-up is stronger in two-dimensional simulations, as vortex stretching ($\omega \cdot \nabla \boldsymbol{u} = 0$) is suppressed and three-dimensionality helps to break up the cross-stream coherence (Cantero *et al.*, 2007). The presence of strong vortices, and their interactions, results in greater entrainment compared with three-dimensional simulations, and periods of large acceleration and deceleration not found in three-dimensional work (Cantero *et al.*, 2007; Özgökmen *et al.*, 2004). In a particulate flow, vortices transport particles vertically within the flow. Unphysical vortices can lead to overestimates of the capacity of the flow to maintain particle suspensions, and thus overestimates of run-out lengths (Necker *et al.*, 2002, 2005). The vortices also impact the energy budget of the

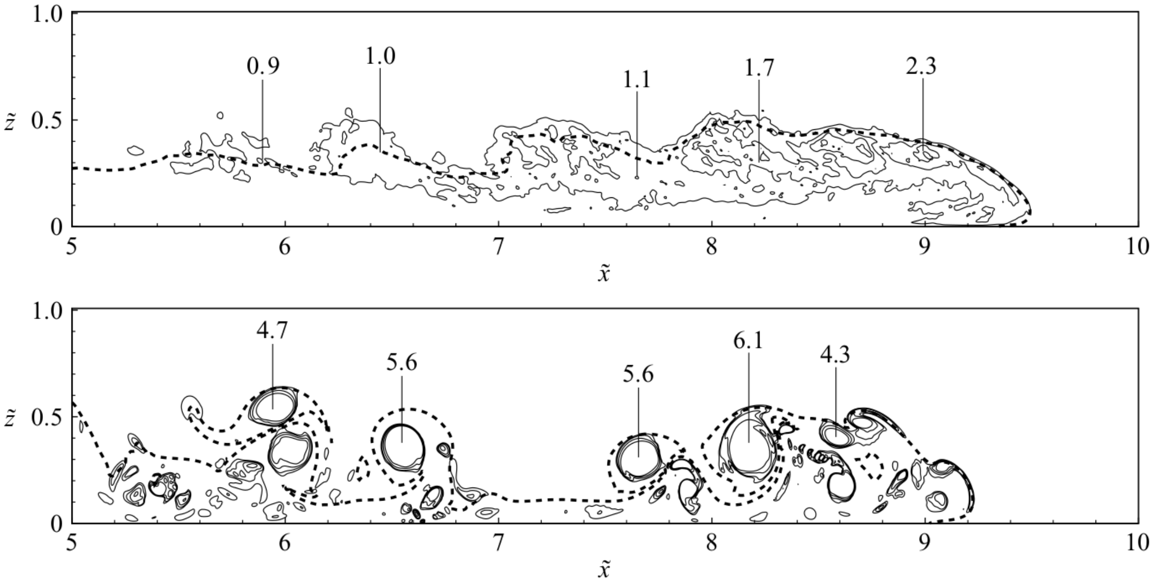

Figure 2.8: Taken from Cantero *et al.* (2007), contours of swirling strength defined by Zhou *et al.* (1999) illustrating the unphysical vortices present in two-dimensional simulations, by comparing equivalent two-dimensional (bottom) and cross-stream averaged three-dimensional (top) simulations of the same flow. The dashed line is a contour of density demonstrating the flow boundary, and numbers indicate local values of swirling strength.

flow, with kinetic energy decaying less rapidly in two-dimensional work (Necker *et al.*, 2002). Even three-dimensional simulations can overestimate entrainment compared with real-world flows because of the idealised nature of the domain (Özgökmen *et al.*, 2004).

Despite the capacity of numerical work to investigate the effect of Schmidt/Prandtl number, very few works have so far applied this ability to gravity current flows. The vast majority of numerical works assume $Sc \sim 1$ (Bhaganagar, 2017; Birman & Meiburg, 2006; Cantero *et al.*, 2007, 2008; Härtel *et al.*, 2000; Necker *et al.*, 2002; Özgökmen *et al.*, 2004, 2006; Pelmard *et al.*, 2020). A few justify this assumption with test calculations (Birman *et al.*, 2005; Necker *et al.*, 2005), but to the author's knowledge only two investigations have performed simulations of gravity currents with $Sc \gg 1$. Ooi *et al.* (2007) compared a single $Sc = 600$ simulation to an otherwise equivalent $Sc = 1$ flow, and concluded that there was little impact on front velocity. Bonometti & Balachandar (2008) conducted a more extensive parameter study considering $100 < Re < 10000$ and $1 < Sc < 1000$, with the highest Schmidt numbers achieved by removing the term that is inversely proportional to the Schmidt number from the governing equations (i.e. setting the right hand side of (3.13) to 0). In both cases, the conclusions are heavily (Bonometti & Balachandar, 2008) or exclusively (Ooi *et al.*, 2007) based on two-dimensional simulations. The effect of Schmidt number on three-dimensional flow features is therefore unknown.

2.5 Summary

A summary of existing understanding of gravity current structure has been presented, with an emphasis on those investigations considering the flow body. Despite the extensive research into gravity current flows in general, understanding of body structure remains limited. This chapter has highlighted the need for additional experimental and numerical investigations to resolve remaining questions regarding the gravity current body, specifically: the nature of large-scale structures within the body, the level of three-dimensionality within the body, and the importance of Schmidt number to body structure.

Chapter 3

Methodology

The ubiquitous nature of gravity currents means that they have been extensively studied, as discussed in Chapter 2. However, this work has primarily focused on the head, despite the body often forming the largest part of the flow. Additionally, the majority of the existing work has focused on lock-exchange rather than constant-influx type flows. There therefore remain significant gaps in understanding of the structure and mechanics of the gravity current body.

The following chapter outlines the technical details of the investigations here used to quantify the velocity structure of constant-influx gravity currents. Both laboratory-based and numerical techniques are discussed, including all experimental variables and parameters. Section 3.1 describes the details of the planar laboratory investigations, Section 3.2 the volumetric laboratory investigations, and Section 3.3 the three-dimensional numerical work.

3.1 Planar Particle Image Velocimetry

In the present study, two experimental techniques were employed to establish the effect of Reynolds number on the turbulence structure of the body of constant-influx gravity currents – planar particle image velocimetry (PIV) and Shake-the-Box particle tracking velocimetry (STB). In this section, the experimental setup is outlined, with justification of design choices, along with details of seeding particles, timings, camera configuration and reconstruction settings for the PIV work.

3.1.1 Background

Planar PIV is a non-intrusive technique for generating the two-dimensional velocity field of a flow. It is described in detail in several places, e.g. Adrian & Westerweel (2011); Raffel *et al.* (2018), and the steps involved are summarised in Figure 3.1. PIV has been used extensively to study a wide variety of flows, including gravity currents. Some

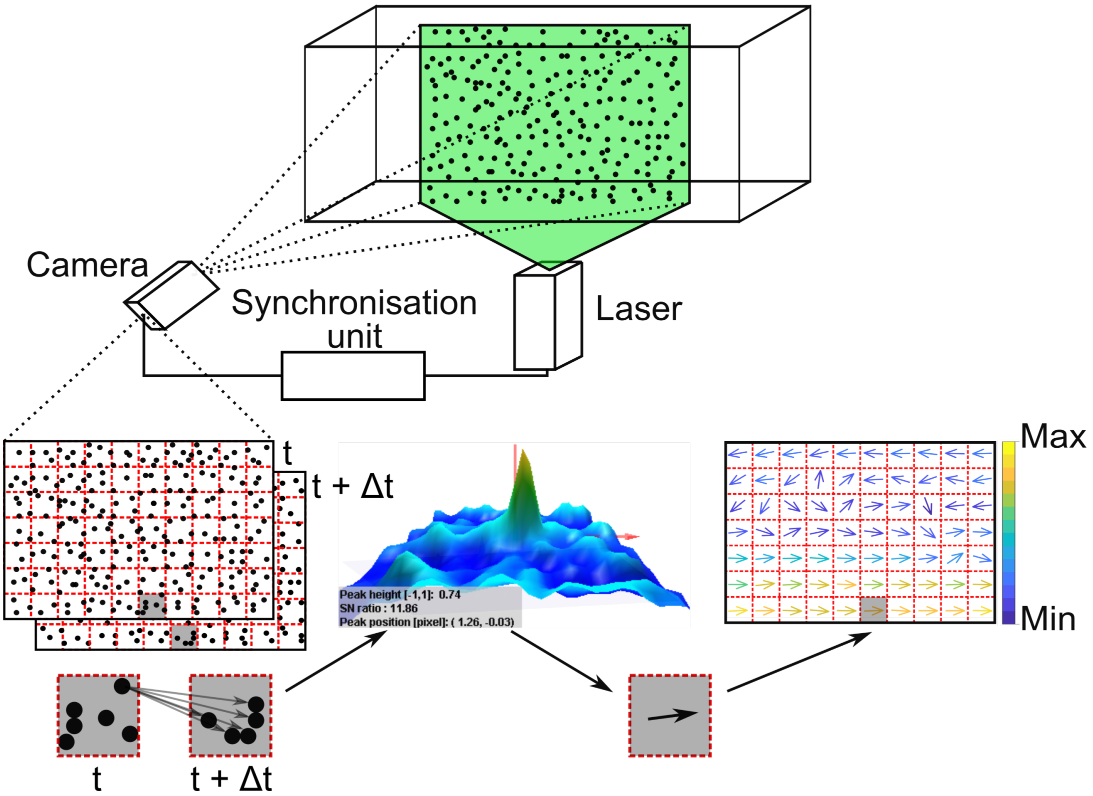

Figure 3.1: The steps involved in generating a velocity field from planar PIV images.

examples of work investigating gravity current structure using PIV are summarised in Table 3.1. The technique is able to rapidly collect large amounts of data that qualitatively and quantitatively describe the flow (Norconk, 2011; Unsworth, 2015). Additionally, the whole-field nature of PIV allows application of analysis techniques not applicable to data collected with point-wise techniques. However, as PIV is an optical technique there is a restriction on density difference due to the need for refractive index matching.

3.1.2 Experimental Setup

When investigating environmental flows, it is not typically possible to consider a full-scale flow. Therefore scale models that demonstrate some level of similarity with the real-world flow are designed (Heller, 2011; Rubinato, 2015). The similarity could be:

- geometric,
- kinematic, and/or
- dynamic.

Geometric similarity indicates that the model and full-scale structures have the same shape, with all linear dimensions having the same scaling ratio. Kinematic similarity requires geometrically similar motions, for example the ratio between horizontal and vertical velocities in the model and the real-world flows should be the same. In this case, motion that is circular in one case will also be circular in the other. Dynamic similarity

Author	Current Type	Key Focus
Alahyari & Longmire (1996)	Solute, axisymmetric lock-release	Vortex formation.
Patterson *et al.* (2006)	Solute, axisymmetric lock-release	Development and propagation of the flow.
Samothrakis & Cotel (2006)	Solute, constant-influx	Propagation into stratified ambient, mixing.
Zhu *et al.* (2006)	Solute, lock-release	Velocity and vorticity structure of the slumping phase over time.
Gerber (2008)	Solute, constant-influx	Reynolds stresses, Reynolds fluxes.
Martin & García (2009)	Solute, arrested constant-influx	Mixing at the current front.
Odier *et al.* (2012)	Solute, constant-influx	Mixing processes on inclined plane gravity currents.
Krug *et al.* (2013)	Solute, constant-influx	Entrainment and dynamics near the turbulent/non-turbulent interface.
Nogueira *et al.* (2013)	Solute, lock-release	Effect of bed roughness.
Nogueira *et al.* (2014)	Solute, lock-release	Dynamics and development of the head.
Krug *et al.* (2015)	Solute, constant-influx	Entrainment and dynamics near the turbulent/non-turbulent interface.
Lombardi *et al.* (2015)	Solute, lock-release	The effect of the current flowing upstream.
Yuan & Horner-Devine (2017)	Solute, constant-influx	Vortices, comparison of spreading and unconfined flows.

Table 3.1: Some examples of the existing gravity current research using PIV.

	Definition	Force Balance
Froude number (Fr)	$\frac{U_c}{\sqrt{gL_c}}$	Inertial/Gravitational
Euler number (Eu)	$\frac{\rho U_c^2}{\Delta p}$	Inertial/Pressure
Reynolds number (Re)	$\frac{\rho U_c L_c}{\mu}$	Inertial/Viscous
Weber number (We)	$\frac{U_c}{\sqrt{\sigma/\rho L_c}}$	Inertial/Capillarity
Peclet number (Pe)	$\frac{L_c U_c}{D}$	Advection/Diffusion

Table 3.2: Dimensionless parameters for dimensional analysis, where U_c and L_c are characteristic velocity and length scales, g is gravitational acceleration, ρ is density, Δp is pressure difference, μ is dynamic viscosity, σ is surface tension, and D is the mass diffusivity (Birman *et al.*, 2005; Chung, 2002; Heller, 2011; Johnson & Hogg, 2013).

indicates that the magnitudes of forces at corresponding points in the full-scale flow and the model are in a fixed ratio (Zohuri, 2015).

These similarities are established by considering a dimensional analysis that takes into account fluid properties such as density and viscosity, the geometry of the flow, and flow properties such as velocity, and results in a number of dimensionless parameters (specifically the Froude, Euler, Reynolds, Weber, and Peclet numbers) (Chung, 2002; Heller, 2011). The critical dimensionless parameter or parameters to match depend on the forces that dominate in the system, and must match exactly between the laboratory-scale and real-world flows. For this work, the key parameter to match is the Reynolds number.

Prototypes

The work in this thesis focuses on solute-based flows. This is justified as in Kneller & Buckee (2000) by considering that while many natural examples of gravity currents are particulate based, solute-based flows are the simplest case and thus form a sensible control data set without the addition of particles limiting the measurement tools available. Additionally, solute-based flows are considered analogous to conservative fine-grained particulate flows while being easier to control experimentally (García & Parsons, 1996; Parsons & García, 1995).

A ducted flow was considered, in an attempt to avoid the surface waves that appear at the air-ambient interface of open-channel gravity current flows. If the ambient fluid is of finite thickness, there may be interactions between ambient surface waves and current flow. The effects of these interactions, such as a reduction in front velocity and a decrease in turbulence (Baker *et al.*, 2017; Musumeci *et al.*, 2017; Viviano *et al.*, 2018) can be difficult to separate from the current (Ho *et al.*, 2018).

Before arriving at the final experimental setup, two prototypes as shown in Figure 3.2 were designed. First, a proof of concept simply involving an airtight 10 cm×10 cm duct with an inflow at one end and an outlet at the other. This successfully demonstrated

Author	Tank Dimensions ($H \times W \times D$) (m)
Ellison & Turner (1959)	$0.20 \times 0.15 \times 5.00$
Middleton (1966)	$0.50 \times 0.154 \times 5.00$
Hacker *et al.* (1996)	$0.50 \times 0.21 \times 3.48$
Kneller *et al.* (1997)	$0.18 \times 0.20 \times 4.50$
Kneller *et al.* (1999)	$0.10 \times 0.2 \times 2.15$
Buckee *et al.* (2001)	$1.50 \times 0.50 \times 6.0$
Thomas *et al.* (2003)	$0.25 \times 0.20 \times 2.00$
Gray *et al.* (2005)	$0.50 \times 0.30 \times 6.00$
Martin & García (2009)	$0.50 \times 0.30 \times 3.00$
Gerber *et al.* (2010)	$0.30 \times 0.25 \times 3.00$
Adduce *et al.* (2011)	$0.30 \times 0.20 \times 3.00$
Nogueira *et al.* (2014)	$0.30 \times 0.20 \times 3.00$
Sher & Woods (2015)	$0.36 \times 0.15 \times 3.00$
Sher & Woods (2017)	$0.50 \times 0.10 \times 5.00$

Table 3.3: Some examples of the dimensions of tanks used to investigate gravity currents experimentally in previous work.

that, having filled the system with ambient, opening the outlet and pumping dense fluid in through the inlet would not cause the overall level of fluid to change. For the second prototype, a drop was added above the outlet to prolong the duration of the flow prior to the ambient becoming polluted. The system was made taller relative to the width (a cross-section of 10 cm× 20 cm) to minimise interaction between the lid and the current. The extra height also increased the amount of ambient fluid relative to the current height and therefore slowed the rate of pollution. Flow visualisation was carried out in each prototype by adding dye to the dense fluid, shown in Figure 3.3.

Tank Geometry

The final experimental design is shown in Figure 3.4, and is made from ∼10 mm thick Perspex. The dimensions were considered reasonable as both the dimension magnitudes and the aspect ratio are similar to those used to investigate gravity currents in previous work (see Table 3.3). From the second prototype, raised sections were added at either end to capture any air entering through the inlet or outlet. A bubble trap was also added to remove any small bubbles entering the system as a result of pumping of the dense fluid. These measures prevented any bubbles entering the measurement region and causing laser reflections that could reduce the quality of the data, and potentially damage the camera. The tank was mounted on a mechanism that could be tilted to produce a variable bed slope, θ, and coarse mesh was placed over the inlet in an attempt to produce a homogeneous inflow. The drop above the outlet was extended and the tank lengthened to further prolong the duration of the pseudo-steady body (see Figure 3.5). The 6 mm thick full-width Perspex sheet near the inlet was included to promote horizontal spreading of the dense fluid, and limit the initial height of the flow to 0.05 m.

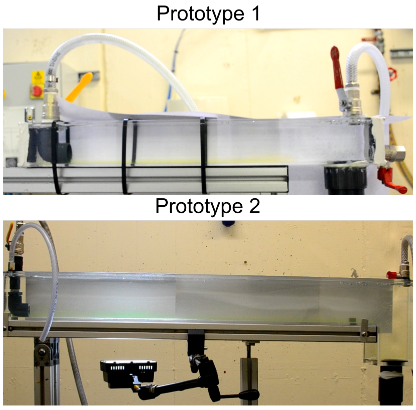

Figure 3.2: The prototypes.

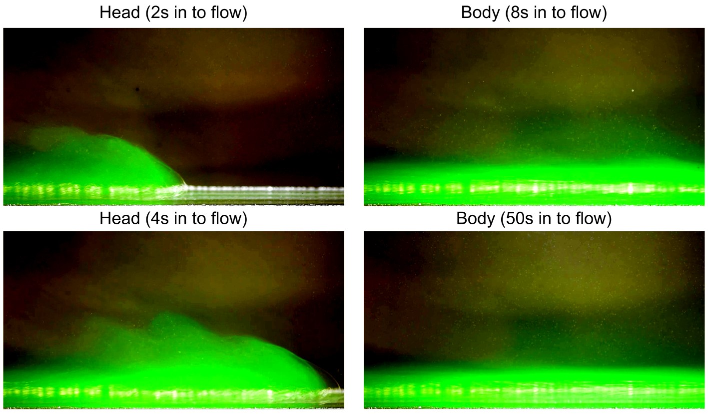

Figure 3.3: Visualisation of flow in prototype 2.

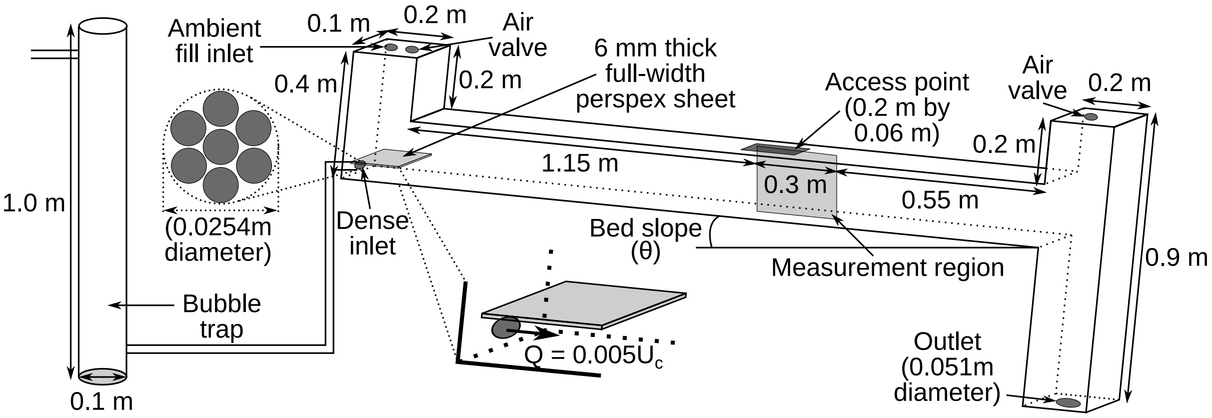

Figure 3.4: Experimental setup.

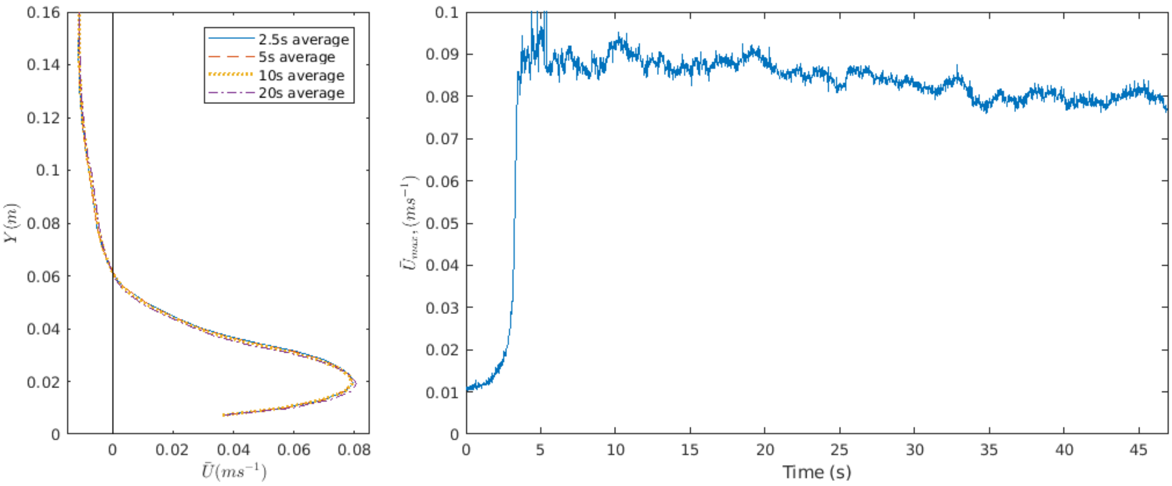

Figure 3.5: Plots demonstrating statistically steady flow in the current body for one case, (left) comparison of downstream velocity time averages over different durations, (right) maximum downstream velocity over time.

	Substance	ρ (kg m^{-3})	n	η (Pa s)
Current	KDP solution, 6% by mass	1041.4	1.3400	0.001133
Ambient	Glycerol solution, 6% by mass	1012.0	1.3400	0.001157

Table 3.4: Properties of the fluids making up the ambient and the current (Haynes, 2014).

Fluids

As PIV is an optical technique, the current and ambient fluids, as well as mixtures of the two, must be refractive index (RI) matched (Norconk, 2011; Unsworth, 2015). This means that when light travels between the fluids there is no reflection or refraction, effectively rendering the entire system transparent and preventing any blurring or distortion of the images produced (Alahyari & Longmire, 1994). According to Alahyari & Longmire (1994), in order to obtain usable PIV images the RI within the measurement region must be constant to within 0.0002. They recommend solutions of glycerol and potassium dihydrogen phosphate (KDP) in tap water, as they have certain useful properties such as being inert, easy to mix, and stable enough to be left for a few days. In this work 6% by mass solutions of glycerol (ambient fluid) and KDP (current fluid) were used, producing a 3% density difference (see Table 3.4 for details), a slightly larger density difference than the sodium chloride and ethanol combination used by Krug *et al.* (2015); Odier *et al.* (2012).

The solutions were produced in mixer tanks as shown in Figure 3.6 with LAFERT IEC-60034 motors. In order to produce KDP solution in the volumes needed, a large batch was mixed in a 130 L tank, and then a smaller quantity placed in a 30 L transfer tank connected to the gear pump. The density and RI of these solutions were measured using an Anton Paar DMA$^{\text{TM}}$ 35 basic portable density meter (accurate to 0.001 g cm^{-3}) and a Reichert AR200 automatic digital refractometer (accurate to 0.0001 units). The temperature was also measured during production of the solutions to ensure that any temperature difference would not significantly impact on the RI matching later on. To ensure the solutions were fully mixed, it was required that there be 3 consistent consecutive RI measurements per solution taken 5 minutes apart, and that the RI of the two solutions be matched exactly (to the precision of the refractometer) in those measurements. The density was then measured to ensure that it was within the expected range based on temperature and RI.

The tank was initially filled with ambient fluid using the glycerol mixer pump to around 1 cm from the top of the raised sections at either end of the tank. This level remained approximately fixed throughout all experiments, and never dropped below the level of the main section lid. Denser fluid was pumped in through the inlet using a Universal Motors IEC34-30 gear pump fitted with an LS Industrial Systems SV-iC5 inverter, to provide a smooth and continuous influx that could be manually varied from run to run. Figure 3.7 shows the relationship between pump frequency and flow rate produced by the gear pump. To vary the Reynolds number of the flow, the influx was

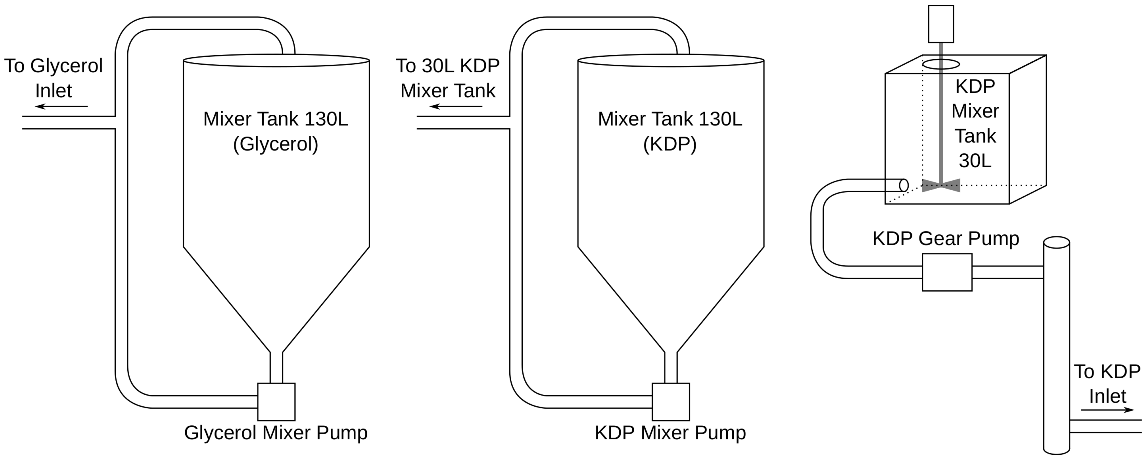

Figure 3.6: The equipment used to mix the glycerol and KDP solutions.

Case	1	2	3	4	5	6	7
Influx (Ls^{-1})	0.07	0.09	0.11	0.12	0.14	0.16	0.18
Fr_S	1.65	2.05	2.44	2.84	3.24	3.64	4.04
Δt (ms)	20	20	20	20	20	20	20

Table 3.5: Details of the influx, the source Froude number (Fr_S), and the time between images for each planar PIV case.

varied while keeping the bed slope fixed (see Table 3.5 for a list of cases). The bed slope was always chosen to be $\sim 0.1^\circ$ to avoid the formation of large, static bubbles on the lid which could cause strong reflections and damage the camera. Also included in Table 3.5 is a source Froude number for each case, $Fr_S = U_c/\sqrt{g' L_c}$, where the characteristic velocity scale $U_c = Q/A$, Q ($\mathrm{m^3\,s^{-1}}$) is the fluid influx Q, divided by the area of the inlet $A = 5.07 \times 10^{-4}\,\mathrm{m}^2$, g' is the reduced gravity, and $L_c = 0.0254\,\mathrm{m}$ is the diameter of the inlet. For all cases, Fr_S is above 1 (in the range 1.65 to 4.04) suggesting that wave disturbances generated at the inlet cannot affect the flow front.

Seeding Particles

In PIV, the fluids involved are seeded with tracer particles that are visible to the camera. There are a number of factors related to these particles to be optimised (Adrian & Westerweel, 2011; Raffel *et al.*, 2018; Wieneke, 2017). They should fulfil various criteria, namely being: small enough to follow the flow without influencing it; large enough to have good illumination properties; chemically inert; close to neutrally buoyant; and symmetrical (Hadad & Gurka, 2013). Silver-plated hollow glass spheres with mean diameter 10 µm (distribution 2–20 µm) and density $1400\,\mathrm{kg\,m^{-3}}$ were therefore selected. The particles are symmetrical, and highly reflective. They are also small enough to follow the flow, as can be shown by calculating the Stokes velocity ($U_g = \frac{d_p^2(\rho_p - \rho)\boldsymbol{g}}{18\eta} = 1.72 \times 10^{-5}\mathrm{m\,s^{-1}}$ where d_p is particle diameter, ρ_p the particle density, ρ the liquid density, $\boldsymbol{g}$ the gravitational acceleration, and η the dynamic viscosity of the fluid) and relaxation time ($\tau_r = \frac{d_p^2 \rho_p}{18\eta} = 6.86 \times 10^{-6}\mathrm{s}$) using the particle details and KDP fluid details in Table

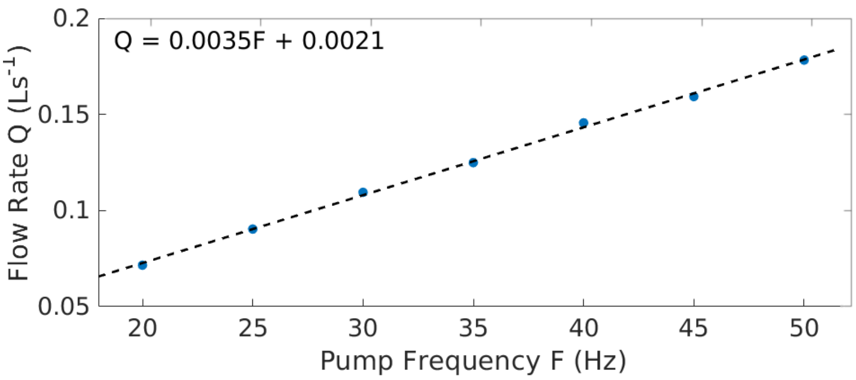

Figure 3.7: Flow rate vs. pump setting for the gear pump in the planar PIV work.

3.4 (Raffel *et al.*, 2018). These indicate that the settling velocity is significantly smaller than the typical measured velocity, and that the particles accelerate rapidly to the fluid velocity. Therefore the particles selected are appropriate for the measurements taken.

The PIV System

Creation of a light sheet in PIV typically uses lasers as they produce coherent, monochromatic light with high energy density that can be shaped into a thin sheet (Raffel *et al.*, 2018). As two images are taken very close together a double-pulsed laser is often used to avoid the need for a second laser, with the pulses synchronised with image collection (Adrian & Westerweel, 2011). Additionally, pulsed laser systems provide the needed light intensity while also effectively freezing particle motions by controlling image exposure (Grayson, 2018). The light sheet should be kept as thin as possible, as the goal is to capture two-dimensional flow and this technique is not able to distinguish motion in the third dimension. Here, a pulsed 532 nm Nd:YAG laser with maximum energy of 50 mJ was used to illuminate a central vertical plane in the tank parallel to the flow.

A camera, positioned perpendicular to the flow, is used to take images synchronised with the laser pulses at a specified time difference (Δt). In this work, the camera used was a DANTEC Dynamics SpeedSense camera with a Zeiss ZF.2 50 mm f/1.4 lens with aperture set to f/2.0 that captured roughly 0.2 m of flow horizontally (approximately halfway between the inlet and outlet) and 0.18 m vertically. The top and back of the tank were covered with a black aluminium polyethylene composite panel both to improve the image quality and contain the laser light. This panel also covered the top 2 cm of the front to further protect against camera damage due to bubbles. The tank was surrounded with light-tight laser curtains, and ambient illumination was minimised. To maximise the measurement duration while still capturing the full flow, the images were collected after the dense fluid had started being pumped into the tank but several seconds before the head would reach the measurement region. In each case, images were collected for 70 s at a rate of 50 Hz.

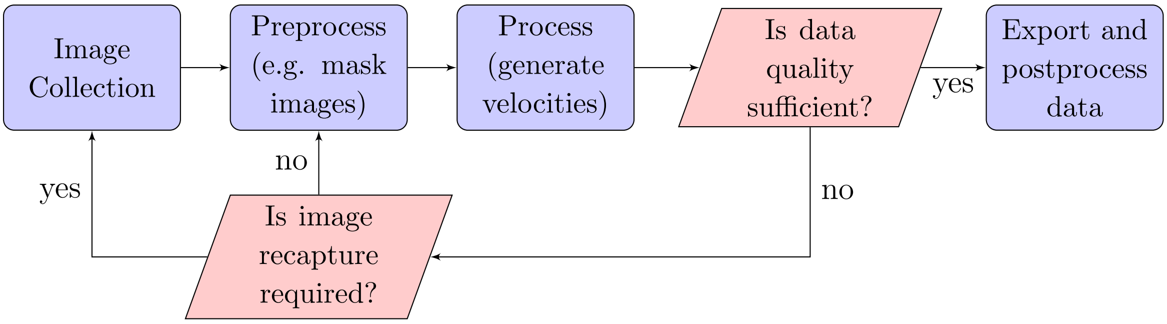

Figure 3.8: Flow chart illustrating the steps involved in planar PIV.

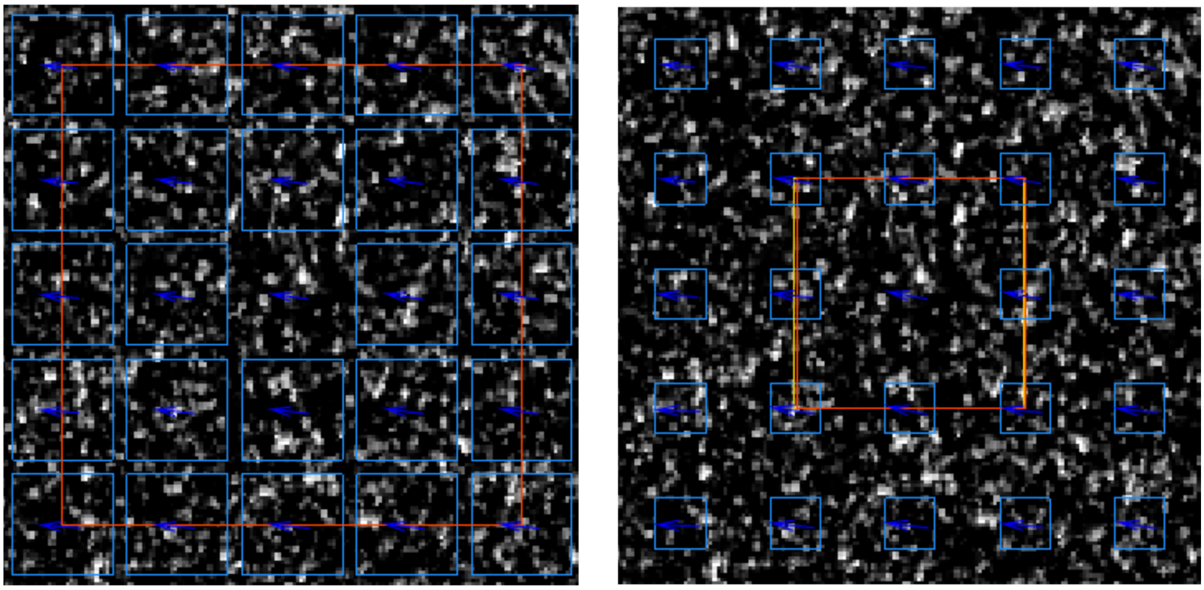

Figure 3.9: Images illustrating the adaptive PIV technique from a PIV case in this work. The left image illustrates a section of the vector field after the first adaptive PIV iteration, and the right image the same section after the second iteration. The blue squares indicate the locations of interrogation areas associated with the identified velocity vectors scaled such that they do not overlap, and the red/yellow squares show actual interrogation area size for the vector in the middle of the section.

3.1.3 The Adaptive PIV Algorithm

Preprocessing

Prior to processing, the images were modified to improve their quality. The effects of image artefacts (such as reflections from the Perspex walls of the tank, and shadows due to residual seeding from previous runs or bubbles attached to the side-walls) were removed. This was achieved by calculating a mean of all collected images from a single run, and subtracting this mean from each image individually.

Adaptive PIV

The velocity field was generated using the adaptive PIV method in DANTEC Dynamic Studio version 6.4 (described in detail in DantecDynamics (2018)). This technique initially establishes a scale factor – the conversion ratio between pixel displacement and displacement in metres – by the user specifying a known physical distance in a calibration image. The images are then divided into interrogation areas (IAs) with user-specified size and spacing. In this work, for all cases the space between IAs was set to 16 pixels both horizontally and vertically. A cross-correlation technique is used to compare each IA between images (separated by time Δt). In essence, a matrix is created for each IA containing the possible pixel displacements due to each particle in the first image having moved to the position of each particle in the second image. If the IA is sufficiently small, the 'actual' displacement of every particle within an IA will be similar, and different to the contributions from the 'incorrect' possible motions. Therefore, when the cross-correlation matrix is examined there will be a peak at the 'correct' displacement.

The choice of Δt is crucial, as a major source of error in PIV is the loss of a particle between the first and second images. When this is a result of in-plane motion, namely because the original particle was close to the edge of the interrogation area, the effect may be minimised by overlapping the interrogation areas, which also increases the resolution of the velocity field produced (Willert & Gharib, 1991). In order to maximise the ability of the software to track a particle between images, it is recommended that particles not move more than $\sim 1/4$ of the size of the IA in time Δt (Adrian & Westerweel, 2011). Out-of-plane motions, where particles move out of the illuminated plane due to three-dimensional motions, are harder to overcome. The only remedy is to reduce Δt. Therefore, Δt should be sufficiently large to detect the particle motions and sufficiently small to prevent too many particles leaving the measurement region. Figure 3.11 demonstrates typical motion of particles in this work between images with the chosen value of $\Delta t = 20\,\text{ms}$ as stated in Table 3.5.

When conducting adaptive PIV, the size and shape of the IAs, and hence the resolution of the velocity field, is dependent on the number of seeding particles in a given volume of fluid. Therefore, to an extent increasing the number of particles results in a higher-resolution velocity field. However, the particles must not become so closely packed that they are indistinguishable. Keane & Adrian (1992) and Unsworth (2015) recommend at least ~ 10 particles per IA. Through trial and error, it was determined that a concentration of $0.0015\,\text{g}\,\text{L}^{-1}$ in the current and $0.0014\,\text{g}\,\text{L}^{-1}$ in the ambient was appropriate for these experiments, as shown in Figures 3.10 and 3.11.

User-specified conditions dictate whether the generated displacement is accepted or rejected, for example by considering a minimum required signal to noise ratio (which uses the root mean square of the negative correlation values to estimate the noise level and assumes the displacement to be valid if correlation peak to noise level ratio is larger than the user-specified value) or an absolute peak height requirement. In this work, a particle was deemed to have been detected if the grey scale peak was 5 times the background noise floor, and only correlation peaks above 0.25 were accepted. Any rejected values are replaced with an average of the results from neighbouring IAs (here, validation and substitution was based on a 5×5 neighbourhood with a minimum normalisation of 0.1

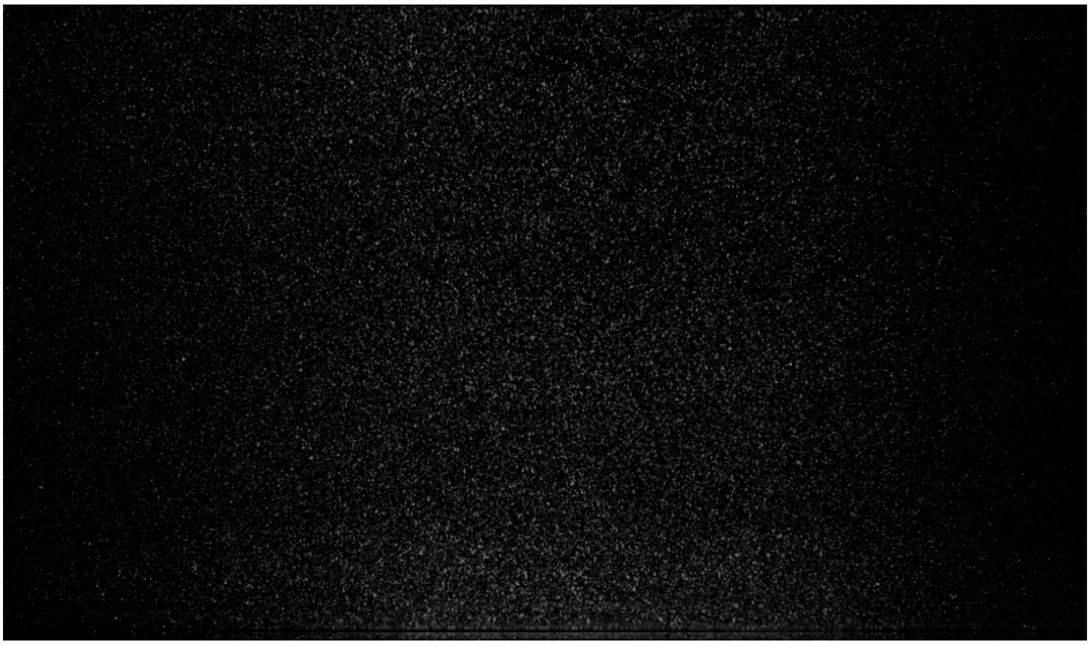

Figure 3.10: Example whole-field PIV image illustrating seeding density.

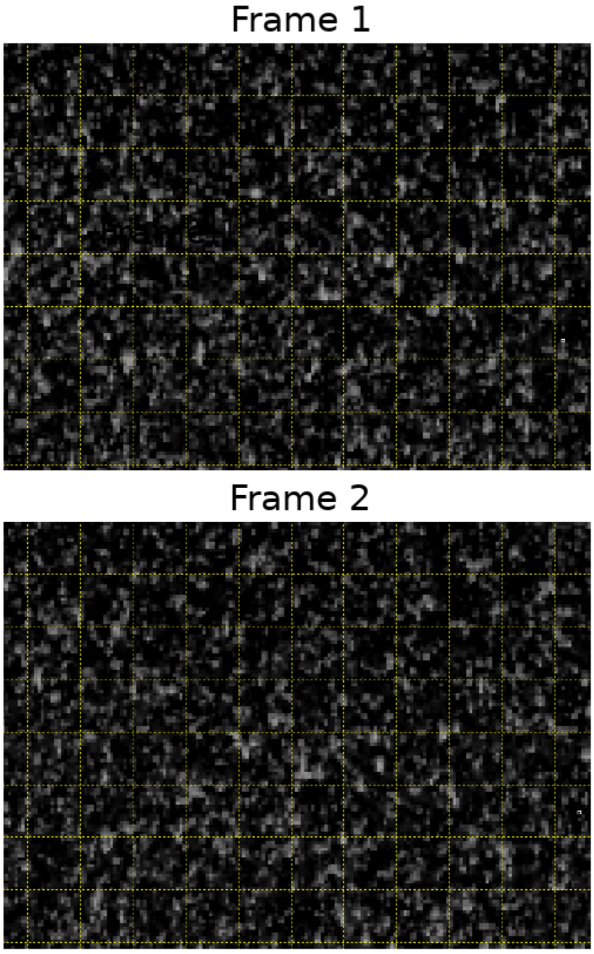

Figure 3.11: PIV images showing seeding density and movement of particles in time Δt, with yellow lines indicating interrogation areas.

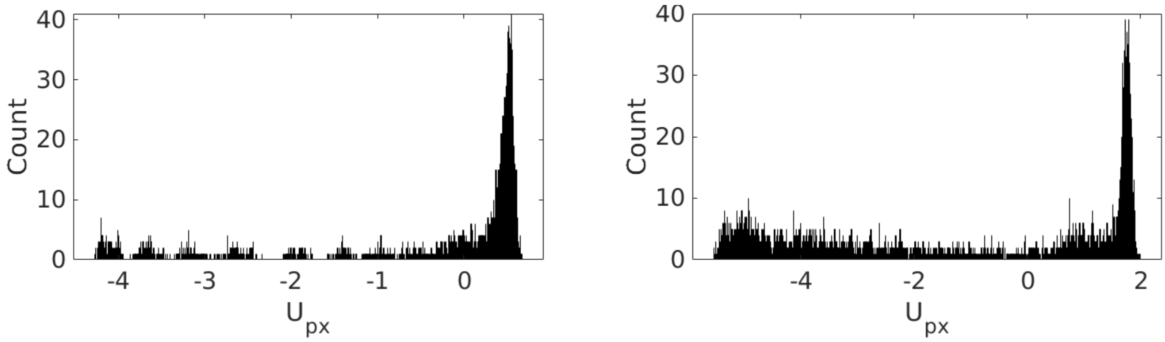

Figure 3.12: Histograms showing (left) potential peak locking and (right) no peak locking.

and an acceptance limit of 2). In this way an estimated pixel displacement for each IA is obtained, which can be converted to a velocity using the time between images and the scale factor.

In adaptive PIV, the size and shape of the IAs subsequently iterates through smaller and smaller sizes, repeating this process until user-specified conditions on local seeding density and velocity gradients within each IA are met. The minimum and maximum allowable IA sizes are user-specified (here, the minimum and maximum IA sizes were chosen to be 32 and 128 pixels respectively both horizontally and vertically), and the maximum size is used for the first iteration. Subsequent iterations reduce the size of the IA only where this is justified by seeding density and flow gradients. In this work, the IA size was adjusted in order to find ~ 10 particles per IA. The shape of the IAs was automatically adjusted in an attempt to enforce the magnitude of each velocity gradient being ≤ 0.1, and the combined effect of the gradients

$$\sqrt{\left(\frac{\partial U}{\partial X}\right)^2 + \left(\frac{\partial V}{\partial X}\right)^2 + \left(\frac{\partial U}{\partial Y}\right)^2 + \left(\frac{\partial V}{\partial Y}\right)^2} \leq 0.2, \tag{3.1}$$

where U and V are the downstream and vertical velocity vectors (here in the form of pixel displacements) and X and Y are the horizontal and vertical directions (here with units of pixels). This resizing/reshaping was done iteratively, with iterations stopping for a particular IA once the translational component of the shape correction for that IA was less than 0.01 or once ten iterations had been reached.

Repeating this method using the second and third images (and so on) allows the velocity field over time to be generated. The velocity field produced in this work was on a grid with spacial resolution $3\,\text{mm} \times 3\,\text{mm}$.

Checking Data Quality

The generated displacements were inspected to ensure effects such as peak locking (in which the measured displacements are biased towards integer values) were not present (Michaelis *et al.*, 2016). This was done by considering histograms of downstream and vertical pixel displacement for a particular timestep (see Figure 3.12). These histograms

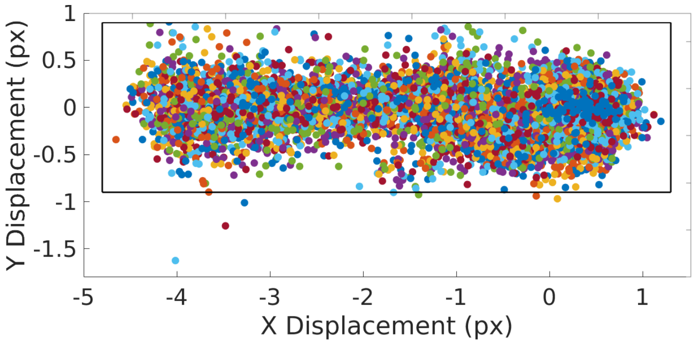

Figure 3.13: Scatter plot illustrating the identification of spurious vectors.

also aided in the identification of spurious vectors, with displacements well outside the typical range. Figure 3.13 shows an example scatter plot of downstream and vertical displacements. Vectors outside the box were considered spurious. For the data presented in this work, the number of spurious vectors identified in each data set was low ($< 0.5\%$ of the total vectors in the body).

3.2 Shake-the-Box Particle Tracking Velocimetry

3.2.1 Background

A different experimental method is needed to investigate the third component of velocity. Generally, two classes of technique have been used to conduct time-resolved measurement of flows with velocity in three dimensions: extensions to the PIV method (for example tomographic PIV, tomo-PIV), and particle tracking velocimetry (PTV) (Schanz *et al.*, 2013, 2014). Like planar PIV, they are non-intrusive, optical techniques for generating instantaneous whole-field velocity fields. Tomo-PIV requires a tomographic reconstruction of the particle field and a subsequent three-dimensional cross-correlation to establish a gridded velocity field (Elsinga & Westerweel, 2012; Scarano, 2012). This allows the use of high seeding densities, and the gridded nature of the fields produced allows easy computation of quantities like vorticity and swirling strength. However, there is also a high incidence of ghost particles that may bias velocity results, and each timestep is computationally expensive (Schanz *et al.*, 2013).

PTV uses triangulation to establish particle positions and constructs Lagrangian particle tracks by finding matching particles across timesteps (Schanz *et al.*, 2013; Tan *et al.*, 2019). The computational cost of each timestep is lower than for tomo-PIV, and particle tracks can give additional information about the flow compared to a gridded field (for example more accurate accelerations). However, the seeding density is typically required to be an order of magnitude lower than that used in tomo-PIV, reducing the resolution of the reconstructed velocity field (Raffel *et al.*, 2018; Schanz *et al.*, 2015).

The Shake-the-Box PTV (STB) algorithm overcomes the seeding density limitations of PTV (Novara *et al.*, 2016; Schanz *et al.*, 2013, 2014, 2016; Tan *et al.*, 2019). The

Author	Flow Type
Schröder *et al.* (2016)	Coherent structures in near-wall turbulence.
Huhn *et al.* (2017)	Flow in a thermal plume.
Jux *et al.* (2018)	Flow around a full-scale cyclist.
Steinmann *et al.* (2019)	Drop impact at air-water interface.
Usherwood *et al.* (2020)	Lift generated by gliding raptors.

Table 3.6: Some examples of the existing research using Shake-the-Box PTV.

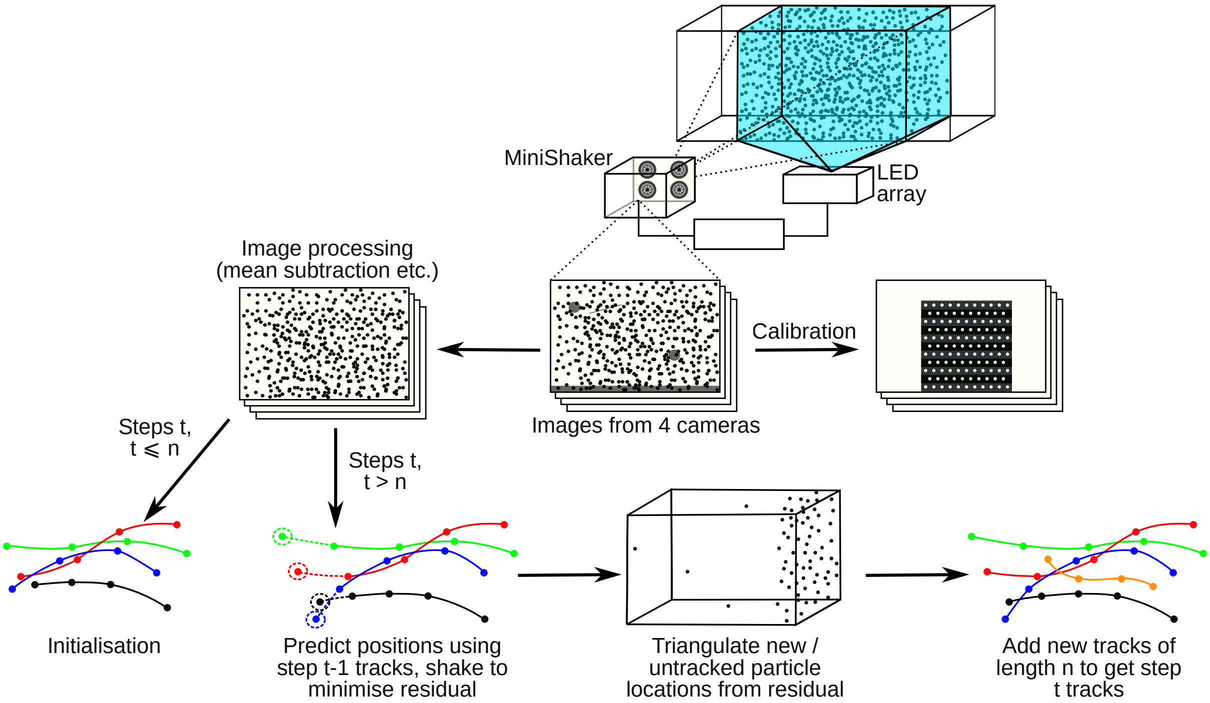

Figure 3.14: The steps involved in generating particle tracks from Shake-the-Box images.

algorithm assumes that if the trajectory of a particle is known for several timesteps, then that particle should not disappear within the measurement region and its location in the next timestep can be accurately predicted. Small errors can be corrected using image matching schemes. This assumption allows reconstruction of a particular timestep with greater accuracy, with higher seeding densities and faster reconstruction times. The technique is described in detail in Schanz *et al.* (2013, 2016), and the steps involved are summarised in Figure 3.14. As a relatively new technique it has not yet been applied to as wide a range of flows as planar PIV, however Table 3.6 lists some of the existing research using STB. The produced velocity fields have been demonstrated to be comparable in quality to those from tomo-PIV with similar seeding densities, but are generated in a much shorter time frame (Novara *et al.*, 2016; Schanz *et al.*, 2013, 2014). What follows is a more detailed description of those steps, ways in which high quality data can be obtained, and the experimental setup used in this work.

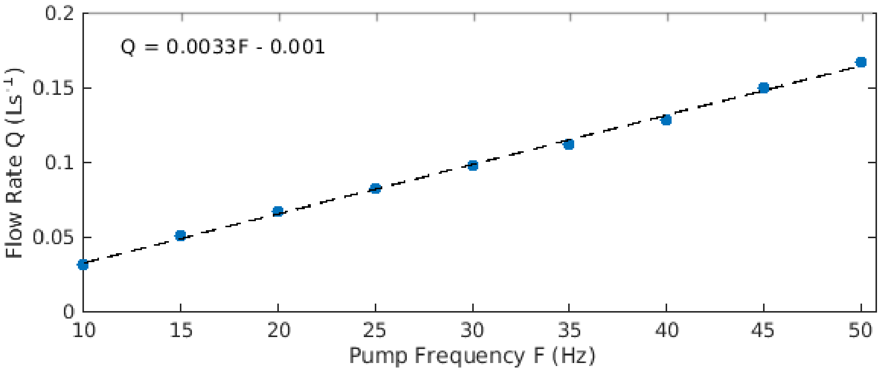

Figure 3.15: Flow rate vs. pump setting for the gear pump in the STB work.

3.2.2 Experimental Setup

Fluids

The STB experiments were conducted in the same experimental setup as the PIV work. Similar to planar PIV, STB is an optical technique and the same refractive index restrictions apply to the choice of fluids. Therefore the same fluids were used as for the planar PIV work, prepared in the same way. However, due to a significant amount of time elapsing between the planar PIV and STB work, the gear pump had been serviced resulting in a significantly different relationship between pump frequency and flow rate, shown in Figure 3.15.

Seeding Particles

The particles needed for STB have similar requirements to planar PIV. However, as the particles across the entire measurement depth must be in focus (requiring a smaller optical aperture), larger particles are needed to increase the image intensity (Scarano *et al.*, 2015). As with planar PIV, the particle concentration must be low enough to identify individual particles (Schanz *et al.*, 2015). As a volume is illuminated and imaged rather than a plane, the particle concentration in the fluid must be lower than for planar PIV. For accurate reconstruction of the velocity field, the seeding density should be restricted to $\mathcal{O}(0.1)$ particles per pixel (Schanz *et al.*, 2014).

For this work, two different particle types were used. First, LaVision Polyamide particles HQ with mean diameter 60 µm and density $1030\,\mathrm{kg\,m^{-3}}$ were used at concentration $0.003\,\mathrm{g\,L^{-1}}$ in both the current and ambient fluids. Second, Cospheric polyethylene microspheres UVPMS-BO-1.00 125-150 µm with density $1000\,\mathrm{kg\,m^{-3}}$ and $> 90\%$ of particle diameters within the stated range were used at concentration $0.033\,\mathrm{g\,L^{-1}}$ in the current fluid and $0.020\,\mathrm{g\,L^{-1}}$ in the ambient fluid. The Cospheric particles were coloured fluorescent orange. The wavelengths of the light reflected by these particles are different to that reflected by the Perspex walls of the tank. Therefore application of an appropriate

Case	8	9	10	11	12	13
Influx (Ls^{-1})	0.03	0.03	0.08	0.08	0.15	0.15
Fr_S	0.73	0.73	1.86	1.86	3.36	3.36
Δt (ms)	20	20	20	10	10	10
Seeding	Pa	Fl	Pa	Fl	Pa	Fl

Table 3.7: Details of the influx, source Froude number, time between images, and seeding type for each STB case. Fl refers to the fluorescent Cospheric particles, and Pa to the LaVision polyamide particles.

filter, with a cutoff at wavelength 610 nm, to the camera lens resulted in improved image quality with less impact from Perspex and bubble reflections.

The Cospheric particles are hydrophobic. In order to encourage homogeneous distribution of the particles in the experimental fluids, they must be coated with surfactant prior to use. After weighing out the desired quantity of particles, the seeding particles for each fluid were placed in a solution of 20 mL deionised water and 0.1 g Tween 80 surfactant, and rotated for at least 4 hours in a Stuart SB3 tube rotator. While this did appear to improve the distribution of particles, a large proportion of the particles floated on the fluid and remained in the mixing tanks rather than being evenly distributed. The polyamide particles also required a small amount of surfactant, in this case ILFORD ILFOTOL wetting agent, and were shaken by hand with a small volume of the experimental fluids and a drop of surfactant.

The Stokes velocity (U_g) and relaxation times (τ_r) of these particles can be calculated to demonstrate their suitability for this work. Considering these particles in the two experimental fluids, the fluorescent Cospheric particles had U_g between -3.77×10^{-4}m s^{-1} and -1.07×10^{-4}m s^{-1} and τ_r between 9.08×10^{-4}s and 9.27×10^{-4}s and the polyamide particles had U_g between -1.97×10^{-5}m s^{-1} and 3.05×10^{-5}m s^{-1} and τ_r between 3.20×10^{-4}s and 3.27×10^{-4}s. These indicate that the settling velocity was significantly smaller than the typical measured velocity, and that the particles accelerated rapidly to the fluid velocity. Therefore the particles selected were appropriate for the measurements taken.

The STB System

The STB setup consisted of illumination from a LaVision Blue LED-Flashlight 300, an array of 72 LEDs operated above nominal LED current to generate short pulses with very high light intensities. This was combined with a LaVision MiniShaker TR-L, a set of 4 Imager M-lite 2M cameras in a fixed arrangement, that captured a volume within the tank that extended throughout the entire height, to ∼5 mm from each side-wall, and ∼0.275 m horizontally, with the closest edge being 0.5 m from the closest point of the outlet drop (illustrated in Figure 3.16). To maximise the measurement duration while still capturing the full flow, the images were collected after the dense fluid had started being pumped into the tank but several seconds before the head reached the measurement region. Data were collected for either 25 s or 50 s, depending on whether images were collected at 50 Hz

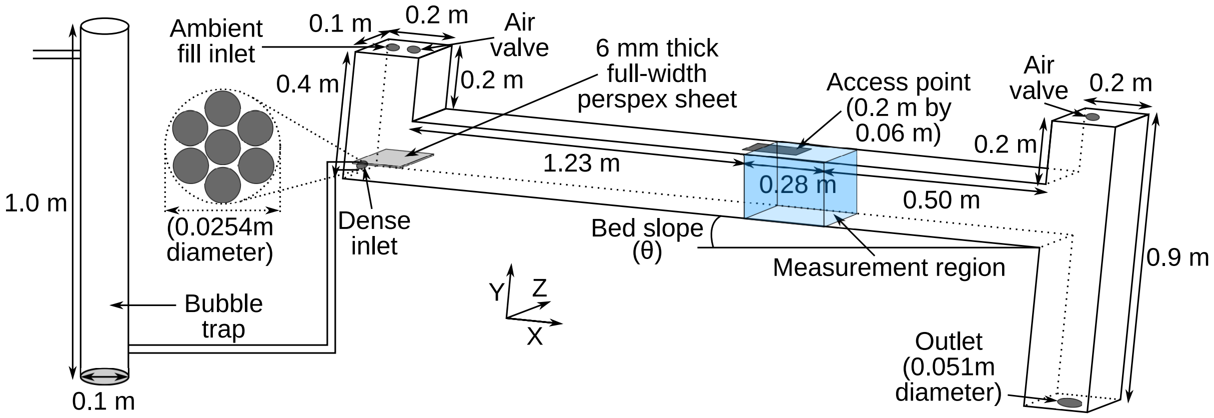

Figure 3.16: Schematic of the STB setup

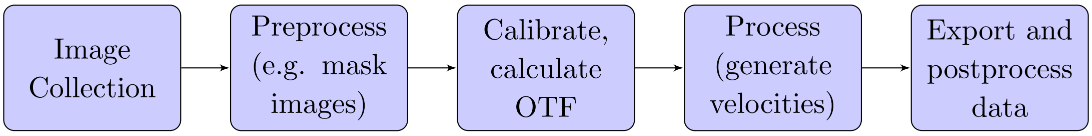

Figure 3.17: Flow chart illustrating the steps involved in Shake-the-Box PTV. Here, OTF refers to the optical transfer function.

or 100 Hz (see Table 3.7). In order to calibrate the images, a LaVision 106-10 double-sided calibration plate was used and placed on the bottom surface of the tank, central in the cross-stream direction and approximately central within the illuminated volume in the downstream direction.

3.2.3 The Shake-the-Box Algorithm

Figure 3.17 shows the steps involved in generating velocity fields using STB. What follows is a description of each step in turn. The software used for this work was a combination of LaVision DaVis 10.0.5 and 10.1.0.

Preprocessing

Prior to processing, the images were modified to improve their quality. Reflections from Perspex walls, and scratches, fixed bubbles, or smearing on internal walls, were removed. A mask was also applied to any areas outside the measurement region. The steps taken to improve image quality in each case depended on the seeding particles used. For the polyamide particles, an average of all images was subtracted from each image, while for the Cospheric particles the minimum intensity value for each pixel across all images was identified and subtracted. For both particle types, any pixel intensities below a certain value were set to 0 and the LaVision image preprocessing tool was applied. This involved subtracting a 5-pixel sliding minimum from each image, along with applying 5 × 5 pixel Gaussian smoothing, sharpening, and multiplication of each pixel intensity by a factor of 5.

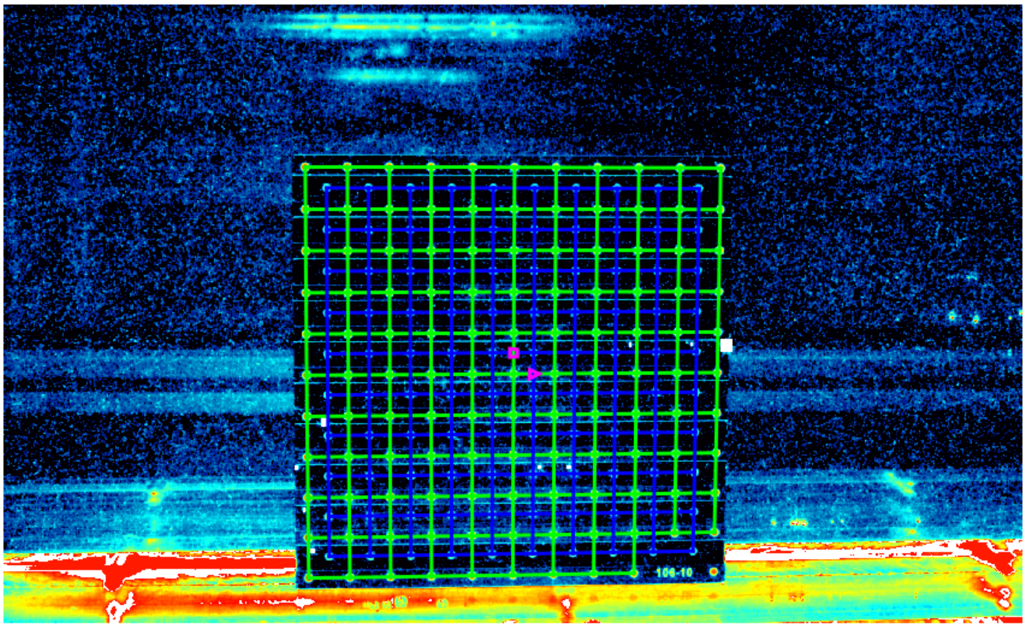

Figure 3.18: Example image of the calibration target after mark identification.

Calibration

Calibration for STB involves three stages. The first requires collection of images of a three-dimensional image plate, positioned centrally in the cross-stream direction (Schanz *et al.*, 2013; Schröder *et al.*, 2015). These images were analysed using pinhole calibration. As many as possible of the white marks on the calibration plate images are identified, thereby identifying the conversion between pixel and metre distances for each camera. In order to identify a sufficient proportion of the marks, the images needed some masking and processing to remove the effects of bubbles and remnants of seeding from previous runs. A separate set of calibration plate images, with collection of 10 target images per camera, were collected for each data set, barring two cases that were conducted on the same day. For 5 out of 6 cases, $> 98.5\%$ of marks were successfully identified during calibration, while only 93% were identified for the final case. An example target image, after automated identification of the mark positions, is included in Figure 3.18.

The second stage – volume self-calibration – is an iterative process intended to refine the previous calibration step (Schanz *et al.*, 2012; Wieneke, 2018). Errors could arise, for example, due to slight inaccuracies in target manufacture, thermal expansion, errors in the identified mark locations, or slight movement of the cameras between target image and data image collection. In this work, between 250 and 500 images from the actual data set were used for this purpose. The two-dimensional positions of each seeding particle are identified, and possible three-dimensional locations from the combination of two-dimensional images proposed based on an allowed error larger than the maximum expected calibration error (Schanz *et al.*, 2012; Wieneke, 2018). Mapping these three-dimensional locations back on to two-dimensional images results in slightly different two-dimensional locations to the original images. A disparity map is then produced for each

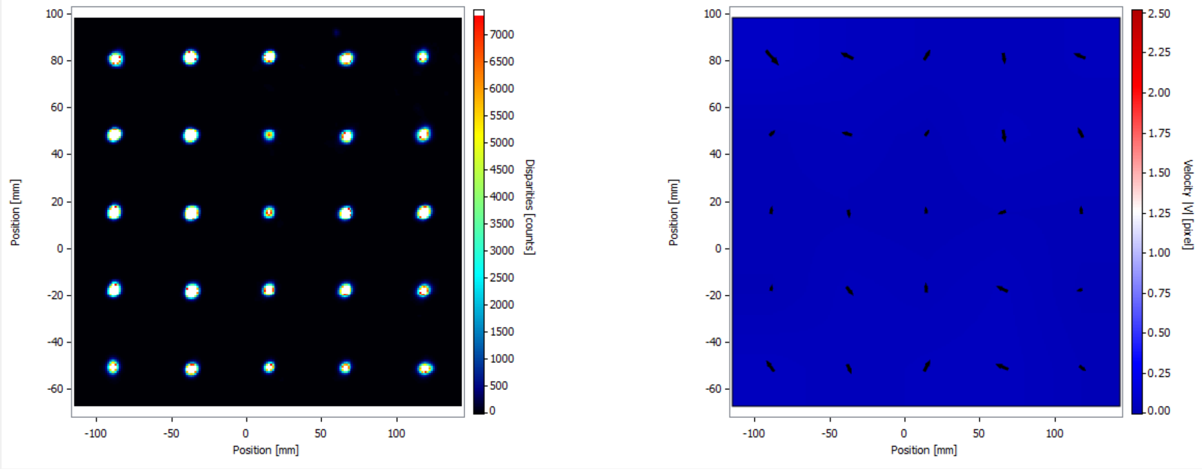

Figure 3.19: Example disparity field from volume self-calibration of one camera in this work.

camera, with concentrated signals corresponding to the ‘true’ disparity while false values due to ‘ghost’ particles are randomly distributed (Wieneke, 2018). To allow the disparity to vary spatially, each three-dimensional volume is divided into $n_x \times n_y \times n_z$ subvolumes, and the disparity for each subvolume calculated separately. One example disparity field from this work is shown in Figure 3.19.

The final part of volume self-calibration requires calculation of an optical transfer function (OTF) – a mapping between pixel and voxel intensities which describes how, for example, a spherical particle in voxel space would be imaged by a camera in two-dimensions (Schanz *et al.*, 2012). The optical transfer function is allowed to vary in space and for each camera to ensure that when two-dimensional images are used to reconstruct the three-dimensional volume, the particles within the reconstructed volume are spherical regardless of imaging distortions (Schanz *et al.*, 2012; Wieneke, 2012). An example representation of an OTF for one camera in this work is included in Figure 3.20. With this function, the projection of a particle p with position (X_p, Y_p, Z_p) and intensity I_p onto the image recorded by camera i can be calculated (I^i_{part}) (Wieneke, 2012).

Initialisation

A key principle of STB is that existing particle tracks may be used to predict particle positions at future times (Novara *et al.*, 2016; Schanz *et al.*, 2013, 2014, 2016; Wieneke, 2012). However, for the first few timesteps no particle track data is known. These timesteps are known as the initialisation phase, during which all potential particle locations are identified using iterative triangulation, also called iterative reconstruction of volumetric particle distribution (IPR) (Wieneke, 2012).

IPR uses triangulation with an allowed error of 1 voxel to identify a possible volumetric particle distribution. By combining the expected contributions of particles located at these triangulated potential positions to the two-dimensional camera images (I^i_{part}), an

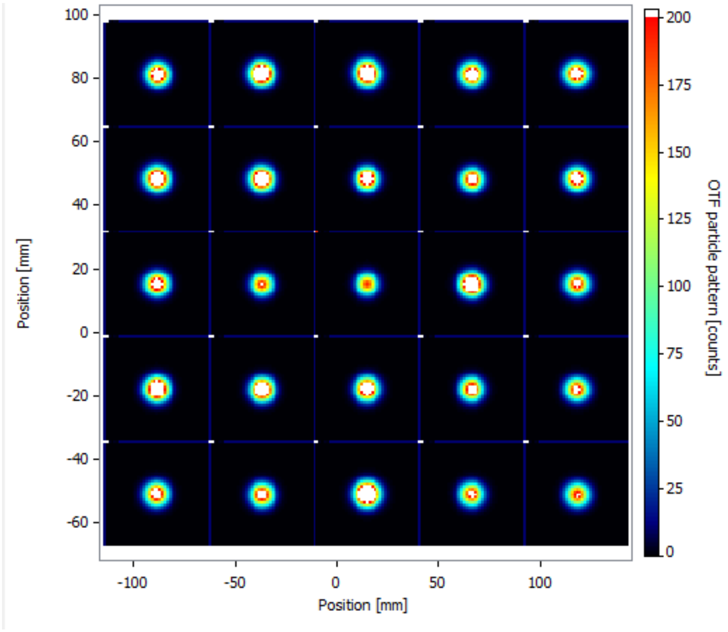

Figure 3.20: Example optical transfer function from one camera for this work.

overall projected image can be generated for each camera i (Wieneke, 2012),

$$I^i_{proj} = \sum_p I^i_{part}. \tag{3.2}$$

Subtraction of these projected two-dimensional images from the originally captured flow images (I_{orig}) generates a residual image

$$I^i_{res} = I^i_{orig} - I^i_{proj}. \tag{3.3}$$

The particle positions and intensities are updated through a number of iterations of ‘shaking’ (described below) and new residual images are generated (Schanz *et al.*, 2016). In this work, 4 iterations of shaking were performed. Further IPR iterations (in this work 3 further iterations) are carried out on the residual images for each timestep (Schanz *et al.*, 2016; Wieneke, 2012). Before each iteration, as many traces of previously identified particles as possible are removed from the residual images using the optical transfer function (Schanz *et al.*, 2016). Having identified the particle distributions in this manner for a set number of timesteps, n (in this work, $n = 4$), a search radius is applied around each particle in the reconstructed volume from timesteps $t + 1 - n$ to t, allowing the identification of particle tracks of length n (Schanz *et al.*, 2016). These tracks are checked to ensure velocities and accelerations are within certain limits, here displacements no greater than 20 voxel with 1 voxel maximum absolute change in particle position.

Shaking

The initial volumetric locations ($X_p,\ Y_p,\ Z_p$) and intensities (I_p) of the particles are updated to ($X'_p,\ Y'_p,\ Z'_p$) and I'_p by analysing the particle-augmented residual (Schanz *et al.*, 2016). The particles are iteratively moved in small steps (here $\delta_S = 0.1$ voxel) in each spatial direction. Beginning with the downstream position, the particles are moved from their initial positions to $X'_1 = X_p - \delta_S,\ X'_2 = X_p,\ X'_3 = X_p + \delta_S$. The local residual ($R$) is calculated using the recorded images, I_{orig}, the projected images, I_{proj}, and the projection of the currently treated particle, $I_{part[X,Y,Z,I_P]}$, as

$$R[X', Y', Z', I_p] = \sum_{i,x_i,y_i} (I^i_{res+p} - I^i_{part[X',Y',Z',I_p]})^2, \tag{3.4}$$

where $I^i_{res+p} = I^i_{res} + I^i_{part[X,Y,Z,I_p]}$, and R is the sum over all cameras and over a small window around the projected particle centre (with size determined by the OTF and with spatial positions $x,\ y$) (Schanz *et al.*, 2016; Wieneke, 2012). The 3 values of R, calculated at $X'_1,\ X'_2,\ X'_3$, are fitted using a second order polynomial function, and the minimum of this function determined. The particle position is updated to the point between X'_1 and X'_3 that minimises the residual (Schanz *et al.*, 2016; Wieneke, 2012). This is repeated for the Y and Z directions using the updated X (and Y) location as an initial position. The particle intensities are updated as (Schanz *et al.*, 2016; Wieneke, 2012)

$$I'_p = I_p \sqrt{\frac{\sum_{p,x_i,y_i} (I_{res+p})}{\sum_{p,x_i,y_i} (I_{part[X'_I,Y'_I,Z'_I,I_p]})}}. \tag{3.5}$$

Here, particles were deleted if their intensity dropped below 10% of the average particle intensity, if they were within 1 voxel of another particle, or if their predicted location was outside the measurement region.

Tracking

For the remaining timesteps, the computational effort involved in locating particles in space can be considerably reduced by using the known particle track information (Schanz *et al.*, 2013, 2014, 2016). The tracks are extended by applying a Weiner filter to give predicted particle locations, with parameters adjusted to account for reduced accuracy of particle positions due to experimental noise, or to consider the increased accuracy of longer tracks. These predicted locations are assumed to be within a couple of pixels of the 'true' locations, which are identified through a few iterations of 'shaking'. The use of tracks to validate particles eliminates most 'ghost' particles, which typically do not produce coherent tracks over several timesteps (Novara *et al.*, 2016).

Having used this tracking technique to identify the locations of the majority of particles (Schanz *et al.*, 2013, 2014, 2016), untracked particles and those newly entering the

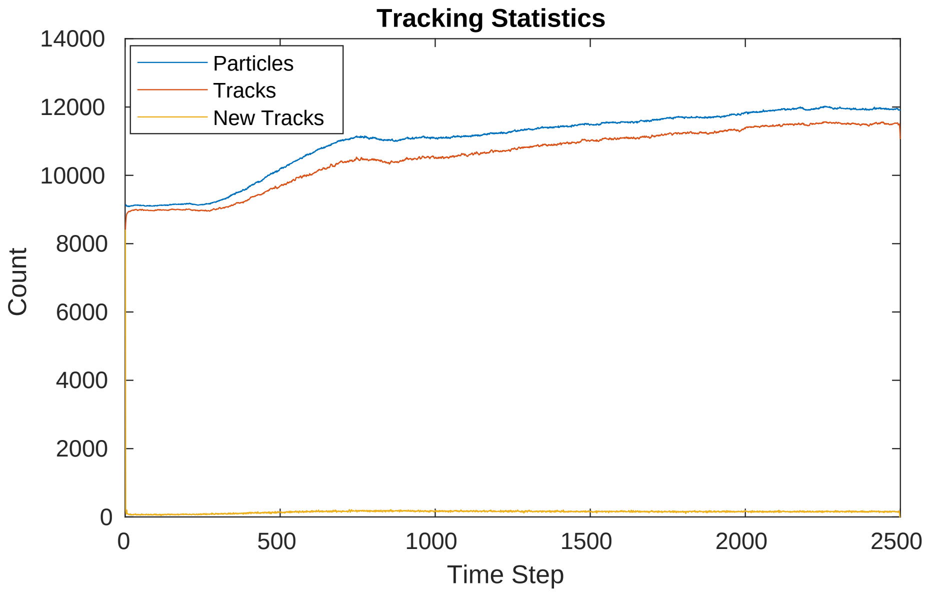

Figure 3.21: Plot of the number of identified particles, tracked particles, and newly identified tracks at each timestep for one case.

measurement region are identified. This is done by applying IPR to the residual images calculated after removing the contributions of tracked particles. These residuals will be considerably sparser than the original images, resulting in a less complex reconstruction problem than in the initialisation phase and fewer/faster IPR iterations are needed. When calculating the residuals, to ensure that the identified particles are removed from the images as thoroughly as possible, a wide sampling of the OTF is used (unlike the narrow sampling applied when calculating R during a shake step) and the particle intensities are multiplied by a constant (here 1.5). Having identified the new potential particles, any new particle tracks of length n are identified in the same way as during initialisation. Here, to ensure the identified tracks were sufficiently smooth, a median filter was applied.

For the algorithm to accurately and rapidly reproduce particle tracks, the positions of a high percentage of particles should be tracked rather than triangulated (Schanz *et al.*, 2016). A plot showing the distribution of identified particles, tracked particles, and newly added tracks at each timestep for an example case in this work is shown in Figure 3.21.

Export and Postprocessing

In order to analyse the velocity field and compare to the PIV work, the particle tracks were converted into a gridded velocity field. This was done through ‘binning’. Here, the velocity components at a grid point were calculated by 2nd order polynomial regression of the closest available particles over 5 timesteps. The values were ‘binned’ using subvolumes of 128 voxel, with 83.33% overlap. This corresponded to grids with spacing 21 voxels, or 2.6 mm. Grid points corresponding to subvolumes with no tracked particles contained no velocity information.

3.3 Direct Numerical Simulation

In the present study, the spectral element solver Nek5000 (Nek5000, 2017) was employed to establish the effects of both Reynolds and Schmidt numbers on turbulence in the body of constant-influx gravity currents through three-dimensional direct numerical simulation (DNS). Below, the numerical setup is outlined, with justifications of design choices and setup parameters.

3.3.1 Background

As with PIV, numerical methods in general and DNS in particular have been used extensively to investigate the structure and dynamics of gravity currents. DNS is a technique for generating quantitative data characterising a flow by numerically solving the governing equations of the flow, resolving all scales of motion. It is described in detail in several places, e.g. Moin & Mahesh (1998), and the steps involved are summarised in the following sections. The DNS data can be compared directly to the experimental data described previously, but is not limited by the density and Schmidt number restrictions resulting from refractive index matching requirements. However, there are limitations such as the large computational cost that limits the range of Reynolds and Schmidt numbers that can be investigated. Table 3.8 summarises some of the existing numerical investigations into gravity current work.

3.3.2 The Governing Equations

Before conducting any numerical investigation, the equations that govern the system of interest must be identified. Gravity current flows are governed by the incompressible Navier-Stokes, salinity and continuity equations, which take the form

$$\rho\left(\partial_t \boldsymbol{U} + \boldsymbol{U}\cdot\nabla\boldsymbol{U}\right) = -\nabla p + \nabla\cdot\tau + \rho\boldsymbol{g}, \tag{3.6}$$

$$\partial_t S + \boldsymbol{U}\cdot\nabla S = D\nabla\cdot\left(\nabla S\right), \tag{3.7}$$

$$\nabla\cdot\boldsymbol{U} = 0, \tag{3.8}$$

where $\tau = \mu[\nabla\boldsymbol{U} + \nabla\boldsymbol{U}^T]$, and $\boldsymbol{g} = g\hat{\boldsymbol{g}}$. Here ρ is density, $\boldsymbol{U}$ fluid velocity, p pressure, τ the stress tensor, μ dynamic viscosity, g and $\hat{\boldsymbol{g}}$ the magnitude and direction of the body force $\boldsymbol{g}$ (in this case gravitational acceleration), S salinity, and D mass diffusivity.

As the difference in density between the current and ambient fluids in this work is small, the Boussinesq approximation can be applied (Härtel *et al.*, 2000; Simpson &

Author	Current Type	Key Focus
Härtel *et al.* (2000)	DNS, two-dimensional and three-dimensional solute, lock-release	Structure of the head, comparing no-slip and slip boundaries.
Necker *et al.* (2002)	DNS, two-dimensional and three-dimensional particle-laden, lock-release	Current structure and particle sedimentation.
Özgökmen & Chassignet (2002)	DNS, two-dimensional solute, lock-release	Effect of bottom slope and salinity on current structure.
Özgökmen *et al.* (2004)	DNS, three-dimensional solute, lock-release	Effects of three-dimensional motions on the structure of sloped gravity currents.
Cantero *et al.* (2007)	DNS, two-dimensional and three-dimensional solute, lock-release	Influence of planar vs. cylindrical currents and lock volume on three-dimensional structure, front propagation.
Bonometti & Balachandar (2008)	Two-dimensional DNS and three-dimensional volume of fluid solute, lock-release	Effect of Schmidt number on current structure.
Huang *et al.* (2008)	RANS with $k - \epsilon$ closure, lock-release/sustained inflow	Effect of bed slope and inflow type on current structure.
Zgheib *et al.* (2015)	DNS, three-dimensional particle-laden, lock-release	Vortical structures in cylindrical currents.
Ottolenghi *et al.* (2016b)	LES, three-dimensional solute, lock-release	Impact of an upwards bottom slope and domain aspect ratio on dynamics, in particular entrainment.

Table 3.8: Summary of some previous numerical work conducted on gravity currents.

Parameter	Non-Dimensionalisation
Length	$\tilde{x} = x/L_c$
Velocity	$\tilde{\boldsymbol{U}} = \boldsymbol{U}/U_c$
Time	$\tilde{t} = (U_c/L_c)t = t/t_c$
Pressure	$\nabla\tilde{P} = (L_c/\rho_a U_c^2)\nabla P$
Stress tensor	$\nabla\cdot\tilde{\tau} = (L_c^2/U_c\nu\rho_a)\nabla\cdot\tau$
Salinity	$\Delta\tilde{S} = (S - S_a)/(S_I - S_a) = \Delta S/\Delta S_I$

Table 3.9: Definitions of the non-dimensionalisations used in this work, where x is position, t is time, $t_c = L_c/U_c$ a characteristic time, $\Delta S = S - S_a$, and $\Delta S_I = S_I - S_a$.

Britter, 1979). This states that the density may be assumed to be constant ($\rho = \rho_a$ where ρ_a is the density of the ambient fluid) everywhere except for the $\rho\boldsymbol{g}$ term. For this term, the dependence of density on salinity must be considered. Specifically, here the simplified linear dependence described by Penney (2017) will be employed,

$$\rho \approx \rho_a(1 + \beta(S - S_a)) = \rho_a(1 + \beta\Delta S), \tag{3.9}$$

where $(\cdot)_a$ is a property of the ambient fluid, $(\cdot)_I$ a property of the dense fluid, and $\beta = \frac{1}{\rho}\frac{\partial\rho}{\partial S}$ the coefficient of haline contraction. Applying these to (3.6) results in

$$\rho_a\left(\partial_t\boldsymbol{U} + \boldsymbol{U}\cdot\nabla\boldsymbol{U}\right) = -\nabla p + \nabla\cdot\tau + \rho_a(1 + \beta\Delta S)\boldsymbol{g}. \tag{3.10}$$

The non-dimensionalisations defined in Table 3.9 can then be used to find the non-dimensional, Boussinesq Navier-Stokes equation,

$$\frac{\partial\tilde{\boldsymbol{U}}}{\partial\tilde{t}} + \tilde{\boldsymbol{U}}\cdot\nabla\tilde{\boldsymbol{U}} = -\nabla\tilde{P} + \frac{1}{Re}\nabla\cdot\tilde{\tau} + \frac{1}{Fr_d^2}\Delta\tilde{S}\hat{\boldsymbol{g}}, \tag{3.11}$$

where $\tilde{(\cdot)}$ indicates a dimensionless variable, $P = p + \rho g Y$, and the Reynolds (Re) and densimetric Froude (Fr_d) numbers are defined as $Re = U_c L_c/\nu$, and $Fr_d = U_c/\sqrt{g\prime L_c} = U_c/\sqrt{\beta\Delta S_I g L_c}$ with U_c and L_c being characteristic velocity and length scales of the flow. The effect of adding a slope θ on $\boldsymbol{g}$ must also be considered, specifically

$$\boldsymbol{g} = (g\sin(\theta), g\cos(\theta), 0). \tag{3.12}$$

Similar treatment can be applied to the equation for salinity. Applying the non-dimensional parameters in Table 3.9 to (3.7) results in the non-dimensional salinity equation

$$\partial_{\tilde{t}}\tilde{S} + \tilde{\boldsymbol{U}}\cdot\nabla\tilde{S} = \frac{1}{ReSc}\nabla\cdot\nabla\tilde{S}, \tag{3.13}$$

where $Sc = \nu/D$ is the Schmidt number, and ν the kinematic viscosity. The product of

Re and Sc can also be called the Peclet number, $Pe = ReSc = U_c L_c / D$.

3.3.3 Direct Numerical Simulation

The governing equations may be modified to make them less computationally expensive to solve. The most accurate choice is not to modify the equations at all and instead to carry out direct numerical simulation (DNS) (Meiburg & Kneller, 2010; Pope, 2001; Wilcox, 2006). In this case, the mesh used must be sufficiently fine to resolve all scales of motion explicitly. This requires a very fine grid combined with a small timestep, and as such can be extremely computationally expensive. DNS is therefore not typically an option for environmental flows, though it is becoming increasingly popular as the requisite hardware becomes more available and less expensive.

A computationally cheaper option is large eddy simulation (LES), in which scales of motion below a certain level (determined by the grid spacing) are not resolved but rather are modelled (Meiburg *et al.*, 2015; Pope, 2001; Wilcox, 2006). The governing equations are filtered to remove the smaller scale motions, and the effect of all filtered motion appears as an additional subgrid-scale (SGS) stress term, $\xi_{ij} = \overset{\smile}{U_i U_j} - \breve{U}_i \breve{U}_j$, in the momentum equation and an SGS flux term, $\kappa_j = \overset{\smile}{U_i S} - \breve{U}_i \breve{S}$, in the salinity equation

$$\frac{\partial \breve{U}_j}{\partial x_j} = 0, \tag{3.14}$$

$$\frac{\partial \breve{U}_i}{\partial t} + \breve{U}_j \frac{\partial \breve{U}_i}{\partial x_j} = -\frac{\partial \breve{p}}{\partial x_i} + \nu \frac{\partial^2 \breve{U}_i}{\partial x_j x_j} - \frac{\partial \xi_{ij}}{\partial x_j}, \tag{3.15}$$

$$\frac{\partial \breve{S}}{\partial t} + \breve{U}_i \frac{\partial \breve{S}}{\partial x_i} = D \frac{\partial^2 \breve{S}}{\partial x_i \partial x_i} - \frac{\partial \kappa_j}{\partial x_j}, \tag{3.16}$$

where $\breve{(\cdot)}$ indicates a filtered quantity (Akselvoll & Moin, 1996; Chumakov, 2005; Chumakov & Rutland, 2005). Both (3.15) and (3.16) have terms that require a model for closure. Many such models have been proposed, such as eddy-viscosity or Smagorinsky models, each with their own advantages (Kumar & Dewan, 2016). LES is able to produce detailed, time-dependent large-scale flow structures, using a coarser mesh than would be needed for DNS. This reduces computational cost, allowing the study of flows with higher Reynolds numbers. However, when simulating flow in gravity currents even LES is typically limited to lower Reynolds numbers than are seen in environmental flows due to the presence of a solid boundary (which introduces a need to resolve small eddies and boundary layers in the near-wall region). Additionally, the solutions obtained using LES are less accurate than those from DNS, though depending on the purpose of the simulations they may be sufficient.

Reynolds-Averaged Navier-Stokes (RANS) simulations reduce the computational cost still further, allowing the study of high Reynolds number flows (Magoulès, 2011; Meiburg *et al.*, 2015). The solution is found by numerically integrating the RANS equations, which themselves are found by time- or ensemble-averaging the governing equations for continuity, momentum and density (Meiburg *et al.*, 2015; Tu *et al.*, 2018). The equations look similar to (3.14), (3.15), and (3.16), however $\breve{(\cdot)}$ indicates an ensemble-averaged quantity, ξ_{ij} represents the Reynolds stresses and κ_j the scalar fluxes (Meiburg *et al.*, 2015). In order to compute ξ_{ij} and κ_j, additional closure equations are required, often in the form of a transport equation for turbulent kinetic energy (k) and dissipation rate (ϵ) (Magoulès, 2011; Meiburg *et al.*, 2015; Tu *et al.*, 2018). Such simulations produce only mean flow characteristics, and the solutions found are less accurate than either LES or DNS. Additionally, while the SGS terms in the LES equations depend primarily on the more universal smaller unresolved eddies, the equivalent terms in the RANS equations depend on larger flow structures that vary with boundary conditions. This makes a universal RANS model difficult to construct, and obtaining high quality RANS predictions requires significant modification depending on the flow conditions (Magoulès, 2011; Meiburg *et al.*, 2015; Tu *et al.*, 2018).

As the purpose of this work is to consider turbulence structures within the body of the flow, and therefore time-dependent solutions of high accuracy are required, DNS was employed. As a result, the Reynolds and Schmidt numbers will be limited to those that can be simulated using the available computational resources.

3.3.4 The Spectral Element Method

In a situation where it is not possible to find an analytical solution to the governing equations, as in this work, they must be solved numerically. This requires appropriate discretisation in space and time. What follows is a brief summary of some of the common methods of spatial discretisation, along with their advantages and disadvantages. For simplicity, any descriptions will be in 1D space only.

Among the simplest techniques is the finite difference method (Iserles, 2009; van Kan *et al.*, 2005). Here, the domain is divided into a grid with spacing Δx. The location of each grid point can be expressed as x_i, where i indicates the horizontal position. Boundary conditions are imposed such that the solution is known on the domain boundaries, and the solution to the governing equations at each grid point is estimated by approximating derivatives using Taylor series expansions (Causon & Mingham, 2010):

$$\begin{aligned} U_{i+1} &= U_i + \left(\frac{\partial U}{\partial x}\right)_i \Delta x + \left(\frac{\partial^2 U}{\partial x^2}\right)_i \frac{(\Delta x)^2}{2} + \left(\frac{\partial^3 U}{\partial x^3}\right)_i \frac{(\Delta x)^3}{6} + \dots\ , \\ U_{i-1} &= U_i - \left(\frac{\partial U}{\partial x}\right)_i \Delta x + \left(\frac{\partial^2 U}{\partial x^2}\right)_i \frac{(\Delta x)^2}{2} - \left(\frac{\partial^3 U}{\partial x^3}\right)_i \frac{(\Delta x)^3}{6} + \dots\ . \end{aligned} \tag{3.17}$$

As Δx is small, (3.17) can be simplified by assuming that higher order terms of Δx are sufficiently small that they can be neglected – i.e. the sequence may be truncated. The expression is said to be first order accurate if terms of order $(\Delta x)^2$ and above are truncated, second order accurate if terms of order $(\Delta x)^3$ and above are truncated, and so on.

Rearranging the first order truncation of (3.17) leads to the first order forward and backward difference expressions (Iserles, 2009; van Kan *et al.*, 2005),

$$\begin{aligned}\left(\frac{\partial U}{\partial x}\right)_i &= \frac{U_{i+1} - U_i}{\Delta x} + \mathcal{O}(\Delta x),\\ \left(\frac{\partial U}{\partial x}\right)_i &= \frac{U_i - U_{i-1}}{\Delta x} + \mathcal{O}(\Delta x),\end{aligned} \tag{3.18}$$

where U_i is the velocity at grid point x_i, and $\mathcal{O}(\Delta x)$ indicates that the magnitude of the truncation error (that is, the error introduced by truncating (3.17)) is of the same order of magnitude as the grid spacing Δx. The truncation error for these expressions may be reduced by using a smaller Δx (i.e. by using more points), by including higher order terms from (3.17), or by using higher order polynomials that include more distant points. The central difference expression for example, found by subtracting the expressions in (3.17), looks like (Iserles, 2009; van Kan *et al.*, 2005)

$$\left(\frac{\partial U}{\partial x}\right)_i = \frac{U_{i+1} - U_{i-1}}{2\Delta x} + \mathcal{O}(\Delta x)^2, \tag{3.19}$$

which achieves the same increase in accuracy using a factor $\sqrt{2}$ decrease in grid spacing that forward differencing achieves with a factor 2 decrease (LeVeque, 2007; van Kan *et al.*, 2005). This method is generally comparatively straightforward to implement and easy to parallelise, but non-uniform meshes and some boundary conditions can be more complex (Coleman & Sandberg, 2010). Finite volume methods are an alternative method, in which the domain is divided into arbitrary control volumes. They avoid the need for coordinate transforms (sometimes required in finite difference methods), by definition conserve properties such as mass, momentum, and energy, and allow use of both structured and unstructured meshes (making finite volume methods more applicable to complex geometries) (Blazek, 2015; Tu *et al.*, 2018). However, as well as being easier to implement in general, finite difference methods allow easier use of high-order approximations (leading to high-order accuracy of the spatial discretization) (Blazek, 2015; Tu *et al.*, 2018).

The finite element method (FEM) divides the domain into elements that need not be of the same size or shape (Hutton, 2004; Iserles, 2009; Liu & Quek, 2013; van Kan *et al.*, 2005). The solution is explicitly calculated on the vertices of these elements, or nodes, and interpolation is used to approximate the solution within the elements. If a general differential or integral equation in the domain $x \in [0, L]$, $\mathcal{L}U(x,t) - f(x) = 0$, is considered, where $\mathcal{L}$ is some differential or integral operator, the weak form of the problem is established through multiplying by some test function and integrating,

$$\int_0^L \psi(x)\mathcal{L}U(x) - \int_0^L \psi(x)f(x) = 0, \tag{3.20}$$

where $\psi(x)$ is the test function. The weak form is discretised, with the nodal solution values treated as unknown variables and the problem solution expressed as a sum of the nodal values multiplied by global basis functions that are only locally non-zero (e.g. tent functions),

$$U(x,t) = \sum_{i=1}^{N} U_i(t)\phi_i(x), \tag{3.21}$$

where $\phi_i(x)$ are basis functions. This expansion is substituted back into the weak formulation, and the integrals evaluated locally. This gives rise to an expression containing two sparse matrices, which can be solved algebraically.

As in FEM, spectral methods approximate the solution to the differential equation $\mathcal{L}U(x) = f(x)$ as a sum of basis functions $\phi_n(x)$,

$$U(x) \approx U_N(x) = \sum_{n=0}^{N} a_n\phi_n(x), \tag{3.22}$$

however these basis functions are here high order polynomials. The derivatives can then be defined globally rather than locally (Boyd, 2001; Mendes *et al.*, 2019), and as a result the solution can be approximated in the whole domain rather than one small section at a time. The coefficients a_n are chosen to minimise the residual function, which is defined to be $R = LU_N(x) - f(x)$ and is equal to 0 for the exact solution. One way to calculate these coefficients is using 'collocation', or the 'pseudospectral method', for which the residual, $U(x) - U_N(x)$, is required to be equal to 0 at a set of points equal in number to the undetermined coefficients (Boyd, 2001). This requires a conversion between these grid points ('real' space) and the expansion coefficients ('Fourier' space) – a Fourier transform. This can be costly, however if a Fast Fourier Transform (FFT) can be used, the cost of which is relatively low ($\mathcal{O}(N \log N)$), it is less computationally expensive than alternative methods of calculating a_n (which typically require evaluating integrals). Generally, nonlinear products are computed in 'real' space, and spatial derivatives in 'Fourier' space, with linear operations being performed in whichever space minimises the number of transforms required.

Spectral methods exhibit exponential convergence, giving them a significant advantage over grid-based methods when it comes to high accuracy requirements. Additionally, the high order of such methods results in higher accuracy, and fewer degrees of freedom being required (Boyd, 2001; Mendes *et al.*, 2019). Spectral methods are therefore memory minimising, and are able to tackle some problems that cannot be solved using grid-based methods owing to memory limitations. However, each degree of freedom in a spectral method is more computationally expensive than grid-based methods due to, for example, the ability of FEMs to utilise sparse matrix equations. Spectral methods are therefore not well suited to problems where the geometry is irregular or the solution is not smooth (Boyd, 2001; Mendes *et al.*, 2019).

Spectral element methods (SEM) are a subclass of Galerkin methods which are similar to FEM, but use high degree piecewise polynomials as basis functions (such as

$$\phi_i(x) = \frac{P'_N(x)(x^2-1)}{N(N+1)P_N(x_i)(x-x_i)}, \tag{3.23}$$

constructed from high order Legendre polynomials P_N shown in Figure 3.22 (Boyd, 2001; Fornberg, 1998; Lotfi & Alipanah, 2019; Rud, 2016)). Typically, this is done in conjunction with a non-equidistant point distribution such as the Gauss-Legendre-Lobatto (GLL) distribution shown in Figure 3.23 to avoid the large oscillations that result from a regular grid (the Runge phenomenon) (Malm, 2011). This leads to an exponential decrease in the error in the calculated solution as in spectral methods, with the ability to model more complex geometries of FEM. They therefore require fewer degrees of freedom than a general FEM (which requires a much finer mesh to achieve the same accuracy), however complex geometries are still more difficult to model (Wang *et al.*, 2013). Due to the slightly complicated nature of the domain considered in this work, as well as the desire to minimise file size (thus reducing transfer times and storage requirements) and take advantage of the exponential convergence properties of spectral methods, a spectral element method was considered most appropriate.

3.3.5 Nek5000

The DNS work was conducted using the spectral element code Nek5000 to solve the non-dimensional governing equations. This software was chosen because it is free and open source, with strong parallelisability and scalability. Additionally, it has previously been used to study similar flows to good effect (e.g. by Özgökmen *et al.* (2004)).

Time Discretisation

As well as spatial discretisation, the equations need to be discretised in time. Time stepping in Nek5000 is done through a semi-implicit method combining k^{th} order (in this work 2^{nd} order) backwards differencing and extrapolation (BDFk/EXTk) schemes (Nek5000, 2015). A general time-dependent problem subject to initial conditions $\boldsymbol{U}_0$ is given by

$$\frac{\partial \boldsymbol{U}}{\partial t} = \mathcal{L}[\boldsymbol{U}], \quad \boldsymbol{U}(t_0, \boldsymbol{x}) = \boldsymbol{U}_0, \tag{3.24}$$

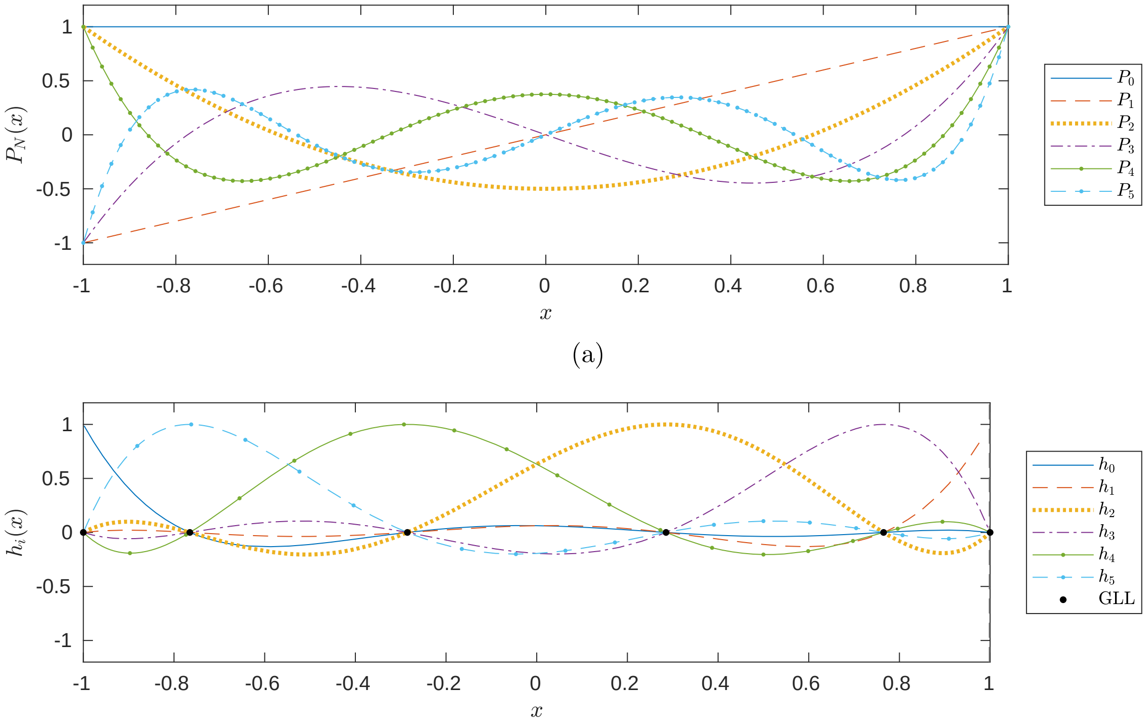

(a)

(b)

Figure 3.22: Illustration of (a) the first 5 Legendre polynomials, and (b) the basis functions constructed from the first 5 Legendre polynomials (Boyd, 2001; Fornberg, 1998; Lotfi & Alipanah, 2019; Rud, 2016). Six GLL points are also included, demonstrating that at each GLL point there is a single non-zero Legendre basis function with value 1.

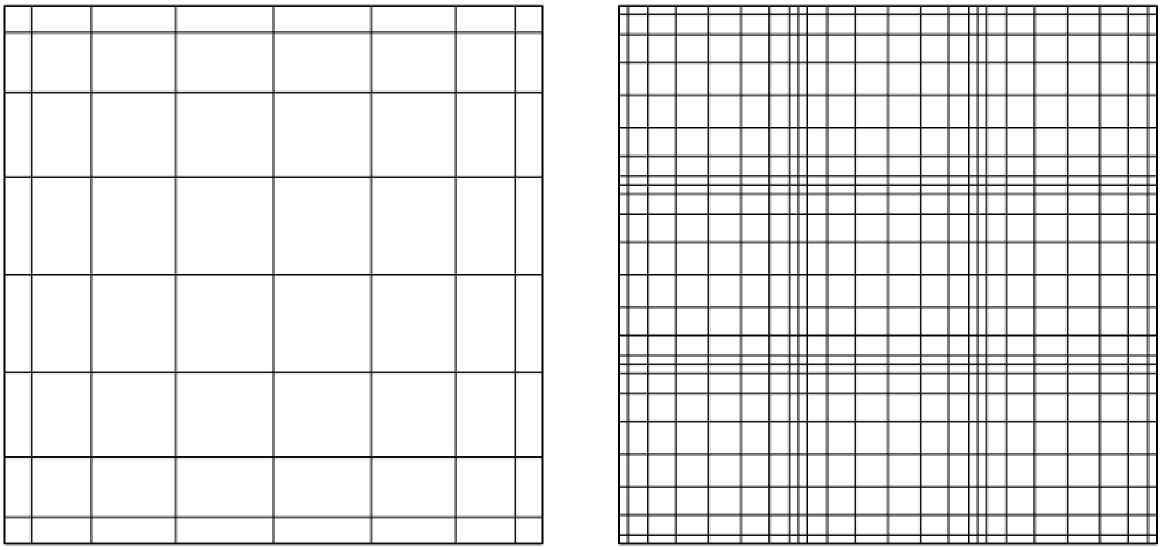

(a)

(b)

Figure 3.23: Two-dimensional GLL distribution with 9 spatial points within each element in each dimension (order 8 polynomials) for (a) a single element, and (b) a combination of 9 elements (Boyd, 2001).

where $\mathcal{L}[\cdot]$ incorporates all spatial operators. The k-th order backward differentiation formula for approximation of the partial time derivative looks like

$$\sum_{j=0}^{k} b_j \boldsymbol{U}^{n+1-j} = \Delta t \mathcal{L}[\boldsymbol{U}^{n+1}], \tag{3.25}$$

where $\boldsymbol{U}^n$ is the solution at timestep n. As backwards differentiation is implicit, and therefore computationally expensive, removal of at least some of the implicit behaviour in $\mathcal{L}[\cdot]$ is desirable. This can be done using the k-th order extrapolation formula

$$\mathcal{L}[\boldsymbol{U}^{n+1}] = \sum_{j=1}^{k} a_j \mathcal{L}[\boldsymbol{U}^{n+1-j}]. \tag{3.26}$$

When using an explicit time stepping method, the maximum timestep that can be used while maintaining stability is determined by the Courant number (Iserles, 2009; Morton & Mayers, 2005),

$$C = \frac{U_{RMS}\Delta t}{\Delta x} < 1, \tag{3.27}$$

where U_{RMS} is the root mean square of the velocity. To maintain the stability of the simulations, the Courant number in this work was limited to 0.5. While restricting it to less than 1 should be sufficient, the size of a particular timestep is based on the flow behaviour during the previous timestep. Restriction to 0.5 allows for acceleration without breaking the stability requirement.

Computational Cost

In order to resolve all scales of motion, as required for DNS, the magnitude of the smallest motions must be identified. For turbulent flows, this is generally stated as being the Kolmogorov scales (Pope, 2001) for length (η_K), time (τ_η), and velocity (u_η), which are given by

$$\eta_K \equiv \left(\frac{\nu^3}{\epsilon}\right)^{1/4}, \quad \tau_\eta \equiv \left(\frac{\eta_K}{\epsilon}\right)^{1/2}, \quad \text{and} \quad u_\eta \equiv (\nu\epsilon)^{1/4}, \tag{3.28}$$

where ϵ is the rate of kinetic energy dissipation and ν the kinematic viscosity. For cases with $Sc > 1$, it is in fact the more restrictive Batchelor scale (Andersson *et al.*, 2011; Donzis *et al.*, 2014),

$$\eta_B = \eta_K Sc^{-1/2}, \tag{3.29}$$

which characterises the diffusion length for the solute that needs to be resolved. What follows is a discussion of the impact of this requirement on the computational cost of DNS.

The number of grid points, N_p, along a mesh with increments of size Δx must be

$$N_p \Delta x > L_E, \tag{3.30}$$

where L_E is the length scale associated with the larger eddies in the flow. It can be shown that (Lipatnikov, 2012; Sheng *et al.*, 2000)

$$\epsilon \approx U_{RMS}^3 / L_E, \tag{3.31}$$

where

$$U_{RMS} = \sqrt{\frac{\overline{U'}^2 + \overline{V'}^2 + \overline{W'}^2}{3}} \ , \quad \text{and } \overline{U'}^2 = \overline{(U_i - \overline{U}_i)^2} \ . \tag{3.32}$$

Substituting, this results in the expression

$$\eta_K = \left(\frac{\nu^3 L_E}{U_{RMS}^3} \right)^{1/4} . \tag{3.33}$$

It is required that $\Delta x \leq \eta_B$ in order to resolve this scale, and therefore

$$N_p > \frac{L_E}{\eta_B} \ . \tag{3.34}$$

Substituting the expression for η_B,

$$\frac{L_E}{\eta_B} = \left(\frac{U_{RMS} L_E}{\nu} \right)^{3/4} Sc^{1/2}. \tag{3.35}$$

A Reynolds number can be defined using U_{RMS} and L_E as velocity and length scales, $Re_T = \frac{U_{RMS} L_E}{\nu}$ is the turbulent Reynolds number. From there, it can be seen that

$$\frac{L_E}{\eta_B} = Re_T^{3/4} Sc^{1/2}. \tag{3.36}$$

Therefore, in three dimensions, the number of required grid points

$$N_p^3 > Re_T^{9/4} Sc^{3/2}. \tag{3.37}$$

The total cost of the DNS is dependent not only on the number of grid points, but also on the number of timesteps. For stability, the Courant number is restricted to $C < 1$ (Iserles, 2009; Morton & Mayers, 2005). The total time simulated is generally on the order of four times the turbulence time scale (Pope, 2001), $\tau \approx 4 L_E / U_{RMS}$. The total number of timesteps may therefore be estimated as

$$\frac{\tau}{\Delta t} = \frac{4 L_E}{U_{RMS}} \frac{U_{RMS}}{C \Delta x} = \frac{4 L_E}{C \Delta x} = \frac{4 L_E}{C \eta_B} \ . \tag{3.38}$$

However, as

$$N_p > \frac{L_E}{\eta_B} \ , \tag{3.39}$$

(3.38) can also be approximated as

$$\frac{\tau}{\Delta t} = \frac{4L_E}{C\eta_B} \approx \frac{4N_p}{C} \approx 4Re_T^{3/4}Sc^{1/2}. \tag{3.40}$$

Therefore, the total number of timesteps $N_t \propto Re_T^{3/4}Sc^{1/2}$.

The total number of operations, N_o, which provides an indication of the computational cost of the calculation, is proportional to both the number of grid points, N^3, and the number of timesteps, N_t, i.e.

$$N_o \propto Re_T^{9/4}Sc^{3/2}Re_T^{3/4}Sc^{1/2}, \tag{3.41}$$

or when simplified,

$$N_o \propto Re_T^3 Sc^2 \ . \tag{3.42}$$

This level of computational cost is clearly prohibitive, not only for environmental flows (Meiburg *et al.*, 2015) but also for the experimental work described earlier (for which $Re = \mathcal{O}(5000)$ is typical and $Sc = \mathcal{O}(1000)$ (Andersson *et al.*, 2011; Bird *et al.*, 2007; Bonometti & Balachandar, 2008; Reynolds, 1974)). As a result, compromises were necessary regarding the maximum value of Sc that could be considered in this work. It was, however, possible to establish patterns in the effect of increasing Sc and therefore predict whether this limitation was responsible for any differences between the experimental and DNS work. Bonometti & Balachandar (2008) assert that at high $Re = \mathcal{O}(10,000)$, the effect of Sc on the head of gravity currents is small. This leads to an expectation that for the higher Re cases, there should be little difference between the two strands of work. However their discussion of the effects of Sc on the far less chaotic body, and on three-dimensional flow features, is limited.

3.3.6 Numerical Setup

The numerical domain is depicted in Figure 3.24. All walls are no-slip, i.e. $\boldsymbol{U} = 0$ on the walls. The non-dimensionalisation, and how the values of Re and Fr will be varied, must be considered. The parameters are chosen to closely replicate the experimental work. Taking the height of the horizontal plastic near the inlet, which restricts the initial current height, as the characteristic length scale ($L_c = 0.05\,\mathrm{m}$), the maximum average velocity within the flow as the characteristic velocity scale ($U_c = 0.065\,\mathrm{m\,s^{-1}}$), the ratio of the two as the characteristic time scale ($t_c = L_c/U_c = 0.77\,\mathrm{s}$), and accepting that the fluid viscosities are sufficiently close that the viscosity of the dense fluid can be chosen rather than allowing it to vary throughout the flow, the lowest influx PIV case has $Re = 3250$.

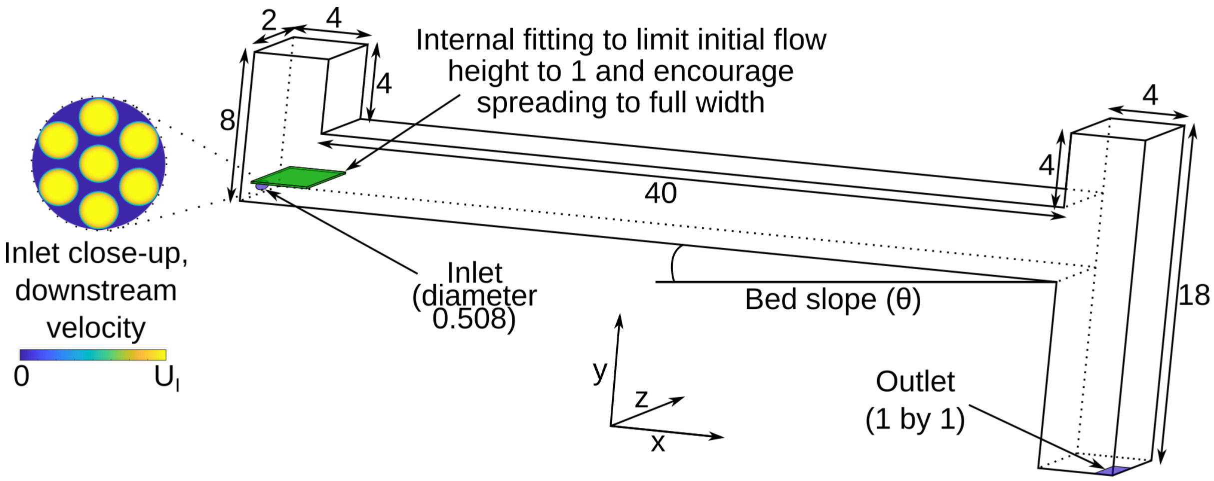

Figure 3.24: DNS setup.

Re	Sc	Pe	ν ($\mathrm{m^2\,s^{-1}}$)	Fr_D	U_I ($\mathrm{m\,s^{-1}}$)	D ($\mathrm{m^2\,s^{-1}}$)
100	1	100	3.26×10^{-5}	0.54	0.22	3.26×10^{-5}
100	10	1000	3.26×10^{-5}	0.54	0.22	3.26×10^{-6}
100	100	10000	3.26×10^{-5}	0.54	0.22	3.26×10^{-7}
500	1	500	6.53×10^{-6}	0.54	0.22	6.53×10^{-6}
500	10	5000	6.53×10^{-6}	0.54	0.22	6.53×10^{-7}
1000	1	1000	3.26×10^{-6}	0.54	0.22	3.26×10^{-6}
3000	1	3000	1.09×10^{-6}	0.54	0.22	1.09×10^{-6}

Table 3.10: Parameters for the various simulations conducted in this work, along with a haline contraction coefficient of $\beta = 1$ and $S_I - S_a = 0.03$ to achieve a 3% density difference. The characteristic length (L_c), velocity (U_c) and time (t_c) scales for every case are $L_c = 0.05\,\mathrm{m}$, $U_c = 0.065\,\mathrm{m\,s^{-1}}$, and $t_c = L_c/U_c = 0.77\,\mathrm{s}$.

A $Re = 3000$ DNS case can be constructed to match this PIV case. The viscosity and L_c are chosen to be the same as for the PIV case, and $U_c = 0.065\,\mathrm{m\,s^{-1}}$ chosen to give the desired $Re = 3000$. To ensure that the lower Reynolds number DNS cases are comparable to this $Re = 3000$ case, fluid viscosity is varied from the experimental value while keeping the characteristic velocity and length scales constant. This gives a constant value of Fr for all cases. Similarly, the inlet velocity from the $Re = 3250$ PIV case can be estimated by dividing the influx by the inlet area. This is used as the inlet velocity for all DNS cases (resulting in a fixed supercritical source Froude number of $Fr_S = 1.65$). See Table 3.10 for the parameters for each case, and the characteristic scales.

Modelling was performed for the inlet flow, with the inlet velocity distribution intended to mimic the effects of the coarse mesh placed over the inlet in the experimental domain. Seven smaller circles were defined within the original inlet circle, which had a dimensionless radius of 0.254 and was centred at $(\tilde{Y}, \tilde{Z}) = (0.35, 1)$. The smaller circles each had dimensionless radius 0.078 as defined experimentally, and were centred at

$$(\tilde{Y}, \tilde{Z}) = (0.350, 1.000),\ (0.531, 1.000),\ (0.169, 1.000),\ (0.441, 1.150),\\ (0.260, 1.150),\ (0.441, 0.850),\ (0.260, 0.850). \tag{3.43}$$

(Re, Sc)	No. Elements	Polynomial Order
$(100, 1)$	28720	8
$(100, 10)$	28720	12
$(100, 100)$	28720	12
$(500, 1)$	28720	12
$(500, 10)$	28720	12
$(1000, 1)$	28720	10
$(3000, 1)$	28720	12

Table 3.11: The number of elements and polynomial order used for each DNS case.

As the exact inlet velocity distribution could not be easily measured, a simple distribution described by

$$\tilde{U} = \tilde{U}_I \sqrt{\sin((0.5 + 0.5\tilde{r}^2)\pi)} \tag{3.44}$$

was employed (where $\tilde{r}$ varied from 0 to 1 across each small circle). Where the velocity on the inlet was non-zero, the salinity was chosen to be $\tilde{S} = 1.03$ compared to 1 in the rest of the domain (and therefore $\Delta S_I = 0.03$), with a haline contraction coefficient of $\beta = 1$. The outlet was also simplified, with a square outlet placed in a corner of the lowest plane of the domain rather than a central circle in the same plane as in the experimental work. Both simplifications were far from the DNS measurement region.

The domain was divided into elements, with the point distribution within each element based on a GLL distribution. This was done using a Nek5000 tool, `genbox`, which divides the domain into connected cubic regions (or elements) with a user-specified number of elements in each dimension. The elements were clustered towards the bottom of the main section, near the flow of interest. The elements were minimised in the raised sections at either end of the domain, and in the drop above the outlet, where the flow was not of interest to the investigation. Table 3.11 shows the number of elements and the polynomial order used for each case. Figure 3.25 shows slices from an example mesh used in this work.

3.3.7 Establishing sufficient resolution

As noted by Esfeh *et al.* (2017), while many publications state that mesh independence analysis has been conducted, most fail to describe the techniques or criteria that have been used. While the resolution in areas of the domain far from the measurement region and that do not impact the main flow (specifically the raised sections at either end of the domain, and the drop above the outlet) will likely not have been sufficient to capture all scales of motion, within the main section of the domain sufficient resolution was established. Here, two different techniques were used to establish that the meshes were sufficiently refined to capture all scales of motion. First, the wall y^+, x^+, and z^+

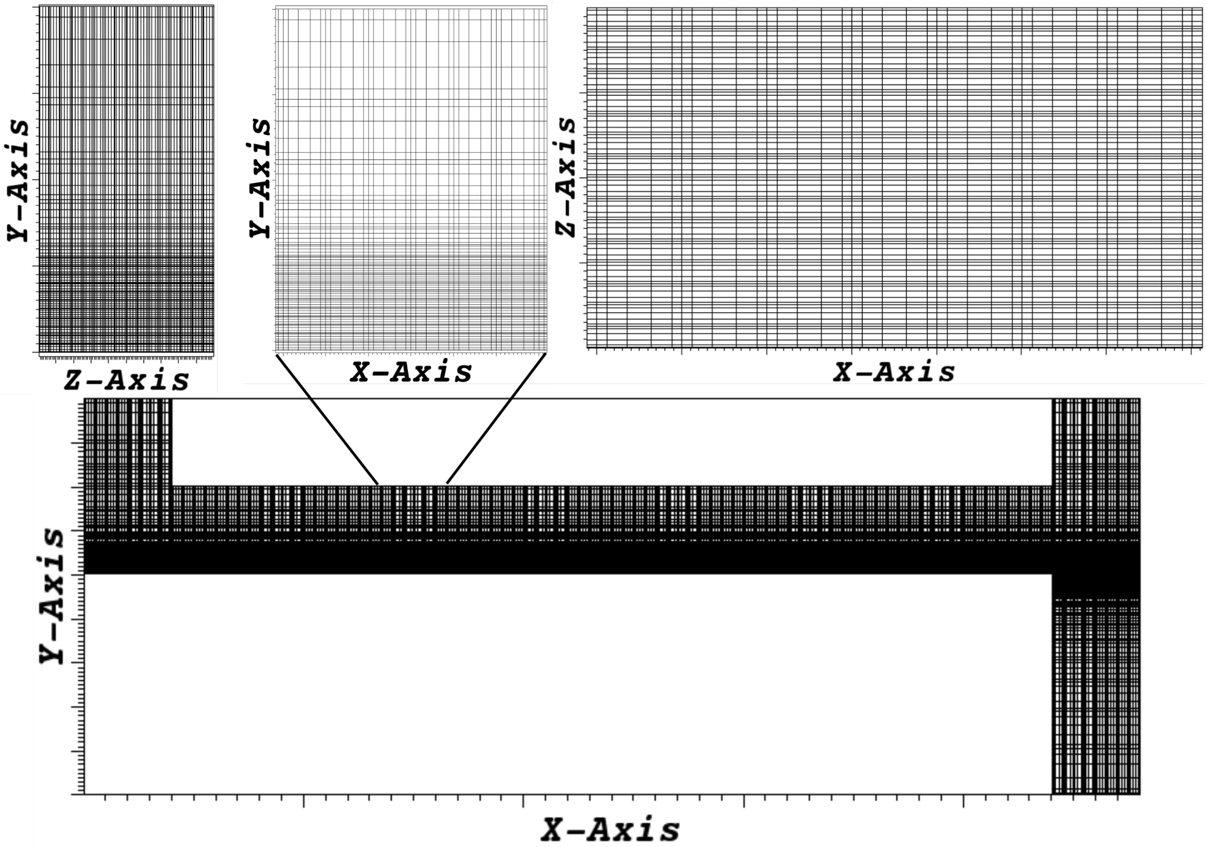

Figure 3.25: Slices from one of the meshes used in this work including (bottom) an overall X-Y slice, (top left) an overall Y-Z slice from the measurement region, (top centre) a partial X-Y plane from the measurement region, and (top right) a partial X-Z plane from the measurement region.

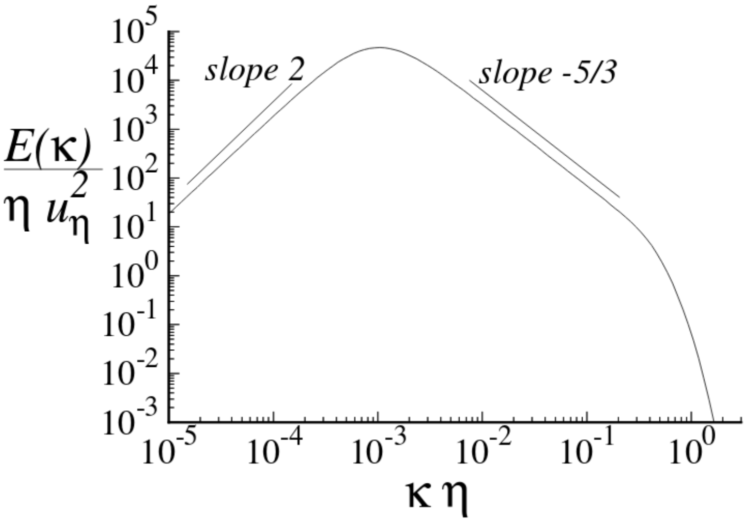

Figure 3.26: Example energy spectrum, taken from Pope (2001, p. 229) showing the energy spectrum (E) as a function of wave number ($\boldsymbol{k}$) normalised by the Kolmogorov length (η_K) and velocity (u_η) scales.

Re (→) Sc (↓)	100	500	1000	3000
1	●	●	●	●
10	●	●		
100	●			

Table 3.12: Parameter space, ● = case conducted.

values were considered (Wilcox, 2006). These are defined as $y^+ = u_w y/\nu$ (and equivalent statements for the other two spatial dimensions) where y is the distance from the grid point to the nearest wall, $u_w = \sqrt{\tau_w/\rho}$ the friction velocity, and τ_w the wall shear stress (Magoulès, 2011). For turbulent flows, these values should be kept below 0.05 for the first point away from the wall, and the first 10 points should be within $y^+ < 10$ (Coleman & Sandberg, 2010; Kim *et al.*, 1987). Working within these constraints should ensure sufficient resolution in the near-wall regions.

As discussed by Pope (2001), the energy spectrum can also be considered. The turbulent fluctuations in the velocity field must be identified, and the two-point correlation function of these fluctuations calculated. A log-log plot of the absolute value of the Fourier transform of the correlation function is then plotted against the frequency. In the centre of the frequency range, the gradient of the plot will in theory be $-5/3$. If the resolution is sufficient to capture all scales of motion, the dissipative subrange, identified by a steeper negative gradient, will also be captured (see Figure 3.26). If this steeper section is not present, the spatial resolution may not be sufficient to capture all energy levels in the flow. Bonometti & Balachandar (2008); Cantero *et al.* (2006, 2007); Necker *et al.* (2002) claim, however, that 6 to 8 decades of decay in the energy spectrum for all variables indicates sufficient resolution in a turbulent flow. In this work, the more stringent change in gradient indicating the dissipative subrange was used to indicate sufficient resolution. In regions considered sufficiently far from the flow of interest that the main flow would not be affected (the raised sections at either end of the domain, and the drop above the outlet), the spatial resolution was reduced to save computational cost. In these outlying regions, it is therefore likely that the smallest scales of motion were not captured.

3.3.8 Cases Investigated

The parameter space investigated was as shown in Table 3.12. The Reynolds and Schmidt numbers were varied by changing the kinematic viscosity and the mass diffusivity. To keep the DNS cases comparable to the experimental work, the bed slope was chosen to be $\theta = 0.1°$. Cases were conducted on the ARC3 and ARC4 high performance computing clusters at the University of Leeds.

Chapter 4

The Structure of the Pseudo-Steady Body

Internal gravity waves have been postulated to exist in gravity currents, yet they have never been observed experimentally. In this chapter, Particle Image Velocimetry (PIV) is used to generate instantaneous two-dimensional experimental measurements of gravity current body flow. The modal dynamics of internal waves are directly observed in the body of a constant-influx experimental gravity current flow. Spectral analysis and dynamic mode decomposition, of streamwise and vertical velocity, are used to identify the dominant internal waves within the flow. The estimated, Doppler shifted, Brunt-Väisälä buoyancy frequencies of these key spectral modes show that they are gravity waves. The experimental data, gathered using particle image velocimetry, enables the instantaneous, whole-field, dynamics of constant-influx solute gravity currents to be resolved. The internal waves observed in the gravity current propagating over a smooth surface are thus demonstrated as generated by interfacial instabilities between the flow and ambient fluid. A critical layer is identified within the flow, located at the height of the maximum internal velocity. Irreversible internal wave breaking that has been postulated to occur at this critical layer suggests formation of internal eddy transport barriers, demonstrating that new dynamic models of turbulent mixing in gravity currents are needed.

4.1 Background

Gravity currents, also known as density currents, are a common class of geophysical flow that occur in many natural and man-made environments (Simpson, 1997; Ungarish, 2009). They are of particular relevance to the study of atmospheres and oceans, with examples including thunderstorm outflows, and sediment transport in lakes and oceans (Bonnecaze *et al.*, 1993; Britter & Linden, 1980; Parsons & García, 1998; Simpson, 1997; Talling, 2014). Owing to their prevalence, and the fact that they are the primary mechanism for the transport of sediment, solutes, and heat in oceans (Dorrell *et al.*, 2019; Talling, 2014), extensive research has been conducted to establish the structure and dynamics of gravity currents through both experimental (Ellison & Turner, 1959; Gray *et al.*, 2005; Hacker *et al.*, 1996; Hallworth *et al.*, 1996; Kneller *et al.*, 1999; Middleton, 1966) and numerical investigations (Cantero *et al.*, 2007; Hogg *et al.*, 2016; Meiburg *et al.*, 2015; Özgökmen *et al.*, 2004; Stacey & Bowen, 1988).

Experimentally, gravity currents can be categorised by mode of generation. Two often-discussed examples are constant-flux and constant-volume flows. There are significant differences in structure between the two flow types (Gerber *et al.*, 2010; Nogueira *et al.*, 2014). In a constant-flux current, the continuous replenishment of dense fluid results in the bulk of the head and body of the current remaining undiluted (Hallworth *et al.*, 1996). This category of flow has a prolonged body, which is assumed to be statistically steady with only small variations in characteristic variables, such as velocity and density (Gerber *et al.*, 2010; Kneller & Buckee, 2000). In a constant-volume flow, this body section is much shorter with a proportionally far more prominent head section. Existing experimental research has primarily considered constant-volume type flows, and examined the structure of the head of the flow over periods ranging from 10 s to a few minutes (Hacker *et al.*, 1996; Hallworth *et al.*, 1996; Middleton, 1966). However, in oceanic gravity currents the head typically is not present, or forms only a small portion of the flow. Such currents are either quasi-permanent (for example the flow resulting from the connection between the Mediterranean Sea and the Black Sea (Sumner *et al.*, 2014)) or have been observed to persist for several hours, or even days, and as a result the flow is assumed to be predominantly statistically steady (Azpiroz-Zabala *et al.*, 2017; Khripounoff *et al.*, 2003; Parsons *et al.*, 2007; Peakall & Sumner, 2015; Simpson, 1997). However, despite the body of gravity currents normally forming the bulk of the flow (Azpiroz-Zabala *et al.*, 2017; Özsoy *et al.*, 2001; Sumner *et al.*, 2014), the structure of turbulence within the body remains poorly understood (Wells & Dorrell, 2021).

There are two primary mixing processes that occur in the head of the flow (Hacker *et al.*, 1996; Kneller & Buckee, 2000; Simpson, 1997; Ungarish, 2009): vortices that form as a result of Kelvin-Helmholtz instabilities generated by shear between the current and ambient fluid; and ambient fluid incorporated into the current as the raised nose of the current propagates over a no-slip surface, leading to a three-dimensional lobe-and-cleft structure (Simpson, 1997). Existing experimental work has primarily considered lock-exchange constant-volume type flows with short statistically steady sections, or are based on at-a-point or profile measurements of constant-flux flows which limit the analysis techniques available (Buckee *et al.*, 2001; Cossu & Wells, 2012; Davarpanah Jazi *et al.*, 2020; Gray *et al.*, 2006; Islam & Imran, 2010; Kneller *et al.*, 1999). Properties such as instantaneous and time-averaged Reynolds stress and turbulent kinetic energy have been measured in several previous works (Buckee *et al.*, 2001; Cossu & Wells, 2012; Gray *et al.*, 2006; Islam & Imran, 2010). For example, Buckee *et al.* (2001) examined a time-averaged profile of turbulent kinetic energy, and identified shear from the mean flow as the primary source of turbulence in the body of gravity currents, and Kneller *et al.* (1999) used instantaneous velocity fluctuations and Reynolds stresses to suggest the presence of eddies with size on the same order as the height of the body. Interfacial instabilities, in the form of Holmboe waves, between the flow and the ambient, have been observed in a gravity current in an inclined duct (Lefauve *et al.*, 2018). However, there remains very little work on coherent flow structures within the body of gravity currents.

The currently accepted structure of gravity current body velocity and density profiles are shown in Figure 4.1a (Abad *et al.*, 2011; Buckee *et al.*, 2001; Dorrell *et al.*, 2019; Kneller & Buckee, 2000; Kneller *et al.*, 2016; Sequeiros *et al.*, 2010). The body is generally assumed to be two-dimensional and quasi-steady, with structure that can be divided into upper and lower layers by the height of the velocity maximum (Gray *et al.*, 2006; Islam & Imran, 2010; Kneller & Buckee, 2000). The upper layer structure is determined by density stratification and shear with ambient fluid, and the shape appears comparable with that of a wall-bounded jet. Unlike the jet, however, the lower layer of the gravity current can be approximated as similar to an open-channel flow (Dorrell *et al.*, 2019). Recent field measurements and laboratory experiments have suggested that this model may need to be revised to a dynamic version considering forcing of flow-scale turbulent structures (Best *et al.*, 2005; Dorrell *et al.*, 2018; Kostaschuk *et al.*, 2018). Flow-scale mixing by periodic internal gravity waves has been postulated to explain the structure of field-scale gravity currents in data collected from the body of a natural saline gravity current (Dorrell *et al.*, 2019). A thorough understanding of the structure of the body of gravity currents is critical for accurate predictions of flow duration and interaction with the surroundings (Azpiroz-Zabala *et al.*, 2017; Kneller *et al.*, 1999).

In this chapter, particle image velocimetry (PIV) is used to generate non-intrusive whole-field measurements of the instantaneous velocity structure of constant-influx, solute-based gravity currents. Quantification of the turbulence structure within the pseudo-steady body is used to improve existing understanding of gravity current flows. Therefore, it enables a far more detailed analysis of the nature of turbulence and flow structure within the body of a density current. Specifically, the key aims are to assess: i) whether the pseudo-steady body of gravity currents can be described by flow-scale structures in the form of internal gravity waves, ii) how these waves change with flow Reynolds number, iii) what these waves imply for our existing understanding of gravity currents, and iv) how such waves interact with the environment. The experimental setup is described in Section 4.2, followed by discussion of the turbulence structure in Sections 4.3 and 4.4.

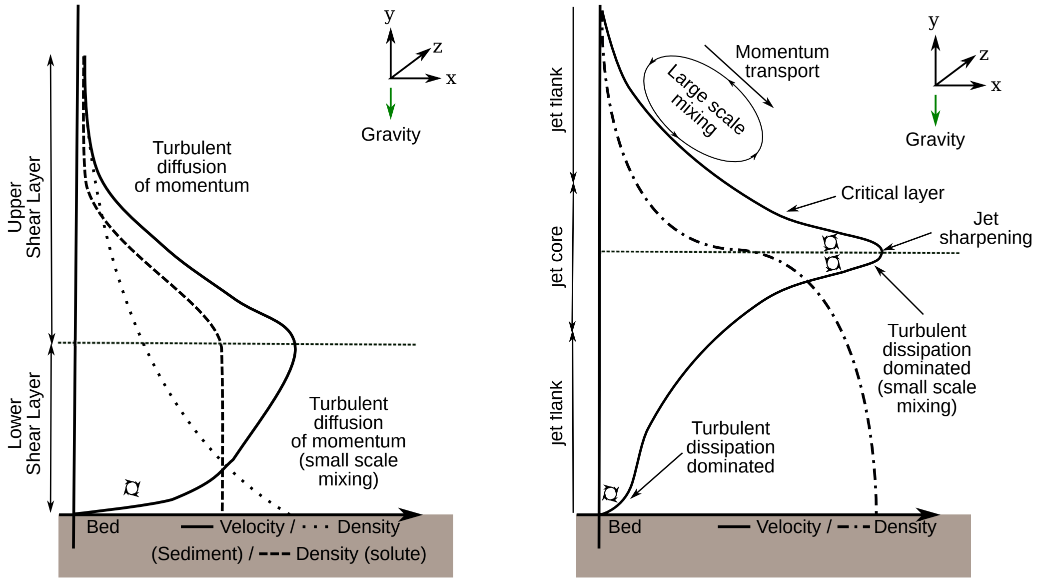

(a) (b)

Figure 4.1: (a) the currently accepted idealised structure of gravity current body velocity and density profiles (Abad *et al.*, 2011; Altinakar *et al.*, 1996; Davarpanah Jazi *et al.*, 2020; García, 1994; Kneller & Buckee, 2000; Sequeiros *et al.*, 2010) and (b) a postulated flow structure from Dorrell *et al.* (2019) based on field-scale gravity current measurements and comparison with zonal jet flows (Dritschel & Scott, 2011). In (b), the coherent structure associated with large-scale mixing is equivalent to a wave depending on frame of reference. The presence of dispersive waves leads to momentum transport due to anti-diffusive mixing and radiation stresses (Dorrell *et al.*, 2019). Internal waves break close to the critical layer, leading to deposition of angular momentum and flow acceleration.

4.2 Methodology

The constant-flux gravity current experiments are conducted in a tank 0.1 m wide, 0.2 m deep and 2 m long (schematic shown in Figure 4.2). The system is designed such that fluid leaves the outlet at the same rate that it is pumped in through the inlet. Raised sections, added at either end, prevent air entrainment through the inlet or outlet reaching the measurement region. The bed slope (θ) for these experiments is set to 0.1°. A large sump at the outlet prolongs flow duration by slowing the rate of current fluid pollution into the ambient fluid. The tank is initially filled with ambient solution, a 6% by mass solution of glycerol. The dense fluid, a 6% by mass solution of potassium dihydrogen

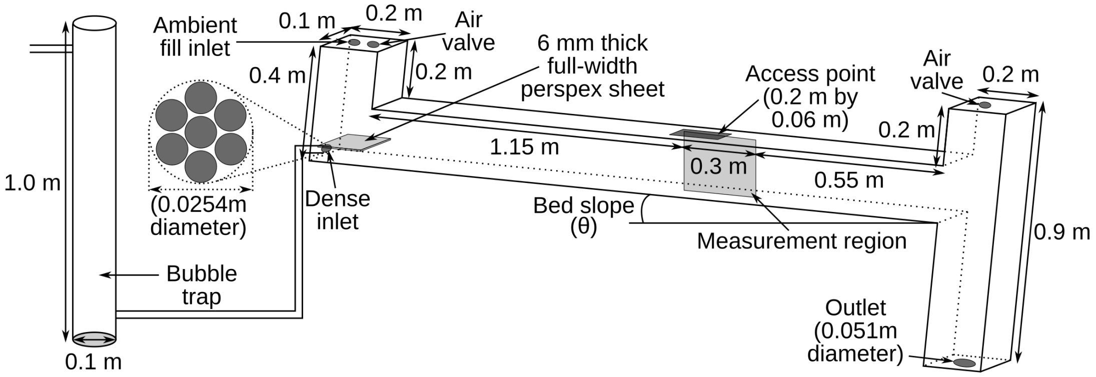

Figure 4.2: Schematic of the experimental setup.

Solute	ρ (kg m^{-3})	ν (m^2 s^{-1})	n
Glycerol (ambient fluid)	1012.0	1.14×10^{-6}	1.3400
Potassium dihydrogen phosphate (current fluid)	1041.4	1.09×10^{-6}	1.3400

Table 4.1: Details of the density, ρ, kinematic viscosity, ν, and refractive index, n, of 6% by mass solutions of the ambient (glycerol) and dense (potassium dihydrogen phosphate) solutes in tap water at 20 °C, from Haynes (Haynes, 2014).

phosphate (KDP), is pumped in at a constant rate through the inlet using a positive-displacement gear pump to provide a steady inflow with an inverter to control the flow rate. A coarse mesh with holes of diameter 7.8 mm is fitted over the inlet to provide a homogeneous inflow. Before entering the tank, the dense fluid first passes through a bubble trap, removing any air entrained by the gear pump. The bubble trap consists of a 1 m long, 0.1 m diameter cylinder filled with dense fluid. The dense fluid is pumped in to the top of this cylinder and out at the bottom, removing any small bubbles. The top and back of the tank are covered in black aluminium polyethylene composite panels to improve the image quality and contain the laser light.

4.2.1 Refractive Index Matching

Two 150 L mixing tanks are used to mix the ambient and dense fluids, which have a $\sim 3\%$ density difference (see Table 4.1). These two fluids, as well as a mixture of the two, are refractive index matched as required for PIV (Alahyari & Longmire, 1994). The fluid concentration and refractive index matching is tested using both a Reichert AR200 digital refractometer and an Anton Paar DMA™ 35 Basic density meter as well as by monitoring the temperature (which can have a significant impact on refractive index). The refractive index of each fluid is required to be equal to the reference value in Table 4.1 to the precision of the refractometer (5 significant figures) and constant across 3 consecutive readings at least 5 minutes apart. The density of the fluids is allowed to vary from the reference values due to temperature variation, with readings in the ranges 1012.9 ± 0.2 kg m^{-3} for the glycerol solution and 1043.0 ± 0.5 kg m^{-3} for the KDP.

4.2.2 The PIV System

Planar particle image velocimetry (PIV) is used to generate measurements of downstream and vertical velocities (Adrian & Westerweel, 2011; Raffel *et al.*, 2018). Silver-coated hollow glass spheres are used as PIV seeding particles, with mean diameter of 10 µm and density of 1400 kg m^{-3}, at concentrations of 0.0015 g L^{-1} and 0.0014 g L^{-1} for the current and ambient fluids respectively. The Stokes velocity of these seeding particles, $U_g = \frac{d_p^2(\rho_p - \rho)\boldsymbol{g}}{18\mu} \approx 1.70 \times 10^{-8}\,\mathrm{m\,s^{-1}}$, and their relaxation time, $\tau_r = \frac{d_p^2 \rho_p}{18\mu} \approx 6.50 \times 10^{-9}\,\mathrm{s}$, suggests that they follow the flow sufficiently for them to be suitable for use as PIV seeding particles.

A central vertical plane, parallel to the flow direction, is illuminated using a 532 nm Nd:YAG laser (with maximum energy 50 mJ). The images are captured using a DANTEC Dynamics SpeedSense camera with a Zeiss ZF.2 50 mm f/1.4 lens with aperture set to f/2.0 that captures approximately 0.3 m of flow horizontally and 0.18 m vertically (see Figure 4.2). The images are captured at a rate of 50 Hz in single-frame mode, and processed using DANTEC Dynamic Studio version 6.4 adaptive PIV. The resulting velocity field is on a grid with spatial resolution 0.003 m × 0.003 m.

4.2.3 The Experimental Cases

A series of experiments are designed to establish the effect of influx (and therefore Reynolds number) on gravity current dynamics, in particular the turbulence structure of the body of the gravity current. The influx rates for this set of experiments are shown in Table 4.2, along with characteristic length L_c, velocity U_c and time t_c scales, and Reynolds ($Re = U_c L_c/\nu$) and densimetric Froude ($Fr_D = U_c/\sqrt{g' L_c}$) numbers, where ν is the kinematic viscosity, and g' is the reduced gravity. Here, the characteristic scales are defined using averaged profiles. In order to calculate time averages of the body data ($\overline{U}$, $\overline{V}$), the location of the body must be identified. Here, the body is defined by measuring the time taken for the current front to travel across the measurement region, and then waiting that length of time again before averaging across all downstream locations and time. For all cases this results in consistent downstream velocity averages, whether averaging over 5 s or 20 s of data (shown in Figure 4.3), suggesting that this section of flow is approximately quasi-steady.

The characteristic velocity scale is taken to be the maximum downstream average velocity, $U_c = \overline{U}_{max}$, and the length scale the Ellison and Turner integral length scale (Ellison & Turner, 1959). This scale is defined as

$$L_c = \frac{\left(\int \bar{\bar{U}} dY\right)^2}{\int \bar{\bar{U}}^2 dY}, \tag{4.1}$$

where $\bar{\bar{U}}$ is the mean velocity relative to that in the ambient. The Ellison and Turner length scale is observed to be different from the current height (where the downstream velocity averaged over time $\overline{U} = 0$). The characteristic time scale is the ratio of the two, $t_c = L_c/U_c$. The kinematic viscosities of the dense and ambient fluids are very similar (see Table 4.1) and for these calculations we use the viscosity of the dense fluid. These characteristic scales lead to Reynolds and Froude numbers that are output parameters, and therefore a doubling of influx does not result in a doubling of Reynolds number. The experiments captured between 35 and 55 s of data, including both the head and body of the flow, dependent on the rate of pollution of the ambient as a result of mixing. This

Case	Influx ($\mathrm{L\,s^{-1}}$)	L_c (m)	U_c ($\mathrm{m\,s^{-1}}$)	t_c (s)	Re	Fr_D
1	0.07	0.035	0.071	0.50	2292	0.69
2	0.09	0.038	0.081	0.48	2842	0.76
3	0.11	0.041	0.080	0.52	3034	0.73
4	0.12	0.043	0.085	0.51	3325	0.75
5	0.14	0.047	0.091	0.52	3927	0.77
6	0.16	0.048	0.086	0.56	3778	0.72
7	0.18	0.050	0.094	0.53	4284	0.78

Table 4.2: Details of the influx rate, characteristic length (L_c), velocity (U_c) and time (t_c) scales, and Reynolds and Froude numbers for cases $1-7$, $Re = U_c L_c/\nu$ and $Fr_D = U_c/\sqrt{g' L_c}$ where $U_c = \overline{U}_{max}$, L_c is the Ellison and Turner integral length scale (Ellison & Turner, 1959), and $t_c = L_c/U_c$.

flow duration is shorter for the higher influx cases owing to the higher rate of mixing, and the smaller ratio of ambient fluid to dense fluid.

4.3 Results

As seen in some previous works (Best *et al.*, 2005; Kostaschuk *et al.*, 2018), the height of the velocity maximum oscillates over time for influx values greater than $0.11\,\mathrm{L\,s^{-1}}$ (see Figure 4.4), which may be linked to cross-stream flow, the presence of low frequency waves, and enhanced turbulent mixing (Dorrell *et al.*, 2018). Mean velocity profiles collapse by shifting velocities by dividing by U_c, and the vertical location by subtracting the averaged height of the velocity maximum, and then dividing by L_c,

$$\begin{aligned} U^* &= U/U_c, \\ Y^* &= (Y - Y_{\overline{U}_{max}})/L_c, \\ t^* &= t/t_c\ . \end{aligned} \tag{4.2}$$

For all cases, this normalisation unexpectedly results in average non-dimensional current height ~ 1. The downstream velocity averages for data in the body of each case are shown in Figure 4.5a, with averaged $\overline{(dU^*/dt)}$ and $d\overline{U^*}/dY^*$ for two cases in Figures 4.5b and 4.5c. The addition of lines illustrating the average height of the velocity maximum, the height of minimum $d\overline{U^*}/dY^*$, and current height h, defined as the point where the average downstream velocity changes from positive to negative allows closer comparison between the two cases. Both cases have local maxima in $\overline{dU^*/dt^*}$ (Figure 4.5b) that coincide with the height of the local minimum in $d\overline{U^*}/dY^*$ (Figure 4.5c), suggesting flow acceleration at this height. The higher influx case also has a local maximum in acceleration at the average height of the velocity maximum, though the lower influx case is decelerating at this height.

Subtracting the average profiles in Figure 4.5a from the instantaneous data in the body gives the downstream and vertical fluctuations from the mean ($U^{*\prime} = U^* - \overline{U^*}$,

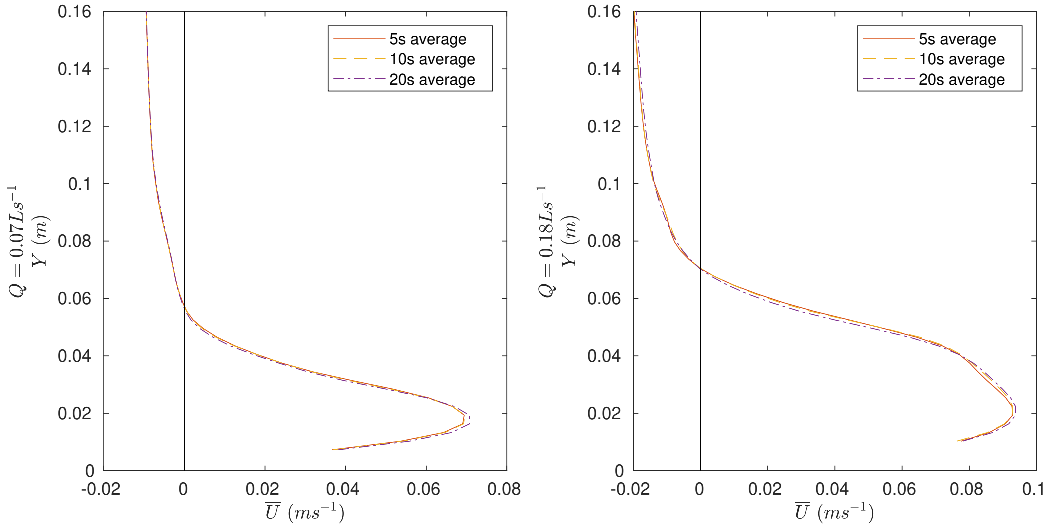

Figure 4.3: Averages of downstream velocity over downstream location and time windows ranging from 5 s to 20 s for (left) $Q = 0.07\,\mathrm{L\,s^{-1}}$ and (right) $Q = 0.18\,\mathrm{L\,s^{-1}}$.

$V^{*\prime} = V^* - \overline{V^*}$). As in previous work (Buckee *et al.*, 2001), cross-stream velocity fluctuations $W^{*\prime}$ are assumed to be small compared with $U^{*\prime}$ and $V^{*\prime}$ and the averaged normalised turbulent kinetic energy is defined as $\overline{k^*} = 0.5(\overline{U^{*\prime 2} + V^{*\prime 2}})$. There are significant similarities between the profiles of time-averaged normalised turbulent kinetic energy presented in Figure 4.5d and those presented in previous studies (Buckee *et al.*, 2001; Cossu & Wells, 2012; Gray *et al.*, 2006; Islam & Imran, 2010), specifically a local minimum just above the velocity maximum and a local maximum between the velocity maximum and current height, here close to the height of maximum negative shear. The maximum value of $\overline{k^*}$ is highly dependent on the time range chosen for averaging (suggesting significant temporal variation) though the profile shape remains similar. All cases here have a maximum value of $\overline{k^*}$ located below the velocity maximum.

In order to examine the structure within the body, the instantaneous data $U^{*\prime}$, $V^{*\prime}$, and $k^* = 0.5(U^{*\prime 2} + V^{*\prime 2})$ are presented for each case. Figure 4.6 shows vertical velocity fluctuations at a central non-dimensional downstream location, i.e. fixed X^* (where $X^* = X/L_c$ and X is downstream location), as a function of Y^* within the body over time. This central location is defined as the centre of the images, with the exact location varying slightly from case to case but always $\sim 1.5\,\mathrm{m}$ from the inlet. In the low influx cases there is a regular pattern within the current body. As Reynolds number increases, this pattern becomes less regular and higher frequency. Additionally, as influx increases, a second regular structure appears at the height of the current with a frequency that decreases with increasing Reynolds number.

Figure 4.7 shows k^* at a central downstream location for each case. These plots suggest significant temporal variation within the body. For the lowest influx cases, this takes the form of intermittent peaks at the height of maximum negative shear (marked with a dashed line). As influx increases, intermittent peaks begin to appear at the height

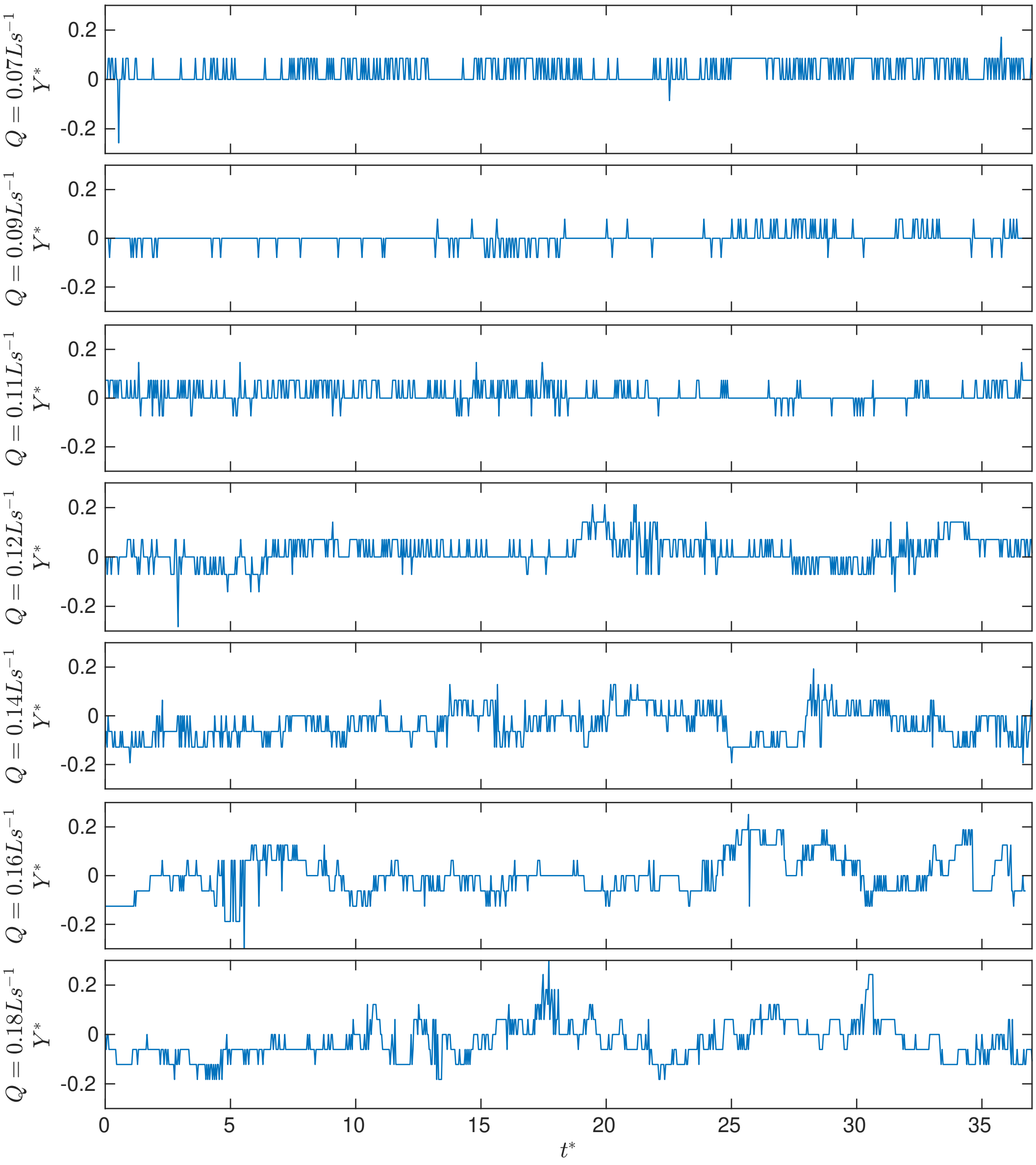

Figure 4.4: Plots of the height of the velocity maximum over time at a central downstream location for the body data for each case, defined as in Figure 4.5a. This location is always $\sim 1.5\,\mathrm{m}$ from the inlet.

of the velocity maximum. By $Q = 0.16\,\mathrm{L\,s^{-1}}$, these intermittent peaks are also present at the upper interface. Time averaging turbulence statistics may therefore discard data important for the understanding and modelling of turbulence structure. As V is small compared with U, U_{max}^2 is representative of the kinetic energy in the mean flow. As the magnitudes of $\overline{k^*}$ and k^* are small ($\ll 1$), the energy contained within turbulent fluctuations is small compared with that in the mean flow.

Having established the presence of spatio-temporal structure in the body, suitable techniques to analyse this structure are required. This analysis will focus on two representative cases with the lowest incidence of spurious vectors – one low influx case ($Q = 0.09\,\mathrm{L\,s^{-1}}$), and one high influx case ($Q = 0.16\,\mathrm{L\,s^{-1}}$). Some motions with significant impact on the flow can be identified purely by examination of the plots of $V^{*\prime}$. Figure 4.8 is a closer view of the vertical velocity fluctuations in these two cases. Figure 4.8a

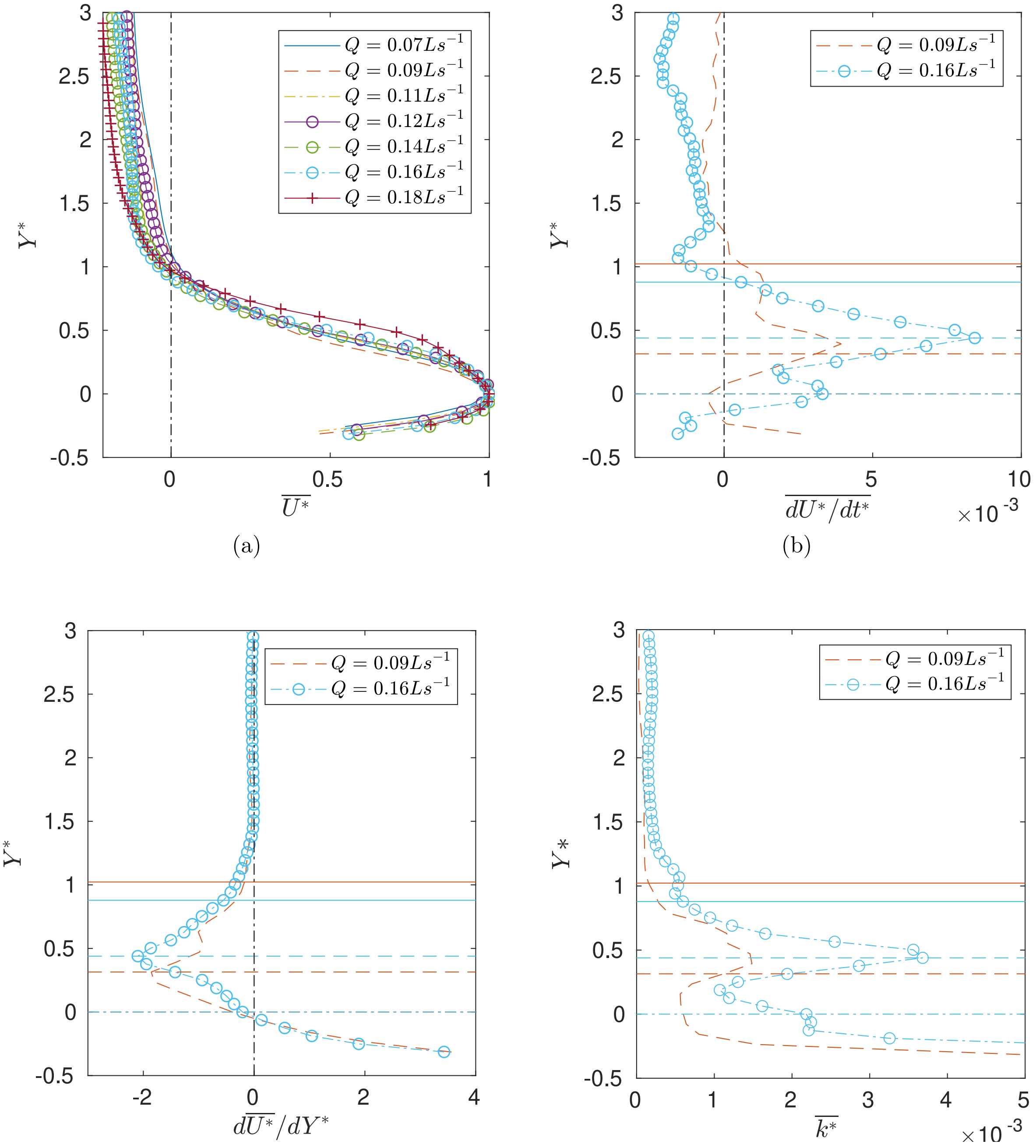

(a) (b) (c) (d)

Figure 4.5: (a) Normalised downstream velocity averaged over all downstream locations and 10 s body timesteps for all cases, (b) differential of the same data for the cases with $Q = 0.09\,\mathrm{L\,s^{-1}}$ and $Q = 0.16\,\mathrm{L\,s^{-1}}$ with respect to time, then averaged over all downstream locations and included timesteps, (c) the plots from (a) for the same two cases differentiated with respect to Y^*, and (d) $\overline{k^*} = 0.5(\overline{U^{*\prime 2} + V^{*\prime 2}})$ for the same two cases, where $\overline{k^*}$ is averaged over the same range as the profiles in (a). The horizontal lines indicate (solid) the height of the upper interface defined as the point where the downstream velocity changes direction, (dashed) the height of maximum negative shear, and (dot-dash) the height of the downstream velocity maximum from the downstream velocity average defined in (a) (where the body is defined by measuring the time taken for the current front to cross the measurement region and then waiting that time again before including data).

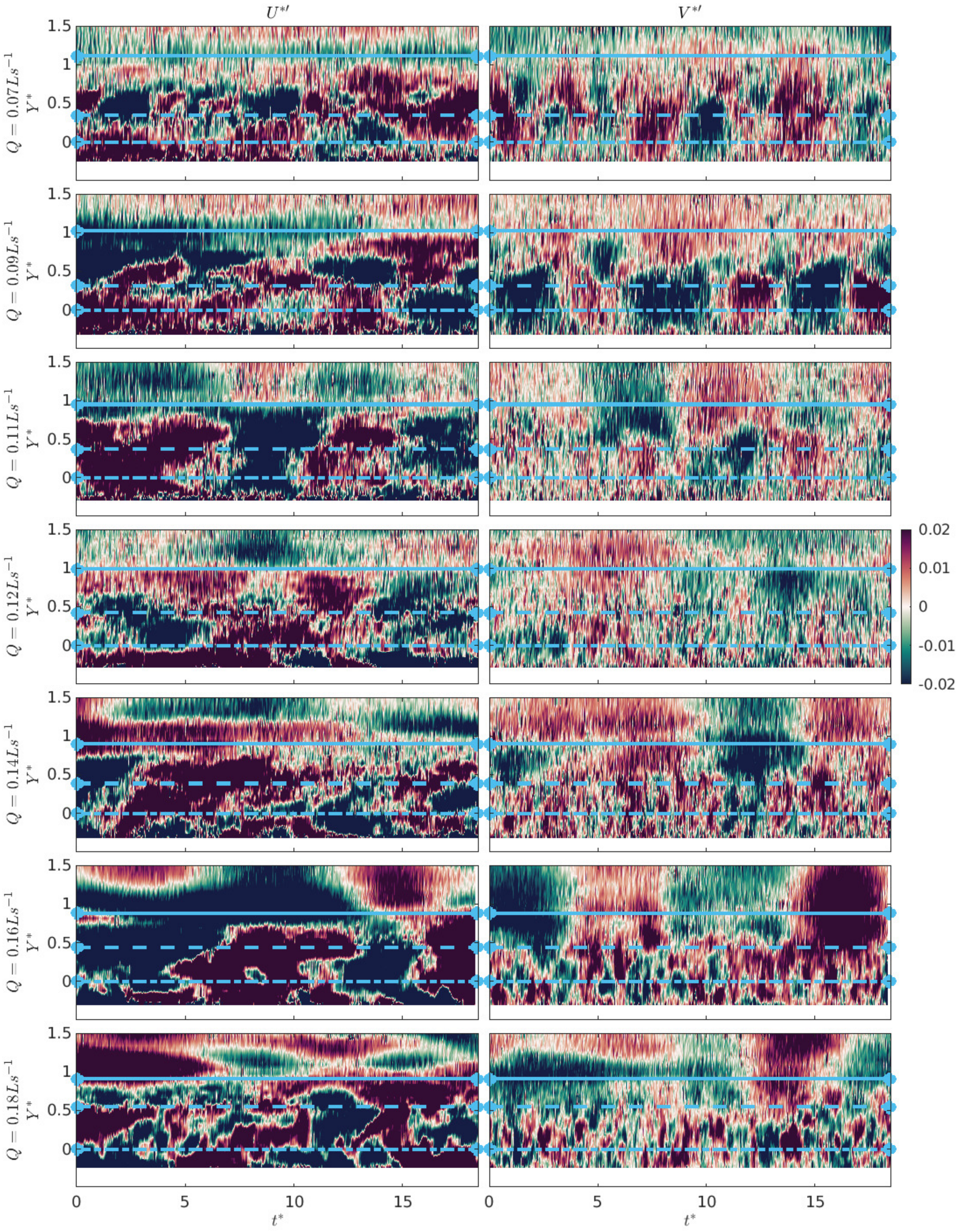

Figure 4.6: Plots of (left) $U^{*\prime}$ and (right) $V^{*\prime}$ data over time for (top to bottom) increasing influx from $Q = 0.07\,\mathrm{L\,s^{-1}}$ to $Q = 0.18\,\mathrm{L\,s^{-1}}$. The velocity fluctuations $U^{*\prime}$ and $V^{*\prime}$ are defined by subtracting the averaged vertical velocity profiles (averaged over the same range as the profiles in Figure 4.5a) from the instantaneous data used to calculate the averages. These plots show the data at the central downstream location within the measurement area as defined in Figure 4.4.

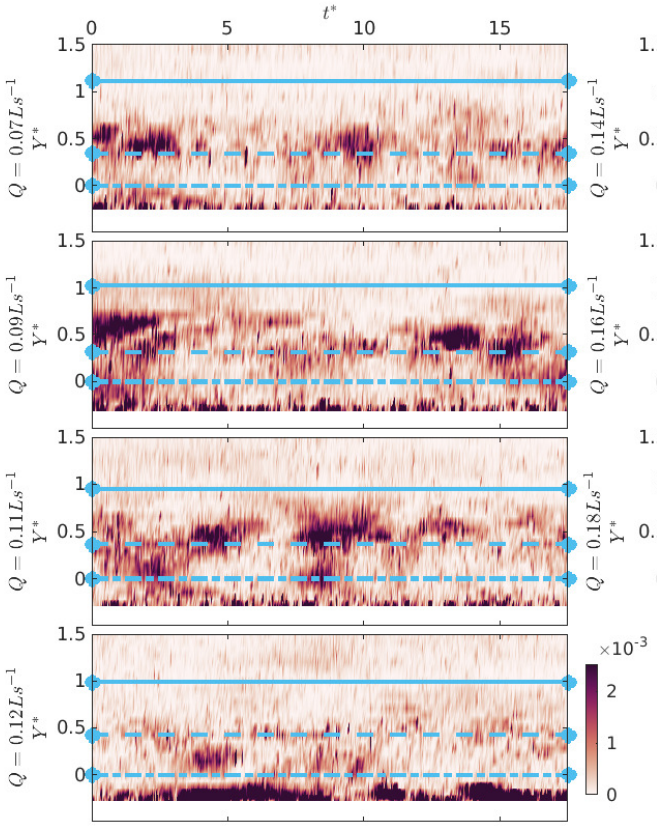

Figure 4.7: Plots of $k^* = 0.5(U^{*\prime 2} + V^{*\prime 2})/\overline{U^*}^2_{max}$ over time for increasing influx from $Q = 0.07\,\mathrm{L\,s^{-1}}$ to (b) $Q = 0.18\,\mathrm{L\,s^{-1}}$ in the body (defined as in Figure 4.5a) at a central downstream location (defined as in Figure 4.4).

shows motions with period $\sim 3\,\mathrm{s}$ above the velocity maximum in the $0.09\,\mathrm{L\,s^{-1}}$ case, and Figure 4.8b motions with a period $\sim 5\,\mathrm{s}$ on the upper interface in the $0.16\,\mathrm{L\,s^{-1}}$ case. It is therefore expected that motions with frequency $\sim 0.33\,\mathrm{Hz}$ and $\sim 0.20\,\mathrm{Hz}$ respectively have a significant impact on the flow. For a more detailed analysis of these motions and their structure, we here employ discrete Fourier transforms, wavelet transforms, and Dynamic Mode Decomposition (DMD). These techniques will be used in combination, with the aim of providing a thorough understanding of the flow structure, and will be applied to the data in dimensional form.

4.3.1 Fast Fourier Transform

A discrete Fourier transform in time (Briggs & Henson, 1995; Iftekharuddin & Awwal, 2012) is used to decompose a signal of N data snapshots that are equally spaced over time into the frequencies that make up that signal, $\varsigma \rightarrow \hat{\varsigma}$ where $\hat{\varsigma}$ is the data ς transformed into the frequency domain. Here, a central downstream location is selected and a fast Fourier transform over time performed using the MATLAB `fft` function (MATLAB, 2020) on the body data (defined as the data used to calculate the averages shown in Figure 4.5a). Figure 4.9 shows the frequencies that dominate the flow. For $Q = 0.09\,\mathrm{L\,s^{-1}}$, the FFT identifies key frequencies of interest: $0.35\,\mathrm{Hz}$, $0.50\,\mathrm{Hz}$, $0.65\,\mathrm{Hz}$, and $0.85\,\mathrm{Hz}$. As

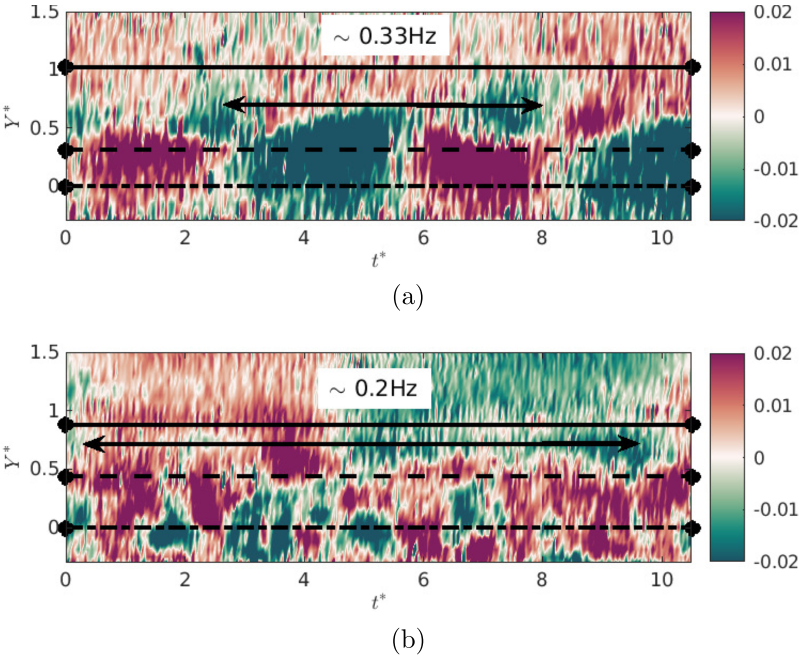

(a)

(b)

Figure 4.8: Plots of $V^{*\prime}$ data over $10t^*$ of time for (a) $Q = 0.09\,\mathrm{L\,s^{-1}}$ and (b) $Q = 0.16\,\mathrm{L\,s^{-1}}$ showing the presence of structure with period (a) $\sim 3\,\mathrm{s}$ and (b) $\sim 5\,\mathrm{s}$. The vertical velocity fluctuations $V^{*\prime}$ are defined by subtracting the averaged vertical velocity profiles (averaged over the same range as the profiles in Figure 4.5a) from the instantaneous data used to calculate the averages. These plots show the data at the central downstream location within the measurement area as defined in Figure 4.4.

the frequency of these modes increases, the height of the relevant mode gradually moves from the height of maximum negative shear to slightly above. There is far more variation in the FFT data for $Q = 0.16\,\mathrm{L\,s^{-1}}$. A mode with frequency 0.20 Hz is present at the height of the current. Compared with the lower influx case, other key modes are more difficult to identify. There is an indication of modes at 0.35 Hz and 0.50 Hz at the height of maximum negative shear, along with a variety of higher frequency modes with smaller magnitude at the same height and that of the height of maximum downstream velocity. However, this analysis does not show us the structure of these motions.

4.3.2 Wavelet Transform

The Fourier transform uses global functions, sines and cosines, to decompose a signal. Wavelet analysis uses local functions with a variety of scales, and is therefore able to capture how the frequencies of the most significant modes within the flow change over time (Grossmann *et al.*, 1990; Sadowsky, 1994). Here a continuous wavelet transform is used to plot the scalogram (Bolós & Benítez, 2014),

$$S_x(d,b) = \frac{1}{|d|}\left|\int_{-\infty}^{\infty} \boldsymbol{x}(t)\vartheta^{\dagger}\left(\frac{t-b}{d}\right)dt\right|^2, \tag{4.3}$$

where S is the energy of the signal $\boldsymbol{x}$ at scale d (where $d > 0$) and time b, $(\cdot)^{\dagger}$ indicates the complex conjugate, and ϑ is the selected wavelet. The scalogram illustrates the energy contained in the data $\boldsymbol{\varsigma}$ at each scale over time (Bolós & Benítez, 2014), and

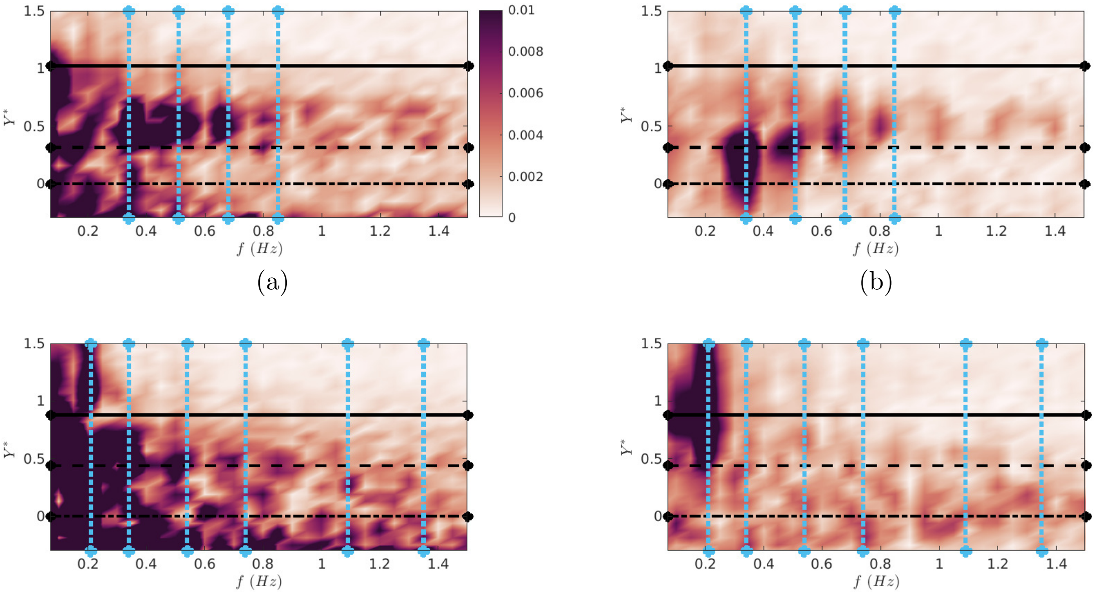

(a) (b)

(c) (d)

Figure 4.9: Amplitude spectrum of the FFT data of (a,c) downstream velocity and (b,d) vertical velocity data from (a,b) $Q = 0.09\,\mathrm{L\,s^{-1}}$ and (c,d) $Q = 0.16\,\mathrm{L\,s^{-1}}$ cases at a central downstream location. The vertical lines indicate the frequencies of the most significant motions identified in this work by combined inspection of the FFT and DMD mode amplitudes.

allows the identification of the scales that contribute the most energy to the signal at each timestep. The choice of wavelet has a significant impact on the result of the wavelet decomposition; however, as only the scalogram is being considered, here any wavelet shape should provide the same qualitative result (Torrence & Compo, 1998). For this work, we use the Morlet wavelet and the MATLAB `cwt` function (MATLAB, 2020). This wavelet has been shown to be appropriate for gravity current flows (Felix *et al.*, 2005). The Morlet wavelet is non-orthogonal and complex which is desirable for oscillatory behaviour with continuous variations in wavelet power (Kostaschuk *et al.*, 2018; Torrence & Compo, 1998). This technique is applied to the same timesteps and downstream location as the Fourier transform, both at the average height of the downstream velocity maximum and the height of maximum negative shear.

The scalograms are shown in Figure 4.10. For $Q = 0.09\,\mathrm{L\,s^{-1}}$ (Figure 4.10a), the scalogram data identifies significant modes with very similar frequencies to the FFT data (as shown by the dotted horizontal lines). The lowest frequency modes, 0.35 Hz and 0.50 Hz, are present throughout the body data. The mode at 0.63 Hz, however, is intermittent and present only between 10 s and 15 s. A mode with frequency 0.85 Hz not clearly identified by the FFT data is also highlighted, present between 5 s and 10 s. For $Q = 0.16\,\mathrm{L\,s^{-1}}$ (Figure 4.10b), the lowest two frequency modes (0.20 Hz and 0.35 Hz) identified from the FFT are again present throughout the body data. The 0.50 Hz mode suggested by the FFT appears to be present only between 5 s and 10 s. The scalogram data suggests possible intermittent modes not highlighted by the FFT data with frequencies 0.75 Hz (present between 5 s and 7.5 s and between 12.5 s and 17.5 s), 1.10 Hz (present between 2.5 s and 7.5 s and between 15 s and 17.5 s), and 1.35 Hz (present between 5 s and 8 s and between 12.5 s and 17.5 s). We still wish to identify the structure of these motions.

4.3.3 Dynamic Mode Decomposition

To consider the structure of the motions, DMD is utilised to decompose the body data (defined as in the FFT analysis) into modes in the form of waves with particular frequencies (Kou & Zhang, 2017; Schmid, 2010; Tu *et al.*, 2014). In this work, the downstream and vertical velocities for each timestep were combined into a single matrix such that the technique was applied to all data simultaneously. A linear relationship is assumed between N data snapshots $\boldsymbol{\varsigma^{1:N}} = \{\boldsymbol{\varsigma_1}, \boldsymbol{\varsigma_2}, ..., \boldsymbol{\varsigma_N}\}$ separated by time Δt,

$$\boldsymbol{\varsigma^{2:N}} = \boldsymbol{A}\boldsymbol{\varsigma^{1:N-1}}. \tag{4.4}$$

As the relationship is linear, the eigenvalues of $\boldsymbol{A}$ contain the dynamical characteristics of the system (Tu *et al.*, 2014). However, the dimensionality of $\boldsymbol{A}$ is very large, so for practicality and accuracy in this work a similar matrix to $\boldsymbol{A}$, $\grave{\boldsymbol{A}}$, is constructed, with fewer dimensions (Kou & Zhang, 2017). This can be done using singular value decomposition, which is a generalisation of eigendecomposition to a non-square matrix. This decomposes a data matrix of size $p \times q$ into 2 unitary matrices, $\boldsymbol{C}$ and $\boldsymbol{D}$, with sizes $p \times p$ and $q \times q$ respectively, and a diagonal matrix, $\boldsymbol{\Lambda}$, of size $p \times q$ containing the 'singular values'

$$\boldsymbol{\varsigma^{1:N-1}} = \boldsymbol{C}\boldsymbol{\Lambda}\boldsymbol{D}^{H}\ , \tag{4.5}$$

$$\grave{\boldsymbol{A}} = \boldsymbol{C}^{H}\boldsymbol{\varsigma^{2:N}}\boldsymbol{D}\boldsymbol{\Lambda}^{-1}\ , \tag{4.6}$$

where H indicates a Hermitian transpose. As they are similar matrices, the eigenvalues and eigenvectors of $\grave{\boldsymbol{A}}$, ζ_j and $\boldsymbol{\chi_j}$, are a subset of those of $\boldsymbol{A}$, and contain the same dynamical information. These eigenvalues and eigenvectors are used to calculate the dynamic modes $\boldsymbol{\varphi_j} = \boldsymbol{C}\boldsymbol{\chi_j}$, the modal angular frequencies $\omega_j = Im(log(\zeta_j))/\Delta t$ (and corresponding modal physical frequencies $f_j = \omega_j/2\pi$), growth rates $\varrho_j = Re(log(\zeta_j))/\Delta t$, and amplitudes $\boldsymbol{a_j} = 1/||\boldsymbol{G(:,j)}||$ (where $\boldsymbol{G} = \boldsymbol{D}\boldsymbol{\Lambda}^{-1}\boldsymbol{\chi}$). Each mode is a wave of the form $\boldsymbol{\varphi_j} = \boldsymbol{a_j}e^{(\varrho_j + i\omega_j)t}$ (Kou & Zhang, 2017; Richecoeur *et al.*, 2012; Schmid, 2011; Tu *et al.*, 2014). In this case, singular value decomposition was carried out using the MATLAB `svd` function with the 'econ' parameter (MATLAB, 2020).

Figure 4.11 shows the amplitudes of the dynamic modes for the $Q = 0.09\,\mathrm{L\,s^{-1}}$ and $Q = 0.16\,\mathrm{L\,s^{-1}}$ cases. These mode amplitudes align well with the FFT analysis data, highlighting significant modes with similar frequencies in the same locations within the flow. Figures 4.12a and 4.12b show the structures of those modes, including plots of the

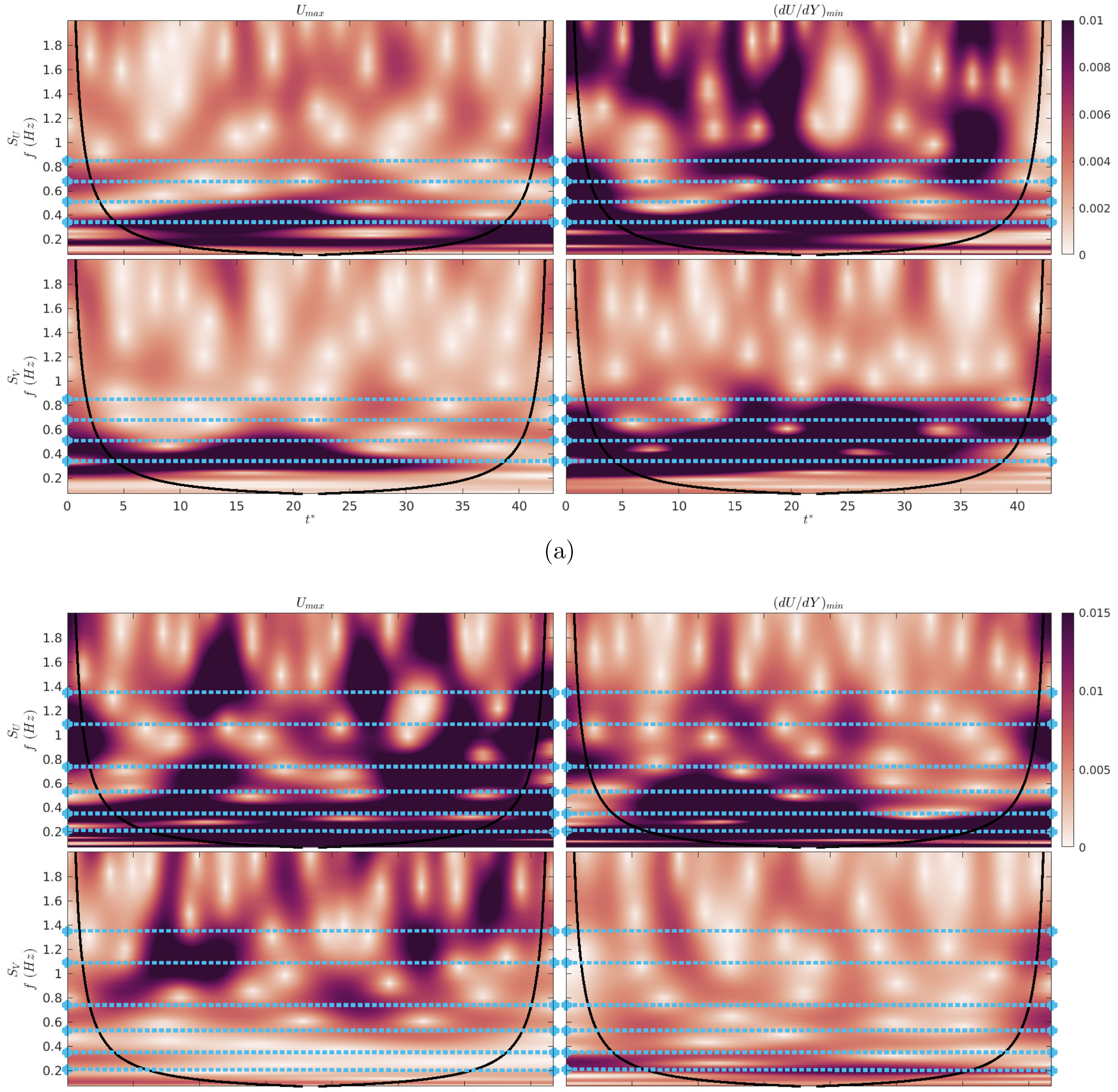

(a)

(b)

Figure 4.10: Wavelet transform of 20 s body data (as defined in Figure 4.5a) of (top) U and (bottom) V at the height of (left) average height of U_{max} and (right) average height of maximum negative shear at a central downstream location for (a) $Q = 0.09\,\mathrm{L\,s^{-1}}$ and (b) $Q = 0.16\,\mathrm{L\,s^{-1}}$. The solid black lines show the cone of interest of the wavelet transform, and the horizontal lines indicate the frequencies of the most significant motions identified in this work.

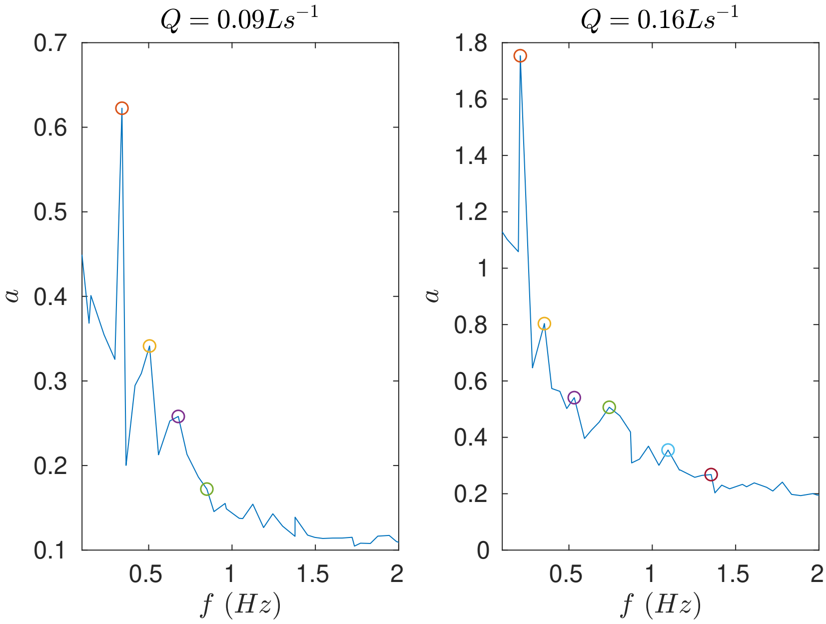

Figure 4.11: Plots of DMD mode amplitude against mode frequency for cases with (left) $Q = 0.09\,\mathrm{L\,s^{-1}}$ and (right) $Q = 0.16\,\mathrm{L\,s^{-1}}$, with circles indicating the modes plotted in Figures 4.12a and 4.12b. These amplitudes were calculated based on DMD of 20 s body data for these two cases (as defined in Figure 4.5a).

downstream and vertical velocities and vorticity associated with the example modes, along with streamlines of downstream and vertical velocity. These streamlines were determined using the MATLAB `streamslice` function (MATLAB, 2020). As indicated by the FFT data, the vertical location of these waves varies between the height of the current and the height of the velocity maximum. For the $Q = 0.09\,\mathrm{L\,s^{-1}}$ case, the waves are at the height of maximum negative shear. For $Q = 0.16\,\mathrm{L\,s^{-1}}$, there are also waves at the current height and the height of the velocity maximum. The abrupt end to many of the velocity streamlines in the regions of rotation suggests possible three-dimensional motions not captured by the two-dimensional velocity data presented here.

Similar modes can be identified across all cases, and their frequencies and phase speeds compared. Figure 4.13a shows the wavelength of particular modes plotted against Reynolds number. These wavelengths were estimated by inspection of the mode velocity and vorticity plots (as in Figure 4.12). The cases with $Re < 3250$ contain modes with a smaller range of frequencies than the higher Re cases. The frequencies of most modes stay roughly constant, with only small increases as Re increases. The frequency of those modes present at both high and low Re however experiences a significant increase when Re increases beyond ~ 3750. Figure 4.13b shows the wavelengths of those modes against frequency, and demonstrates two distinct categories of wave with the modes collapsing onto two separate lines. When plotting the phase speed, $c = f\lambda$, of the modes against Re as in Figure 4.13c, those modes on the lower line in Figure 4.13b all have $c \approx 0.025\,\mathrm{m\,s^{-1}}$. Those modes on the upper line have a wider spread of phase speeds, between $0.06\,\mathrm{m\,s^{-1}}$ and $0.1\,\mathrm{m\,s^{-1}}$. Those cases with $Re < 3250$ exclusively have modes with $c \approx 0.025\,\mathrm{m\,s^{-1}}$,

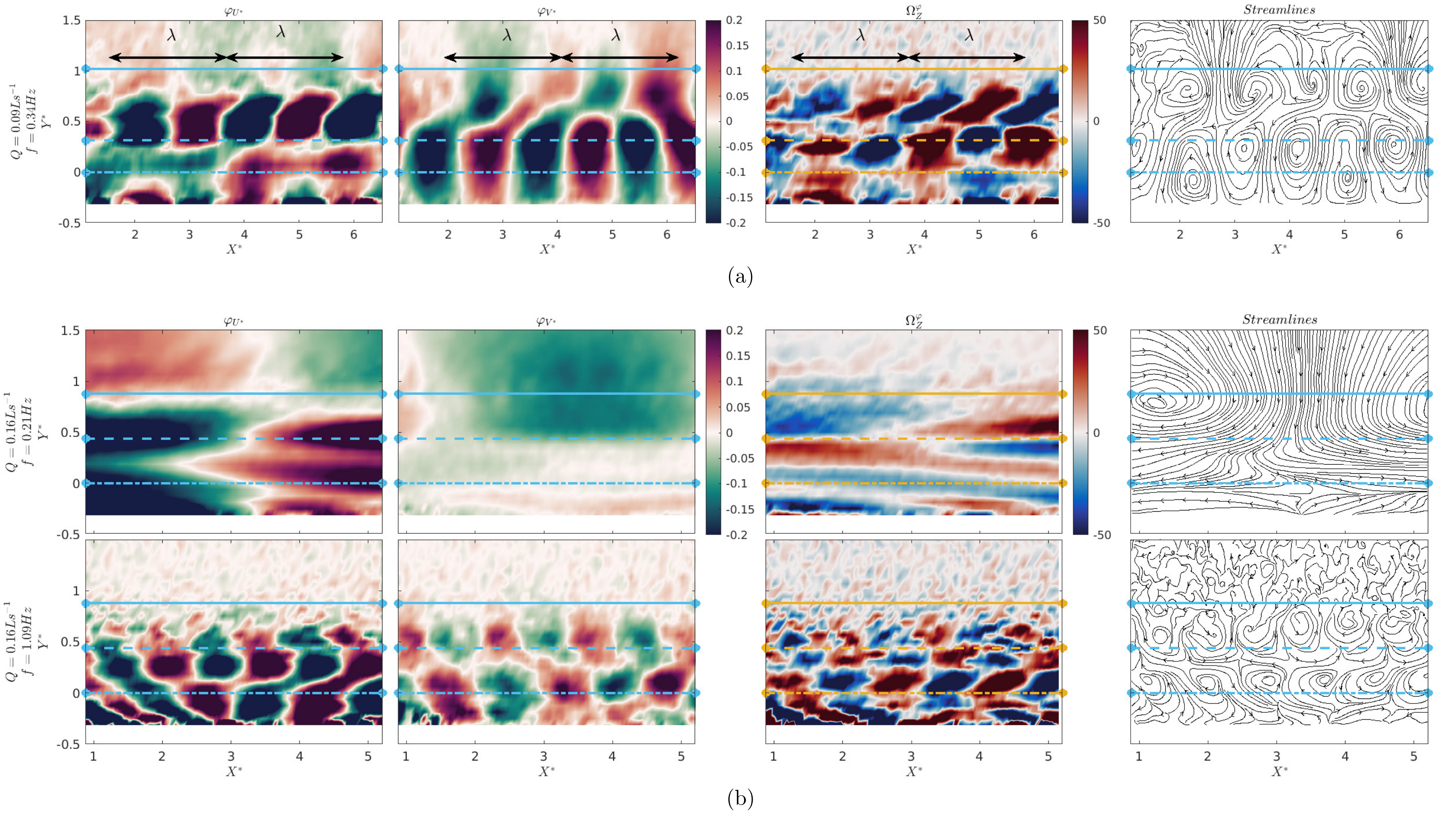

(a)

(b)

Figure 4.12: DMD modes representative of the modes with significant amplitude for (a) $Q = 0.09\,\mathrm{L\,s^{-1}}$ and (b) $Q = 0.16\,\mathrm{L\,s^{-1}}$, from the transform of 20 s body data. From left to right, the plots show mode downstream velocity, vertical velocity, vorticity, and streamlines of downstream and vertical velocity.

Q ($\mathrm{L\,s^{-1}}$)	0.0720	0.0896	0.107	0.125	0.142	0.160	0.177
F_I ($\mathrm{kg\,s^{-1}}$)	0.0021	0.0026	0.0031	0.0037	0.0042	0.0047	0.0052
$\overline{\rho}_e^{max}$ ($\mathrm{kg\,m^{-3}}$)	13	13	14.75	15.5	15.5	17.25	16.25

Table 4.3: Details of the inlet excess density flux F_I calculated by taking the product of the fluid influx and the excess density of the KDP, and the estimated maximum excess density within the body calculated by requiring $F_I = F_e$ (where F_e is defined in (4.8)).

while the higher Re cases contain internal waves with a wider spread of phase speeds.

To demonstrate whether the observed waves are due to buoyancy, inspection of the density profile would be advantageous. This data is not available from the PIV experiments, and instead simplifying assumptions are employed to obtain a heuristic estimate of the Brunt-Väisälä buoyancy frequency, N, which is the upper bound on the angular frequency of internal waves due to buoyancy gradient (Sutherland, 2010),

$$N \approx \sqrt{-\frac{g}{\rho_0}\frac{d\overline{\rho}}{dY}}\ , \tag{4.7}$$

where $\overline{\rho}$ is the average density profile, and ρ_0 is taken to be the mean of the glycerol and KDP densities. An excess density distribution similar to that in Figure 4.1 for solute-based flows is assumed based on profiles obtained through three-dimensional direct numerical simulation, with constant excess density ($\rho_e = \rho - \rho_a$, where ρ_e is the excess density, and $\rho_a = 1012\,\mathrm{kg\,m^{-3}}$ is the density of the ambient fluid) both above the current height and below the velocity maximum and a linear distribution between the two. Above the current, the excess density is taken to be $\rho_e = 0$. Below the velocity maximum, the excess density is estimated by requiring conservation of density flux between the inlet and the data. The inlet excess density flux (F_I) is estimated by taking the product of the fluid influx, Q, and the excess density of the KDP. If the velocity and density profiles are assumed to be constant in the cross-stream direction, the excess density flux from the data (F_e) may be estimated by

$$F_e = W_T \int \overline{\rho}\overline{U}\,dY, \tag{4.8}$$

where W_T is the width of the tank. The excess density below the velocity maximum is estimated for each case by requiring that $F_I = F_e$ (Table 4.3), and hence an approximate density profile for each case is established. As the maximum velocity will slow towards the side-walls, these are likely underestimates of the maximum density within the body.

Figure 4.14 shows the percentage difference between our observed wave frequencies and the estimated buoyancy frequencies after applying the Doppler shift due to the mean flow (Sutherland, 1999),

$$N_{DS} = N + U_0 k_x, \tag{4.9}$$

where N_{DS} is the frequency measured by a stationary observer, and k_x the downstream wavenumber, as it has been assumed that the waves propagate purely downstream. As seen in Figure 4.14 many of the observed waves are within 25% of the estimated values. Given that the vertical location and wavenumber of the wave, and therefore the mean flow speed and hence Doppler shift, are approximate, that any wave propagation in the cross-stream or vertical directions would act to decrease the observed frequencies, and that the exact density profile is unknown, all frequencies observed here are the right order of magnitude and are considered sufficiently close to indicate that these are internal waves due to buoyancy. The greater difference between the observed waves and the estimated values included in Figure 4.14b may be attributed to larger uncertainty in the height of the wave compared to those in Figure 4.14a, or could be the result of some more complex three-dimensional structure. Figure 4.15 demonstrates that the phase speed of some of these gravity waves is approximately equal to the mean downstream flow speed at the wave height. This suggests the presence of critical layers, defined to be where $\overline{U} = c$ (Maslowe, 1986), within the flow.

4.4 Discussion

Fourier transforms, wavelet transforms, and dynamic mode decomposition have been used to identify the most energetic motions in the body of gravity current flows. This analysis has been used to identify flow-scale internal gravity waves centred on the height of maximum negative shear, and the velocity maximum. The wavelet transforms suggest a wave with a particular frequency may not be permanent, but the importance of the waves as a whole does not decrease over time. As Reynolds number increases, the frequencies of the dominant waves within the flow change. The modes at the height of maximum negative shear become less significant, and the wavelengths of the most energetic modes decrease and their frequencies increase. At this point we also find the height of the velocity maximum starts to vary, and modes on the velocity maximum become significant in terms of flow dynamics.

It has been shown that for some of these waves the wave phase speed is approximately equal to the mean flow speed, indicating a potential critical layer within the gravity current body. The presence of internal waves in the gravity current body has been postulated by Dorrell *et al.* (2019), who suggest that the gravity current body has a structure similar to that of a zonal jet (Figure 4.1b) (Bower & Hogg, 1996; Dritschel & Scott, 2011; Maxworthy, 1984; Rossby & Zhang, 2001). In zonal jets, the breaking of dispersive internal waves near a critical layer results in self-organisation of the flow and net momentum transport towards the jet core (Bühler, 2014; Dorrell *et al.*, 2019; Dritschel & McIntyre, 2008; Dritschel & Scott, 2011). Close to critical layers, breaking waves homogenise potential vorticity and steepen the potential vorticity gradient (Dorrell *et al.*, 2019). Unless they have sufficient strength, this steep gradient is difficult for

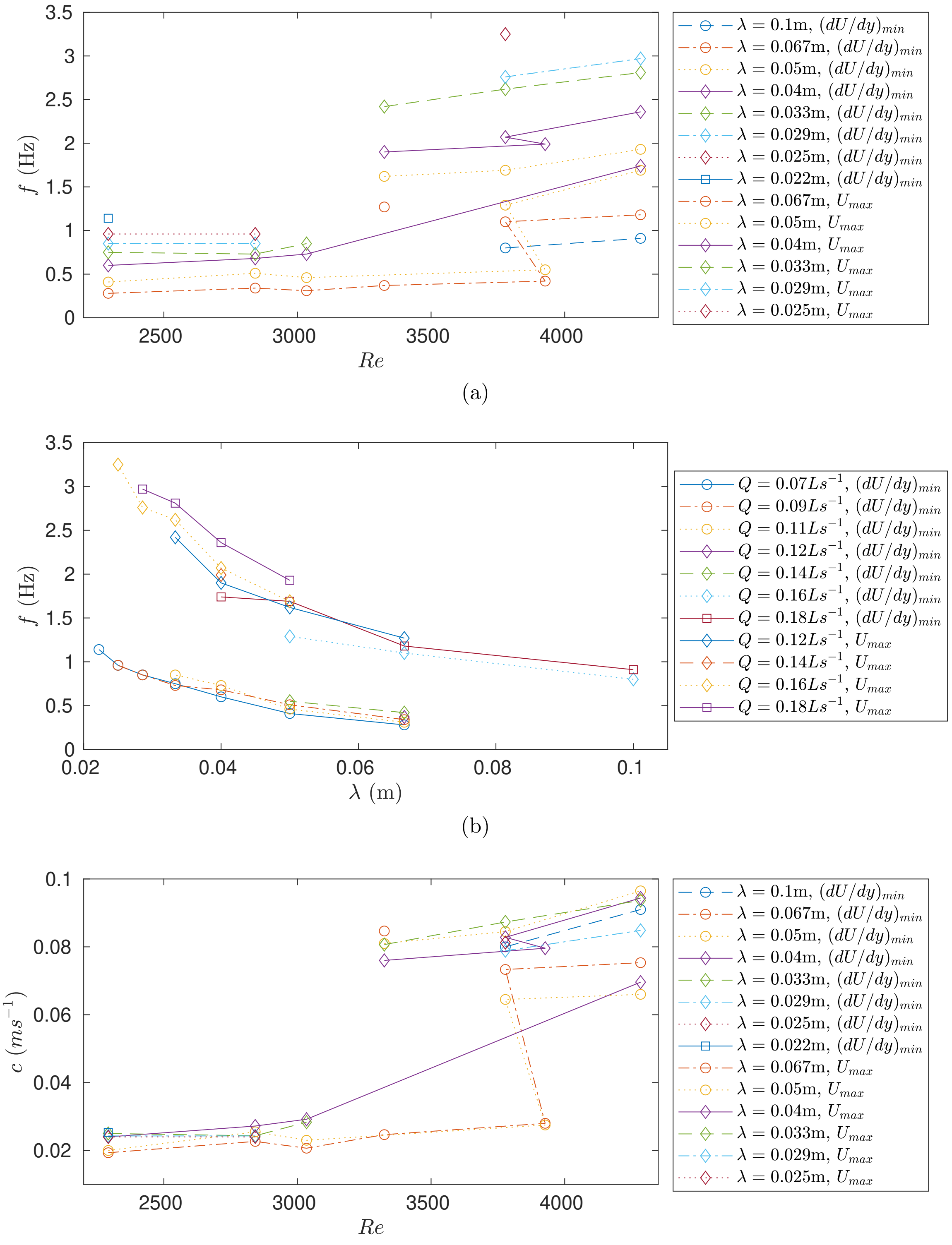

Figure 4.13: Plots tracking similar modes showing (a) modes with a particular frequency tracked across each influx investigated, with the frequency of the mode plotted as a function of *Re*, (b) mode wavelength plotted against frequency as a function of influx and mode location, and (c) modes with a particular frequency tracked across each influx investigated, with the phase speed of the mode plotted as a function of *Re*.

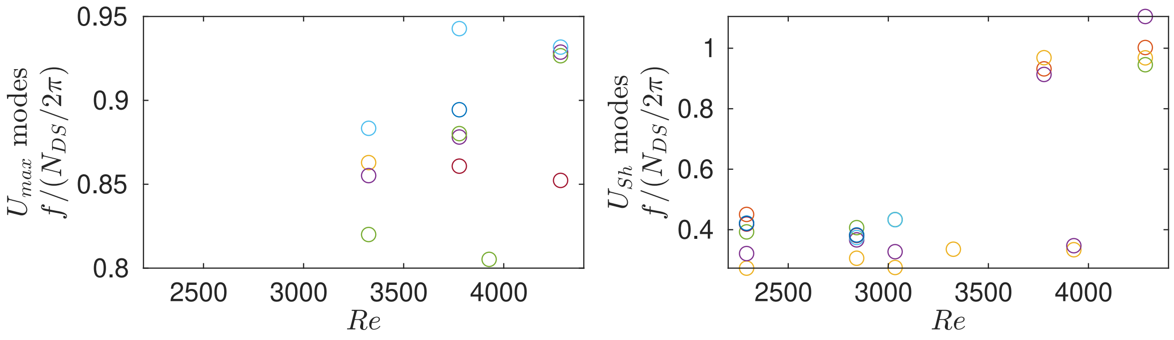

(a) (b)

Figure 4.14: Scatter plots of the observed mode frequencies divided by the buoyancy frequency Doppler shifted by the mean flow at the estimated wave height for (a) modes at the velocity maximum and (b) modes above the velocity maximum.

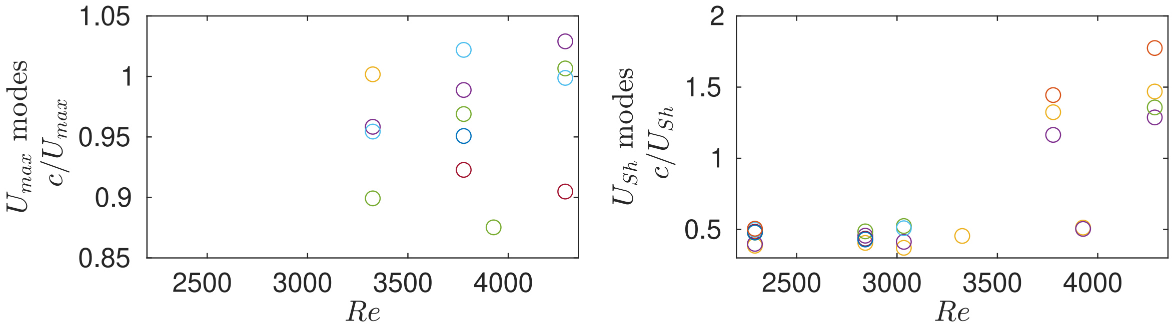

(a) (b)

Figure 4.15: Scatter plots showing the phase speed of the observed waves divided by the mean flow speed at the estimated wave height for (a) modes at the velocity maximum and (b) modes above the velocity maximum.

eddies to penetrate. The gradient therefore acts as a barrier to mixing between the flow above and below the critical layer, preventing dilution of the lower part of the flow and sharpening the density profile. Thus, the presence of a critical layer may result in the maintenance of far stronger density stratification than predicted by existing models (Booker & Bretherton, 1967; Dorrell *et al.*, 2019; Dritschel & McIntyre, 2008; Maslowe, 1986). This would lead to faster flow velocities and longer flow durations than expected from the current theory.

Internal waves absorbed at the critical layer transfer horizontal momentum into the mean flow (Booker & Bretherton, 1967; Maslowe, 1986; Thorpe, 1975), increasing the mean downstream velocity. This would imply that the gravity current body may not be statistically steady as typically assumed (Gray *et al.*, 2006; Islam & Imran, 2010; Kneller & Buckee, 2000). Indeed, acceleration of the flow at the height of the internal waves has been identified in this work. As this acceleration is largely in the upper part of the flow, this acceleration would change the profile of dU/dt, with the maximum downwards shear moving further from the velocity maximum and closer to the current height over time. The presence of these waves thus may help to explain discrepancies between data from a real-world flow in the Black Sea (Dorrell *et al.*, 2019) and predictions from traditional models of the gravity current body. As waves are present even in flows over smooth surfaces, and a rough surface would act to increase the prevalence of gravity waves (Aguilar & Sutherland, 2006; Sarkar & Scotti, 2017), their existence may be an inherent characteristic of gravity current body flow. This reinforces the need for a dynamic model of body flow, allowing for sharpening of density and velocity profiles.

Real-world thermohaline gravity currents (Ivanov *et al.*, 2004; Legg *et al.*, 2009), for example flow at the Strait of Gibraltar, are a crucial and common class of geophysical flow responsible for driving oceanic circulation. Furthermore, comparison can be made between the structures of thermohaline flows and of sediment-driven turbidity currents (García, 1994; Kneller & Buckee, 2000; Moodie, 2002). It is, therefore, interesting to consider how applicable the results presented in this work are to such sediment-laden flows. It has previously been claimed that solute-based flows are dynamically similar to fine-grained conservative gravity current flows (Cossu & Wells, 2012; Kneller & Buckee, 2000). While the structure of coarse-grained non-conservative gravity currents may differ in some respects (Cossu & Wells, 2012; Hogg *et al.*, 2005; Kneller & Buckee, 2000; Stacey & Bowen, 1988; Wells & Dorrell, 2021), for example an expected decrease in current height, increase in downstream velocity, and greater stratification of the density profile in the lower part of the current, the potential for internal gravity waves to form requires only that stable stratification of density exists (Staquet & Sommeria, 2002). The formation of a critical layer requires only that the phase speed of these waves equals the flow speed (Maslowe, 1986). It is, therefore, reasonable to suppose that similar structures may be present in sediment-laden flows also.

4.5 Conclusions

For the first time, internal gravity waves have been identified within the pseudo-steady body of laboratory-scale constant-influx solute-based gravity currents using dynamic mode decomposition. The presence of these gravity waves during flow over a smooth surface implies that they are an inherent characteristic of the body flow due to instability at the upper interface. There is also an indication that, due to internal velocity variation, these waves may form a critical layer within the flow, generating a barrier to mixing, preventing the dilution of the lower part of the current, and changing the expected structure of the density and velocity profiles. The presence of internal waves suggests that the body is not statistically steady as typically assumed. Instead, internal waves transfer horizontal momentum within the flow, deposited at critical layers. Wave breaking at critical layers acts as a barrier to mixing between the upper and lower parts of the current, controlling flow concentration and velocity profiles.

Chapter 5

The Three-Dimensional Structure of the Pseudo-Steady Body

In this chapter, Shake-the-Box particle tracking velocimetry (STB) is used to present instantaneous, volumetric, whole-field velocity measurements of experimental gravity current flows. Flow in the body of gravity currents is typically assumed to be statistically two-dimensional, and cross-stream flow is neglected (Meiburg *et al.*, 2015; Simpson, 1997). The measurements presented in this chapter indicate that cross-stream and vertical velocities, and velocity fluctuations, are equivalent in magnitude. As in Chapter 4, spectral analysis and dynamic mode decomposition of the velocity data (extended to consider the full volume and to include cross-stream velocity) are used to identify internal gravity waves within the current body, along with a critical layer at the height of the downstream velocity maximum. It is demonstrated that in the highest Reynolds number case the identified waves are associated with coherent three-dimensional motions within the flow.

5.1 Background

As described in Chapter 2, gravity currents are flows driven by gravity, due to a density difference between the current and surrounding ambient fluids (Simpson, 1997; Ungarish, 2009). This density difference could result from, for example, the presence of a temperature difference, suspended sediment, or a solute. They are a common class of geophysical flow, with the potential to cause significant environmental damage as well as being a key driver of global sediment transport (Gray *et al.*, 2006; Kneller & Buckee, 2000; Simpson, 1997). Therefore, there has been significant research into their structure and dynamics.

As stated by Hacker *et al.* (1996); Hallworth *et al.* (1996); Islam & Imran (2010); Middleton (1966); Wells & Dorrell (2021), the majority of existing research considering the structure of gravity currents has focused on the head, despite the fact that the body often forms by far the largest part of the flow (Azpiroz-Zabala *et al.*, 2017; Özsoy *et al.*, 2001; Sumner *et al.*, 2014). In a constant-flux current, dense fluid is continuously replenished and the bulk of the head and body is not diluted. Such flows have a prolonged body section, which can be quasi-permanent or persist for hours or days (Azpiroz-Zabala *et al.*, 2017; Khripounoff *et al.*, 2003; Parsons *et al.*, 2007; Peakall & Sumner, 2015; Simpson, 1997; Sumner *et al.*, 2014). This body is often assumed to be statistically steady and two-dimensional, as observed by Dorrell *et al.* (2019); Kneller *et al.* (2016); Meiburg *et al.* (2015); Simpson (1997).

Gravity current body structure, as described in the existing literature, is divided into two layers by the height of the velocity maximum (Altinakar *et al.*, 1996; Dorrell *et al.*, 2019; Wells & Dorrell, 2021). The upper layer structure, determined by shear between the current and ambient fluids and by density stratification, is similar to that in a wall-bounded jet while the lower layer structure is similar to that of an open-channel flow (Altinakar *et al.*, 1996; Dorrell *et al.*, 2019; Kneller *et al.*, 1999; Sequeiros *et al.*, 2010). However, the presence of periodic internal gravity waves has been postulated to explain the structure observed in recent field measurements (Dorrell *et al.*, 2019), suggesting that a revised, dynamic model of the gravity current body is needed.

In Chapter 4, internal gravity waves were identified in two-dimensional PIV measurements of a gravity current flow. Further, these waves were shown to form a critical layer within the flow (a region where the mean flow speed is similar to the wave phase speed (Bühler, 2014)). It has been suggested that internal gravity waves interacting with a critical layer in the flow could transfer momentum to the mean flow (Dorrell *et al.*, 2019; Wells & Dorrell, 2021). This would cause local flow acceleration, questioning the assumption of a statistically steady flow. Additionally, wave breaking at the critical layer could reinforce an eddy transport barrier resulting from sharp density gradients across the velocity maximum (Dorrell *et al.*, 2019; Wells & Dorrell, 2021). This would in turn sharpen the density profile and maintain the current/ambient density difference over larger distances than previously thought. However, this eddy transport barrier cannot exist in a two-dimensional flow, instead requiring cross-stream flow and density variations (Dorrell *et al.*, 2019; Wells & Dorrell, 2021), questioning the validity of neglecting cross-stream flow.

Three-dimensional structures are known to exist in gravity current flows, for example the lobe-and-cleft structures that form when the head over-runs buoyant ambient fluid (see Figure 6.6). At high enough Reynolds number, the flow is known to be highly three-dimensional as a result of, for example, the breakdown of Kelvin-Helmholtz structures behind the head (Balasubramanian & Zhong, 2018; Cantero *et al.*, 2008; Lowe *et al.*, 2002; Pelmard *et al.*, 2020). Three-dimensional motions may also originate with, or be enhanced by, side-wall effects in cross-stream constrained flows (such as flow in submarine channels (Peakall & Sumner, 2015)), or with flow over three-dimensional bed forms (Nasr-Azadani & Meiburg, 2014; Paik *et al.*, 2009). Indeed, Islam & Imran (2010) performed instantaneous three-dimensional velocity measurements along vertical lines within the body of a gravity current flow, and concluded that cross-stream velocity had a larger contribution to turbulent kinetic energy than did vertical, and that it should therefore be included in calculations.

Volumetric velocity measurements of gravity current flows have been conducted by Krug *et al.* (2015), Neamtu-Halic *et al.* (2019) and Lefauve *et al.* (2018), though unanswered questions regarding three-dimensional flow structures remain. The volume considered by Krug *et al.* (2015) was small (4 cm × 4 cm × 2 cm in a domain 200 cm × 50 cm × 50 cm), and while this was expanded by Neamtu-Halic *et al.* (2019) (four connected regions of 9 cm × 9 cm × 4 cm in the same domain) both volumes were limited to the current-ambient interface. The work of Lefauve *et al.* (2018) considers the formation of waves in an exchange-type flow, in which the magnitude of downstream velocity is equivalent in the two fluids. Most gravity current research considers flows in which the magnitude of downstream velocity in the current is much greater than that in the ambient. This difference will result in a substantial change in the amount of shear. Additionally, both Krug *et al.* (2015) and Lefauve *et al.* (2018) use quasi-instantaneous scanning techniques rather than instantaneous measurements such as those generated through Shake-the-Box particle tracking velocimetry (STB).

In this chapter, STB is used to generate instantaneous, whole-field, three-dimensional velocity measurements of an experimental gravity current body. These measurements are used to discuss the three-dimensional nature of the flow, and to further quantify the turbulence structure of the body. Specifically, the key aims are to assess whether: i) it is reasonable to neglect cross-stream flow in the gravity current body, ii) similar structures to those identified in the planar PIV data are also present in this volumetric velocity data, iii) these structures are associated with three-dimensional motions, and iv) the nature of the structures is affected by increased Reynolds number.

5.2 Methodology

5.2.1 The Experimental Setup

The experiments in this work consist of constant-influx, solute-based gravity current flows in a tank 0.1 m wide, 0.2 m deep and 2 m long (see Figure 5.1). The raised sections at either end capture air entrained through the inlet or outlet, and the 0.5 m drop above the outlet prolongs the body section of the flow by slowing the rate of current fluid pollution into the ambient fluid. In order to prevent the formation of bubbles on the lid of the tank, the bed slope is set to 0.1°.

Initially, the tank is filled with ambient fluid (a 6% by mass solution of glycerol (GLY)). Dense fluid (a 6% by mass solution of potassium dihydrogen phosphate (KDP))

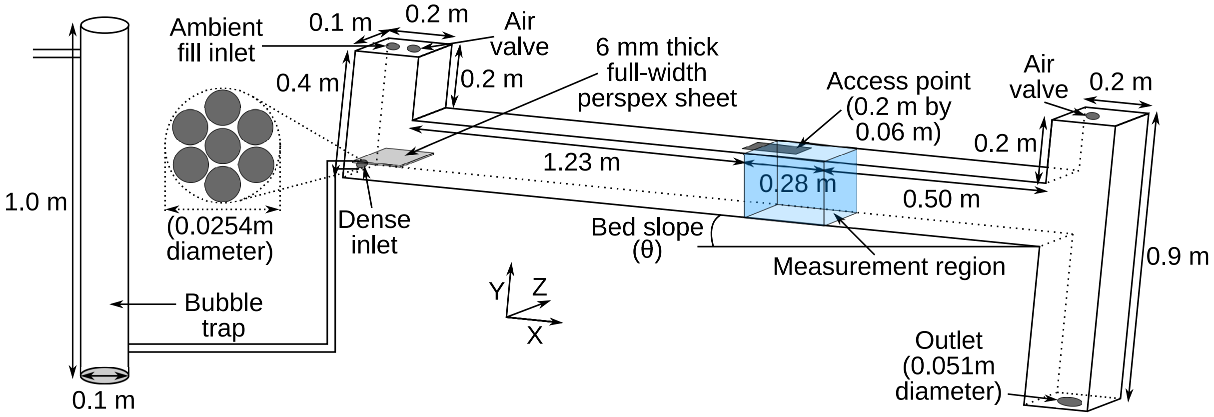

Figure 5.1: Schematic of the STB setup.

	ρ ($\mathrm{kg\,m^{-3}}$)	ν ($\mathrm{m^2\,s^{-1}}$)	n
Glycerol (ambient fluid)	1012.0	1.14×10^{-6}	1.3400
Potassium dihydrogen phosphate (current fluid)	1041.4	1.09×10^{-6}	1.3400

Table 5.1: Details of the density, ρ, kinematic viscosity, ν, and refractive index, n, of 6% by mass solutions of ambient (glycerol) and dense (potassium dihydrogen phosphate) solutes in tap water at 20°, from Haynes (2014).

is then pumped in through the inlet at a constant rate using a positive-displacement gear pump to provide a steady inflow with an inverter to control the flow rate. A coarse mesh, with holes of diameter 7.8 mm, is fitted over the inlet to provide a homogeneous inflow. Before entering the tank, the dense fluid passes through a bubble trap (a 1 m long, 0.1 m diameter cylinder filled with dense fluid) to remove air entrained by the gear pump. The airtight design results in fluid flowing through the outlet at the same rate that it is pumped through the inlet by the gear pump. Black aluminium polyethylene composite panels are used to cover the back and top of the tank to improve the image quality.

5.2.2 The Experimental Fluids

The experimental fluids, which have a density difference of 3% (see Table 5.1) are mixed in two 130 L mixing tanks. The two fluids, as well as a mixture of the two, are refractive index matched as required for optical techniques such as PIV and STB (Alahyari & Longmire, 1994). The density and refractive index of each fluid is tested using both a Reichert AR200 digital refractometer and an Anton Paar DMA$^{\mathrm{TM}}$ 35 Basic density meter, and the temperature is monitored. To be deemed refractive index matched, the fluids are required to be equal to the value in Table 5.1 to the precision of the refractometer (5 significant figures) and consistent across 3 readings at least 5 minutes apart. While temperature differences result in variations, density was always within the range $1012.9 \pm 0.1\,\mathrm{kg\,m^{-3}}$ for the glycerol solution and $1041.5 \pm 0.5\,\mathrm{kg\,m^{-3}}$ for the KDP.

	d_p (µm)	ρ ($\mathrm{kg\,m^{-3}}$)	Concentration ($\mathrm{g\,L^{-1}}$)	U_g ($\mathrm{m\,s^{-1}}$)	τ_r (s)
Pa	60	1030	0.003/0.003	3×10^{-5}	3.2×10^{-4}
Fl	138	1000	0.020/0.033	3×10^{-4}	9.2×10^{-4}

Table 5.2: Details of the average particle diameter, d_p, density, ρ, concentration of seeding used in fluid (GLY/KDP), and estimates of Stokes velocity (U_g), and relaxation time (τ_r) for each of the seeding particles used in the Shake-the-Box experiments. The first, Pa, being LaVision polyamide particles HQ, and the second, Fl, being fluorescent Cospheric polyethylene microspheres UVPMS-BO-1.00.

5.2.3 The STB System

Shake-the-Box particle tracking velocimetry (STB) is used to generate instantaneous three-dimensional volumetric measurements of velocity (Schanz *et al.*, 2016; Wieneke, 2012). This method consists of adding seeding particles to the flow, and repeatedly photographing an illuminated volume at a known time interval using a synchronised array of cameras with overlapping fields of view. Particle positions are reconstructed using triangulation and by extrapolation of particle tracks identified from previous timesteps (see Section 3.2 for a full method description).

Two different kinds of seeding particle are used in this work – LaVision Polyamide particles HQ (Pa), and fluorescent Cospheric, polyethylene microspheres UVPMS-BO-1.00 (Fl). Table 5.2 includes details of these particles, the concentrations of each used in the STB work, and estimates of the Stokes velocity and relaxation times for the particles demonstrating that they are suitable for use as seeding in these experiments.

A volume within the flow is illuminated using a LaVision Blue LED-Flashlight 300. The images are captured using a LaVision MiniShaker TR-L that captures 0.275 m horizontally, 0.15 m vertically, and to within 5 mm of the side-walls. The location of this measurement volume is shown in Figure 5.1. When fluorescent seeding particles are used, a filter with a cutoff at wavelength 610 nm is applied to each camera to reduce the effect of reflections from the perspex walls.

Image collection begins several seconds before the current head reaches the measurement region. Data storage limitations restrict the duration of flow measurement, with collected images covering either 25 s or 50 s depending on whether image collection is at 100 Hz or 50 Hz (see Table 5.3). The binned velocity field is on a grid with spatial resolution 2.6 mm × 2.6 mm × 2.6 mm. Image calibration is done using a LaVision 106-10 double-sided calibration plate on the bottom surface of the tank in a central cross-stream location and approximately central within the measurement region in the downstream direction. The three-dimensional velocity field is reconstructed using the Shake-the-Box algorithm in LaVision DaVis 10.0.5 and 10.1.0.

5.2.4 The Experimental Cases

The cases considered cover a range of influx values (Q) determined by the pump. The lowest and highest influx cases are dictated by the minimum ($Q = 0.032\,\mathrm{L\,s^{-1}}$) and

Case	8	9	10	11	12	13
Influx ($\mathrm{L\,s^{-1}}$)	0.032	0.032	0.082	0.082	0.148	0.148
Δt ($\mathrm{m\,s^{-1}}$)	20	20	20	10	10	10
Seeding	Pa	Fl	Pa	Fl	Pa	Fl

Table 5.3: Details of the influx, time between images, and seeding type for each STB case (additional to the seven PIV cases conducted in Chapter 4). Fl refers to the fluorescent Cospheric particles, and Pa to the LaVision polyamide particles.

maximum ($Q = 0.148\,\mathrm{L\,s^{-1}}$) stable settings of the pump, and the third is an intermediate value ($Q = 0.082\,\mathrm{L\,s^{-1}}$). Each influx case is carried out twice, once with each seeding type. The details of the influx, collection frequency, and seeding for each STB case are shown in Table 5.3.

5.3 Flow on a Central Slice

Body flow is defined as in Chapter 4, by measuring the time taken for the current front to travel across the measurement region and then waiting that length of time again before averaging across all downstream locations and time. As with the PIV data, this gives consistent averages, whether averaging over 5 s or 20 s of data taken from the beginning of the body section (Figure 5.2). Profiles of downstream velocity, averaged over all downstream locations and time within the body are shown in Figure 5.3. Excepting the lowest Reynolds number case (which has positive flow in the ambient, possibly as a result of an air valve not being fully closed), all cases have the same averaged structure. Non-dimensionalising vertical location, by subtracting the average height of the velocity maximum and dividing by the Ellison and Turner integral length scale, and downstream velocity, by dividing by maximum average downstream velocity,

$$\begin{gathered}
Y^* = (Y - Y_{\overline{U}_{max}})/L_c,\ X^* = X/L_c,\ Z^* = (Z - 0.05)/L_c,\\
U^* = U/U_c,\ V^* = V/U_c,\ W^* = W/U_c,\\
L_c = \frac{\left(\int \bar{\bar{U}} dy\right)^2}{\int \bar{\bar{U}}^2 dy},\\
U_c = \overline{U}_{max},
\end{gathered} \tag{5.1}$$

where $\bar{\bar{U}}$ is the mean velocity relative to that in the ambient, collapses the profiles. Suitable characteristic length (L_c) and velocity (U_c) scales for calculation of Reynolds number, $Re = U_c L_c/\nu$, and densimetric Froude number, $Fr_D = U_c/\sqrt{g' L_c}$ (where g' is the reduced gravity), are therefore chosen to be the Ellison and Turner length scale and the maximum average downstream velocity. From this, a characteristic time scale, $t_c = L_c/U_c$, can be defined. These parameters are shown in Table 5.4.

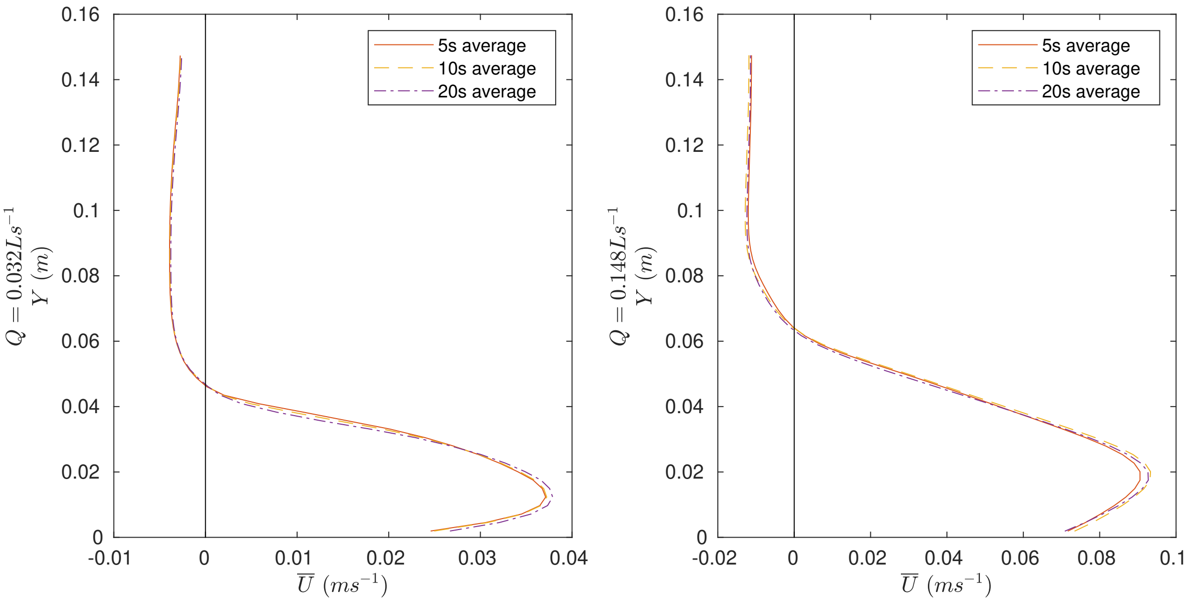

Figure 5.2: Averages of downstream velocity over downstream location and time windows ranging from 5 s to 20 s from the beginning of the body data for (left) $Q = 0.032\,\mathrm{L\,s^{-1}}$ and (right) $Q = 0.148\,\mathrm{L\,s^{-1}}$ from data gathered using the fluorescent seeding.

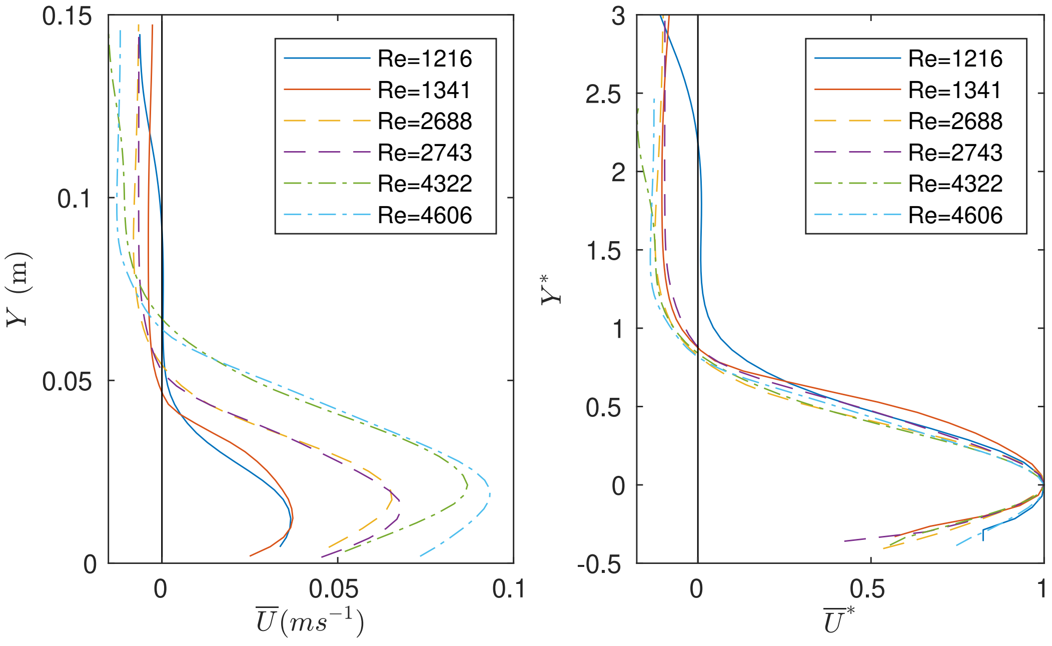

(a)

(b)

Figure 5.3: (a) Downstream velocity and (b) non-dimensional downstream velocity, averaged over all downstream locations and body timesteps on a central $Z^* = 0$ plane.

Case	U_c ($\mathrm{m\,s^{-1}}$)	L_c (m)	t_c (s)	Re	Fr_D
8	0.037	0.036	0.99	1216	0.35
9	0.037	0.039	1.06	1341	0.35
10	0.065	0.045	0.68	2688	0.57
11	0.069	0.043	0.63	2743	0.61
12	0.087	0.054	0.62	4322	0.69
13	0.093	0.054	0.58	4606	0.74

Table 5.4: Characteristic velocity, $U_c = \overline{U}_{max}$, length, L_c, and time, t_c, scales, along with the Reynolds, $Re = U_c L_c/\nu$, and densimetric Froude, $Fr_D = U_c/\sqrt{g' L_c}$ numbers for each STB case (additional to the seven PIV cases conducted in Chapter 4).

Figures 5.4 and 5.5 show instantaneous plots of velocity (U, V, W) and velocity fluctuations from the mean ($U' = U - \overline{U}$, $V' = V - \overline{V}$, and $W' = W - \overline{W}$) at central cross-stream and downstream locations over time. In all cases the vertical velocity has a similar structure of alternating positive/negative regions, though the magnitude of the velocity increases significantly with Reynolds number, as does the frequency of the motions. In the lowest Reynolds number case these regions are less well defined.

As well as the magnitude of cross-stream velocity increasing with increased Reynolds number, the structure changes. In the lowest Reynolds number case, cross-stream velocity takes the form of low magnitude bands. As Reynolds number increases, the structure becomes similar to that of the vertical velocity – alternating regions of positive and negative velocity. The pairs of cases with similar Reynolds number always have similar structure. Figure 5.5 demonstrates that in every case the magnitude of the cross-stream velocity fluctuations, W', is equivalent to those in the vertical velocity, suggesting that it may not be reasonable to neglect cross-stream flow as often assumed (Meiburg *et al.*, 2015; Simpson, 1997).

Figure 5.6a shows the two-dimensional turbulent kinetic energies on this central slice,

$$k^*_{2D} = 0.5(U^{*\prime 2} + V^{*\prime 2}).$$

These averaged turbulent kinetic energies have a similar structure to those in the existing literature (Buckee *et al.*, 2001; Cossu & Wells, 2012; Gray *et al.*, 2006; Islam & Imran, 2010) and those presented in Chapter 4, with a local minimum close to the velocity maximum and a local maximum between the velocity maximum and current height. In the highest Reynolds number cases there is an additional local maximum just above the velocity maximum. The difference in magnitude between cases (for example the low magnitude in the $Re = 2688$ case) may be linked to the time-dependent nature of the data, which can be seen in the instantaneous turbulent kinetic energy plots in Figure 5.6b. The instantaneous turbulent kinetic energy is intermittent, particularly at higher Reynolds numbers, suggesting that by averaging information about the structure of the flow is lost.

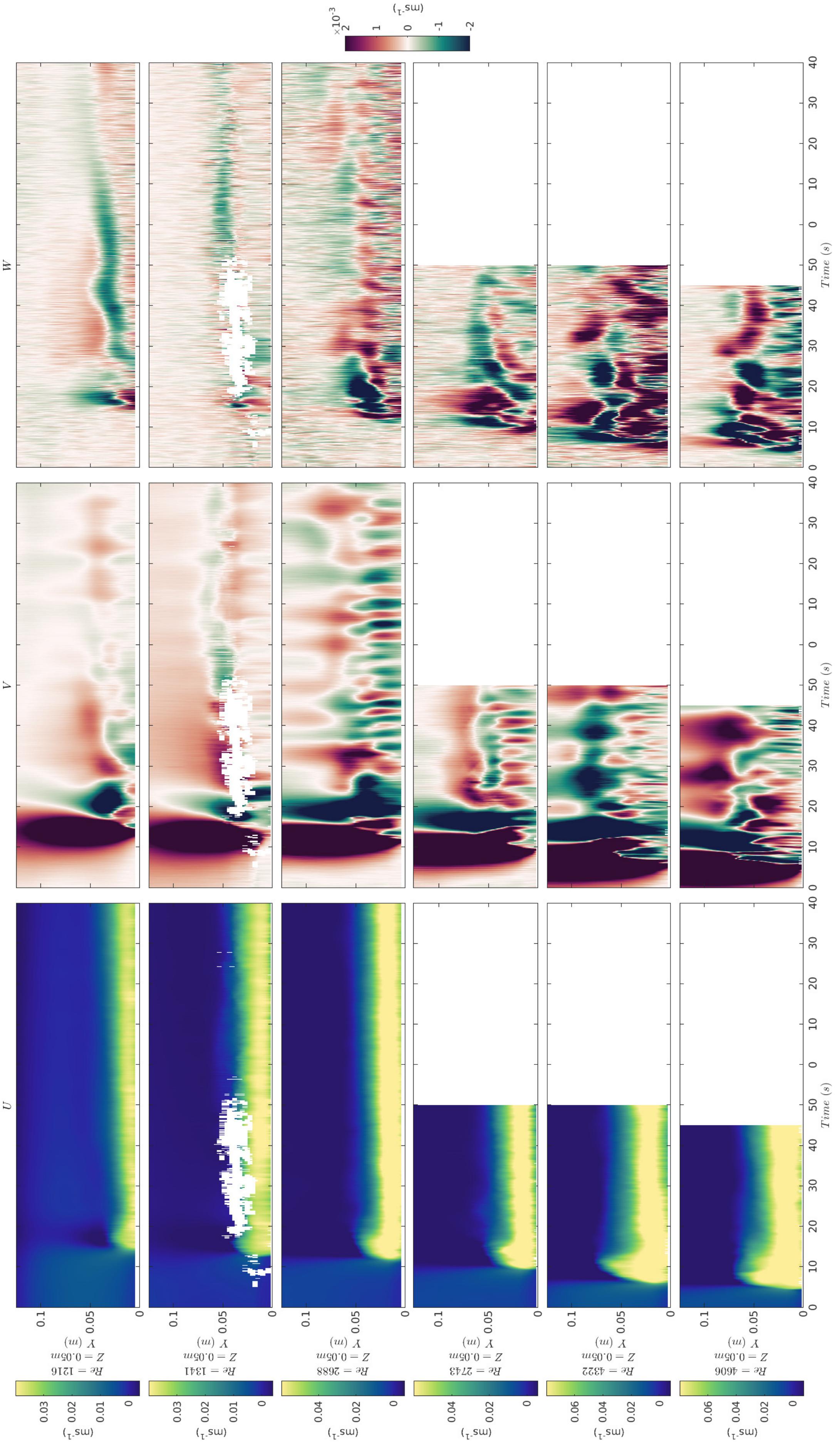

Figure 5.4: (left) Downstream, (middle) vertical, and (right) cross-stream velocities from the STB cases on a central cross-stream slice.

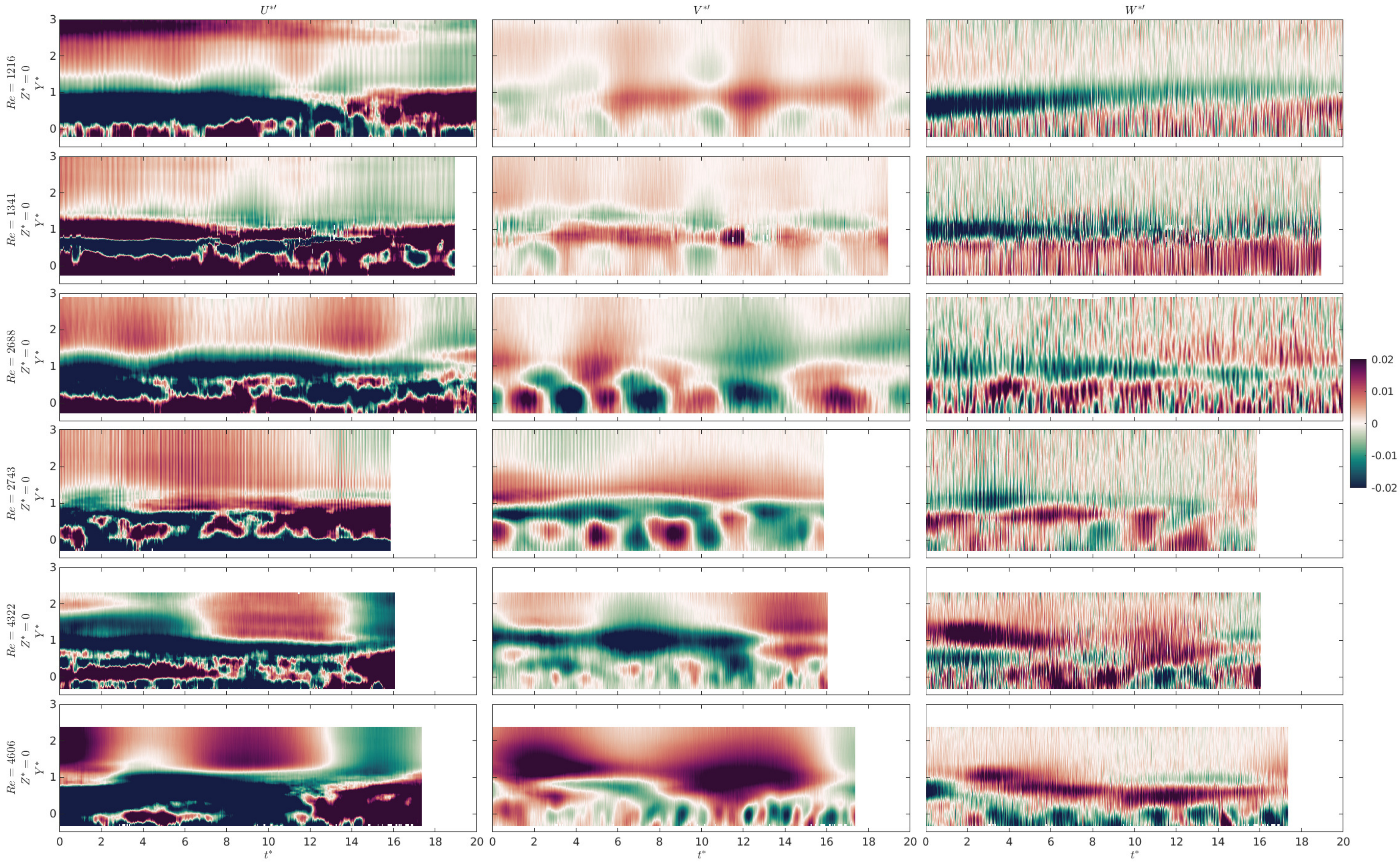

Figure 5.5: Instantaneous dimensionless fluctuations in (left) downstream (middle) vertical and (right) cross-stream velocities in the gravity current body from the STB cases on a central $Z^* = 0$ cross-stream slice.

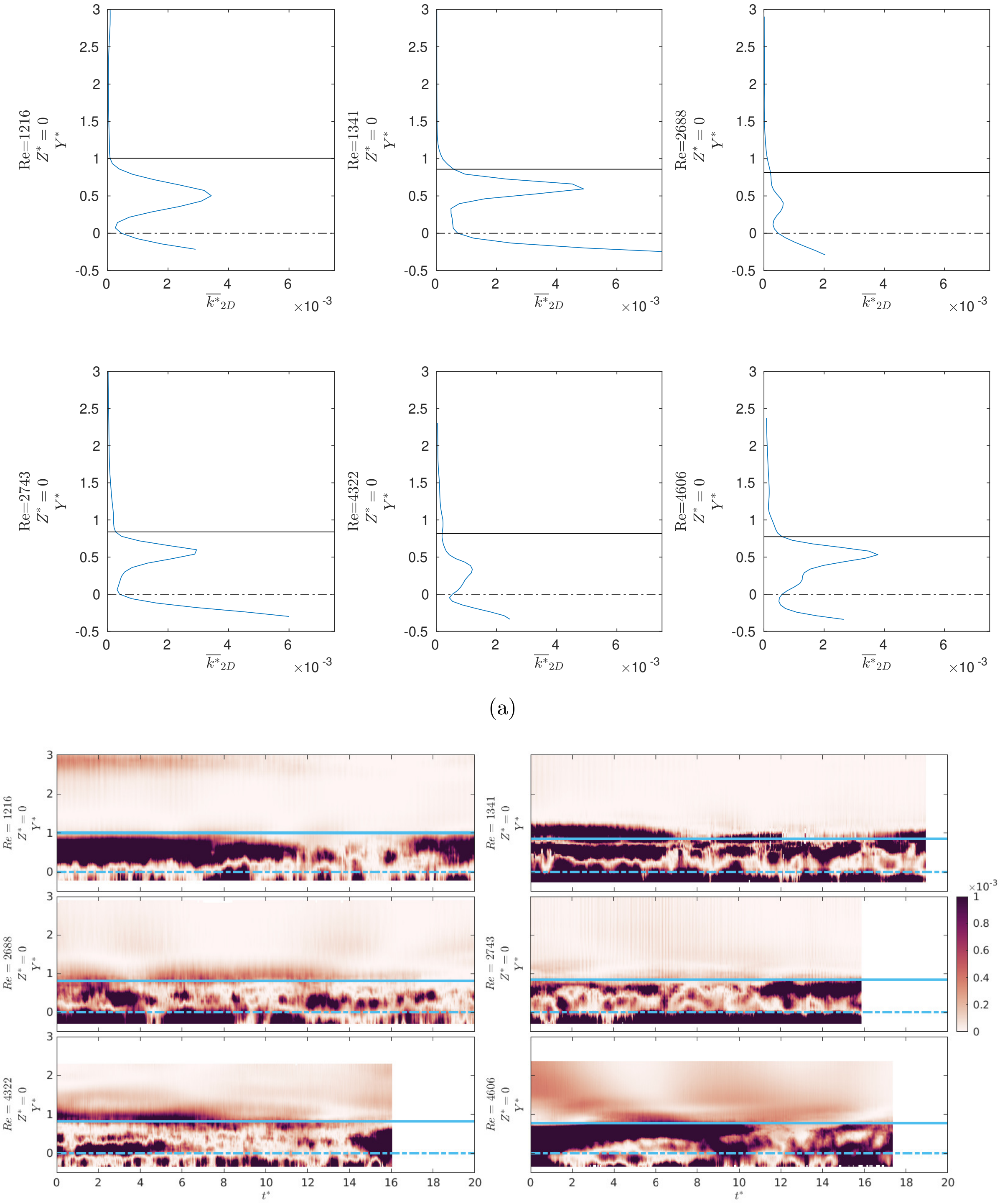

(a)

(b)

Figure 5.6: Plots of $k^*_{2D} = 0.5(U^{*\prime 2} + V^{*\prime 2})$ on a central cross-stream slice, (a) averaged over all downstream locations and body timesteps for each of the STB cases, and (b) the instantaneous data at a central downstream location over time. The solid horizontal line indicates the height of the current on the central cross-stream slice (defined as where downstream velocity changes from positive to negative), and the dot-dash line the height of the average velocity maximum on the central cross-stream slice.

The three-dimensional velocity measurements in this work allow consideration of the effect of cross-stream velocity on the calculation of turbulent kinetic energy,

$$k^*_{3D} = 0.5(U^{*\prime 2} + V^{*\prime 2} + W^{*\prime 2}).$$

Figures 5.7a and 5.7b show the difference between the two- and three-dimensional calculations. The average contribution (Figure 5.7a) has almost the same structure in every case – the biggest contributions being at the height of the velocity maximum (where the contribution from $W^{*\prime}$ is equivalent in magnitude to the contributions from $U^{*\prime}$ and $V^{*\prime}$), and a smaller increase at the current height. This hides some significant structural differences between cases (5.7b). At the lowest Reynolds number, the contribution at the current height decreases over time, and that at the velocity maximum increases. However, the contributions are relatively consistent. As Reynolds number increases, the effect of cross-stream velocity at the velocity maximum becomes intermittent, and the contribution at the current height no longer decreases over time.

5.4 Alternative Slices

Figure 5.8 shows downstream velocity averaged over time and downstream locations for a variety of cross-stream locations covering the central half of the tank. For all cases, moving towards the walls decreases the average magnitude of the downstream velocity of the flow. This effect is reduced as Reynolds number increases, with little difference between the central profile and that at $Z^* = 0.25$ for the highest Reynolds number cases. This may be a result of greater variability in cross-stream velocity. Figure 5.9 shows velocity fluctuations at $Z^* = 0.5$ and a central downstream location over time. Compared with 5.5, the velocity fluctuations have broadly similar structure and amplitude regardless of the plane considered for each case.

Figure 5.10 shows flow on X-Z planes over time at the height of maximum downstream velocity at a central downstream location, and the fluctuations from the mean calculated by averaging over all body timesteps. From here on, only the data gathered using the fluorescent seeding particles will be presented, as despite the lower seeding density a greater depth of the flow was captured compared to the other seeding. Again, these plots demonstrate that the magnitude of cross-stream and vertical velocities and velocity fluctuations are equivalent. As Reynolds number increases there are significant changes in the velocity components. For the lowest Reynolds number case, the cross-stream velocity shows the fluid moving towards the centre of the measurement region at this height. There is a clear separation of positive and negative cross-stream velocities along a line close to the cross-stream centre. As Reynolds number increases, this separation

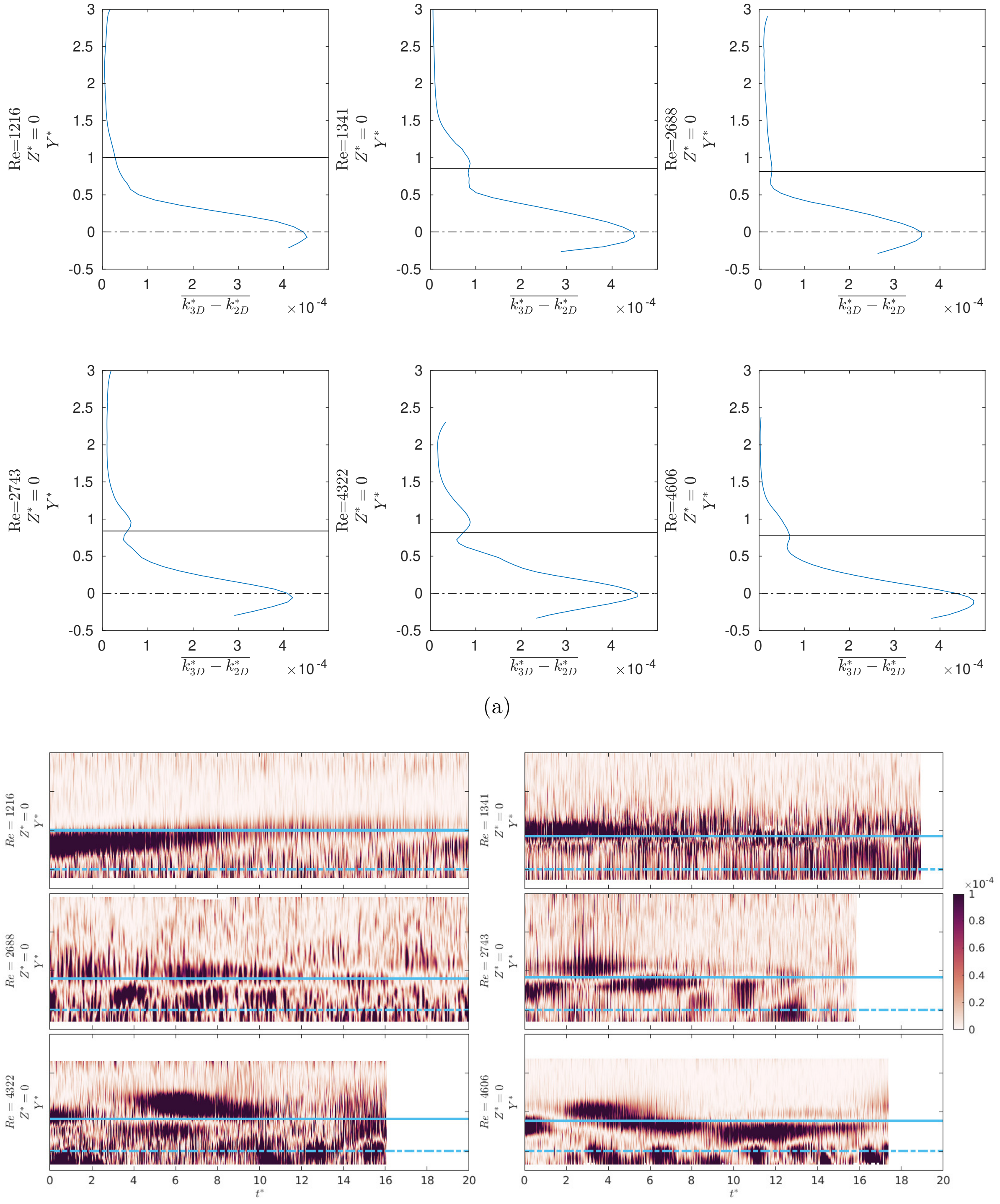

(a)

(b)

Figure 5.7: The difference between two- and three-dimensional calculation of turbulent kinetic energy calculations, $k^*_{3D} - k^*_{2D} = 0.5W^{*\prime 2}$ on a central cross-stream slice, (a) averaged over all downstream locations and body timesteps for each of the STB cases, and (b) the instantaneous data at a central downstream location over time. The solid horizontal line indicates the height of the current on the central cross-stream slice (defined as where downstream velocity changes from positive to negative), and the dot-dash line the height of the average velocity maximum on the central cross-stream slice.

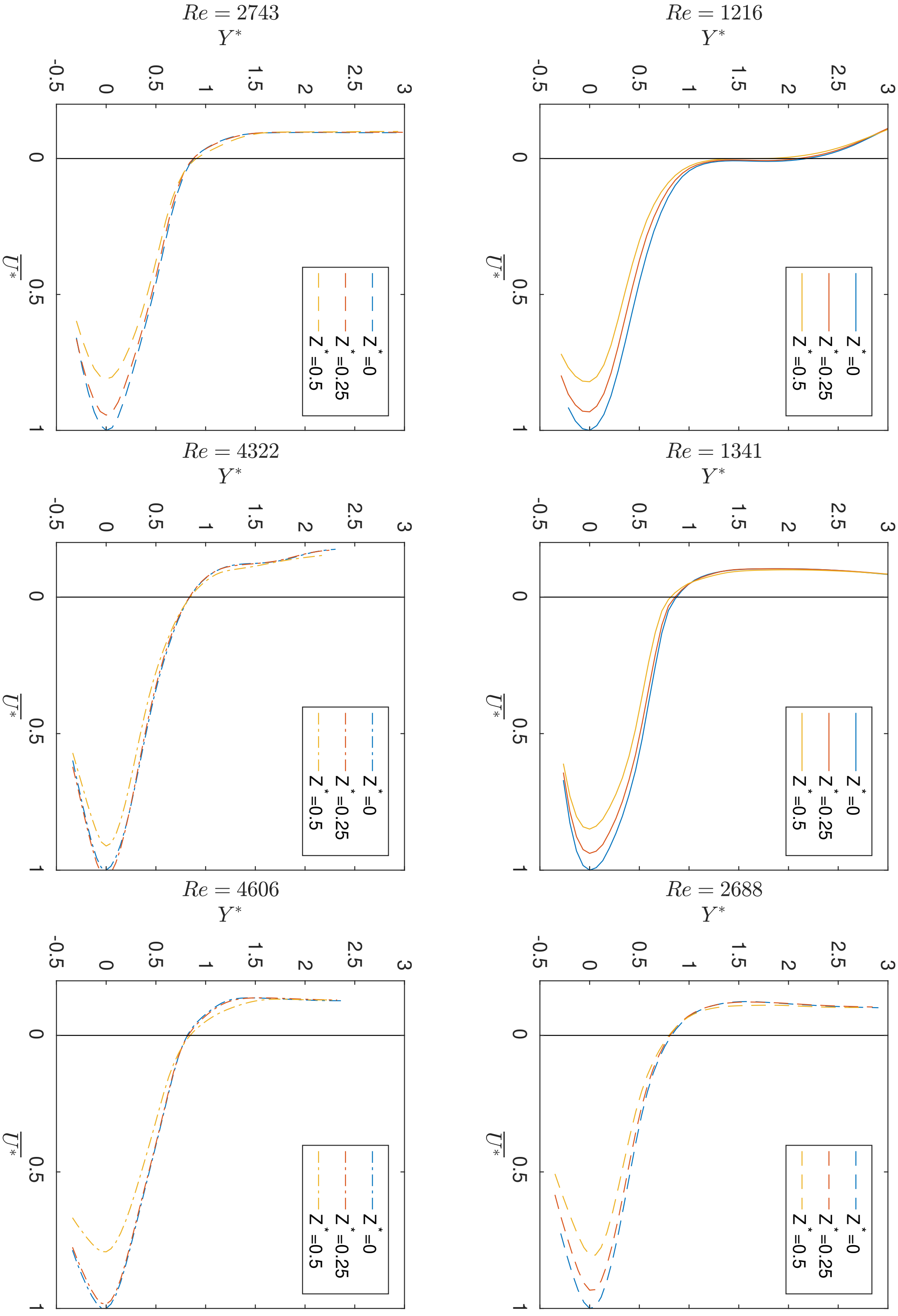

Figure 5.8: Comparisons of average downstream velocity profiles at a central downstream location averaged over all body timesteps for cross-stream locations $Z^* = 0$, 0.25 and 0.5.

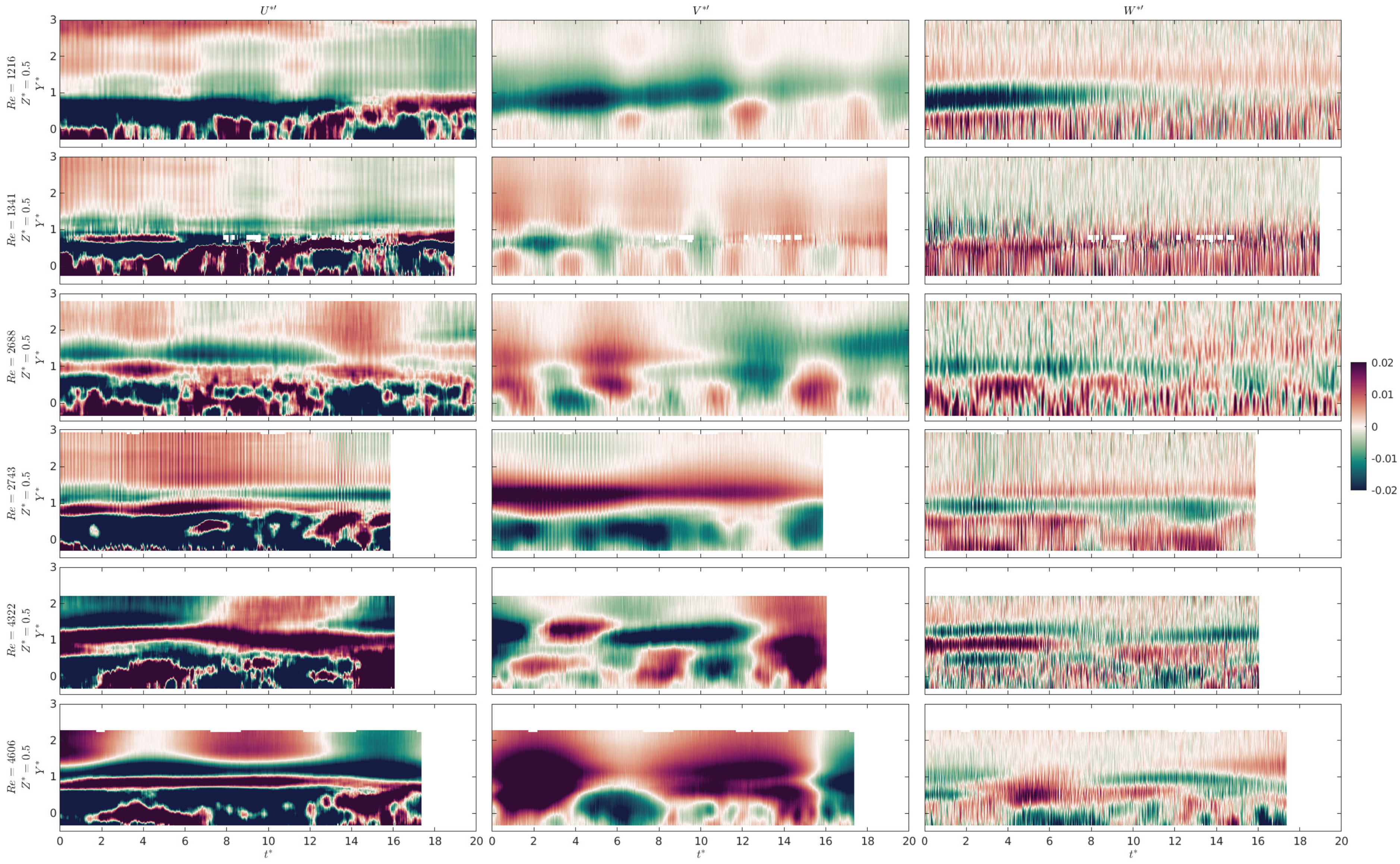

Figure 5.9: Velocity fluctuations (left) $U^{*\prime}$, (centre) $V^{*\prime}$, and (right) $W^{*\prime}$ at $Z^* = 0.5$, for each case at a central downstream location over time.

breaks down, and the centreline has alternating positive/negative regions. By the highest Reynolds number case, the centreline is far less clear in the cross-stream velocity plots.

There are alternating regions of positive and negative vertical velocity in every case. However as Reynolds number increases their structure changes. In the lowest Reynolds number case, the negative vertical velocity motions are concentrated towards the sidewalls and are smaller in magnitude than the higher Reynolds number cases. Some do not extend across the full domain width. The intermediate Reynolds number case has alternating regions of positive and negative vertical velocity that are concentrated in the centre of the domain. In the highest Reynolds number case, these regions are smaller, less regular, and are not limited to the centreline.

5.5 The Three-Dimensional Structure of Coherent Motions

Dynamic mode decomposition can be performed on all three components of velocity in the entire volume simultaneously to give a three-dimensional representation of the coherent structures. As in Chapter 4, all velocity components and time steps are combined into a single matrix such that dynamic mode decomposition is applied to all data simultaneously, and singular value decomposition is carried out using the MATLAB `svd` function with the ‘econ’ parameter (MATLAB, 2020). In order for this to be computationally realistic, the dimensionality of the data must be reduced. Therefore, the data is cropped to just above the current height and alternating downstream locations are discarded. In order to carry out dynamic mode decomposition using the MATLAB functions selected, there cannot be any missing data points. In the $Re = 2743$ and $Re = 4606$ cases, the vast majority of missing data is at the edges of the illuminated volume. As this can be rectified by removing the edge rows or columns with missing data, with small gaps internal to the measurement region filled in using linear interpolation and the MATLAB `interp` function (MATLAB, 2020), frequency analysis is applied to these two cases and not the $Re = 1341$ case. This lower Reynolds number case has more experimental noise, particularly in the cross-stream velocity measurements, and more missing data (possibly as a result of less even distribution of the seeding particles, a greater difference in refractive index between the fluids, or less optimal timestep or reconstruction settings).

As in Chapter 4, the modes with significant contribution to the flow must be identified. This is done using a combination of swirling strength, Fourier transform, wavelet decomposition, and dynamic mode amplitude. Figures 5.11a and 5.11b show plots of swirling strength ζ_{ci} for the two cases, defined by Zhou *et al.* (1999) as the imaginary

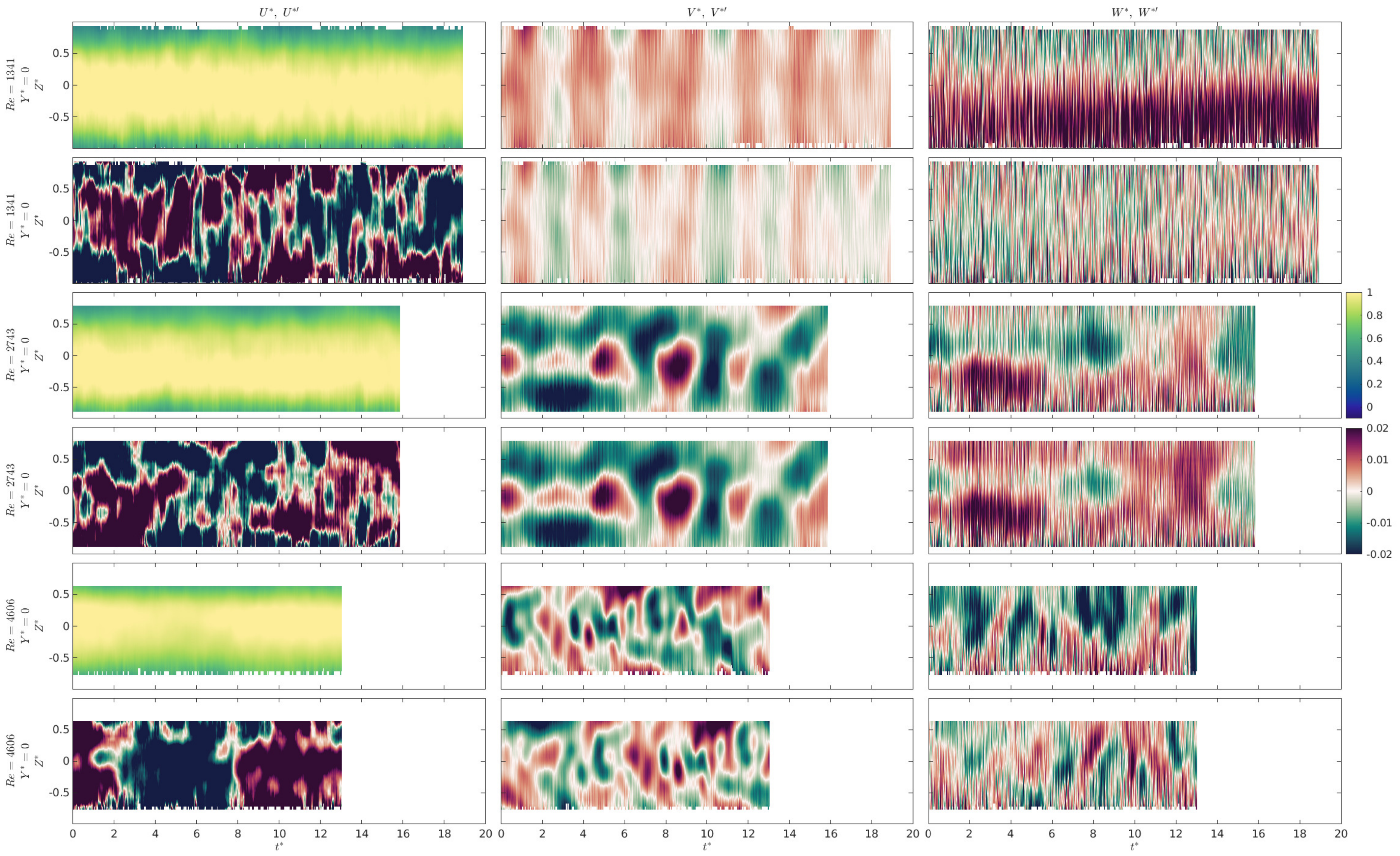

Figure 5.10: (left) Downstream, (centre) vertical, and (right) cross-stream velocities and velocity fluctuations from the mean (calculated by averaging over all body timesteps) at $Y^* = 0$ for the fluorescent seeding cases. Each pair of rows corresponds to a particular Reynolds number case, with the upper row being U^*, V^*, and W^* and the lower row being $U^{*\prime}$, $V^{*\prime}$, and $W^{*\prime}$.

component of the complex eigenvalue of the velocity gradient tensor,

$$\boldsymbol{\nabla U} = \boldsymbol{\Gamma B \Gamma^T}, \tag{5.2}$$

where

$$\boldsymbol{\Gamma} = [\boldsymbol{\Gamma r} \quad \boldsymbol{\Gamma cr} \quad \boldsymbol{\Gamma ci}], \ \boldsymbol{B} = \begin{bmatrix} \zeta r & 0 & 0 \\ 0 & \zeta cr & \zeta ci \\ 0 & -\zeta ci & \zeta_{cr} \end{bmatrix}, \tag{5.3}$$

$\boldsymbol{\nabla U}$ is the velocity gradient tensor, ζr and $\boldsymbol{\Gamma r}$ are the real eigenvalue and eigenvector, and $\zeta cr \pm i\zeta ci$ the complex conjugate pair of complex eigenvalues with corresponding eigenvectors $\boldsymbol{\Gamma cr} \pm i\boldsymbol{\Gamma ci}$. The exclusively positive values of swirling strength presented here are likely a result of shear between the current and ambient fluids. In both cases, the plots show regions of large magnitude swirling strength alternately above and below the velocity maximum. In the highest Reynolds number case, these regions take up less of the flow height. These plots can be compared directly with similar plots from the direct numerical simulation in Chapter 6.

Figure 5.12 shows the amplitudes of the dynamic modes, and Figures 5.13 and 5.14 the Fourier transform (where the Fourier transform is here performed over time on both data at central downstream and cross-stream locations, and at a central downstream location and the height of the velocity maximum) and wavelet decomposition (where the wavelet decomposition is here performed on data at a central downstream and cross-stream location, and at both the height of the velocity maximum and the height of maximum negative shear) of the velocity data. For both the $Re = 2743$ and $Re = 4606$ cases, significant frequencies were found.

Combining the FFT, wavelet, and dynamic mode amplitude plots, the frequencies of motions with significant impact on the flow, their vertical position within the flow, and the times over which they affect the flow can be identified. Figure 5.13 identifies a mode with frequency 0.40 Hz in the $Re = 2743$ case. This mode is primarily seen in the vertical velocity plots, at the height of the downstream velocity maximum. The motion is concentrated in the cross-stream centre of the domain but extends throughout the domain width, and is present throughout the flow duration. The $Re = 4606$ case contains a broader range of frequencies, and frequencies with significant cross-stream FFT amplitude. In particular, a mode with frequency 0.80 Hz is identified. Again, this mode is at the height of the velocity maximum and concentrated in the cross-stream centre of the flow. However, the motions extend less far in the cross-stream direction and unlike the 0.40 Hz mode, it is seen equally in the downstream and cross-stream FFT, and becomes more significant in the wavelet decomposition over time.

Visualisation of the dynamic modes illuminates the structure of the dominant motions for each case. Figure 5.15 illustrates the downstream, vertical, and cross-stream motions

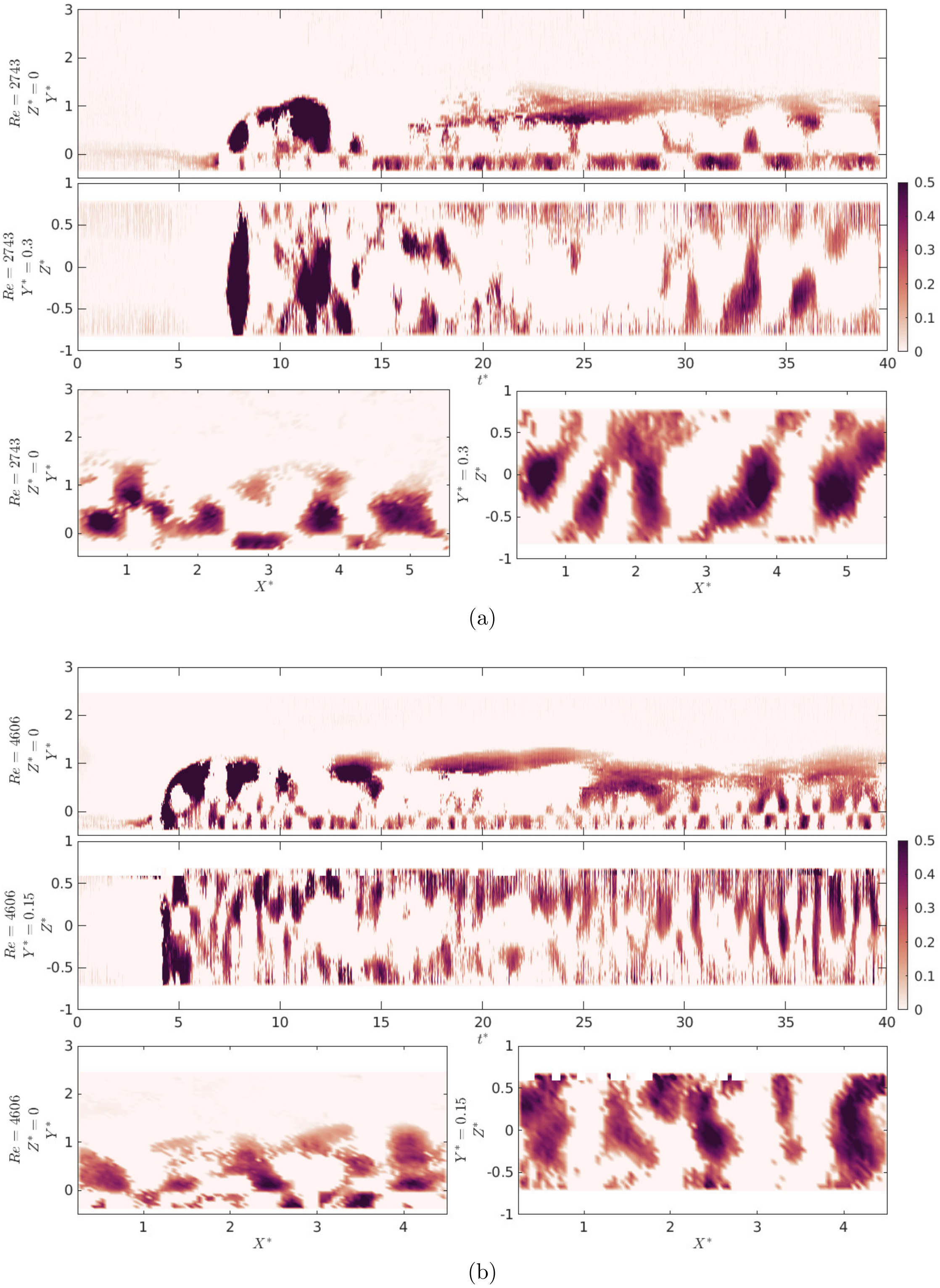

Figure 5.11: Plots of swirling strength for (a) the $Re = 2743$, and (b) the $Re = 4606$ cases on (top) a central cross-stream and central downstream position over time, (middle) a central downstream location and Y^* position above the velocity maximum over time, (bottom left) a central cross-stream X-Y slice and (bottom right) an X-Z slice above the velocity maximum for a timestep within the body.

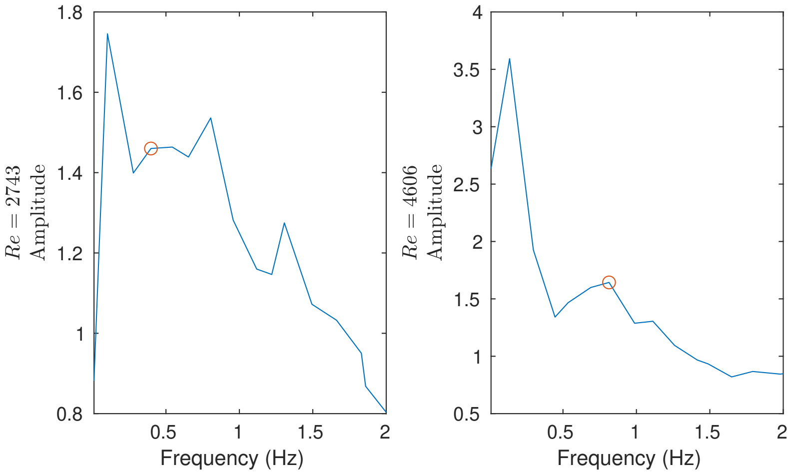

Figure 5.12: Dynamic mode amplitudes for the (left) $Re = 2743$, and (right) $Re = 4606$ cases.

associated with a mode at each Reynolds number. The other dynamic modes from each case have similar structure. In both cases, the dynamic mode shows motions at the expected position within the flow. For the $Re = 2743$ mode, the vertical velocities extend further across the domain width than the $Re = 4606$ mode. Considering the velocity streamlines, the $Re = 4606$ mode is associated with full-width three-dimensional coherent motions (i.e. motions with equivalent magnitude in the cross-stream and vertical directions) not clearly visible in the $Re = 2743$ mode streamlines. The downstream and vertical velocities on the central cross-stream slice have very similar structure to the modes identified in the planar PIV data (Chapter 4), suggesting that similar motions are being identified in both data sets.

In order to establish whether these motions are due to gravity, as in Chapter 4 a heuristic estimate of the Brunt-Väisälä frequency is obtained,

$$N \approx \sqrt{-\frac{g}{\rho_0}\frac{d\overline{\rho}}{dY}}\,, \tag{5.4}$$

where g is the acceleration due to gravity, $\overline{\rho}$ is the average density profile, and ρ_0 is taken to be the mean of the glycerol and KDP densities. The average density profile is estimated as in Chapter 4. Specifically, excess density ($\rho_e = \rho - \rho_a$, where ρ_e is the excess density, and $\rho_a = 1012\,\mathrm{kg\,m^{-3}}$ is the density of the ambient fluid) is estimated to be constant both above the current height (where $\rho_e = 0$ is assumed) and below the velocity maximum (where ρ_e is estimated by requiring conservation of excess density flux between the inlet and the data) with a linear distribution between the two. Inlet density flux (F_I) is estimated by multiplying fluid influx and the excess density of the dense fluid. In order to maintain comparability between the strands of work, the excess density flux from the data (F_e) is again estimated by considering the downstream velocity and density profiles

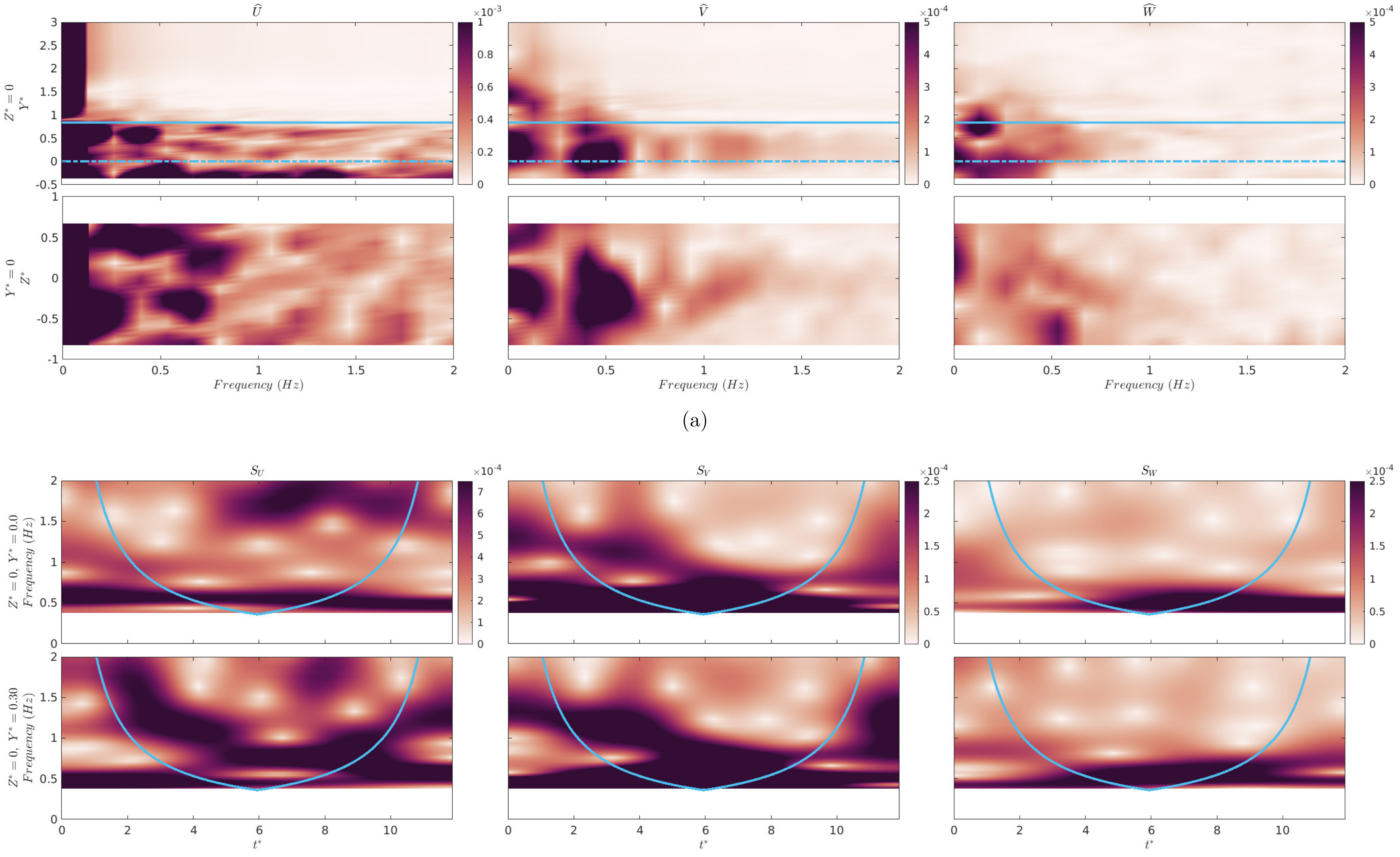

(a)

(b)

Figure 5.13: Plots of data from the $Re = 2743$ case: (a) FFT of downstream, vertical, and cross-stream velocities (top) at a central cross-stream and downstream location and (bottom) at a central downstream location and the height of the downstream velocity maximum, and (b) wavelet transform of velocity components at a central cross-stream and downstream location and (top) the height of the velocity maximum, and (bottom) the height of maximum negative shear. The blue lines in (b) represent the 'cone of influence' of the wavelet spectrum.

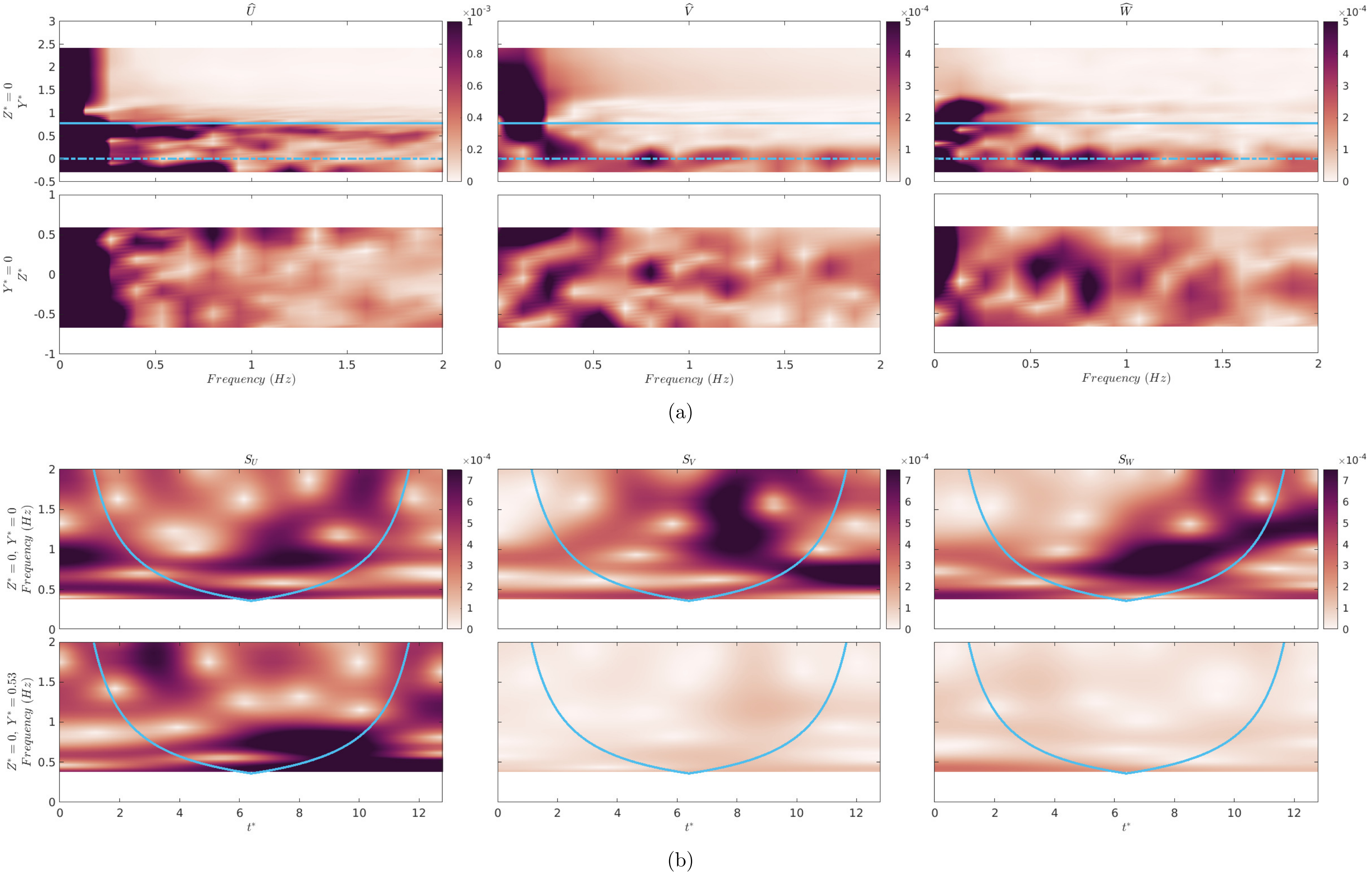

(a)

(b)

Figure 5.14: Plots of data from the $Re = 4606$ case: (a) FFT of downstream, vertical, and cross-stream velocities (top) at a central cross-stream and vertical location and (bottom) at a central downstream location and the height of the velocity maximum, and (b) wavelet transform of velocity components at a central cross-stream and downstream location and (top) the height of the velocity maximum, and (bottom) the height of maximum negative shear. The blue lines in (b) represent the 'cone of influence' of the wavelet spectrum.

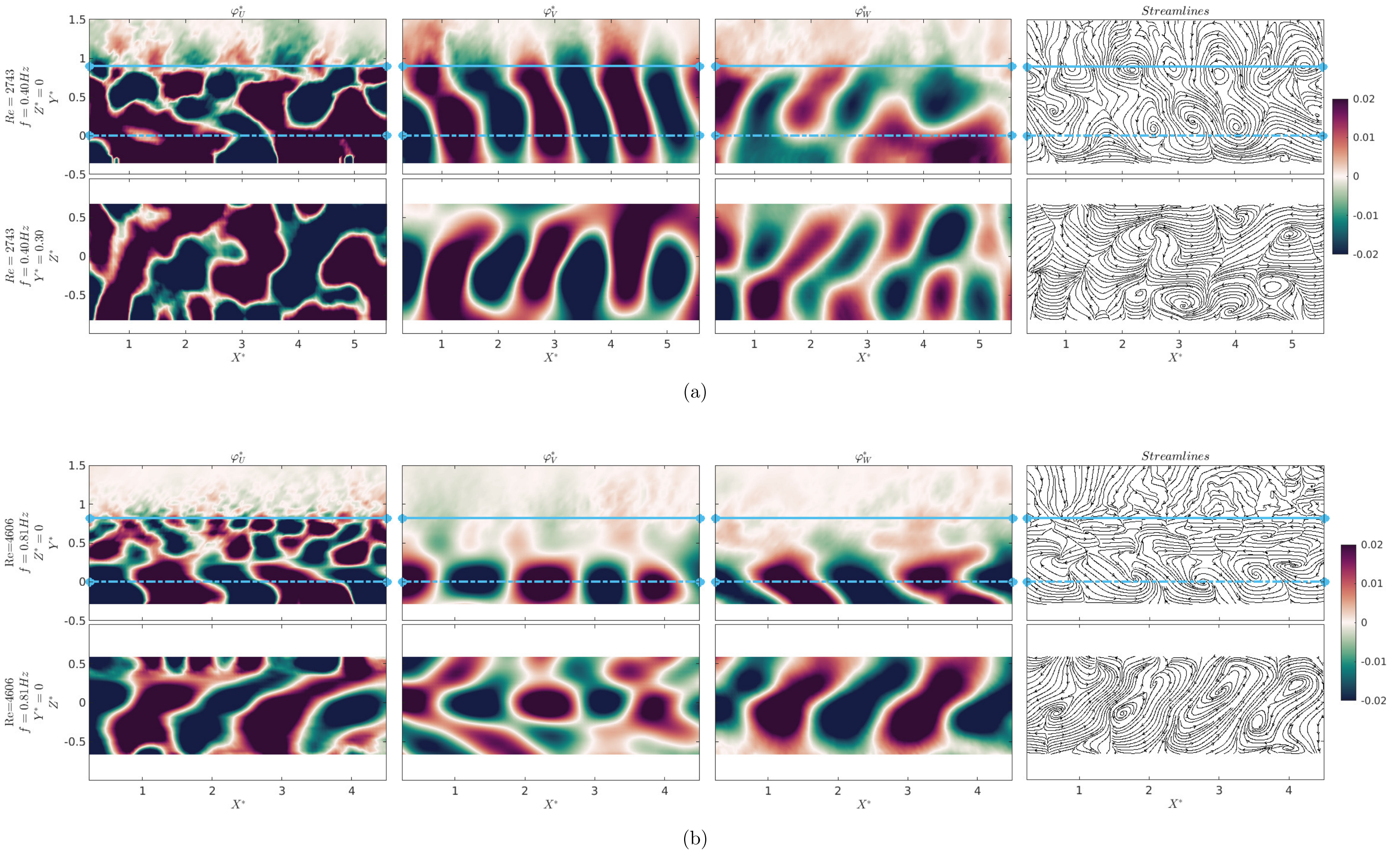

Figure 5.15: Slices showing the structure of (left) downstream, (left-centre) vertical, (centre-right) cross-stream velocities, and (right) two-dimensional velocity streamlines on (top) a central cross-stream slice, and (bottom) slices at $Y^* = 0.3$ ($Re = 2743$) or $Y^* = 0$ ($Re = 4606$) for (a) a mode from the $Re = 2743$ case with frequency 0.40 Hz and (b) a mode from the $Re = 4606$ case with frequency 0.81 Hz.

Q ($\mathrm{L\,s^{-1}}$)	0.082	0.148
F_I ($\mathrm{kg\,s^{-1}}$)	0.0024	0.0044
$\overline{\rho}_e^{max}$ ($\mathrm{kg\,m^{-3}}$)	13.5	14.0

Table 5.5: Details of the inlet excess density flux F_I calculated by taking the product of the fluid influx and the excess density of the KDP, and the estimated maximum excess density within the body calculated by requiring $F_I = F_e$ (where F_e is defined in (5.5)).

Re	f (Hz)	ω	λ (m)	N_{DS}	$\frac{\omega}{N_{DS}}$	c ($\mathrm{m\,s^{-1}}$)	$\frac{c}{U_{wave}}$
2743	0.40	2.51	0.086	3.88	0.65	0.034	1.24
4606	0.81	5.09	0.13	6.30	0.81	0.11	1.13
4606	1.11	6.99	0.10	7.49	0.93	0.11	1.23

Table 5.6: Details of the frequency, f, angular frequency, ω, wavelength, λ, expected maximum frequency of waves due to buoyancy after Doppler shift, N_{DS}, the ratio of ω and N_{DS}, the wave speed, $c = f\lambda$, and the ratio of wave speed to mean flow speed at the approximate wave height c/U_{wave} for dynamic modes identified as having a significant impact on the flow.

only on a central cross-stream plane,

$$F_e = W_T \int \overline{\rho}\overline{U}^{Z^*=0} dY, \tag{5.5}$$

where W_T is the width of the tank. Excess density below the velocity maximum is estimated by requiring $F_I = F_e$ (Table 5.5).

The Brunt-Väisälä frequency, N, is the upper bound on the angular frequency of internal waves due to buoyancy. A Doppler shift due to the mean flow must be applied,

$$N_{DS} = N + U_0 \boldsymbol{k}, \tag{5.6}$$

where N_{DS} is the frequency measured by a stationary observer, U_0 is the mean flow at the height of the wave, and $\boldsymbol{k}$ the wavenumber, which is here taken to be the downstream wavenumber k_x as all observed waves propagate downstream. Details of the frequency, wavelength (estimated by inspecting the velocities in Figure 5.15), wave speed, and Doppler shifted buoyancy frequency for each mode are shown in Table 5.6, along with a comparison of the measured frequency and the upper limit on the expected mode frequency and the wave speed and measured flow speed at the height of the wave. For the $Re = 2743$ case, the mode height is above the velocity maximum (here estimated to be the height of maximum negative shear), while the $Re = 4606$ waves are at the height of the velocity maximum. Given that the density profile is estimated rather than observed, and the wavelengths are approximated by inspecting mode plots such as Figure 5.15, the observed frequencies for all cases are on the right order of magnitude for the modes to be considered internal waves due to gravity. Additionally, given the approximations involved in the wave height and mode wavelength, the estimated wave speed is very close to the measured flow speed at the height of the wave. This indicates the presence of a critical layer in the flow at the height of the velocity maximum.

5.6 Discussion

The volumetric velocity data presented in this chapter questions the validity of neglecting cross-stream flow when discussing the gravity current body. While it is true that the alternating positive/negative regions of vertical and cross-stream velocities leads to small averaged values, the magnitudes of vertical and cross-stream velocity fluctuations are significant and equivalent (Figures 5.5, 5.9, and 5.10). Vertical and cross-stream velocities therefore both have significant and equivalent contribution to the calculation of turbulent kinetic energy. Temporal variations in the presented data highlight that averaging properties such as vertical velocity, cross-stream velocity, and turbulent kinetic energy gives a misleading impression of the flow (Figures 5.4, 5.6, and 5.7).

Further, the volumetric measurements indicate that the cross-stream centreline, which has often been used as the sole measurement location (for example Islam & Imran (2010) and Gray *et al.* (2006)), is not representative of the flow in general and the cross-stream velocity in particular (Figure 5.10). While this is especially true at lower Reynolds numbers, there is still a noticeable effect in the $Re = 4606$ data. While it may be argued that this could linked to the comparatively narrow domain width in this work, the aspect ratio of the flow is comparable to that of previous works quantifying the velocity structure in the current body (Cossu & Wells, 2012; Gray *et al.*, 2006; Islam & Imran, 2010).

Fourier transforms, wavelet transforms, and dynamic mode decomposition (Figures 5.13, 5.14, and 5.15) have been used to illuminate the structure of the body of gravity current flows. As in Chapter 4, the gravity current body has been shown to contain internal gravity waves, and the same changes in these waves have been observed with increased Reynolds number (namely the wave frequency increases and the position moves towards the velocity maximum).

Internal gravity waves have previously been observed in the core of stratified plane channel flows (García-Villalba & del Álamo, 2011; Zonta & Soldati, 2018). These originate from the vertical displacement of a fluid parcel in a stably stratified flow with density decreasing with distance from the lower boundary. The parcel is subject to buoyancy forces aiming to restore the parcel to its original vertical position, with overcorrection resulting in wavy motions (Zonta & Soldati, 2018). The waves observed by García-Villalba & del Álamo (2011) are only associated with vertical velocity data, not cross-stream, suggesting that the associated motions are largely two-dimensional. This is similar to the waves identified in the $Re = 2743$ case here, where peaks in the FFT are found in the downstream and vertical velocity data but not cross-stream (Figure 5.13).

By contrast, the waves identified in the $Re = 4606$ case are associated with peaks in the FFT of cross-stream velocity (Figure 5.14). The streamlines of dynamic modes from this case illustrate coherent motions in all three dimensions, with the mode having a corkscrew-like structure with associated cross-stream velocities being equivalent in magnitude to vertical (Figure 5.15). This cross-stream motion may originate with side-wall effects due to the relatively narrow domain considered here. However, the downstream velocity profiles in Figure 5.8 demonstrate that the highest Reynolds number flow (the only case shown to contain motions affecting the cross-stream FFT data) is less affected by side-walls than the lower Reynolds number flows. Additionally, real-world flows may also be at least partly constrained in the cross-stream direction (for example turbidity currents in submarine channels (Peakall & Sumner, 2015)). This data has demonstrated that even at the moderate Reynolds numbers considered here the flow is unstable to three-dimensional perturbations. The flow could reasonably be expected to become more three-dimensional as Reynolds number (and hence turbulence) is increased further, whatever the original instability triggering the three-dimensionality (for example the breakdown of Kelvin-Helmholtz structures (Meiburg *et al.*, 2015), or flow over bed structures (Bhaganagar & Pillalamarri, 2017)).

It has again been demonstrated that the phase speed of the waves is approximately equal to the mean flow speed, indicating a critical layer within the body. As described in Chapter 4, the presence of a critical layer within the flow, combined with the demonstrated three-dimensional motions, has significant implications for possible flow structure (Dorrell *et al.*, 2019). Wave breaking at the critical layer has the potential to form a barrier to mixing, maintaining a larger density difference than expected based on current understanding of body flow, thus increasing flow speeds and duration. Additionally, absorption of internal waves at the critical layer transfers horizontal momentum to the mean flow, increasing downstream velocities over time and suggesting that the assumption of a statistically steady flow may not be accurate.

5.7 Conclusions

The gravity current body has often been described through averaged properties, and investigated through measurements taken at-a-point or on a single plane. The influence of cross-stream flow has typically been neglected, with few seeking to quantify the magnitude and structure of three-dimensional motions within the body. In this chapter, Shake-the-Box particle tracking velocimetry has been used to generate instantaneous, three-dimensional, volumetric measurements of velocity in constant-influx solute-based gravity current flows.

The presented velocity measurements have been used to illustrate that cross-stream and vertical velocities (and velocity fluctuations) in the flow body are equivalent in magnitude, and therefore that the contribution of these two velocity components to turbulent kinetic energy are equivalent (with cross-stream velocity being most significant at the height of the velocity maximum). This suggests that cross-stream velocity should not be neglected when discussing the gravity current body. Additionally, instantaneous velocity and turbulent kinetic energy data have demonstrated variation (in some cases with a regular pattern) over time, and as such averaging these quantities leads to an inaccurate impression of flow structure.

The presence of three-dimensional motions is significant. In Chapter 4, planar PIV measurements were used to identify internal waves and a critical layer within the gravity current body. The potential for this to lead to an eddy transport barrier and the associated implications (such as sharper density profiles, and maintenance of the density difference over larger distances than previously anticipated) were discussed. However, the formation of this eddy transport barrier requires three-dimensional motions and cross-stream density gradients within the flow. As in Chapter 4, analysis of the velocity data through Fourier transforms, wavelet transforms, and dynamic mode decomposition led to identification of internal gravity waves forming a critical layer within the flow. The volumetric nature of these measurements has allowed three-dimensional corkscrew-like motions associated with these waves to be identified in the highest Reynolds number case.

Chapter 6

Using Direct Numerical Simulation to Establish The Effect of Reynolds and Schmidt Numbers on Gravity Current Flow

In this chapter, Direct Numerical Simulation (DNS) is used to quantify the changes in gravity current flow structure resulting from increased Schmidt number. The data presented indicates that, at the Reynolds numbers considered in this work ($Re_I = 100$ to $Re_I = 3000$), increasing Schmidt number from 1 reduces the size of the mixed region between current and ambient fluids and produces a more defined head region. Additionally, increasing Schmidt number results in the formation of a lobe-and-cleft structure in the head, and the formation of structures in the mixed layer behind the head. Assuming a Schmidt number of 1 may, therefore, lead to substantial structural differences compared with high Schmidt number flows with equivalent Reynolds number.

6.1 Background

As noted in the introductory chapter, gravity currents are primarily horizontal flows arising from a density difference between the current and surrounding ambient fluids. This density difference could be the result of, for example, the presence of solute, suspended sediment, or a temperature difference (Simpson, 1997; Ungarish, 2009). As they are a common class of flow, with examples including thunderstorm outflows and powder snow avalanches (Britter & Linden, 1980; Simpson, 1997), and are the primary mechanism of transport in oceans (Dorrell *et al.*, 2019; Talling, 2014), there exists extensive research into their structure, including numerical investigations (Cantero *et al.*, 2007; Hogg *et al.*, 2016; Meiburg *et al.*, 2015; Özgökmen *et al.*, 2004; Stacey & Bowen, 1988).

The Schmidt number, analogous to the Prandtl number, is defined as the ratio of momentum and mass diffusivities ($Sc = \nu/D$), and is a key parameter in understanding mixing on the molecular level (see (6.1)) (Bonometti & Balachandar, 2008; Miller, 1991). As Schmidt number increases, diffusion decreases and momentum becomes the dominant mass transfer mechanism. Increasing the Schmidt number from 1 reduces the length scales that must be resolved from the Kolmogorov scale (η_K) to the Batchelor scale ($\eta_B = \eta_K Sc^{-1/2}$) (Andersson *et al.*, 2011; Donzis *et al.*, 2014), and mixing is expected to decrease (Miller, 1991; Rahmani *et al.*, 2016). It has also been demonstrated that increasing Schmidt/Prandtl number may cause larger scale structural changes in the flow, such as increased plume length in turbulent jets (Miller, 1991), and stronger three-dimensional motions resulting from changes to density profiles and stronger density gradients (Hanazaki *et al.*, 2009; Langham *et al.*, 2020; Rahmani *et al.*, 2016).

The Reynolds number is defined as the ratio of inertia to viscous forces ($Re = \frac{U_c L_c}{\nu}$). Increasing Reynolds number, below the point of similarity ($Re \approx 1000$, (Simpson, 1997)), changes the head shape in a gravity current including the formation of the lobe-and-cleft structures resulting from the over-riding of ambient fluid and Kelvin-Helmholtz billows behind the head (García & Parsons, 1996; Parsons & García, 1998; Simpson, 1997). Reynolds number also significantly affects rates of mixing and entrainment, with mixing rates affected by whether the primary mechanism is Holmboe waves, Kelvin-Helmholtz vortex rolls, or Kelvin-Helmholtz billows (Balasubramanian & Zhong, 2018; Hogg *et al.*, 2015).

The value of Schmidt number varies dramatically depending on the fluid, for example $\mathcal{O}(1)$ for gases in air, $\mathcal{O}(1000)$ for solutes in water, and $\mathcal{O}(\infty)$ for oil in water (Andersson *et al.*, 2011; Bird *et al.*, 2007; Bonometti & Balachandar, 2008; Reynolds, 1974). Despite this, the existing investigations typically assume $Sc = 1$ (Birman *et al.*, 2005; Bonometti & Balachandar, 2008; Cantero *et al.*, 2007; Hogg *et al.*, 2016; Meiburg *et al.*, 2015; Necker *et al.*, 2005; Özgökmen *et al.*, 2004; Stacey & Bowen, 1988). The large computational cost involved (the cost of DNS scaling with $Re^3 Sc^2$, as demonstrated in Chapter 3) means that few works have so far considered the effect of Schmidt number on gravity current flows. Birman *et al.* (2005) and Necker *et al.* (2005) justify their use of $Sc = 1$ through test calculations that suggest Schmidt number has little influence on gravity current structure for values between 0.2 and 5.

The exception is Bonometti & Balachandar (2008), who use a combination of a pseudo-spectral method and a finite-volume/volume of fluid interface capturing method to investigate the parameter space $1 \leq Sc \leq \infty$ and $100 \leq Re \leq 10000$. For $Re = 10000$, they conclude that neither the front velocity nor the level of mixing are strongly dependent on Sc, though decreasing Sc does increase the size of the mixing region. For the lower Reynolds number flows, they observe that increasing Sc changes head shape, with a depression separating head from body appearing as Sc increases, and that the effect of

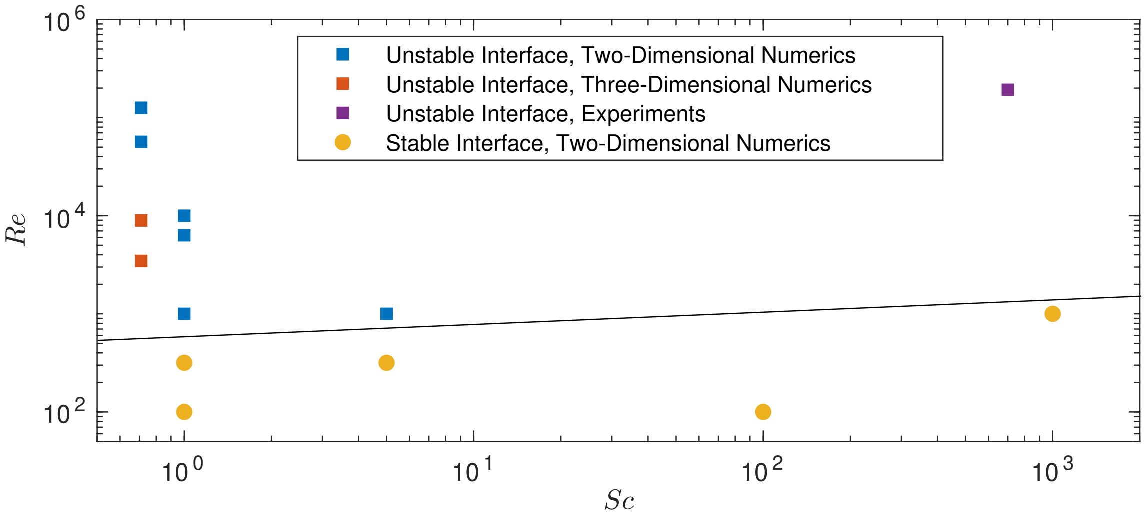

Figure 6.1: Scatter plot showing the distribution of stable/unstable interfaces based on a bulk Richardson number from a table in the work of Bonometti & Balachandar (2008) as a function of Sc and Re.

Sc on front velocity in these flows is highly dependent on the density contour chosen to define the front. They also claim that while the pattern of lobe-and-cleft structures is not strongly dependent on the Schmidt number, the formation of vortices along the body is. Figure 6.1 is a scatter plot based on a table from Bonometti & Balachandar (2008) showing the distribution of stable/unstable interfaces based on a bulk Richardson number for their work and a few other investigations. This suggests that the interface stability is only weakly dependent on Schmidt number, with the interface becoming slightly more stable with increased Sc. However, this data is based almost entirely on two-dimensional data sets. Two-dimensional simulation of gravity currents is not able to reproduce large-scale coherent motions and three-dimensional flow features, such as the formation of lobe-and-cleft structures and the breakdown of interfacial billows, or accurately estimate the energy budget of the flow (Cantero *et al.*, 2008; Espath *et al.*, 2014; Meiburg *et al.*, 2015; Necker *et al.*, 2002; Özgökmen *et al.*, 2004; Paik *et al.*, 2009; Stancanelli *et al.*, 2018). Therefore, three-dimensional simulations are needed to confirm the relationship between interface stability and Schmidt number.

In this work, three-dimensional direct numerical simulation (DNS) is used to provide the instantaneous density field, in addition to the velocity field which can be compared directly with the experimental data in previous chapters, further improving understanding of the flow. As well as considering the effect of Reynolds number, the impact of varying the Schmidt number will be investigated (something that was not possible in the experimental work of Chapters 4 and 5 due to refractive index matching requirements). Questions remain regarding how reasonable an assumption of $Sc = 1$ is for such flows. The effects of varying Reynolds and Schmidt numbers on the head of a gravity current flow will be considered. Specifically, the key aims are to discuss: i) how Reynolds and Schmidt numbers affect the structure of the head, in particular the formation of lobe-and-cleft structures, ii) how Reynolds and Schmidt numbers affect the structure of flow behind the head, in particular the stability of the current-ambient interface, iii) which of the changes observed with increased Schmidt number also occur with increased Reynolds number, and iv) when assuming a low Schmidt number to reduce the computational cost of numerical investigations may be justified.

6.2 Methodology

The spectral element solver Nek5000 is used to simulate three-dimensional gravity current flow in the domain illustrated in Figure 6.2. The governing equations are the non-dimensional, incompressible, Boussinesq Navier-Stokes, salinity, and continuity equations,

$$\begin{aligned} \frac{\partial \tilde{\boldsymbol{U}}}{\partial \tilde{t}} + \tilde{\boldsymbol{U}} \cdot \nabla \tilde{\boldsymbol{U}} &= -\nabla \tilde{P} + \frac{1}{Re} \nabla . \tilde{\tau} + \frac{1}{Fr_d^2} \Delta \tilde{S} \hat{\boldsymbol{g}}, \\ \frac{\partial \tilde{S}}{\partial \tilde{t}} + \tilde{\boldsymbol{U}} \cdot \nabla \tilde{S} &= \frac{1}{ReSc} \nabla \cdot \nabla \tilde{S}, \\ \nabla \cdot \tilde{\boldsymbol{U}} &= 0, \end{aligned} \tag{6.1}$$

where $\boldsymbol{U}$ is the velocity vector, t time, $P = p + \rho_a g h$ where p is the pressure field and h the elevation, $Re = U_c L_c / \nu$ the Reynolds number, τ the stress tensor, $Fr_d = U_c / \sqrt{g' L_c}$ the densimetric Froude number, g and $\hat{\boldsymbol{g}}$ the magnitude and direction of the gravitational acceleration, S salinity, $Sc = \nu / D$ the Schmidt number with ν the kinematic viscosity and D the mass diffusivity, $\beta = \frac{1}{\rho} \frac{\partial \rho}{\partial S}$ the haline contraction coefficient, and $\tilde{(\cdot)}$ indicates a dimensionless variable. The dimensionless variables are defined relative to some characteristic length, velocity, and time scales as shown in Table 6.1. Time advancement is performed using a semi-implicit method combining implicit backwards differentiation and explicit Runge-Kutta schemes as described in Fischer (1997), and spatial discretisation is based on the spectral element method (Boyd, 2001; Fischer, 1997; Fornberg, 1998). To ensure sufficient resolution, the wall y^+, x^+, and z^+ values (defined as $y^+ = u_w y / \nu$ where y is the distance to the nearest wall, and u_w the wall friction velocity with equivalent statements for the other spatial dimensions) are kept below 0.05 for the nearest grid point to the wall, and the first 10 points are within $y^+ < 10$ (Coleman & Sandberg, 2010; Kim *et al.*, 1987). Additionally, decay of several orders of magnitude is observed in the energy spectrum for all variables (Cantero *et al.*, 2006, 2007). In the raised sections at either end of the domain and in the drop above the outlet, the resolution was lower to reduce computational cost. Resolution in these regions was therefore likely not sufficient to capture all ranges of motion, however these areas were considered sufficiently far from the current that the flow data would not be affected.

The characteristic length L_c, velocity U_c, and time t_c scales are defined *a priori*. The characteristic length scale for all cases is chosen to be the height of the internal fitting to

Parameter	Non-Dimensionalisation
Length	$\tilde{x} = x/L_c$
Velocity	$\tilde{\boldsymbol{U}} = \boldsymbol{U}/U_c$
Time	$\tilde{t} = (U_c/L_c)t = t/t_c$
Pressure	$\nabla\tilde{P} = (L_c/\rho_a U_c^2)\nabla P$
Stress tensor	$\nabla\cdot\tilde{\tau} = (L_c^2/U_c\nu\rho_a)\nabla\cdot\tau$
Salinity	$\Delta\tilde{S} = (S - S_a)/(S_I - S_a) = \Delta S/\Delta S_I$

Table 6.1: Definition of non-dimensionalisations used in this work, where x is position, t is time, $t_c = L_c/U_c$ a characteristic time, $\Delta S = S - S_a$, and $\Delta S_I = S_I - S_a$.

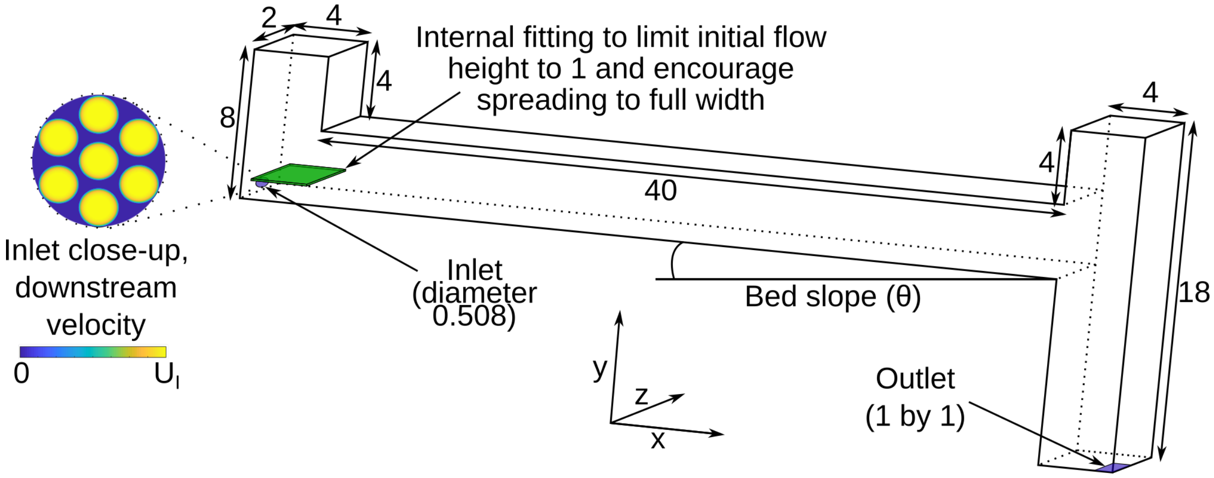

Figure 6.2: DNS setup.

Re_I	Sc	Pe	ν ($\mathrm{m^2\,s^{-1}}$)	$Fr_{D,I}$	U_I ($\mathrm{m\,s^{-1}}$)	D ($\mathrm{m^2\,s^{-1}}$)
100	1	100	3.26×10^{-5}	0.54	0.22	3.26×10^{-5}
100	10	1000	3.26×10^{-5}	0.54	0.22	3.26×10^{-6}
100	100	10000	3.26×10^{-5}	0.54	0.22	3.26×10^{-7}
500	1	500	6.53×10^{-6}	0.54	0.22	6.53×10^{-6}
500	10	5000	6.53×10^{-6}	0.54	0.22	6.53×10^{-7}
1000	1	1000	3.26×10^{-6}	0.54	0.22	3.26×10^{-6}
3000	1	3000	1.09×10^{-6}	0.54	0.22	1.09×10^{-6}

Table 6.2: Parameters for the various simulations conducted in this work, along with a haline contraction coefficient of $\beta = 1$ and $S_I - S_a = 0.03$ to achieve a 3% density difference. The characteristic length (L_c), velocity (U_c) and time (t_c) scales for every case are $L_c = 0.05\,\mathrm{m}$, $U_c = 0.065\,\mathrm{m\,s^{-1}}$, and $t_c = L_c/U_c = 0.77\,\mathrm{s}$.

limit initial flow height, $L_c = 0.05\,\mathrm{m}$. For the highest Reynolds number DNS case, the viscosity is chosen to match that of the experimental work in Chapter 4, $\nu = 1.09\,\mathrm{m^2\,s^{-1}}$, and the characteristic velocity, $U_c = 0.065\,\mathrm{m\,s^{-1}}$, is chosen to give the desired input Reynolds number $Re_I = 3000$. This represents an average velocity under the initial internal fitting. The characteristic time scale is chosen to be $t_c = L_c/U_c = 0.77\,\mathrm{s}$. To reduce the Reynolds number, the characteristic velocity scale is kept constant and the fluid viscosity varied. Schmidt number is varied by changing mass diffusivity, D. The input densimetric Froude number, $Fr_{D,I} = U_c/\sqrt{g'L_c} = 0.54$, is the same for all cases. The input parameters for each case are shown in Table 6.2.

The inlet flow is again intended to match that of the work in Chapter 4. Therefore, the maximum inlet velocity, U_I, is approximated by dividing the influx of the lowest influx PIV case by the inlet area. The inlet has dimensionless radius 0.254, and is covered with a coarse mesh with holes of dimensionless radius 0.078. For the DNS, these holes are centred at locations

$$\begin{gathered}(\tilde{Y},\tilde{Z}) = (0.350, 1.000),\ (0.531, 1.000),\ (0.169, 1.000),\ (0.441, 1.150),\\ (0.260, 1.150),\ (0.441, 0.850),\ (0.260, 0.850),\end{gathered} \tag{6.2}$$

with the inlet velocity approximated by

$$\tilde{U} = \tilde{U}_I\sqrt{\sin((0.5 + 0.5\tilde{r}^2)\pi)}\ , \tag{6.3}$$

where $\tilde{r}$ varies from 0 to 1 from the centre to the edge of each small circle. Where the velocity on the inlet is non-zero, the salinity $\tilde{S} = 1.03$ compared to $\tilde{S} = 1.00$ in the rest of the domain (and therefore $\Delta S_I = 0.03$), with a haline contraction coefficient of $\beta = 1$ for simplicity. The outlet is approximated by a square outlet placed in the bottom right corner of the domain.

6.3 The Effect of Reynolds and Schmidt Numbers on The Head

6.3.1 Density

The effect of Schmidt number on the density structure of the flow can be established by considering contours of proportional excess density ($\Delta\tilde{S}$). Figure 6.3 shows contours of $\Delta\tilde{S}$ at $\tilde{t} = 23.4$ at a central cross-stream location. The right-most column of this figure shows two contours for each case – that with density just above the ambient density, $\Delta\tilde{S} = 0.03$, and that with density approximately halfway between the densities of the ambient fluid and that pumped in at the inlet, $\Delta\tilde{S} = 0.48$. The contour with $\Delta\tilde{S} = 0.03$

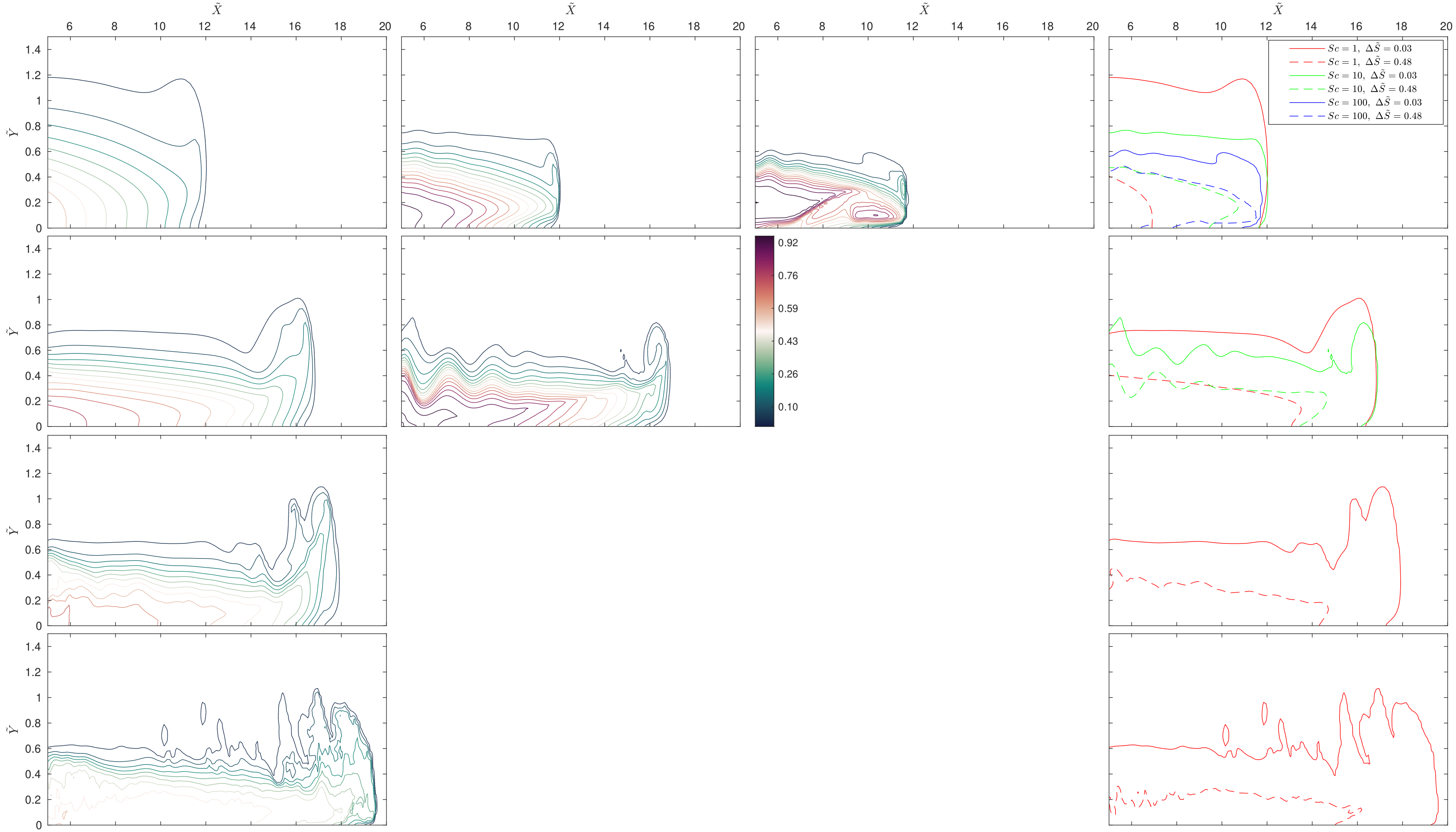

Figure 6.3: Density contours on a central cross-stream slice within the domain at $\tilde{t} = 23.4$. From top to bottom, the inlet Reynolds number $Re_I = 100$, 500, 1000, 3000 and from left to right $Sc = 1$, 10, 100 with the rightmost column showing density contours at $\Delta\tilde{S} = 0.03$ and $\Delta\tilde{S} = 0.48$ for each case.

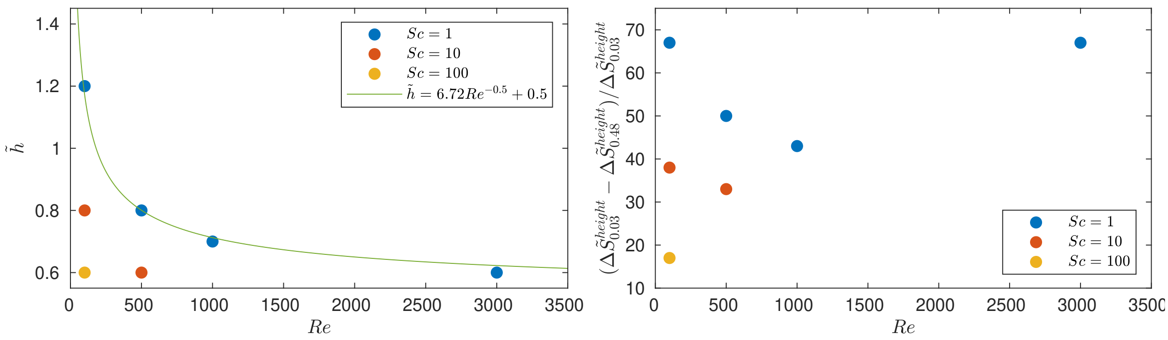

Figure 6.4: Scatter plots showing the effect of Reynolds number on (left) current height (where $\tilde{h}$ is the dimensionless current height) and (right) mixed layer size as a percentage of current height.

is considered to be the current boundary. Increasing Schmidt number has little impact on current front velocity over the short time frame considered here, though increasing Reynolds number increases front velocity as expected. Increasing either Reynolds number or Schmidt number leads to a depression behind the head, angled towards the current front.

For each case, the current height (defined as the height of the $\Delta\tilde{S} = 0.03$ contour), the thickness of the mixed region (defined as the difference in height of the two contours at the left-most point of the figure), and the difference in front positions of the $\Delta\tilde{S} = 0.03$ and $\Delta\tilde{S} = 0.48$ contours are estimated by inspecting Figure 6.3, and listed in Table 6.3. The height of the head is approximately constant across cases with constant Schmidt number. For $Sc = 1$ the head height is ~ 1, reducing to ~ 0.8 for $Sc = 10$. Increasing Schmidt number consistently reduces body height, the thickness of the mixed layer as a proportion of total flow height (Figure 6.4), and the difference in front position of the two contours (illustrating that increasing Schmidt number leads to dense fluid reaching closer to the front of the flow).

The height of the $\Delta\tilde{S} = 0.48$ contour, however, is not strongly affected by increasing Schmidt number, suggesting that evidence of the effect of Schmidt number on quantities such as current height or front velocity is highly dependent on the contour chosen to define the current boundary. In fact, the height of this contour is the same across all cases excepting $Re_I = 3000$, suggesting a greater degree of mixing in this case. Increasing Schmidt number reduces current height, with a 33% decrease between the $(Re_I, Sc) = (100, 1)$ and $(100, 10)$ cases (with a further decrease of 25% between $(Re_I, Sc) = (100, 10)$ and $(100, 100)$), though this decrease is reduced to 25% between $(Re_I, Sc) = (500, 1)$ and $(500, 10)$. Similarly increasing Schmidt number reduces the percentage of the current height taken up by the mixed layer, from 67% to 38% between the $(Re_I, Sc) = (100, 1)$ and $(100, 10)$ cases (to only 17% in the $(Re_I, Sc) = (100, 100)$ case), and from 50% to 33% between $(Re_I, Sc) = (500, 1)$ and $(500, 10)$. Dense fluid reaches closer to the front of the flow as Schmidt number is increased, with the percentage of the flow covered by the $\Delta\tilde{S} = 0.48$ contour increasing from 58% to 88% between the $(Re_I, Sc) = (100, 1)$ and

(Re_I, Sc)	$\Delta\tilde{S}^{height}_{0.03}$	$\Delta\tilde{S}^{height}_{0.48}$	$\frac{\Delta\tilde{S}^{height}_{0.03}-\Delta\tilde{S}^{height}_{0.48}}{\Delta\tilde{S}^{height}_{0.03}}$	$\frac{\Delta\tilde{S}^{front}_{0.48}}{\Delta\tilde{S}^{front}_{0.03}}$
(100, 1)	1.20	0.40	67%	58%
(100, 10)	0.77 (36%)	0.48	38%	88%
(100, 100)	0.60 (50%/22%)	0.48	17%	100%
(500, 1)	0.77 (36%)	0.39	50%	80%
(500, 10)	0.60 (22%/22%)	0.40	33%	88%
(1000, 1)	0.67 (44%)	0.39	43%	81%
(3000, 1)	0.63 (48%)	0.21	67%	83%

Table 6.3: Estimates of the current height (determined by the $\Delta\tilde{S} = 0.03$ contour), the mixed layer thickness as a percentage of current height (defined as the difference in heights of the $\Delta\tilde{S} = 0.03$ and $\Delta\tilde{S} = 0.48$ contours) and the percentage of flow length covered by the $\Delta\tilde{S} = 0.48$ contour. These are based on inspection of Figure 6.3. (Brown text indicates the % decrease from the $Sc = 1$ case with the same Re_I, magenta text the % decrease from the $Sc = 10$ case with the same Re_I, and cyan text the % decrease from the $Re_I = 100$ case with the same Sc).

$(Re_I, Sc) = (100, 10)$ cases (further increasing to 100% in the $(100, 100)$ case) and from 80% to 88% between the $(Re_I, Sc) = (500, 1)$ and $(500, 10)$ cases. This demonstrates that increasing Reynolds number reduces the influence of increased Schmidt number on some flow features, with increasing Schmidt number from 1 to 10 having more impact than increasing beyond 10. Additionally, this $Sc = 100$ case has dense fluid reaching the very front of the flow. This suggests that a further increase to $Sc = \mathcal{O}(1000)$ to match real-world solute based flows would likely result in only minor changes in these parameters.

The effect of Reynolds number is more complex (see Figure 6.4). While reducing viscosity (increasing Reynolds number) consistently reduces current height (in this case, the decrease at $Sc = 1$ is proportional to $Re^{-0.5}$) and increases the percentage of flow length covered by the $\Delta\tilde{S} = 0.48$ contour, the percentage of current height covered by the mixed layer increases in the $Re_I = 3000$ case compared with $Re_I = 1000$, perhaps a result of increased mixing by the Kelvin-Helmholtz structures that form with increased Reynolds number (see Figure 6.5). These structures are also present in the $Re_I = 1000$ case, and may be emerging in the $(Re_I, Sc) = (500, 10)$ case, in which the mixed layer thickness decreases as a proportion of current height compared with the lower Re_I cases. However, the rate of decrease between $Re_I = 500$ and $Re_I = 1000$ is slower than that between $Re_I = 100$ and $Re_I = 500$, which may also be a result of the Kelvin-Helmholtz structures.

The three-dimensional density isosurfaces (Figure 6.5) indicate that these trends extend across the width of the tank. These isosurfaces show signs of structural change with increasing Reynolds and Schmidt numbers. At $Re_I = 100$, the isosurfaces from the cases with $Sc = 1$ and $Sc = 10$ are completely smooth. At $Sc = 100$, ridges appear in the highest density isosurface. In the $(Re_I, Sc) = (1000, 1)$ case the lowest density

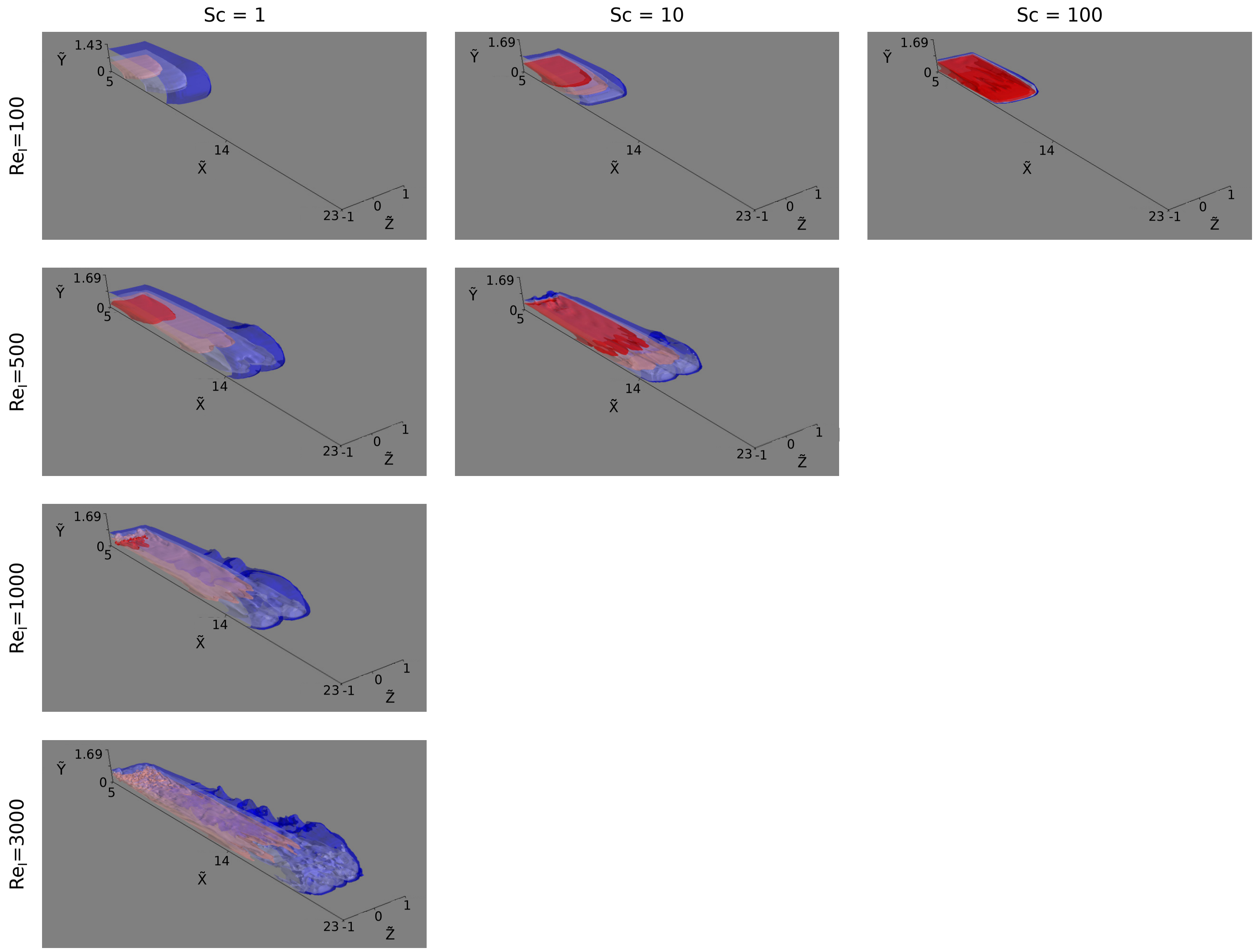

Figure 6.5: Three-dimensional isosurfaces of density at $\tilde{t} = 23.4$. From top to bottom, the inlet Reynolds number $Re_I = 100,\ 500,\ 1000,\ 3000$ and from left to right $Sc = 1,\ 10,\ 100$. The isosurfaces shown are (blue to red) $\Delta\tilde{S} = 0.02$, $\Delta\tilde{S} = 0.25$, $\Delta\tilde{S} = 0.48$, and $\Delta\tilde{S} = 0.71$.

isosurface has oscillations behind the head. By $(Re_I, Sc) = (3000, 1)$, all isosurfaces have lost the smoothness of the $(Re_I, Sc) = (100, 1)$ case, as expected owing to the increase in turbulence. Depending on the Reynolds and Schmidt numbers of the flow, there may be evidence of additional structure in the highest density isosurface, the lowest density isosurface, both, or neither. Additionally, with increasing Reynolds number the perturbations in the density isosurfaces are most pronounced near the head, while for increasing Schmidt number the perturbations become more pronounced with increasing distance from the head. This suggests that there are at least two distinct mechanisms influencing the flow structure.

To investigate the mechanisms responsible for these changes, pseudocolour plots of density both in an $\tilde{X}-\tilde{Z}$ plane at $\tilde{Y} = 0.1$ and in a $\tilde{Z}-\tilde{Y}$ plane near the current front (Figure 6.6) can be inspected. These plots show that cases $(Re_I, Sc) = (100, 100), (500, 10)$, and $(3000, 1)$ contain regions of less-dense fluid surrounded by the denser fluid of the head. The $\tilde{Z} - \tilde{Y}$ plane illustrates that this fluid is absorbed upwards, originating from the over-running of ambient by the raised nose of the flow. Therefore, as well as causing dense fluid to reach closer to the front of the flow, increasing Schmidt number at fixed Reynolds number leads to the formation of lobe-and-cleft structures within the head. These structures also form with increasing Reynolds number.

6.3.2 Velocity

In order to obtain a thorough understanding of the flow structure, the velocity structure will be inspected. Pseudocolour plots of all three velocity components for each case are shown on an $\tilde{X} - \tilde{Z}$ slice close to the bottom boundary (Figure 6.7) and on $\tilde{X} - \tilde{Y}$ slices (Figures 6.8 and 6.9). In addition to Figures 6.5 and 6.6, Figure 6.7 highlights a strong symmetry about the central $\tilde{Z}$-plane in all but the $(Re_I, Sc) = (3000, 1)$ case. Only in this case does the increase in non-linearity owing to higher Reynolds number cause this symmetry to break. Excepting this highest Reynolds number case, the cross-stream velocity for all cases has negligible magnitude on the central $\tilde{Z} = 0$ plane (Figure 6.8), indicating a symmetric solution. However, away from this central plane the magnitude of cross-stream and vertical velocities have equivalent magnitude in all cases (for example the plane at $\tilde{Z} = 0.5$ shown in Figure 6.9). This suggests that the flow is not two-dimensional as commonly assumed (Meiburg *et al.*, 2015; Simpson, 1997). Downstream velocity on the two $\tilde{X} - \tilde{Y}$ planes has the same structure and magnitude in all cases, as does cross-stream velocity in the $Re_I = 3000$ case.

The vertical velocity plots confirm the over-riding of ambient fluid, with Figure 6.7 showing areas of large positive vertical velocity close to the bottom boundary and near the front of the current for the $(Re_I, Sc) = (100, 100)$, $(500, 10)$, and $(3000, 1)$ cases, corresponding to the rising buoyant fluid over-ridden by the current front. Additionally, as

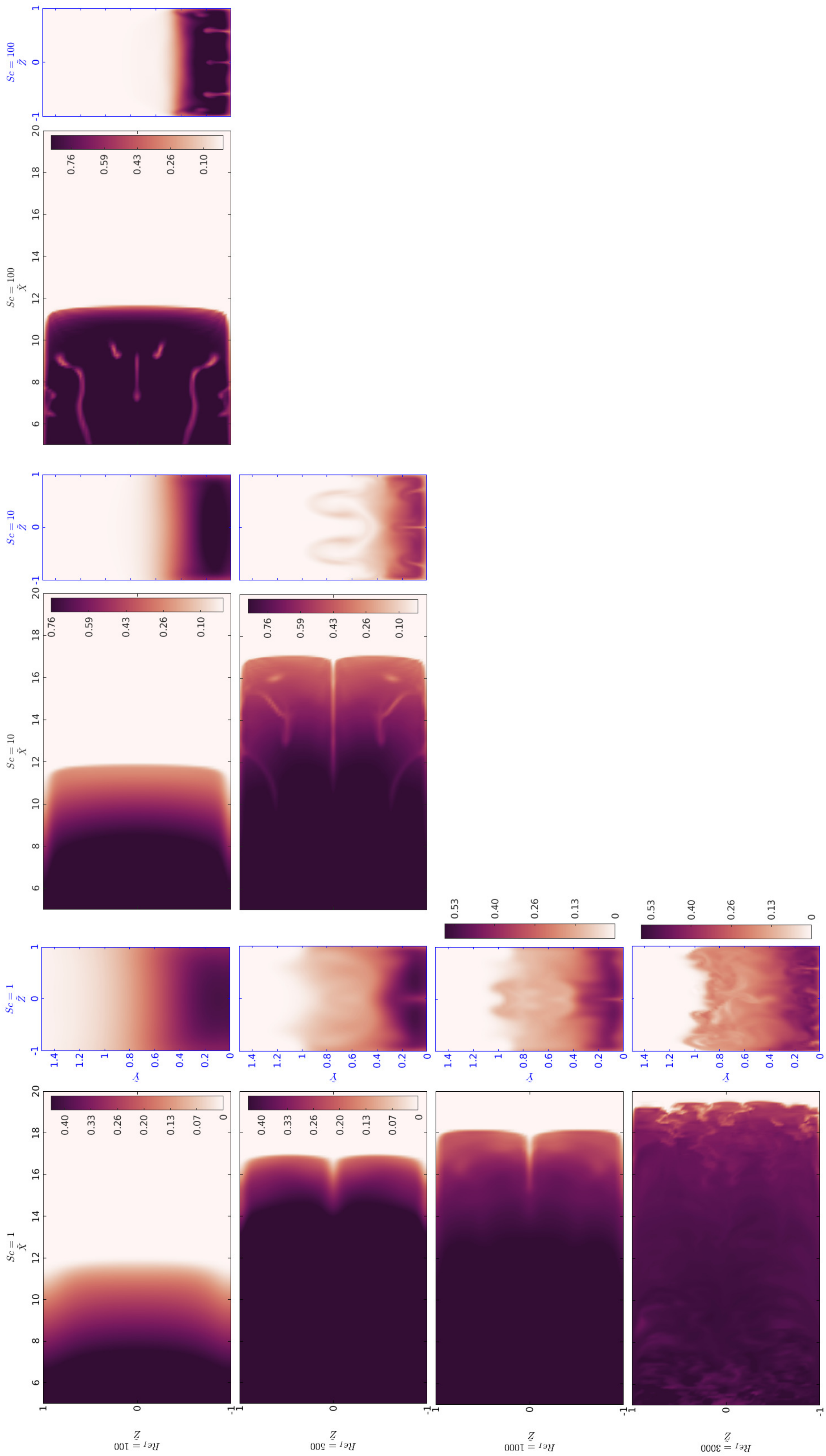

Figure 6.6: Pseudocolour plots of $\Delta\tilde{S}$ at $\tilde{t} = 23.4$ on an $\tilde{X} - \tilde{Z}$ plane at $\tilde{Y} = 0.1$ and a $\tilde{Z} - \tilde{Y}$ plane $\tilde{X} \approx 2$ behind the current front for (top to bottom) increasing Reynolds number and (left to right) increasing Schmidt number.

expected from the density contours, increasing Reynolds number increases downstream velocity within the flow. Increasing Reynolds number also increases variation in all components of velocity within the body, including alternating positive and negative vertical velocity near the side-walls in the $Re_I = 1000, 3000$ cases. Visible in both Figures 6.7 and 6.8, increasing Schmidt number results in a regular alternating pattern of positive and negative vertical velocity at a central cross-stream location, and corresponding positive and negative cross-stream velocity either side of the centre, behind the head of the current. The regular alternating vertical velocity pattern established by increasing Schmidt number is localised to the cross-stream centre of the flow, though increasing Reynolds number increases the width of the motions (Figures 6.7 and 6.9).

Figure 6.10 illustrates the flow behind the head in the $(Re_I, Sc) = (500, 1),\ (500, 10)$ cases at $\tilde{t} = 66.3$, demonstrating that these are not short-term changes. As well as velocity plots, this figure contains plots of density fluctuations from cross-stream averaged density ($\Delta\tilde{S} - \overline{\Delta\tilde{S}}_{\tilde{Z}}$, where $\overline{\Delta\tilde{S}}_{\tilde{Z}}$ is density averaged in the cross-stream direction). The density fluctuations in the $Sc = 10$ case contain a pattern of alternating positive and negative regions correlated with those in vertical velocity but with a $1/4-$wavelength offset (characteristic of internal gravity waves (García-Villalba & del Álamo, 2011)). To understand why decreasing mass diffusivity leads to large-scale changes in flow structure, plots of swirling strength and gradient Richardson number will be inspected.

Figure 6.11 shows plots of swirling strength ζ_{ci} as defined by Zhou *et al.* (1999), as the imaginary component of the complex eigenvalue of the velocity gradient tensor,

$$\tilde{\boldsymbol{\nabla}}\tilde{\boldsymbol{U}} = \boldsymbol{\Gamma}\boldsymbol{B}\boldsymbol{\Gamma}^{\boldsymbol{T}}, \tag{6.4}$$

where

$$\boldsymbol{\Gamma} = [\boldsymbol{\Gamma r}\ \boldsymbol{\Gamma cr}\ \boldsymbol{\Gamma ci}],\ \boldsymbol{B} = \begin{bmatrix} \zeta r & 0 & 0 \\ 0 & \zeta cr & \zeta ci \\ 0 & -\zeta ci & \zeta cr \end{bmatrix}, \tag{6.5}$$

$\tilde{\boldsymbol{\nabla}}\tilde{\boldsymbol{U}}$ is the velocity gradient tensor, ζr and $\boldsymbol{\Gamma r}$ are the real eigenvalue and eigenvector, and $\zeta cr \pm i\zeta ci$ the complex conjugate pair of complex eigenvalues with corresponding eigenvectors $\boldsymbol{\Gamma cr} \pm i\boldsymbol{\Gamma ci}$. These plots reveal that increasing Schmidt number leads to the formation of structures in the mixed layer between the current and the ambient in the centre of the tank in the cross-stream direction (with the mixed layer here defined as the region between the $\Delta\tilde{S} = 0.03$ and $\Delta\tilde{S} = 0.48$ contours). The placement of these structures is identical for the $(Re_I, Sc) = (100, 10), (100, 100)$ cases, and their spacing in the downstream direction is the same for all three $Sc > 1$ cases. Figure 6.11 shows that increasing Reynolds number also leads to the formation of structures within the body, though they differ from those resulting from increased Schmidt number. While some of the structures resulting from increased Reynolds number are within the mixed region, the structures in the higher Reynolds number cases have a less regular pattern (with a different physical spacing to the high Schmidt number cases), and are not limited to the centre in the cross-stream direction. The exclusively positive values of swirling strength are likely a result of the influence of shear between the current and ambient. Figure 6.11 also includes plots of the $\tilde{X}$ component of vorticity, $\Omega_{\tilde{x}} = \frac{\partial \tilde{W}}{\partial \tilde{Y}} - \frac{\partial \tilde{V}}{\partial \tilde{Z}}$ on an $\tilde{X} - \tilde{Z}$ plane, indicating the level of motion perpendicular to the downstream flow. It can be seen that the central structures that appear with increased Schmidt number are linked to three-dimensional motions within the flow.

This change in large-scale structures with Schmidt number is not immediately anticipated, given that Schmidt number is expected to result in changes at the small scale. Figure 6.12 shows the density and downstream velocity profiles on a central cross-stream location averaged over downstream location at the timestep illustrated in Figure 6.10. The change in diffusivity resulting from the Schmidt number increase leads to a change in density profile, specifically the anticipated increase in density in the lower part of the flow and sharper transition from dense to ambient fluid. As there is a greater density difference, there is a corresponding increase in downstream velocity within the body. These changes may affect the stability of the interface. To illustrate this, a gradient Richardson number can be calculated,

$$Ri = \frac{g}{\rho_c} \frac{\partial \overline{\rho} / \partial Y}{(\partial \overline{U} / \partial Y)^2}, \tag{6.6}$$

where ρ_c is the density of the fluid pumped in at the inlet, which gives a measure of the stability of density stratification. If $Ri > 0.25$, then the energy produced by shear is not sufficient to overcome the density stratification and is therefore dissipated (Buckee *et al.*, 2001). Profiles of Ri for the cases with $Re_I = 500$ are shown in Figure 6.12c. Increasing Schmidt number from 1 changes the Ri profile such that the value at the current height moves from above to below this critical level. The same change is seen for every case with $Sc > 1$, while for every case with $Sc = 1$, $Ri > 0.25$ in this area. Therefore, changes in the density and velocity profiles resulting from decreasing mass diffusivity (and therefore increasing Schmidt number) lead to the density stratification becoming less stable such that energy produced from shear is no longer dissipated but instead leads to large-scale structural changes in the flow.

6.4 Discussion

Reducing the fluid viscosity, and thus increasing the flow Reynolds number, has been shown to result in a shorter head, with more velocity fluctuations, and greater front and internal velocities. Excepting the highest Reynolds number case considered in this work, a strong symmetry plane is present at a central cross-stream location for all cases. Attempting to quantify such flows using exclusively a central cross-stream plane could,

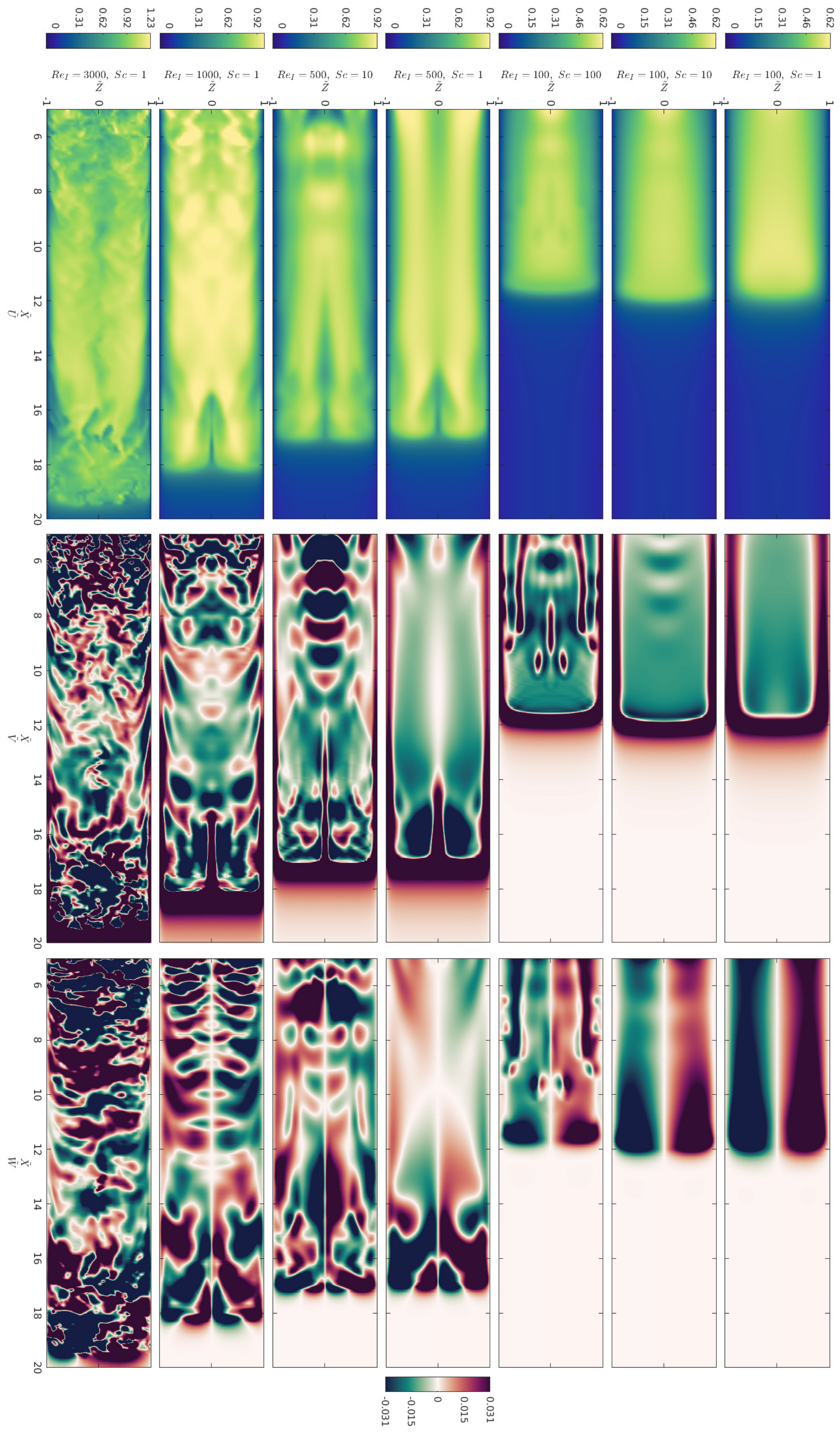

Figure 6.7: (left) Downstream, (centre) vertical, and (right) cross-stream velocity for each case at $\tilde{t} = 23.4$ on an $\tilde{X} - \tilde{Z}$ slice at $\tilde{Y} = 0.1$.

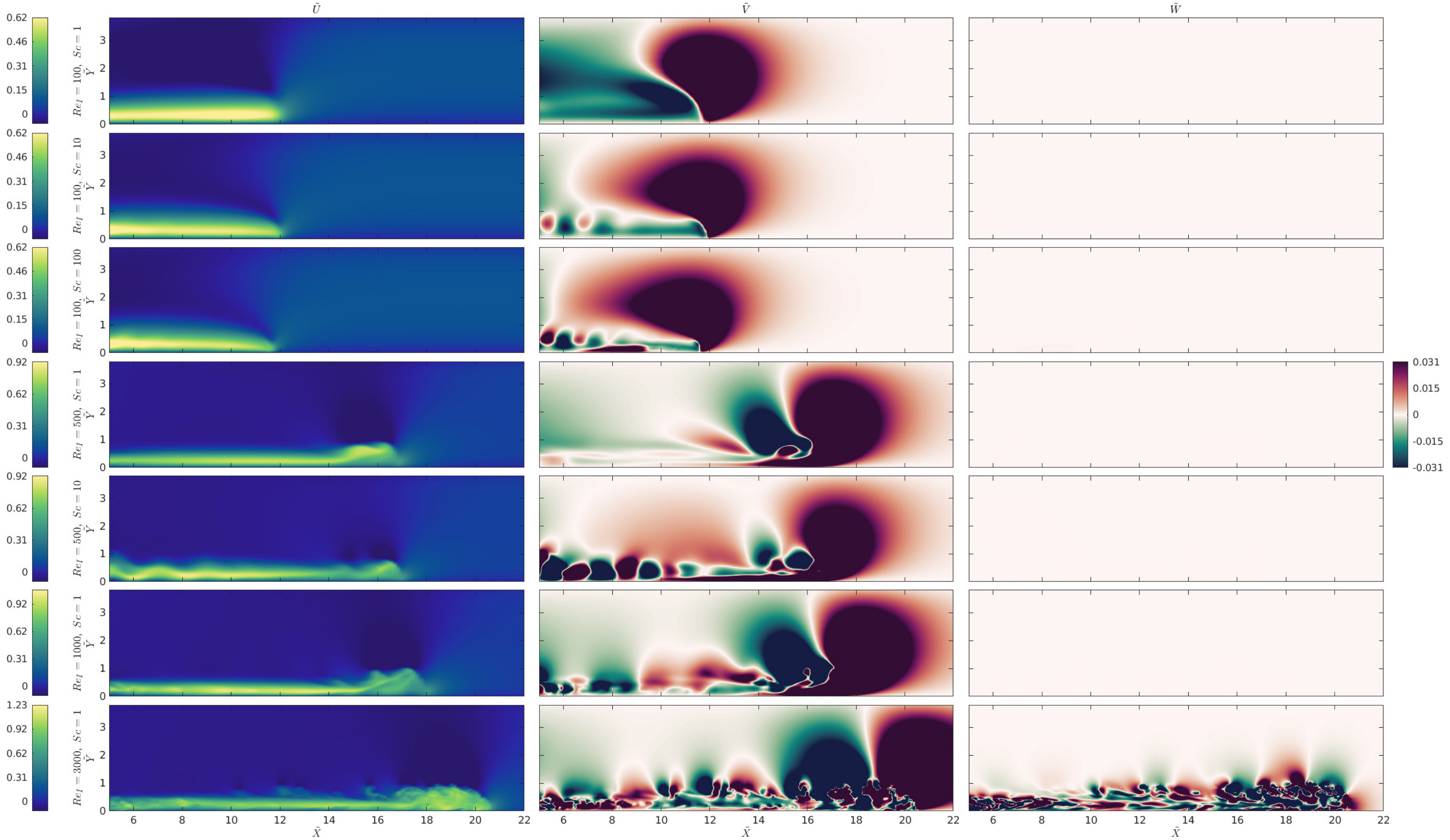

Figure 6.8: (left) Downstream, (centre) vertical, and (right) cross-stream velocity for each case at $\tilde{t} = 23.4$ on an $\tilde{X} - \tilde{Y}$ slice at a central cross-stream location ($\tilde{Z} = 0$).

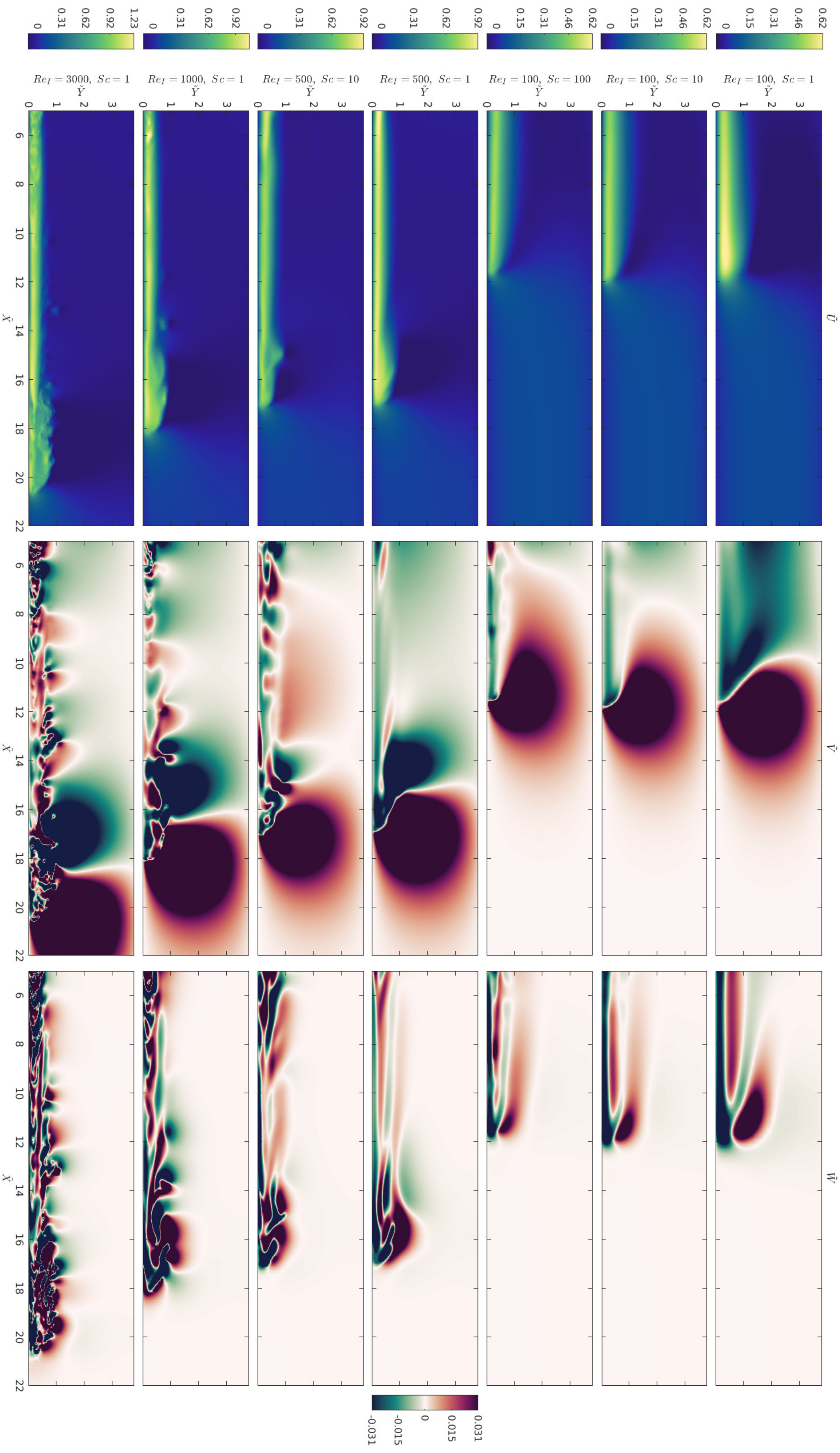

Figure 6.9: (left) Downstream, (centre) vertical, and (right) cross-stream velocity for each case at $\tilde{t} = 23.4$ on an $\tilde{X} - \tilde{Y}$ slice at an off-centre cross-stream location ($\tilde{Z} = 0.5$).

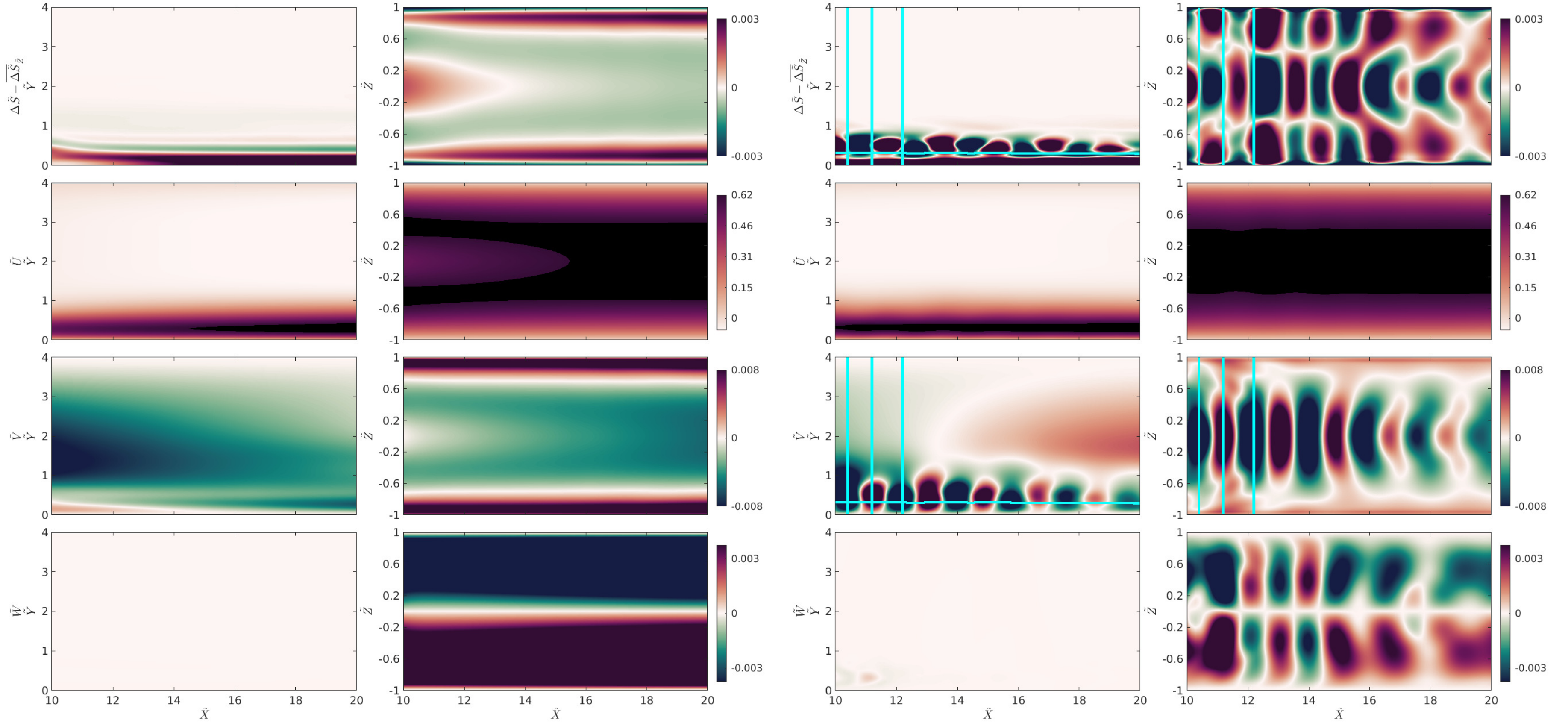

(a)

(b)

Figure 6.10: Comparison of the cases with (a) $(Re_I, Sc) = (500, 1)$ and (b) $(Re_I, Sc) = (500, 10)$ at $\tilde{t} = 66.3$ on (left) a central cross-stream plane and (right) a plane perpendicular to the lower boundary at $\tilde{Y} = 0.35$. From top to bottom, the plots are excess density fluctuations from the cross-stream average value (where the cross-stream average excess density is denoted by $\overline{\Delta\tilde{S}}_{\tilde{Z}}$), and downstream, vertical, and cross-stream velocities. The horizontal lines indicate the height of the downstream velocity maximum, and vertical lines show the approximate downstream locations of $\Delta\tilde{S} - \overline{\Delta\tilde{S}}_{\tilde{Z}} = 0$.

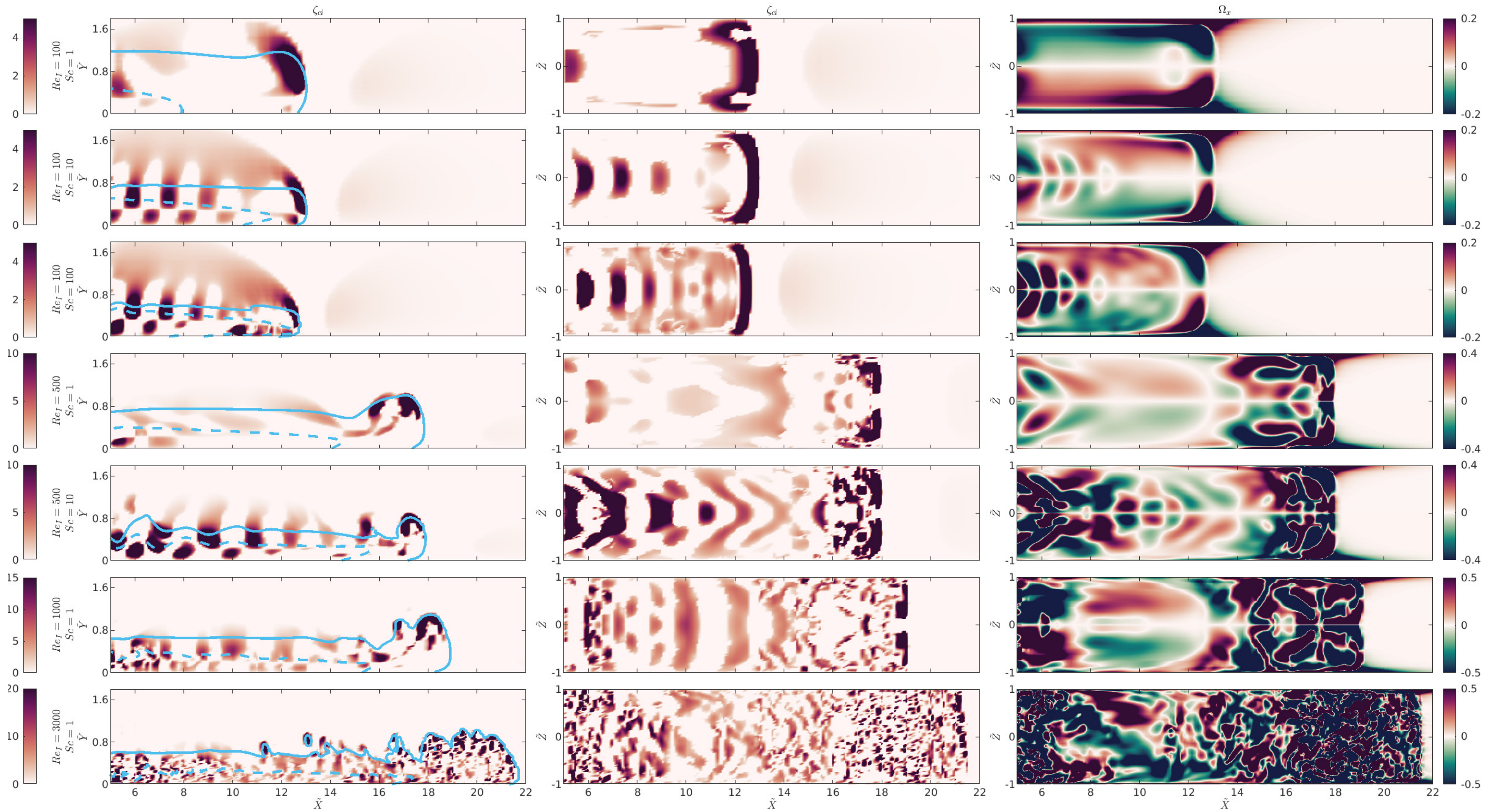

Figure 6.11: Pseudocolour plots of (left, centre) swirling strength and (right) the $\tilde{X}$ component of vorticity at $\tilde{t} = 23.4$ for each DNS case (left) on an $\tilde{X} - \tilde{Y}$ plane at a central cross-stream location, and (centre, right) on an $\tilde{X} - \tilde{Z}$ plane at $\tilde{Y} = 0.5$. The blue lines illustrate the (solid) $\Delta\tilde{S} = 0.03$ and (dashed) $\Delta\tilde{S} = 0.48$ excess density contours.

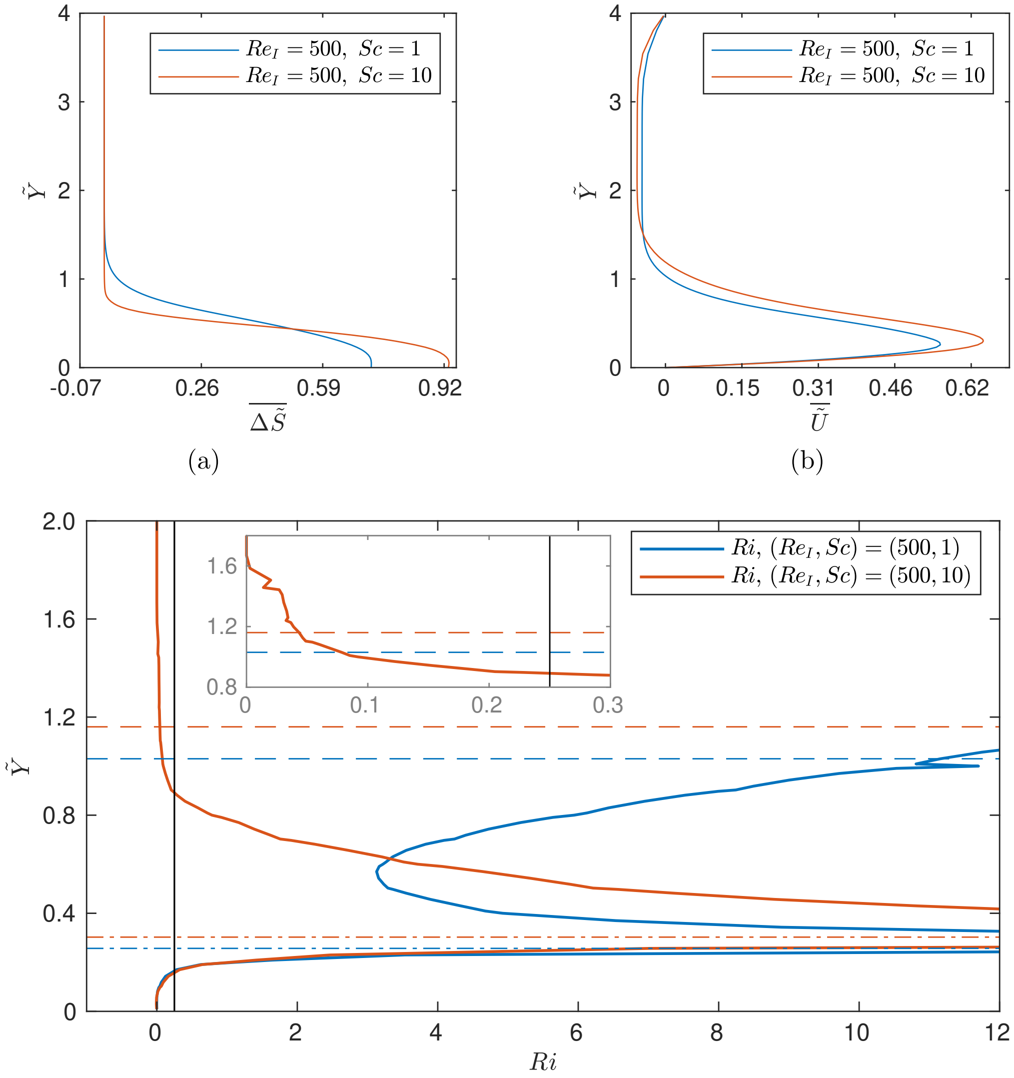

(a)

(b)

(c)

Figure 6.12: Comparison of (a) excess density and (b) downstream velocity averaged over downstream locations at the timestep illustrated in Figure 6.10, and (c) Ri profile for the cases with $(Re_I, Sc) = (500, 1)$ and $(500, 10)$ based on the excess density and velocity profiles shown in (a) and (b). The horizontal lines show (dashed) the height of the current based on where the average downstream velocity profile changes from positive to negative, and (dot-dash) the average height of the maximum downstream velocity, and the vertical line indicates the critical value of $Ri = 0.25$. The insert shows a magnified view of the high Schmidt number case plot near the upper interface, illustrating where flow Ri moves from above to below the critical value.

depending on flow Reynolds number, give a misleading impression of the overall flow particularly in terms of the cross-stream velocity (Figures 6.7, 6.8, and 6.9). For most cases, $\tilde{W}$ was found to be 0 on the central cross-stream plane but elsewhere the magnitude of cross-stream velocity was equivalent to that of vertical velocity suggesting that the flow is not two-dimensional as often assumed (Meiburg *et al.*, 2015; Simpson, 1997).

6.4.1 The Effect of Reynolds and Schmidt Numbers on Flow in the Head

Figure 6.3 and Table 6.3 show that increasing either Schmidt or Reynolds number results in a more defined head, with a forward angled depression in the density contour behind the head. The head height, based on the $\Delta\tilde{S} = 0.03$ density contour, decreases slightly from $\tilde{Y} \approx 1.2$ at $Re_I = 100$ to $\tilde{Y} \approx 1$ at $Re_I = 500$ with no further decrease when Reynolds number is increased further. Increasing Schmidt number does consistently reduce the head height, with a more significant change at lower Reynolds number and when Schmidt number is increased from 1 to 10 compared with 10 to 100. The difference between the right-most positions of the $\Delta\tilde{S} = 0.03$ and $\Delta\tilde{S} = 0.48$ contours as a proportion of current front position decreases with both increased Reynolds and Schmidt numbers, indicating that dense fluid is reaching closer to the front of the flow. In the $(Re_I,\ Sc) = (100,\ 100)$ case, the $\Delta\tilde{S} = 0.48$ contour reaches the front of the flow, suggesting that a further increase in Schmidt number would likely have little impact.

The lobe-and-cleft structures resulting from the over-running of ambient fluid by the current front are present in some cases but not others (Figure 6.6). As lobe-and-cleft structures are associated with some of the largest bed shear stresses (Meiburg & Kneller, 2010; Necker *et al.*, 2002), and changes in rates of mixing (Simpson & Britter, 1979), accurately capturing this feature is important to understanding the flow structure. While the $(Re_I, Sc) = (100, 1)$, $(100, 10)$ and $(500, 1)$ cases do not exhibit over-running of ambient fluid, the $(Re_I, Sc) = (100, 100)$ and $(500, 10)$ cases do. Therefore, for Reynolds numbers $\mathcal{O}(100)$ the presence of lobes-and-clefts in the current head is dependent on the Schmidt number (with Figure 6.13b showing the phase space where these structures are found in this work). This conflicts with the findings of Bonometti & Balachandar (2008), who suggest that lobe-and-cleft structures are not Schmidt number dependent. However, varying Schmidt number here was only possible at Reynolds numbers sufficiently low that these structures were not already present at $Sc = 1$. As over-running of ambient fluid is observed in the $(Re_I, Sc) = (3000, 1)$ case (Figure 6.6), providing the Reynolds number of the flow is sufficiently high this flow feature may be captured without increasing Schmidt number above 1.

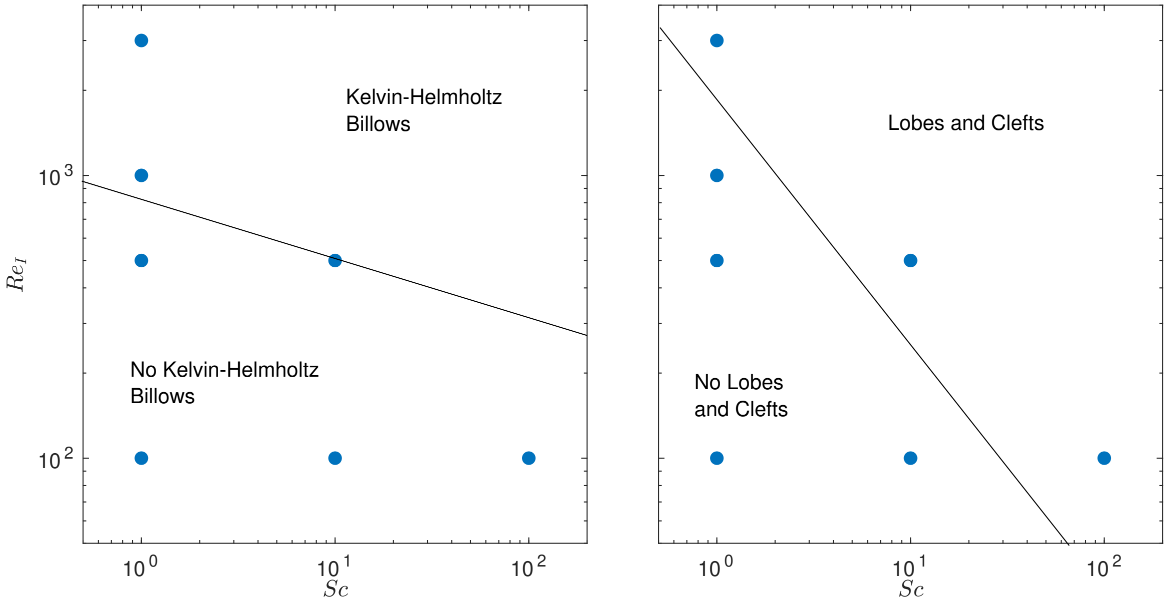

(a) (b)

Figure 6.13: Scatter plots showing the Schmidt and Reynolds numbers where (a) Kelvin-Helmholtz structures, and (b) lobe-and-cleft structures are present.

6.4.2 The Effect of Reynolds and Schmidt Numbers on Flow Behind the Head

Considering flow behind the head, current height decreases with both Reynolds and Schmidt numbers (Figure 6.3 and Table 6.3). However, the height of the $\Delta\tilde{S} = 0.48$ contour seems to be relatively consistent regardless of the Reynolds and Schmidt number of the flow. Increasing Reynolds number from $Re_I = 100$ to $Re_I = 500$ leads to a smaller percentage decrease in current height as Schmidt number is increased. At the Reynolds and Schmidt number range considered in this work, the percentage change in thickness of the mixed layer of fluid behind the head as Schmidt number is increased from 1 to 10 is equivalent in both $Re_I = 100$ and $Re_I = 500$ cases. A further increase from $Sc = 10$ to $Sc = 100$, however, results in a smaller change. Increasing Reynolds number was found to have a more complex effect on mixed layer thickness, with the percentage of flow height taken up by the mixed layer initially decreasing and then increasing when $Re_I = 3000$. This may be a result of increased mixing from the Kelvin-Helmholtz structures (visible in Figure 6.5) that begin to form as Re_I increases. Close examination of the density contours in Figure 6.3 and the isosurfaces in Figure 6.5 indicates that the Kelvin-Helmholtz structures may be emerging in the $(Re_I, Sc) = (500, 10)$ case (but not the $(Re_I, Sc) = (500, 1)$ case). This suggests that increasing Schmidt number may reduce flow stability.

Several changes resulting from increased Schmidt number have been noted in the data from this chapter. In many cases, the impact of increasing Schmidt number beyond one is either reduced by increasing Reynolds number (for example the change in current height), or the same changes are observed with increased Reynolds number (for example the presence of lobes-and-clefts). There are, however, features that are not captured if $Sc = 1$ is assumed. In particular, increasing Schmidt number is related to the formation of structures at the current-ambient interface behind the head. This can be seen in several of the plots presented, for example the waviness in the density contours (Figure 6.3), in the velocity plots (Figures 6.7 and 6.8), and in the swirling strength plots (Figure 6.11), in which wave-like distortions in the density contours correlate with peaks in swirling strength.

All cases with $Sc > 1$ exhibit the formation of structures on the current-ambient interface behind the head that are not diminished as distance from the head increases (Figure 6.11). This appears to be a distinct mechanism from the formation of Kelvin-Helmholtz vortices, the influence of which decreases with distance from the head in this data, and which are present in some cases with $Sc = 1$ (see Figure 6.13a). The vorticity plots in Figure 6.11 indicate that these structures are associated with three-dimensional motions. The velocity and density perturbations associated with these structures (Figure 6.10) have correlated patterns of alternating positive and negative regions, with the $1/4-$wavelength offset characteristic of internal gravity waves (García-Villalba & del Álamo, 2011). The formation of these waves is a result of the decrease in mass diffusivity sharpening the density profile, leading to a change in the stability of the interface. This stability can be quantified by a decrease in gradient Richardson number in the upper part of the flow. In all cases with $Sc = 1$, even those with Kelvin-Helmholtz structures behind the head, the gradient Richardson number in the upper part of the flow is above the critical value. As discussed by Pelmard *et al.* (2020), a gradient Richardson number below 0.25 in the head may lead to the formation of Kelvin-Helmholtz structures that then dissipate some distance behind the head if the value rises above the critical level in the body. Therefore the current-ambient interface in the body may be stable even with the presence of Kelvin-Helmholtz structures near the head.

All cases with $Sc > 1$ have $Ri < 0.25$ in the upper part of the flow, suggesting that density stratification is no longer stable enough to dissipate the energy generated through shear. Crucially, unlike other characteristics, it does not appear to be the case that this effect of increased Schmidt number is diminished by increased Reynolds number in the range considered here. The perturbations in density field are at least as prominent in the $Re_I = 500$ case as in the $Re_I = 100$ cases (Figure 6.3). The effect is also not captured purely by increasing Reynolds number in the range considered in this work. While peaks in swirling strength are found in the $Re_I = 1000, 3000$ cases, they are missing the regularity of those in the higher Sc cases and are not limited to the centre in the cross-stream direction, supporting the suggestion that this is a separate mechanism to those seen with increased Reynolds number.

Examining the velocity and swirling strength plots from Chapter 5 (Figure 5.11), the structure of the motions in the experimental cases has more in common with the higher Schmidt number cases than the lower Schmidt number cases. In both the experimental data and the high Schmidt number numerical data, the motions have a regularity and central cross-stream location. This contrasts with the low Schmidt number cases where the motions are concentrated towards the side-walls. A Schmidt number of 1 is often assumed when performing numerical investigations of gravity current flows. This is largely a result of the rapidly escalating computational cost of DNS, which scales with Re^3Sc^2 (see Chapter 3). The work in this chapter suggests that assuming a Schmidt number of 1 in numerical investigations leads to substantial structural differences compared with higher Schmidt number experimental flows.

When computational resources are limited, deciding whether to prioritise increasing Schmidt or Reynolds number is a complex issue dependent on several factors. There may be no benefit to prioritising Schmidt number at the expense of Reynolds number if data analysis will focus on parameters that are not Schmidt number dependent (such as front velocity), or that are also seen with increased Reynolds number (such as the formation of lobe-and-cleft structures). However, for low Reynolds number flows it is recommended to have Schmidt number sufficiently large that the gradient Richardson number is below the critical value of 0.25. The importance of considering Schmidt number may also depend on flow type, for example the data presented in this work suggests that Schmidt number impact may be greater in a more viscous flow (such as transitional flows).

6.4.3 Application to Real-World Transitional Flows

In this work, Reynolds number was varied by changing the fluid viscosity. As a result of computational cost restrictions, the cases considering the effect of Schmidt number had significantly higher viscosity than the experimental fluids. The $Re_I = 500$ and $Re_I = 100$ cases have viscosity ~ 6 and ~ 30 times that of the fluids used in Chapters 4 and 5, equivalent to that in flows with $\sim 10\%$ to $\sim 50\%$ by volume clay (Amy *et al.*, 2005). Therefore, it may be that the effects of increasing Schmidt number (such as the formation of lobe-and-cleft structures, and structures within the body) are more pronounced in higher viscosity flows. When investigating flows such as real-world transitional flows (defined as flows with behaviour that is transitional between laminar and turbulent states), which typically have $\sim 15\%$ by volume clay (Amy *et al.*, 2005; Peakall *et al.*, 2020), it may therefore be particularly important to consider the effect of Schmidt number. Given the computational costs involved, this may at first seem insurmountable. However, in the data presented in this work, even at $Re_I = 100$ the changes resulting from further increasing Schmidt number from 10 to 100 are largely quantitative rather than qualitative. Therefore, even when investigating a Schmidt number dependent feature of a high Schmidt number flow some concessions to computational cost are likely justified.

6.5 Conclusions

Many numerical investigations of gravity current flows have sought to mitigate the high computational cost of three-dimensional direct numerical simulation (scaling like Re^3Sc^2) by claiming the effect of increasing Schmidt number from 1 is negligible. However, the justifiability of this assumption has been questionable given the lack of understanding regarding the effect of Schmidt number on three-dimensional flow features. In this work, the effects of Reynolds and Schmidt number on constant-influx solute-based gravity current flow structure have been investigated through three-dimensional direct numerical simulation performed using the spectral element solver Nek5000. These results have been used to draw conclusions regarding when a $Sc = 1$ assumption is justified.

The importance of considering Schmidt number is dependent on the flow property of interest, and on the flow itself. Some flow features appear to be independent of Schmidt number (for example current front velocity). Additionally, some of the effects of increased Schmidt number also occur with increased Reynolds number (such as the appearance of lobe-and-cleft structures in the head) or are reduced by increased Reynolds number (such as the change in current height). A notable exception is the reduction in gradient Richardson number.

In flows with $Re_I = 100,\ 500$, increasing Schmidt number from 1 to 10 was found to reduce the gradient Richardson number in the body of the flow from above to below the critical value, resulting in the presence of structures in the mixed layer. When moving from $Re_I = 100$ to $Re_I = 500$, this effect of increased Schmidt number was not reduced. Further, equivalent structures were not apparent in the $Re_I = 3000$ case, suggesting that this feature may not be captured purely by increasing Reynolds number. When considering the structure of the gravity current body in a high Schmidt number flow, assuming $Sc = 1$ may therefore lead to qualitative changes in flow structure. This may be particularly true in higher viscosity cases (such as clay-based transitional flows), though further work considering the impact of Reynolds number on such flows is needed. Even at $Re_I = 100$ the effect of increasing Schmidt number from 10 to 100 was quantitative rather than qualitative, and therefore the structure of solute-based flows ($Sc = \mathcal{O}(1000)$) can likely be captured with the comparatively minor cost of a small increase in Schmidt number rather than the large cost of matching Schmidt number exactly.

Chapter 7

Synthesis

In previous chapters, the turbulence structure of constant-influx, solute-based, gravity current flows has been quantified using data generated through Particle Image Velocimetry (PIV), Shake-the-Box Particle Tracking Velocimetry (STB), and Direct Numerical Simulation (DNS). Instantaneous whole-field velocity measurements have been used to identify internal gravity waves and a critical layer within the gravity current body in Chapter 4. Instantaneous three-dimensional whole-field velocity measurements have been presented in Chapter 5, demonstrating that vertical and cross-stream motions are equivalent in magnitude within the body, and that the identified internal waves are sometimes associated with three-dimensional motions. While a Schmidt number of 1 is typically assumed in numerical gravity current research, in Chapter 6 it has been shown that for a range of Reynolds numbers increasing Schmidt number beyond this value results in the formation of lobe-and-cleft structures within the head and structures in the mixed layer behind the head. This final chapter will bring together these strands of work, establish their comparability, and suggest possible directions for future research.

7.1 Comparison of Averaged Quantities

To establish the comparability of the three data sets, two of the DNS cases described in Chapter 6 have been extended to allow inspection of 10 s of body flow – $(Re_I, Sc) = (1000, 1)$ and $(Re_I, Sc) = (3000, 1)$. The $Re_I = 3000$ case has viscosity equivalent to that in the experimental work, but this viscosity is increased to lower the Reynolds number in the $Re_I = 1000$ case. To demonstrate that only body data is being considered, spatial and temporal averages of downstream velocity and density at a central cross-stream location over a range of time frames (from 1 s to 10 s from the beginning of the data) are shown in Figures 7.1 and 7.2. As all averages are consistent, the measurements included are from body flow.

Having identified the body flow data, downstream velocity profiles may be plotted for each case (both dimensional, Figure 7.3a, and non-dimensional, Figure 7.3b). In order

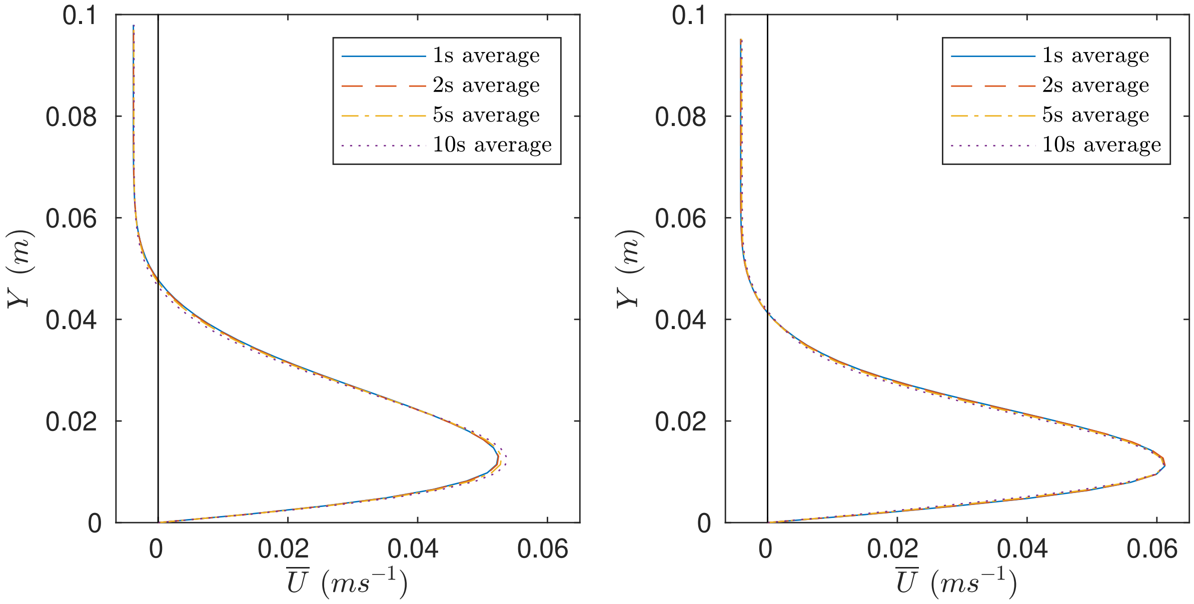

(a) (b)

Figure 7.1: Downstream velocity averaged over downstream locations and time for (a) $(Re_I, Sc) = (1000, 1)$ and (b) $(Re_I, Sc) = (3000, 1)$ over 1 s to 10 s from the beginning of the data.

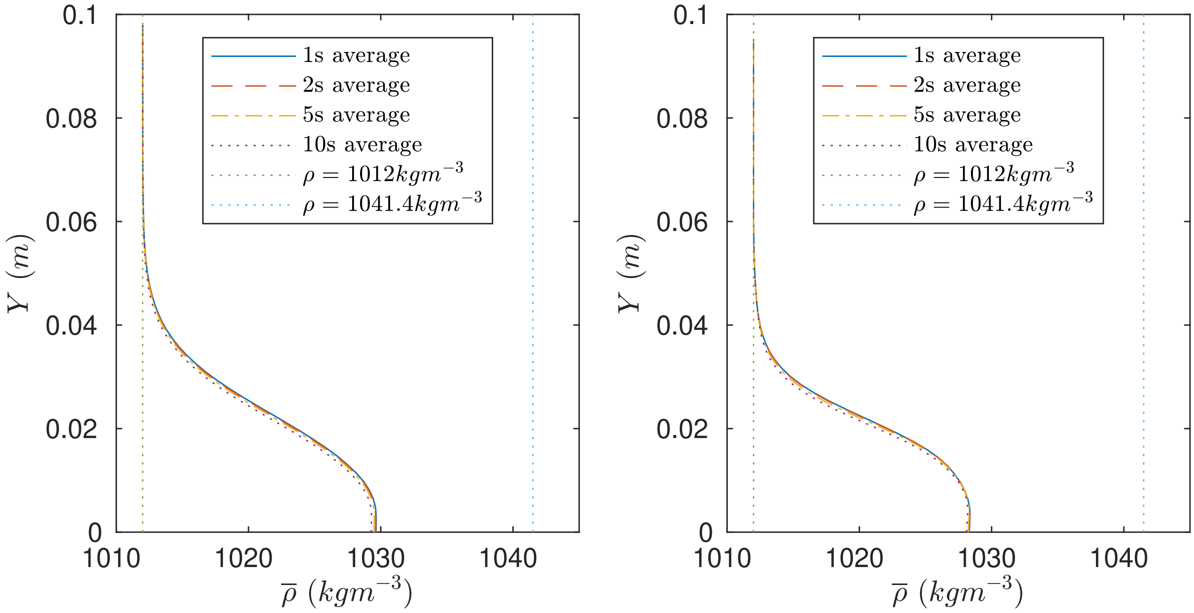

(a) (b)

Figure 7.2: Density averaged over downstream locations and time for (a) $(Re_I, Sc) = (1000, 1)$ and (b) $(Re_I, Sc) = (3000, 1)$ over 1 s to 10 s from the beginning of the data. The vertical lines show the densities of the ambient ($\rho = 1012\,\mathrm{kg\,m^{-3}}$) and current ($\rho = 1041.4\,\mathrm{kg\,m^{-3}}$) fluids.

to make all three data sets (PIV, STB, DNS) comparable, a new non-dimensionalisation is defined for the DNS cases to match the laboratory-based data. The non-dimensionalisation of vertical position is achieved by subtracting the average height of the velocity maximum from vertical location and dividing by some characteristic length scale (here the Ellison and Turner integral length scale (Ellison & Turner, 1959)). Velocity is non-

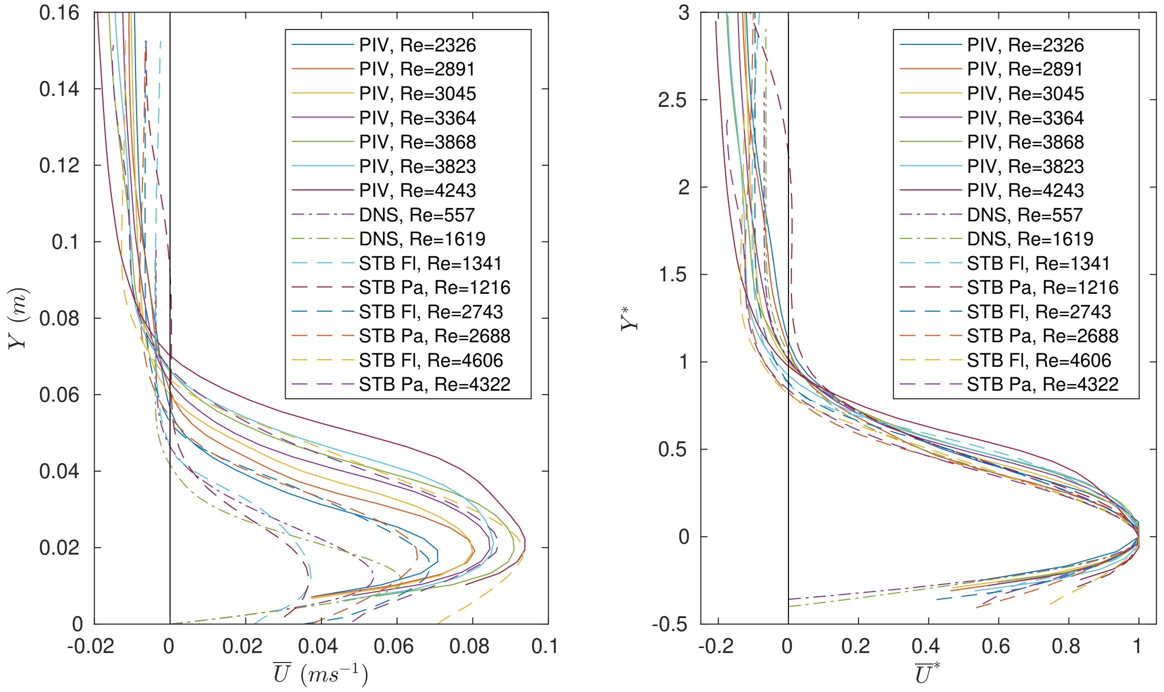

(a) (b)

Figure 7.3: (a) Dimensional and (b) non-dimensional average downstream velocity profile at a central cross-stream location for each PIV, STB (using both polyamide, Pa, and fluorescent polyethylene, Fl, seeding particles), and DNS case.

dimensionalised through dividing by a characteristic velocity scale (here the maximum average downstream velocity), i.e.

$$\begin{aligned} \boldsymbol{U}^* &= \boldsymbol{U}/\overline{U}_{max}, \\ Y^* &= (Y - Y_{U_{max}})/L_c, \\ L_c &= \frac{\left(\int \overline{\overline{U}} dY\right)^2}{\int \overline{\overline{U}}^2 dY}, \end{aligned} \tag{7.1}$$

where $\overline{\overline{U}}$ is the mean velocity relative to that in the ambient. In all cases, across all data collection techniques, this collapses the average downstream velocity data to a set of profiles with height $Y^* \approx 1$. The positive flow in the ambient in the $Re = 1216$ STB case (Chapter 5) is unexpected, and is likely a result of an experimental error (such as an air valve being slightly open).

A new output Reynolds number (Re) is calculated for each DNS case to be comparable to those of the laboratory-based flows presented in Chapters 4 and 5, based on the Ellison and Turner integral length scale and the maximum average downstream velocity within the flow (shown in Table 7.1). By plotting parameters such as maximum average downstream velocity, the Ellison and Turner length scale, the height of the velocity maximum, and the height of the current as a function of this Reynolds number, the flows

Technique	Q (L s^{-1})	L_c (m)	U_c (m s^{-1})	ν (kg m^{-3})	Sc	Re	Fr_D
PIV	0.072	0.0358	0.0707	1.09×10^{-6}	$\mathcal{O}(1000)$	2326	0.69
PIV	0.090	0.0390	0.0806	1.09×10^{-6}	$\mathcal{O}(1000)$	2891	0.75
PIV	0.107	0.0415	0.0799	1.09×10^{-6}	$\mathcal{O}(1000)$	3045	0.72
PIV	0.125	0.0433	0.0845	1.09×10^{-6}	$\mathcal{O}(1000)$	3364	0.75
PIV	0.142	0.0463	0.0909	1.09×10^{-6}	$\mathcal{O}(1000)$	3868	0.78
PIV	0.160	0.0487	0.0855	1.09×10^{-6}	$\mathcal{O}(1000)$	3823	0.71
PIV	0.177	0.0491	0.0938	1.09×10^{-6}	$\mathcal{O}(1000)$	4234	0.78
DNS	0.072	0.0337	0.0538	3.26×10^{-6}	1	557	0.54
DNS	0.072	0.0288	0.0613	1.09×10^{-6}	1	1619	0.67
STB Fl	0.032	0.0393	0.0372	1.09×10^{-6}	$\mathcal{O}(1000)$	1346	0.35
STB Pa	0.032	0.0362	0.0366	1.09×10^{-6}	$\mathcal{O}(1000)$	1219	0.36
STB Fl	0.082	0.0434	0.0689	1.09×10^{-6}	$\mathcal{O}(1000)$	2749	0.61
STB Pa	0.082	0.0448	0.0654	1.09×10^{-6}	$\mathcal{O}(1000)$	2691	0.57
STB Fl	0.148	0.0537	0.0933	1.09×10^{-6}	$\mathcal{O}(1000)$	4606	0.74
STB Pa	0.148	0.0541	0.0869	1.09×10^{-6}	$\mathcal{O}(1000)$	4322	0.69

Table 7.1: Details of the influx, characteristic length scale (here, the Ellison and Turner integral scale), L_c, characteristic velocity scale (here, the maximum average downstream velocity), U_c, kinematic viscosity of the fluid, ν, Schmidt number, Sc, and corresponding Reynolds, $Re = U_c L_c / \nu$, and densimetric Froude, $Fr_D = U_c / \sqrt{g' L_c}$, numbers for each case.

can be directly compared as in Figure 7.4. All cases with the same viscosity follow the same trends in these parameters with increasing Reynolds number. Discrepancies, such as the lower current height in the highest Reynolds number STB case or the larger characteristic length scale in the lower Reynolds number STB cases, are attributable to small variations in experimental parameters such as temperature differences causing variation in fluid density between cases. The higher viscosity DNS case is taller than expected based on the other data sets, with the velocity maximum higher in the flow.

7.2 Comparison of Instantaneous Data

The instantaneous velocity field from equivalent slices of the STB, DNS, and PIV data can be compared directly. Figure 7.5 shows instantaneous velocity components at a central cross-stream and downstream location over time. In all cases, downstream velocity has the same structure. The $Re = 2749$ STB case and the $Re = 2891$ PIV case have similar vertical velocity structure, with alternating regions of positive and negative vertical velocity at $Y^* = 0$, with similar magnitude between the two cases. There are also similarities in vertical velocity structure between the $Re = 4234$ PIV and $Re = 4606$ STB cases. In both cases, below $Y^* = 0$ are small regions of alternating positive/negative vertical velocity, with much larger alternating regions above. Again, the velocity magnitude is similar for these two cases. Therefore, the STB and PIV velocity data show both similar structure and similar structural changes with increased Reynolds number.

While the DNS data has some similarities, there are also significant differences. In

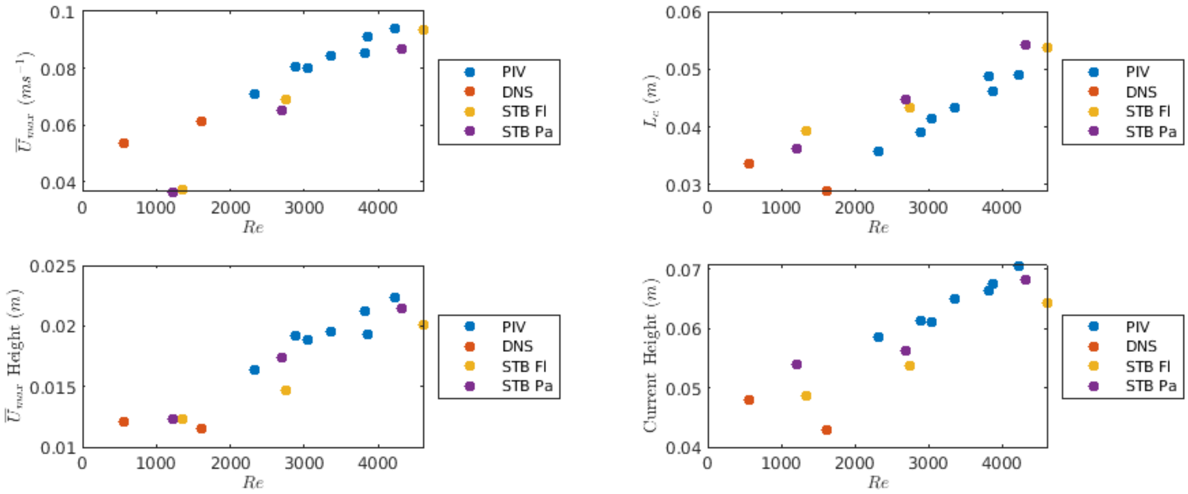

Figure 7.4: Plots of (top left) maximum average downstream velocity, (top right) characteristic length scale, (bottom left) height of the average velocity maximum, and (bottom right) current height defined as the point where average downstream velocity changes from positive to negative for each case against Reynolds number.

Figure 7.5, the vertical velocities in the $Re = 1346$ STB case and the $Re = 1619$ DNS case both have a solid line of constant velocity at $Y^* = 1$ and have similar velocity magnitude. However, the DNS case also has a solid line of constant vertical velocity at the base of the flow. While cross-stream velocity on the $X - Y$ plane in the $Re = 557$ DNS case has little resemblance to the other flows, in the $Re = 1619$ DNS case there is a solid line at $Y^* = 1$ and alternating positive and negative regions at $Y^* = 0$ as seen in the higher Reynolds number STB flows.

Figure 7.6 shows instantaneous data from the cases with volumetric measurement at a central downstream location at $Y^* = 0$ over time. Again, the downstream velocity is similar across all cases. However, these plots make the structural differences between the STB and DNS cases more apparent. While the STB cases have alternating regions of positive and negative vertical velocity (whether full-width, centred in the cross-stream direction, or smaller regions distributed throughout the domain width), the DNS cases have regions of positive vertical velocity concentrated at the side-walls and negative velocity throughout the remaining width.

Discrepancies are also evident in the cross-stream velocity plots in Figure 7.6. The $Re = 1346$ STB case has a cross-stream central divide, with positive cross-stream velocity in one half of the domain and negative in the other. The DNS cases have a different structure. While positive and negative cross-stream velocities are still largely split between the two sides, in the $Re = 557$ DNS case there are perturbations in the central division. These perturbations increase to form alternating regions of positive/negative cross-stream velocity in the $Z^* = 0$ line by the $Re = 1619$ DNS case. The structure of cross-stream velocity in the $Re = 1619$ DNS case is closer to that of the $Re = 4606$ STB case, though the vertical velocity structure is different. Therefore, there are significant

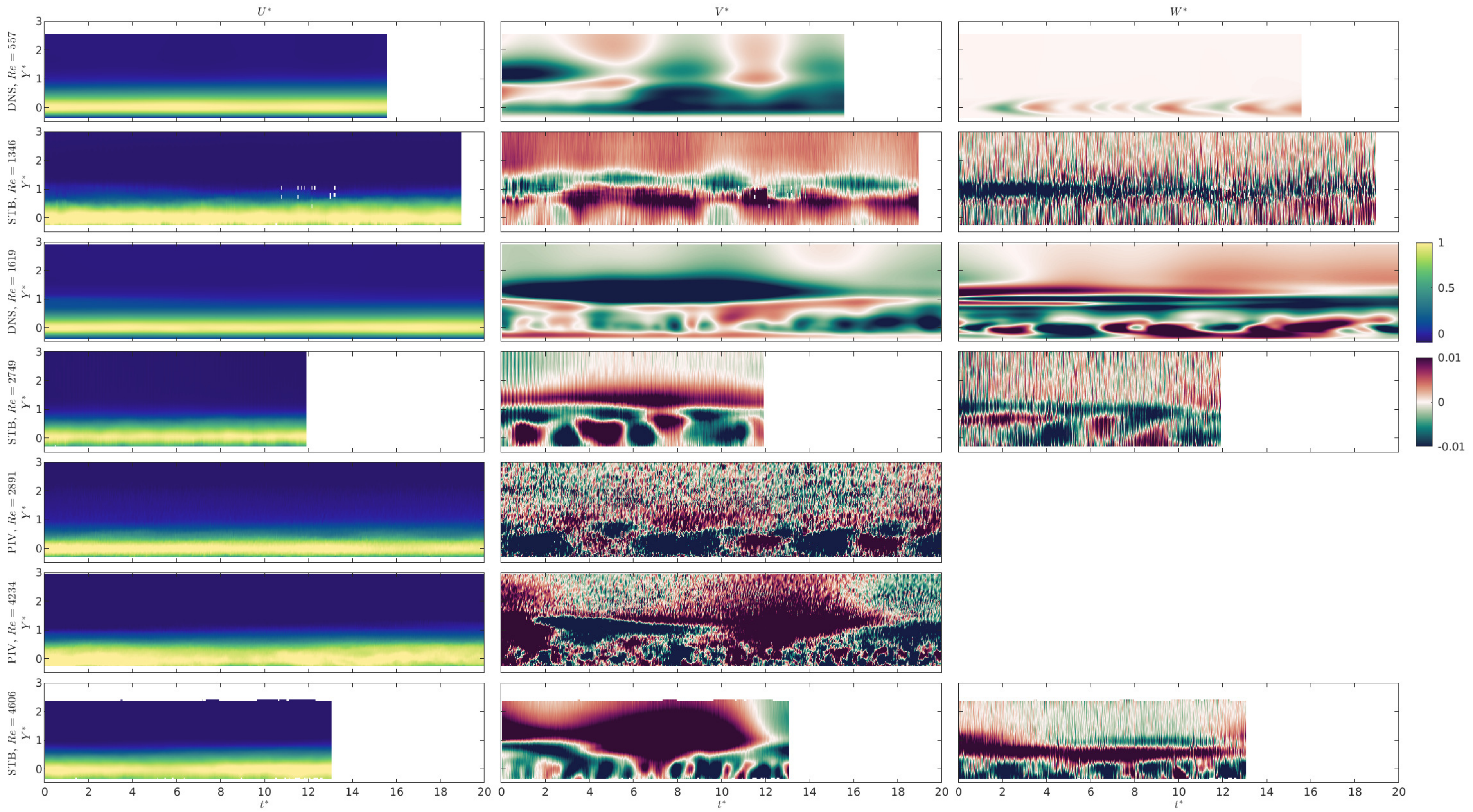

Figure 7.5: Dimensionless (left) downstream, (centre) vertical, and (right) cross-stream velocity over time for (top to bottom) $(Re, Sc) = (557, 1)$ DNS, $(1346, \mathcal{O}(1000))$ STB, $(Re, Sc) = (1619, 1)$ DNS, $(2749, \mathcal{O}(1000))$ STB, $(2891, \mathcal{O}(1000))$ PIV, $(4234, \mathcal{O}(1000))$ PIV, $(4606, \mathcal{O}(1000))$ STB, taken from a central downstream and cross-stream location ($X^* \approx 3$, $Z^* = 0$).

structural differences in vertical and cross-stream velocity between the DNS and the STB data.

7.3 Comparison of Frequency Analyses

Frequency analysis can be used to examine the mechanisms leading to these structural differences, in particular Fourier transform over time and dynamic mode decomposition. Figure 7.7 shows the Fourier transform of the velocity data for the DNS cases. In both cases, the dominant frequencies in vertical velocity are concentrated towards the side-walls in the lower part of the domain, though the range of dominant frequencies is greater for the $Re = 1619$ case. For the $Re = 557$ case, the frequencies of cross-stream velocity with highest amplitude are either side of the velocity maximum, while in the $Re = 1619$ case the dominant frequencies are centred in the cross-stream direction. In contrast, Figure 7.8 shows the Fourier transform over time of the velocity data for the $Re = 2743$ STB case. Here, the dominant frequencies are again concentrated at the height of the velocity maximum, but are centred in the cross-stream direction with little contribution from cross-stream velocity. While the $Re = 1346$ STB case is closer in Reynolds number to the DNS cases, the $Re = 2743$ case was chosen for frequency analysis comparison because of the low level of missing data points (whereas the $Re = 1346$ STB case has more experimental noise, particularly in the cross-stream velocity measurements, and has several regions of missing data, possibly as a result of less evenly distributed seeding or greater differences in refractive index).

As in Chapter 4, the same timestep range is used for the Fourier transform and dynamic mode decomposition, and all velocity components and time steps are combined into a single matrix such that dynamic mode decomposition is applied to all data simultaneously. Singular value decomposition is carried out using the MATLAB `svd` function with the ‘econ’ parameter (MATLAB, 2020). The amplitudes of each of the modes identified through dynamic mode decomposition for the two DNS cases are shown in Figure 7.9. The identified modes with significant amplitude, which correspond with peaks in the Fourier transform plots, are shown in Figures 7.10 and 7.11. As indicated by the Fourier transforms, the structure of the modes is similar in both cases, with alternating regions of vertical velocity near the side-walls that connect in the centre in a U or V shape. The cross-stream velocity structure of the modes is similar to the vertical, though the largest magnitudes are in the cross-stream centre of the flow rather than close to the side-walls. In contrast, the example mode from the $Re = 2743$ STB case (Figure 7.12) has vertical velocity centred in the cross-stream direction and alternating regions of positive and negative cross-stream velocity either side of the central cross-stream position.

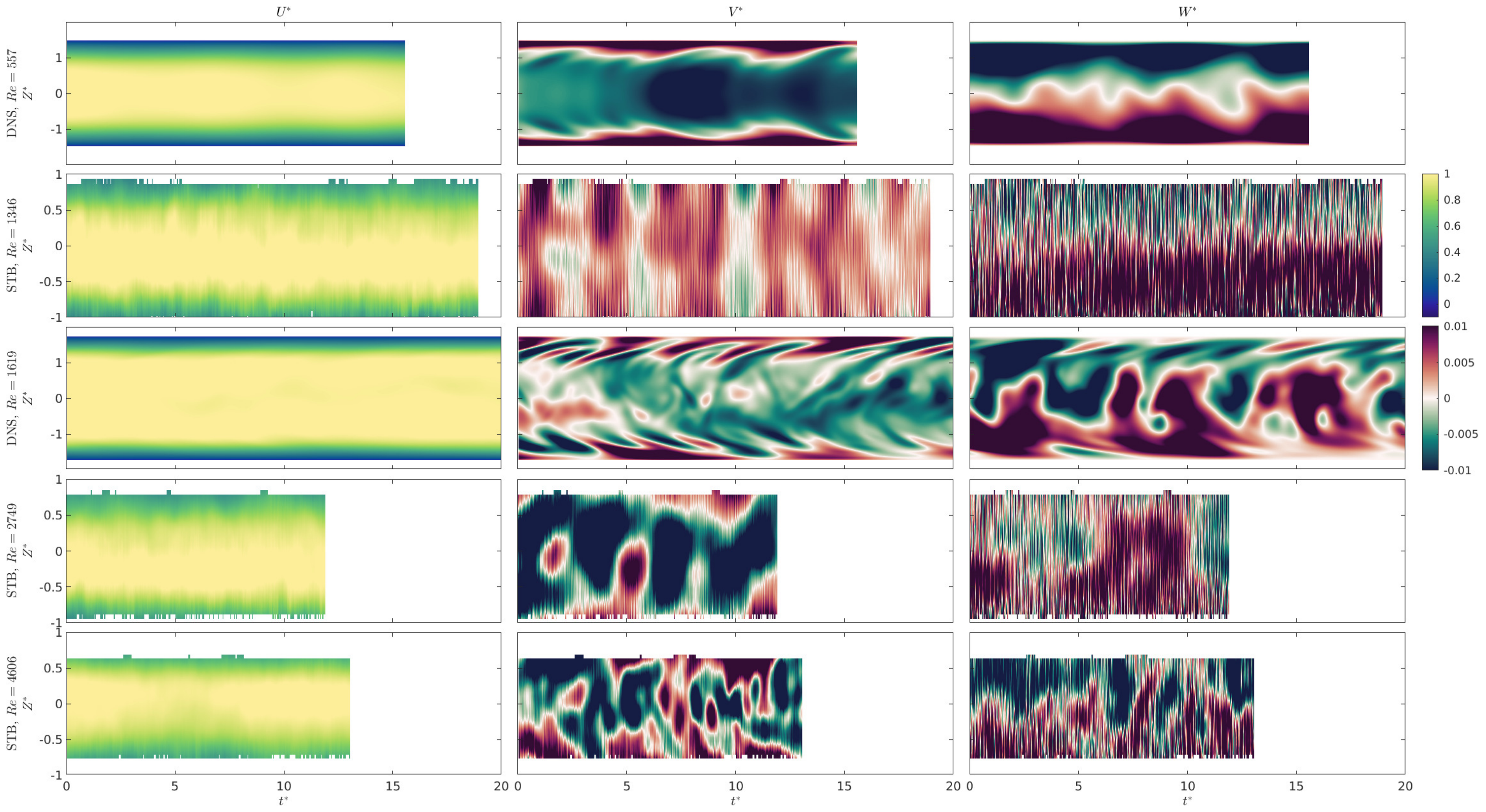

Figure 7.6: Dimensionless (left) downstream, (centre) vertical, and (right) cross-stream velocity over time for (top to bottom) $(Re, Sc) = (557, 1)$ DNS, $(1346, \mathcal{O}(1000))$ STB, $(Re, Sc) = (1619, 1)$ DNS, $(2749, \mathcal{O}(1000))$ STB, $(4606, \mathcal{O}(1000))$ STB, taken from a central downstream location at $Y^* = 0$.

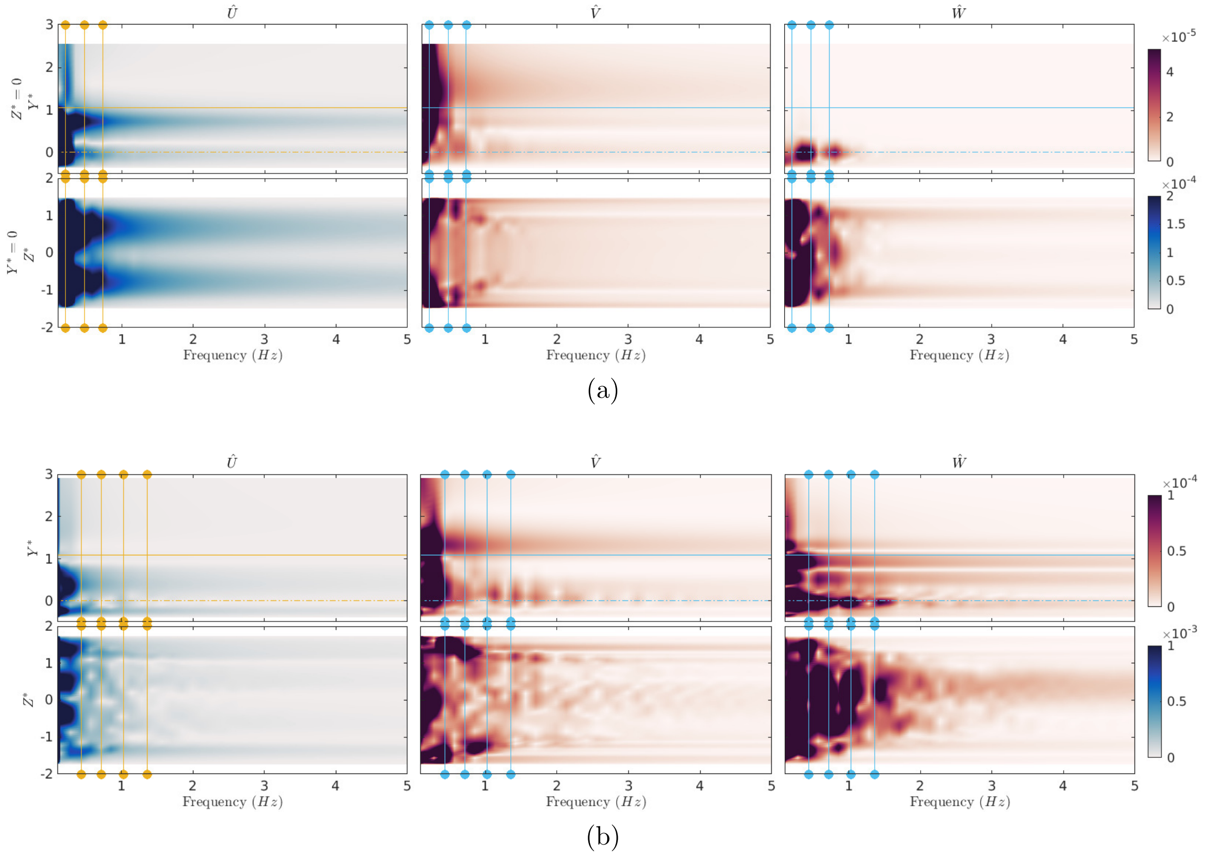

Figure 7.7: Fourier transform of velocity data for the (a) $Re = 557$ and (b) $Re = 1619$ DNS cases, at a central downstream location and (top) at $Z^* = 0$, and (bottom) at $Y^* = 0$ for (left) downstream, (centre) vertical, and (right) cross-stream velocities. The vertical lines indicate the frequencies of the dominant dynamic modes identified in Figure 7.9, and the horizontal lines the (dashed) averaged height of the velocity maximum and (solid) current height.

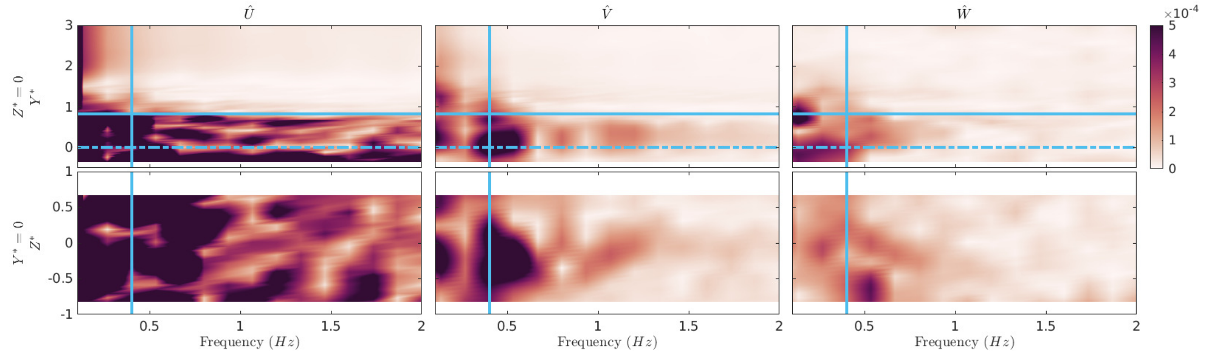

Figure 7.8: Fourier transform of velocity data for the STB case with $Re = 2743$ at a central downstream location and (top) at $Z^* = 0$, and (bottom) at $Y^* = 0.5$ for (left) downstream, (centre) vertical, and (right) cross-stream velocities. The vertical line indicates the frequency of the example dynamic mode identified in Figure 7.12, and the horizontal lines the (dashed) averaged height of the velocity maximum and (solid) current height.

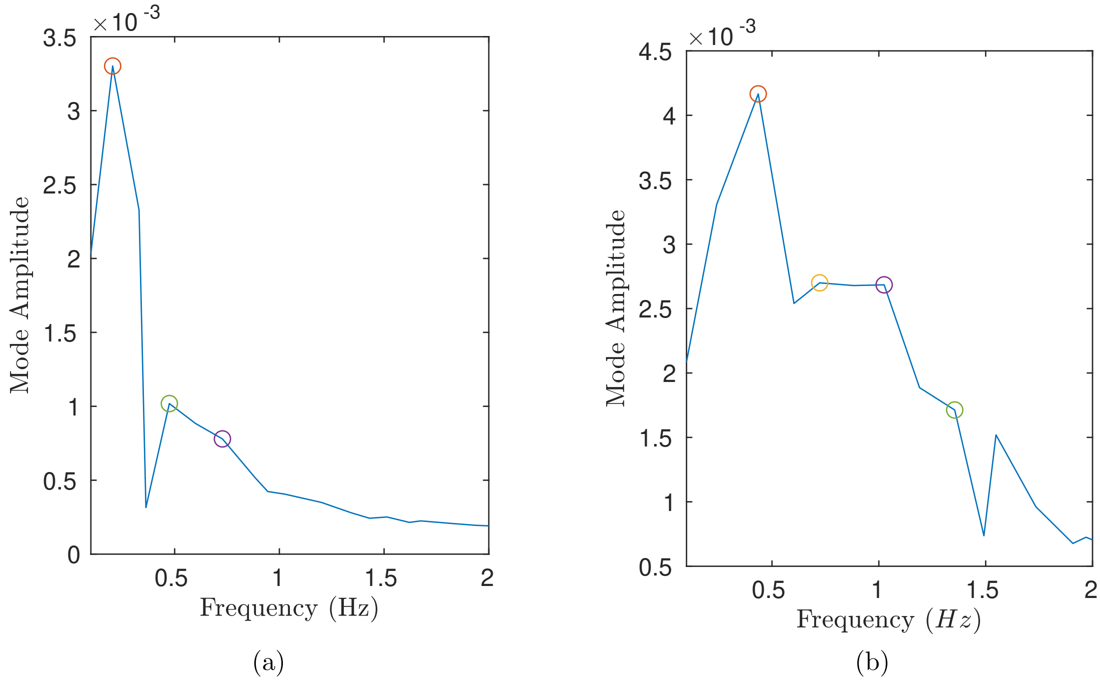

(a) (b)

Figure 7.9: Amplitudes of modes resulting from dynamic mode decomposition of the velocity fields in (a) the $Re = 557$ and (b) $Re = 1619$ cases. The circles indicate the modes illustrated in Figures 7.10 and 7.11.

7.4 Summary of PIV/STB/DNS Comparability

Comparing the three strands of work presented in this thesis, all averaged downstream velocity profiles collapse using the same non-dimensionalisation (Figure 7.3). Additionally, trends in average flow properties such as flow height and velocity maximum are consistent across all cases, excepting discrepancies attributable to the higher fluid viscosity in the $Re = 557$ DNS case and minor variations between experimental cases (Figure 7.4). Therefore, the DNS reliably reproduces averaged properties of the laboratory-based flows.

Plots of instantaneous velocity (Figures 7.5 and 7.6) illustrate that while the PIV and STB datasets have very similar structure, there are significant differences in instantaneous vertical and cross-stream velocity between the laboratory-based and the DNS data. This is particularly evident in the plots of vertical velocity on a cross-stream plane (Figure 7.6), where regions of positive vertical velocity are concentrated towards the side-walls in the DNS data, but there are alternating regions of positive and negative vertical velocity along the $Z^* = 0$ line in the STB data. The frequency analysis, in the form of Fourier transform over time and dynamic mode decomposition of the data, confirms this structural difference. Motions identified in the DNS data have vertical velocity concentrated towards the side-walls in the lower part of the flow (Figures 7.7, 7.10, and 7.11). In comparison, the STB case with $Re = 2743$ contains motions with alternating positive and negative velocity in the upper part of the flow in the cross-stream centre of

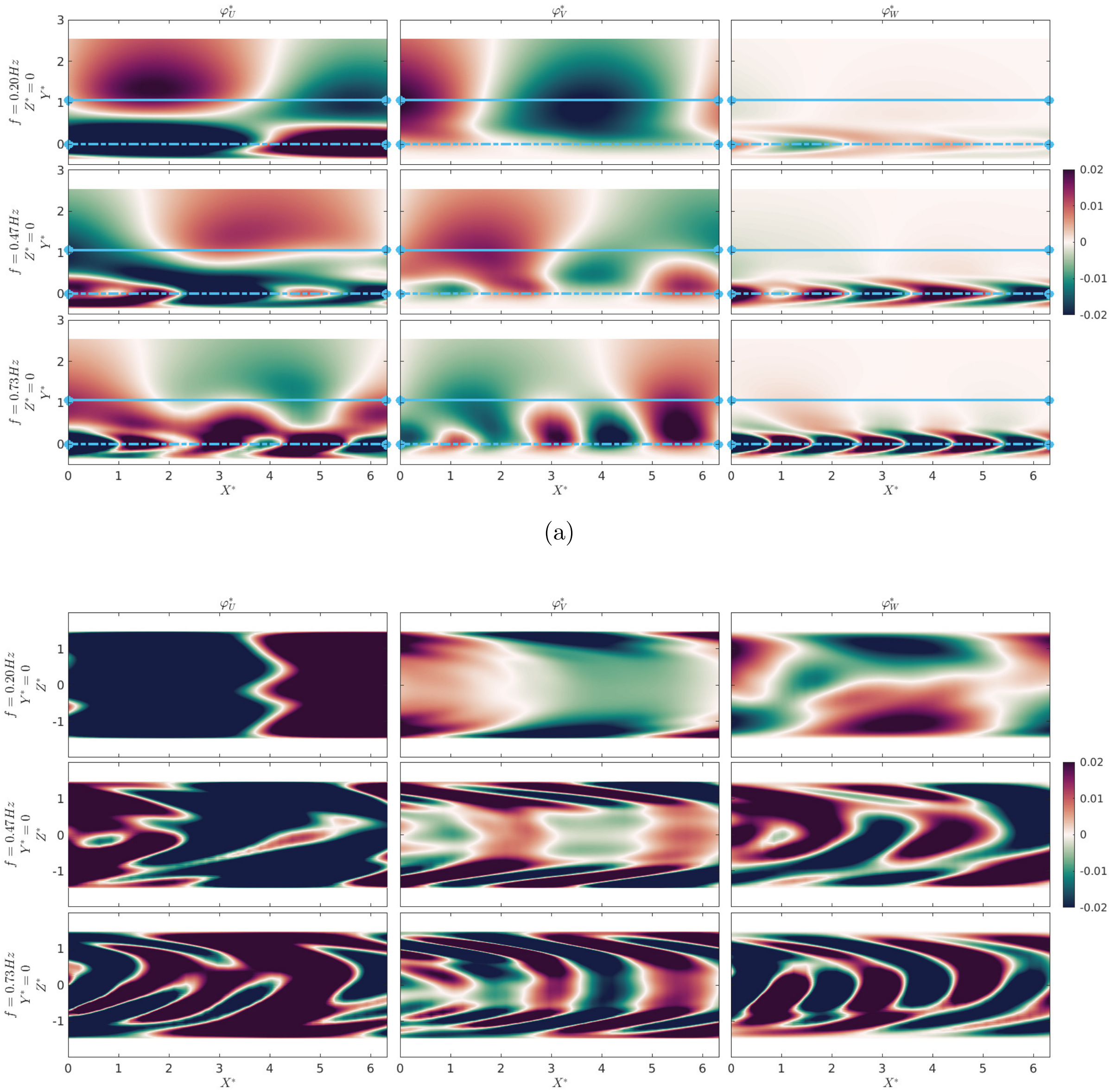

(a)

(b)

Figure 7.10: Modes with frequencies 0.20 Hz, 0.47 Hz, and 0.73 Hz from dynamic mode decomposition of velocity data for the $(Re, Sc) = (557, 1)$ DNS case (a) on an $X - Y$ plane at $Z^* = 0$ and (b) on an $X - Z$ plane at $Y^* = 0$.

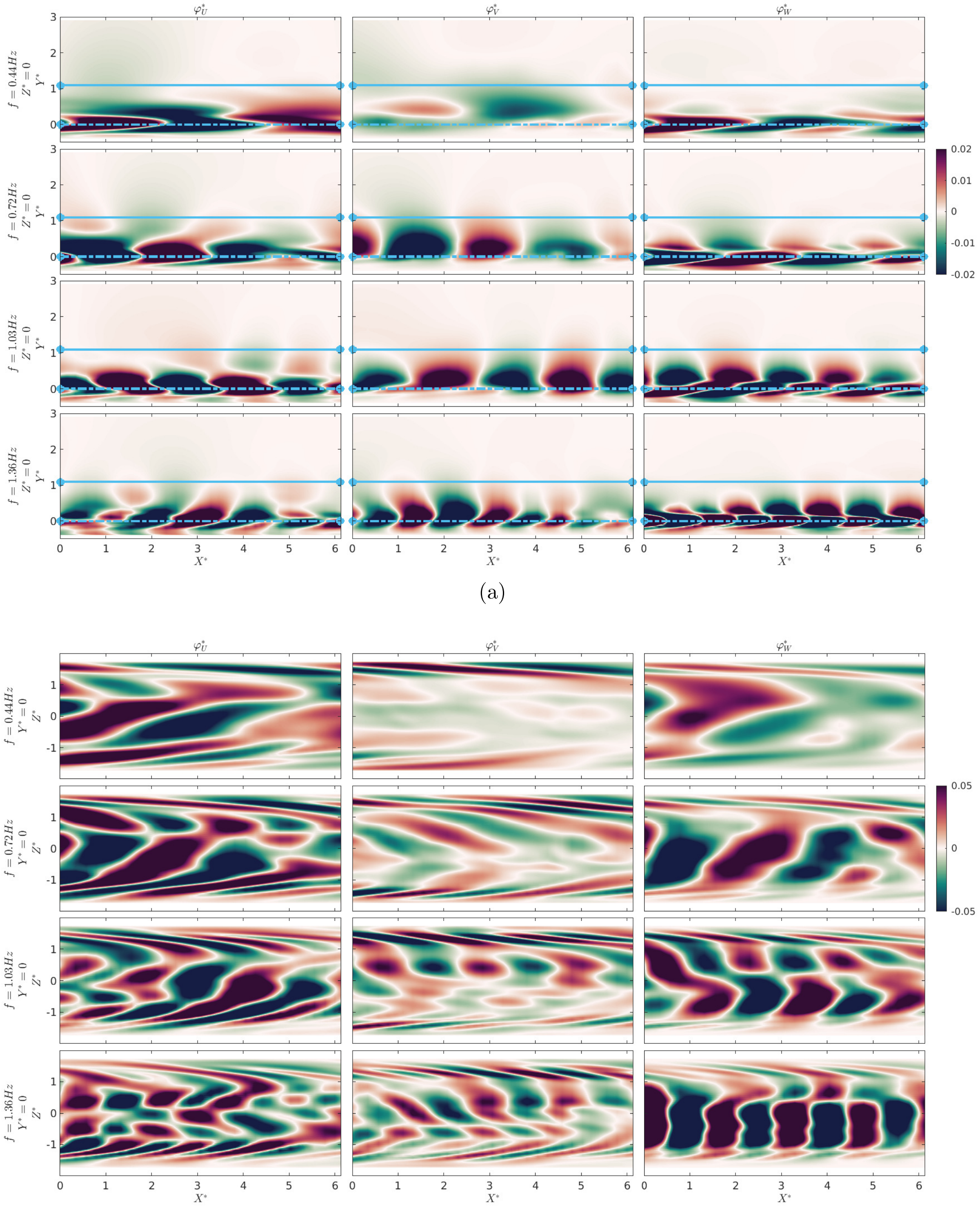

(a)

(b)

Figure 7.11: Modes with frequencies 0.44 Hz, 0.72 Hz, 1.03 Hz, and 1.36 Hz from dynamic mode decomposition of velocity data for the $(Re, Sc) = (1619, 1)$ DNS case (a) on an $X - Y$ plane at $Z^* = 0$ and (b) on an $X - Z$ plane at $Y^* = 0$.

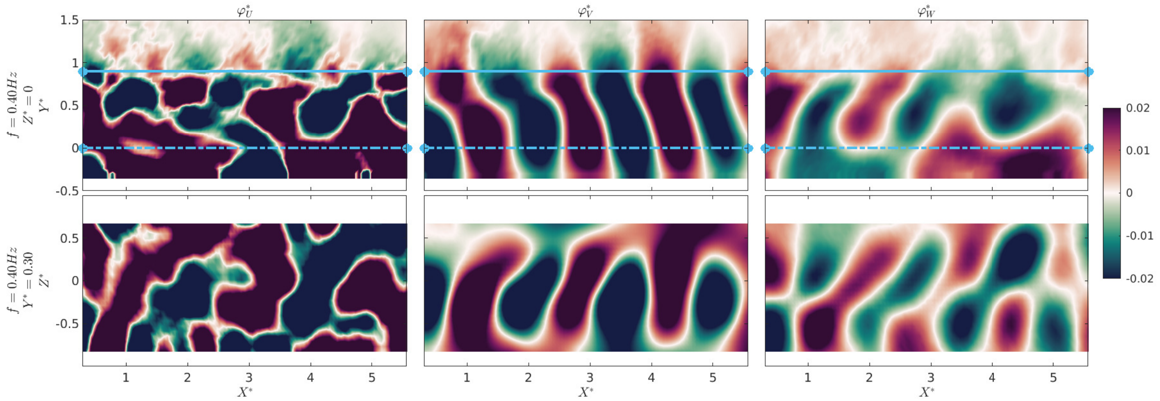

Figure 7.12: An example dynamic mode with frequency 0.40 Hz from the $(Re, Sc) = (2743, \mathcal{O}(1000))$ STB case to compare with the DNS modes, on (top) an $X - Y$ plane at $Z^* = 0$, and (bottom) an $X - Z$ plane at $Y^* = 0.30$.

the domain (Figures 7.8 and 7.12).

As illustrated in Chapter 6, increasing Schmidt number from 1 produces additional modes in the upper region of the flow behind the head, with cross-stream and vertical motions centred in the cross-stream direction. The structure of the density and velocity fluctuations associated with increased Schmidt number cases are correlated with a 1/4−wavelength offset, characteristic of internal gravity waves (García-Villalba & del Álamo, 2011). Further, the motions have a similar structure to the modes identified in the PIV/STB data corresponding to internal gravity waves. While there are other differences between the DNS and STB cases, namely the simplified outlet, the exact inlet velocity distribution, and the Reynolds number, it has been demonstrated that the difference in Schmidt number ($Sc = 1$ for the DNS cases compared with $Sc = \mathcal{O}(1000)$ for the PIV/STB cases) could account for the structural differences between the data sets. Therefore, numerical simulations that assume a Schmidt number of 1 may not accurately reproduce flow in the body.

7.5 Project Conclusions

This work has investigated gravity current flows using three different experimental and numerical techniques – particle image velocimetry, Shake-the-Box particle tracking velocimetry, and direct numerical simulation. The flows considered were constant-influx solute-based flows, with a 3% by mass density difference. The techniques generate the instantaneous whole-field two- or three-dimensional velocity field, and in the case of DNS the concentration field, within the body of the flow. The PIV and STB data sets were shown to have very similar structure, and similar structural changes with increasing Reynolds number. While there were some structural differences between the DNS and PIV/STB flows, the DNS method was shown to accurately reproduce averaged quantities. The work presented has led to a number of advances in understanding gravity current

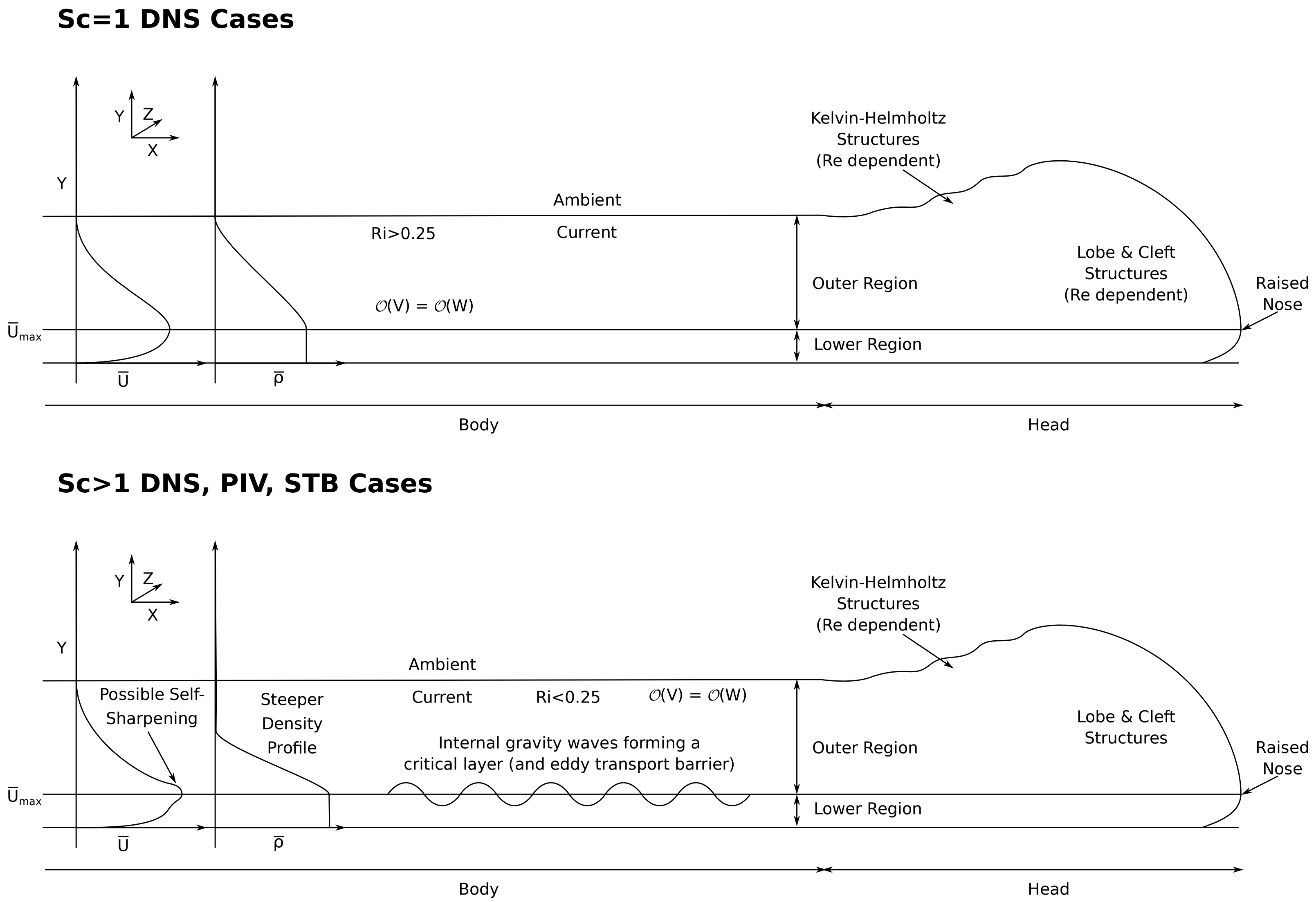

Figure 7.13: Illustration summarising the structure of the gravity current body in (top) the $Sc = 1$ DNS cases, and (bottom) the $Sc > 1$ DNS, PIV, and STB cases in this thesis.

flows (summarised in Figure 7.13 and described below), questioning several common assumptions about the structure of the gravity current body.

First, while it has generally been assumed that the gravity current body can be well described by averaged properties, experimental measurements of flows with a variety of Reynolds numbers identified the formation of internal gravity waves within the body. Further, a critical layer was identified near the height of the velocity maximum. Possible wave breaking that may occur at this level, with associated transfer of momentum to the mean flow, implies that any model of gravity current body flow should allow for acceleration at the height of the critical layer. However, such waves were not identified in the $Sc = 1$ DNS cases. This difference in structure was explained by the observed sharpening of the density profile between the $Sc = 1$ and $Sc > 1$ DNS cases, leading to a change in gradient Richardson number from above to below the critical value in the upper part of the body. This suggests that two models are needed depending on the stability of the current/ambient interface.

Second, cross-stream motion in the gravity current body is typically neglected. The three-dimensional velocity data, from both STB and DNS, illustrated that regardless of Schmidt number cross-stream and vertical velocities are equivalent in magnitude with cross-stream velocity being particularly important near the height of the velocity maximum. Additionally, the waves identified in the highest Reynolds number STB case were shown to be associated with three-dimensional motions. Therefore, a full characterisation of the gravity current body requires measurement of the cross-stream velocity as well as downstream and vertical. In particular when conducting numerical research, two-dimensional simulations will be unable to reproduce three-dimensional flow features within the body, just as they are unable to accurately reproduce such features within the head. The volumetric velocity measurements (both STB and DNS) highlighted that exclusively using a single vertical plane within the domain (as has been done in almost all existing literature for flows with comparable aspect ratio and Reynolds number), in particular a central cross-stream plane, may give a misleading impression of flow structure.

Third, the high computational cost involved in investigating the effect of Schmidt number has led to numerical simulations of gravity current flows typically assuming a Schmidt number of ~ 1. While comparison of experimental and numerical data in this work showed consistent trends in averaged properties within the body across all strands of this work, increasing Schmidt number beyond 1 led to qualitative changes in instantaneous velocity structure in and behind the head. Some of these changes, such as the over-running of ambient fluid by the raised nose at the front of the flow, also occurred with increasing Reynolds number at fixed Schmidt number. However, within the Reynolds number range considered in this work some changes, for example the presence of structures in the upper part of the flow behind the head, did not. A noteworthy change with increased Schmidt number was the reduction in gradient Richardson number. All $Sc = 1$ DNS cases were found to have $Ri > 0.25$ in the body (where 0.25 is the critical value) while all $Sc > 1$ DNS cases had $Ri < 0.25$.

It was shown that the structural differences observed between the PIV/STB data and the DNS data could be a result of choosing $Sc = 1$ to reproduce a $Sc = \mathcal{O}(1000)$ flow. Indeed, this may explain why DNS in existing literature has not identified the internal waves present in the PIV/STB strands of this work. It was argued that works considering high Schmidt number flows with larger viscosities (viscosity larger than that of the fluids used in the experimental work in this thesis), or those that consider the structure of the body in high Schmidt number flows, should consider the effect of increased Schmidt number. However, some concessions to computational cost are likely justified when attempting to qualitatively capture such flows. The numerical investigations presented suggest that increasing Schmidt number beyond 10 led to only quantitative changes in the flow even at Reynolds numbers as low as $Re_I = 100$.

Many real-world gravity current flows are sediment-driven, rather than solute-based. While the findings presented in this work are based purely on solute-based flows, they may also be applicable to sediment-laden flows. Comparisons can be drawn between thermohaline and sediment-laden flows (García, 1994; Kneller & Buckee, 2000; Moodie, 2002), for example fine-grained conservative sediment-laden flows are thought to be dynamically similar to solute-based flows (Cossu & Wells, 2012; Kneller & Buckee, 2000). As discussed in Chapter 4, the structural differences in coarse-grained and non-conservative flows (Cossu & Wells, 2012; Hogg *et al.*, 2005; Kneller & Buckee, 2000; Stacey & Bowen, 1988; Wells & Dorrell, 2021) would not remove the potential for the formation of internal gravity waves and critical layers which require only that there exists stable stratification of density, and that the speed of the resulting waves is equal to the flow speed (Maslowe, 1986; Staquet & Sommeria, 2002). Further, while the Schmidt number of sediment-laden flows varies depending on grain size, it can be significantly higher than solute-based flows (for example being $\mathcal{O}(10^9)$ for 100 µm sand) (Benes *et al.*, 2007). This suggests that the effects of high Schmidt number observed here in solute-based flows likely also apply to sediment-laden flows.

7.6 Future Work

While the work presented in this thesis has provided several new insights into the structure of the gravity current body, there remain many unanswered questions. The largest limitation of this study stems from the lack of density measurements in the experimental runs. The sealed nature of the domain in this work, combined with the focus on volumetric velocity measurements, meant that no experimental observations of density were made. The buoyancy analysis was therefore based on an assumed and idealised density profile derived from the existing literature and backed up by the numerical investigations. While beyond the scope of this work, future research simultaneously measuring both the volumetric velocity and density fields could be used to remove the element of speculation inherent in concluding that the identified internal waves are a result of buoyancy.

The refractive index matching requirements of the experimental techniques led to the considered flows in this work being solute-based. While it was argued that such flows are analogous to conservative fine-grained particulate flows, non-conservative particulate currents are fundamentally different (Wells & Dorrell, 2021), and the applicability of the presented findings to particulate flows is currently speculative. A natural extension to this work, that would extend the applicability of the findings to real-world flows, is measurement of particulate flows and flows with double-diffusive instabilities (such as flows in which the density difference is a result of both a temperature difference and the presence of a solute).

The main controls considered in this thesis were flow aspect ratio, densimetric Froude number (Fr), Reynolds number (Re), and Schmidt number (Sc). While comparable to previous experimental works, the width of the flows considered in this thesis was constant and relatively narrow. Further volumetric measurements of flows in domains with a variety of widths (up to and including flows with no side-walls), whether conducted experimentally or numerically, are needed for a full understanding of the three-dimensional structure of the gravity current body. These additional measurements could also be used to discuss the origins of three-dimensionality within the body, and to establish the extent to which the identified cross-stream motions are a result of side-wall effects.

Investigation of Froude number effects on body structure was beyond the scope of this investigation. While not fixed, there was little variation in densimetric Froude number between cases, with all flows having $Fr < 1$ (typically $\mathcal{O}(0.7)$, see Table 7.1). In real-world flows, Froude numbers can be both above and below 1. The parameter range here could be extended by considering flows on different slopes, or with different density differences. Additionally, while Reynolds number was varied (taking values between ~ 2000 and ~ 4500 in the experimental flows), increases in Reynolds number were always observed to produce changes in body structure. This suggests that the highest Reynolds number may not have been sufficiently high to reach a point of structural similarity. The Reynolds number range could be extended, by considering larger and/or faster flows, to establish the importance of the identified flow features in high Reynolds number real-world flows.

Further investigation is also needed regarding the effect of Schmidt number. In this chapter, it was suggested that the low Schmidt number of the DNS cases was responsible for the difference in velocity structure (namely the formation of internal waves). However, due to the limitations of the data from the low Reynolds number STB case, the DNS cases were compared with PIV/STB data with significantly higher Reynolds number. Comparison of flows closer in Reynolds number would lend credibility to this conclusion, as would extending the duration of the $Sc > 1$ DNS cases to allow for a more thorough investigation of the effect of Schmidt number on the body.

The impact of Schmidt number being greater than 1 on flows with Reynolds number $\mathcal{O}(1000)$ and above was beyond the scope of this project. However, this investigation is needed to establish whether a sufficiently high Reynolds number leads to the same qualitative changes as increased Schmidt number, or whether as suggested here, an accurate quantification of a $Sc > 1$ gravity current flow requires consideration of flows with $Sc > 1$. An additional source of information regarding the effect of Schmidt/Prandtl number could come from whole-field instantaneous measurements of experimental flows with a significantly different Schmidt/Prandtl number to a typical solute-based flow, for example a gas-based (such as carbon dioxide) or temperature-driven flow.

References

Abad, J.D., Sequeiros, O.E., Spinewine, B., Pirmez, C., Garcia, M.H. & Parker, G. (2011). Secondary Current of Saline Underflow In A Highly Meandering Channel: Experiments and Theory. *Journal of Sedimentary Research*, **81**, 787–813. ix, xi, 11, 12, 64, 65

Adduce, C., Sciortino, G. & Proietti, S. (2011). Gravity Currents Produced by Lock Exchanges: Experiments and Simulations with a Two-Layer Shallow-Water Model with Entrainment. *Journal of Hydraulic Engineering*, **138**, 111–121. 27

Adrian, R.J. & Westerweel, J. (2011). *Particle Image Velocimetry*. Cambridge University Press. 23, 30, 31, 33, 66

Aguilar, D.A. & Sutherland, B.R. (2006). Internal wave generation from rough topography. *Physics of Fluids*, **18**, 066603. 84

Akselvoll, K. & Moin, P. (1996). Large-eddy simulation of turbulent confined coannular jets. *Journal of Fluid Mechanics*, **315**, 387–411. 49

Alahyari, A. & Longmire, E.K. (1994). Particle image velocimetry in a variable density flow: application to a dynamically evolving microburst. *Experiments in Fluids*, **17**, 434–440. 29, 66, 88

Alahyari, A.A. & Longmire, E.K. (1996). Development and structure of a gravity current head. *Experiments in Fluids*, **20**, 410–416. 2, 10, 18, 19, 25

Altinakar, M.S., Graf, W.H. & Hopfinger, E.J. (1996). Flow structure in turbidity currents. *Journal of Hydraulic Research*, **34**, 713–718. ix, xi, 11, 12, 65, 86

Amy, L.A., Peakall, J. & Talling, P.J. (2005). Density- and viscosity-stratified gravity currents: Insight from laboratory experiments and implications for submarine flow deposits. *Sedimentary Geology*, **179**, 5–29. 135

Andersson, B., Andersson, R., Håkansson, L., Mortensen, M., Sudiyo, R. & van Wachem, B. (2011). *Computational Fluid Dynamics for Engineers*. Cambridge University Press. 10, 20, 55, 57, 113

Armi, L. (1986). The hydraulics of two flowing layers with different densities. *Journal of Fluid Mechanics*, **163**, 27–58. 7

Azpiroz-Zabala, M., Cartigny, M.J.B., Talling, P.J., Parsons, D.R., Sumner, E.J., Clare, M.A., Simmons, S.M., Cooper, C. & Pope, E.L. (2017). Newly recognized turbidity current structure can explain prolonged flushing of submarine canyons. *Science Advances*, **3**, e1700200. ix, 1, 11, 13, 17, 63, 64, 85, 86

Baines, P.G. (1998). *Topographic Effects in Stratified Flows*. Cambridge Monographs on Mechanics, Cambridge University Press, revised edn. 14, 15

Baker, M.L., Baas, J.H., Malarkey, J., Jacinto, R.S., Craig, M.J., Kane, I.A. & Barker, S. (2017). The Effect of Clay Type On the Properties of Cohesive Sediment Gravity Flows and Their Deposits. *Journal of Sedimentary Research*, **87**, 1176–1195. 26

Balasubramanian, S. & Zhong, Q. (2018). Entrainment and mixing in lock-exchange gravity currents using simultaneous velocity-density measurements. *Physics of Fluids*, **30**, 056601. 8, 86, 113

Benes, K., Tong, P. & Ackerson, B.J. (2007). Sedimentation, Péclet number, and hydrodynamic screening. *Physical Review E*, **76**, 056302. 152

Best, J.L., Kostaschuk, R.A., Peakall, J., Villard, P.V. & Franklin, M. (2005). Whole flow field dynamics and velocity pulsing within natural sediment-laden underflows. *Geology*, **33**, 765–768. 64, 68

Bhaganagar, K. (2017). Role of head of turbulent 3-D density currents in mixing during slumping regime. *Physics of Fluids*, **29**, 020703. 2, 10, 12, 15, 16, 19, 21

Bhaganagar, K. & Pillalamarri, N.R. (2017). Lock-exchange release density currents over three-dimensional regular roughness elements. *Journal of Fluid Mechanics*, **832**, 793. 110

Bird, R.B., Stewart, W.E. & Lightfoot, E.N. (2007). *Transport Phenomena*. Wiley, 2nd edn. 10, 57, 113

Birman, V.K. & Meiburg, E. (2006). High-resolution simulations of gravity currents. *Journal of the Brazilian Society of Mechanical Sciences and Engineering*, **28**, 169–173. 2, 20, 21

Birman, V.K., Martin, J.E. & Meiburg, E. (2005). The non-Boussinesq lock-exchange problem. Part 2. High-resolution simulations. *Journal of Fluid Mechanics*, **537**, 125–144. xix, 21, 26, 113

Blazek, J. (2015). *Computational Fluid Dynamics: Principles and Applications*. Butterworth-Heinemann, 3rd edn. 51

Bolós, V.J. & Benítez, R. (2014). The Wavelet Scalogram in the Study of Time Series. In F. Casas & V. Martínez, eds., *Advances in Differential Equations and Applications*, 147–154, Springer. 74

Bonnecaze, R.T., Huppert, H.E. & Lister, J.R. (1993). Particle-driven gravity currents. *Journal of Fluid Mechanics*, **250**, 339–369. 62

Bonometti, T. & Balachandar, S. (2008). Effect of Schmidt number on the structure and propagation of density currents. *Theoretical and Computational Fluid Dynamics*, **22**, 341. xv, 2, 9, 10, 11, 12, 15, 16, 20, 21, 47, 57, 61, 113, 114, 132

Booker, J.R. & Bretherton, F.P. (1967). The critical layer for internal gravity waves in a shear flow. *Journal of Fluid Mechanics*, **27**, 513–539. 14, 15, 83

Bower, A.S. & Hogg, N.G. (1996). Structure of the Gulf Stream and Its recirculations at 55°W. *Journal of Physical Oceanography*, **26**, 1002–1022. 81

Boyd, J.P. (2001). *Chebyshev and Fourier Spectral Methods*. Dover Publications, 2nd edn. xi, 52, 53, 54, 115

Bretherton, F.P. (1966). Critical layer instability in baroclinic flows. *Quarterly Journal of the Royal Meteorological Society*, **92**, 325–334. 14

Briggs, W.L. & Henson, V.E. (1995). *The DFT: An Owner's Manual for the Discrete Fourier Transform*. Society for Industrial and Applied Mathematics. 73

Britter, R.E. & Linden, P.F. (1980). The motion of the front of a gravity current travelling down an incline. *Journal of Fluid Mechanics*, **99**, 531–543. 62, 112

Britter, R.E. & Simpson, J.E. (1978). Experiments on the dynamics of a gravity current head. *Journal of Fluid Mechanics*, **88**, 223–240. 10, 18

Buckee, C., Kneller, B. & Peakall, J. (2001). Turbulence Structure in Steady, Solute-Driven Gravity Currents. *Particulate Gravity Currents*, 173–187. ix, 2, 7, 9, 12, 13, 15, 16, 17, 18, 27, 63, 64, 69, 92, 125

Bühler, O. (2014). *Waves and Mean Flows*. Cambridge University Press, 2nd edn. 14, 81, 86

Cantero, M.I., Balachandar, S., García, M.H. & Ferry, J.P. (2006). Direct Numerical Simulations of Planar and Cylindrical Density Currents. *Journal of Applied Mechanics*, **73**, 923–930. 61, 115

Cantero, M.I., Lee, J.R., Balachandar, S. & García, M.H. (2007). On the front velocity of gravity currents. *Journal of Fluid Mechanics*, **586**, 1–39. x, 2, 8, 10, 11, 20, 21, 47, 61, 63, 112, 113, 115

Cantero, M.I., Balachandar, S., García, M.H. & Bock, D. (2008). Turbulent structures in planar gravity currents and their influence on the flow dynamics. *Journal of Geophysical Research: Oceans*, **113**. 2, 16, 19, 20, 21, 86, 114

Causon, D.M. & Mingham, C.G. (2010). *Introductory Finite Difference Methods for PDEs*. Bookboon. 50

Chadha, T. (2015). *Numerical study on particle sedimentation and deposition in turbidity currents*. Ph.D. thesis, ETH Zurich. 7, 8

Chumakov, S.G. (2005). *Subgrid models for large eddy simulation: scalar flux, scalar dissipation and energy dissipation*. Ph.D. thesis, University of Wisconsin–Madison. 49

Chumakov, S.G. & Rutland, C.J. (2005). Dynamic structure subgrid-scale models for large eddy simulation. *International Journal for Numerical Methods in Fluids*, **47**, 911–923. 49

Chung, T. (2002). *Computational Fluid Dynamics*. Cambridge University Press. xix, 10, 26

Coleman, G.N. & Sandberg, R.D. (2010). A primer on direct numerical simulation of turbulence - methods, procedures and guidelines. Tech. rep., University of Southampton. 51, 61, 115

Cossu, R. & Wells, M.G. (2012). A comparison of the shear stress distribution in the bottom boundary layer of experimental density and turbidity currents. *European Journal of Mechanics - B/Fluids*, **32**, 70–79. 2, 6, 7, 9, 16, 18, 63, 69, 84, 92, 109, 152

Crouvi, O., Dayan, U., Amit, R. & Enzel, Y. (2017). An Israeli haboob: Sea breeze activating local anthropogenic dust sources in the Negev loess. *Aeolian Research*, **24**, 39–52. ix, 1

DantecDynamics (2018). *DynamicStudio User's Guide, Version 6.4*. Dantec Dynamics. 32

Davarpanah Jazi, S., Wells, M.G., Peakall, J., Dorrell, R.M., Thomas, R.E., Keevil, G.M., Darby, S.E., Sommeria, J., Viboud, S. & Valran, T. (2020). Influence of Coriolis Force Upon Bottom Boundary Layers in a Large-Scale Gravity Current Experiment: Implications for Evolution of Sinuous Deep-Water Channel Systems. *Journal of Geophysical Research: Oceans*, **125**, e2019JC015284. ix, xi, 11, 12, 63, 65

Donzis, D.A., Aditya, K., Sreenivasan, K.R. & Yeung, P.K. (2014). The Turbulent Schmidt Number. *Journal of Fluids Engineering*, **136**, 060912. 10, 20, 55, 113

Dorrell, R.M., Peakall, J., Burns, C. & Keevil, G.M. (2018). A novel mixing mechanism in sinuous seafloor channels: Implications for submarine channel evolution. *Geomorphology*, **303**, 1–12. 64, 68

Dorrell, R.M., Peakall, J., Darby, S.E., Parsons, D.R., Johnson, J., Sumner, E.J., Wynn, R.B., Özsoy, E. & Tezcan, D. (2019). Self-sharpening induces jet-like structure in seafloor gravity currents. *Nature Communications*, **10**, 1381. ix, xi, 5, 12, 14, 15, 17, 63, 64, 65, 81, 83, 86, 110, 112

Dritschel, D.G. & McIntyre, M.E. (2008). Multiple Jets as PV Staircases: The Phillips Effect and the Resilience of Eddy-Transport Barriers. *Journal of the Atmospheric Sciences*, **65**, 855–874. 81, 83

Dritschel, D.G. & Scott, R.K. (2011). Jet sharpening by turbulent mixing. *Philosophical Transactions of the Royal Society A: Mathematical, Physical and Engineering Sciences*, **369**, 754–770. xi, 15, 65, 81

Ellison, T.H. & Turner, J.S. (1959). Turbulent entrainment in stratified flows. *Journal of Fluid Mechanics*, **6**, 423–448. xx, 7, 9, 27, 63, 67, 68, 138

Elsinga, G.E. & Westerweel, J. (2012). Tomographic-PIV measurement of the flow around a zigzag boundary layer trip. *Experiments in Fluids*, **52**, 865–876. 36

Esfeh, H.K., Azarafza, A. & Hamid, M.K.A. (2017). On the computational fluid dynamics of PEM fuel cells (PEMFCs): an investigation on mesh independence analysis. *RSC Advances*, **7**, 32893–32902. 59

Espath, L.F.R., Pinto, L.C., Laizet, S. & Silvestrini, J.H. (2014). Two- and three-dimensional Direct Numerical Simulation of particle-laden gravity currents. *Computers & Geosciences*, **63**, 9–16. 2, 19, 20, 114

Feistl, T., Bebi, P., Christen, M., Margreth, S., Diefenbach, L. & Bartelt, P. (2015). Forest damage and snow avalanche flow regime. *Natural Hazards and Earth System Sciences*, **15**, 1275–1288. ix, 1

Felix, M., Sturton, S. & Peakall, J. (2005). Combined measurements of velocity and concentration in experimental turbidity currents. *Sedimentary Geology*, **179**, 31–47. 75

Fischer, P.F. (1997). An Overlapping Schwarz Method for Spectral Element Solution of the Incompressible Navier–Stokes Equations. *Journal of Computational Physics*, **133**, 84–101. 115

FORNBERG, B. (1998). *A Practical Guide to Pseudospectral Methods*. Cambridge University Press. xi, 53, 54, 115

GARCÍA, M.H. (1994). Depositional Turbidity Currents Laden with Poorly Sorted Sediment. *Journal of Hydraulic Engineering*, **120**, 1240–1263. ix, xi, 11, 12, 65, 84, 152

GARCÍA, M.H. & PARSONS, J.D. (1996). Mixing at the front of gravity currents. *Dynamics of Atmospheres and Oceans*, **24**, 197–205. 10, 26, 113

GARCÍA-VILLALBA, M. & DEL ÁLAMO, J.C. (2011). Turbulence modification by stable stratification in channel flow. *Physics of Fluids*, **23**, 045104. 109, 124, 134, 149

GERBER, G. (2008). *Experimental measurement and numerical modelling of velocity, density and turbulence profiles of a gravity current*. Ph.D. thesis, Stellenbosch: Stellenbosch University. 25

GERBER, G., DIEDERICKS, G. & BASSON, G.R. (2010). Particle Image Velocimetry Measurements and Numerical Modeling of a Saline Density Current. *Journal of Hydraulic Engineering*, **137**, 333–342. 2, 6, 11, 27, 63

GRAY, T.E., ALEXANDER, J. & LEEDER, M.R. (2005). Quantifying velocity and turbulence structure in depositing sustained turbidity currents across breaks in slope. *Sedimentology*, **52**, 467–488. 7, 27, 63

GRAY, T.E., ALEXANDER, J. & LEEDER, M.R. (2006). Longitudinal flow evolution and turbulence structure of dynamically similar, sustained, saline density and turbidity currents. *Journal of Geophysical Research: Oceans*, **111**. ix, 2, 6, 7, 11, 12, 13, 16, 17, 18, 63, 64, 69, 83, 85, 92, 109

GRAYSON, K.J. (2018). *Laser characteristics and configurations for high quality PIV measurements*. Ph.D. thesis, Department of Mechanical Engineering, The University of Melbourne. 31

GROSSMANN, A., KRONLAND-MARTINET, R. & MORLET, J. (1990). Reading and Understanding Continuous Wavelet Transforms. In J.M. Combes, A. Grossmann & P. Tchamitchian, eds., *Wavelets*, 2–20, Springer. 74

HACKER, J., LINDEN, P.F. & DALZIEL, S.B. (1996). Mixing in lock-release gravity currents. *Dynamics of Atmospheres and Oceans*, **24**, 183–195. 2, 10, 27, 63, 85

HADAD, T. & GURKA, R. (2013). Effects of particle size, concentration and surface coating on turbulent flow properties obtained using PIV/PTV. *Experimental Thermal and Fluid Science*, **45**, 203–212. 30

Hallez, Y. & Magnaudet, J. (2009). A numerical investigation of horizontal viscous gravity currents. *Journal of Fluid Mechanics*, **630**, 71–91. 7, 8

Hallworth, M.A., Huppert, H.E., Phillips, J.C. & Sparks, R.S.J. (1996). Entrainment into two-dimensional and axisymmetric turbulent gravity currents. *Journal of Fluid Mechanics*, **308**, 289–311. 2, 5, 6, 10, 18, 63, 85

Hanazaki, H., Konishi, K. & Okamura, T. (2009). Schmidt-number effects on the flow past a sphere moving vertically in a stratified diffusive fluid. *Physics of Fluids*, **21**, 026602. 2, 10, 113

Härtel, C., Meiburg, E. & Necker, F. (2000). Analysis and direct numerical simulation of the flow at a gravity-current head. Part 1. Flow topology and front speed for slip and no-slip boundaries. *Journal of Fluid Mechanics*, **418**, 189–212. 2, 10, 20, 21, 46, 47

Haynes, W.M. (2014). *CRC Handbook of Chemistry and Physics*. CRC press, 95th edn. xix, xx, 29, 66, 88

Heller, V. (2011). Scale effects in physical hydraulic engineering models. *Journal of Hydraulic Research*, **49**, 293–306. xix, 19, 24, 26

Hines, C.O. (1968). Some consequences of gravity-wave critical layers in the upper atmosphere. *Journal of Atmospheric and Terrestrial Physics*, **30**, 837–843. 14

Ho, V.L., Dorrell, R.M., Keevil, G.M., Burns, A.D. & McCaffrey, W.D. (2018). Pulse propagation in turbidity currents. *Sedimentology*, **65**, 620–637. 26

Hogg, A.J. (2006). Lock-release gravity currents and dam-break flows. *Journal of Fluid Mechanics*, **569**, 61–87. 9

Hogg, A.J., Hallworth, M.A. & Huppert, H.E. (2005). On gravity currents driven by constant fluxes of saline and particle-laden fluid in the presence of a uniform flow. *Journal of Fluid Mechanics*, **539**, 349–385. 84, 152

Hogg, A.J., Nasr-Azadani, M.M., Ungarish, M. & Meiburg, E. (2016). Sustained gravity currents in a channel. *Journal of Fluid Mechanics*, **798**, 853–888. 63, 112, 113

Hogg, C.A.R., Dalziel, S.B., Huppert, H.E. & Imberger, J. (2015). Inclined gravity currents filling basins: The influence of Reynolds number on entrainment into gravity currents. *Physics of Fluids*, **27**, 096602. 8, 113

Huang, H., Imran, J. & Pirmez, C. (2008). Numerical Study of Turbidity Currents with Sudden-Release and Sustained-Inflow Mechanisms. *Journal of Hydraulic Engineering*, **134**, 1199–1209. 6, 47

Huang, H., Imran, J., Pirmez, C., Zhang, Q. & Chen, G. (2009). The Critical Densimetric Froude Number of Subaqueous Gravity Currents Can Be Non-Unity or Non-Existent. *Journal of sedimentary research*, **79**, 479–485. 7, 9

Huhn, F., Schanz, D., Gesemann, S., Dierksheide, U., van de Meerendonk, R. & Schröder, A. (2017). Large-scale volumetric flow measurement in a pure thermal plume by dense tracking of helium-filled soap bubbles. *Experiments in Fluids*, **58**, 116. 37

Huppert, H.E. (2006). Gravity currents: a personal perspective. *Journal of Fluid Mechanics*, **554**, 299. 1, 5

Hutton, D.V. (2004). *Fundamentals of Finite Element Analysis*. McGraw-Hill,. 51

Iftekharuddin, K.M. & Awwal, A.A. (2012). *Field Guide to Image Processing*. SPIE Press Bellingham, WA. 73

Iserles, A. (2009). *A First Course in the Numerical Analysis of Differential Equations*. Cambridge University Press, 2nd edn. 50, 51, 55, 56

Islam, M.A. & Imran, J. (2010). Vertical structure of continuous release saline and turbidity currents. *Journal of Geophysical Research: Oceans*, **115**. 6, 7, 16, 17, 63, 64, 69, 83, 85, 86, 92, 109

Ivanov, V.V., Shapiro, G.I., Huthnance, J.M., Aleynik, D.L. & Golovin, P.N. (2004). Cascades of dense water around the world ocean. *Progress in Oceanography*, **60**, 47–98. 84

Johnson, C.G. & Hogg, A.J. (2013). Entraining gravity currents. *Journal of Fluid Mechanics*, **731**, 477–508. xix, 10, 26

Jux, C., Sciacchitano, A., Schneiders, J.F.G. & Scarano, F. (2018). Robotic volumetric PIV of a full-scale cyclist. *Experiments in Fluids*, **59**, 74. 37

Keane, R.D. & Adrian, R.J. (1992). Theory of cross-correlation analysis of PIV images. *Applied Scientific Research*, **49**, 191–215. 33

Khripounoff, A., Vangriesheim, A., Babonneau, N., Crassous, P., Dennielou, B. & Savoye, B. (2003). Direct observation of intense turbidity current activity in the Zaire submarine valley at 4000 m water depth. *Marine Geology*, **194**, 151–158. 63, 86

Kim, J., Moin, P. & Moser, R. (1987). Turbulence statistics in fully developed channel flow at low Reynolds number. *Journal of Fluid Mechanics*, **177**, 133–166. 61, 115

Kneller, B. & Buckee, C. (2000). The structure and fluid mechanics of turbidity currents: a review of some recent studies and their geological implications. *Sedimentology*, **47**, 62–94. ix, xi, 2, 5, 6, 8, 9, 10, 11, 12, 13, 15, 17, 26, 63, 64, 65, 83, 84, 85, 152

Kneller, B., Nasr-Azadani, M.M., Radhakrishnan, S. & Meiburg, E. (2016). Long-range sediment transport in the world's oceans by stably stratified turbidity currents. *Journal of Geophysical Research: Oceans*, **121**, 8608–8620. 7, 64, 86

Kneller, B.C., Bennett, S.J. & McCaffrey, W.D. (1997). Velocity and turbulence structure of density currents and internal solitary waves: potential sediment transport and the formation of wave ripples in deep water. *Sedimentary Geology*, **112**, 235–250. 2, 13, 16, 18, 27

Kneller, B.C., Bennett, S.J. & McCaffrey, W.D. (1999). Velocity structure, turbulence and fluid stresses in experimental gravity currents. *Journal of Geophysical Research*, **104**, 5381–5391. 2, 12, 16, 18, 27, 63, 64, 86

Kostaschuk, R., Nasr-Azadani, M.M., Meiburg, E., Wei, T., Chen, Z., Negretti, M.E., Best, J., Peakall, J. & Parsons, D.R. (2018). On the Causes of Pulsing in Continuous Turbidity Currents. *Journal of Geophysical Research: Earth Surface*, **123**, 2827–2843. 64, 68, 75

Kou, J. & Zhang, W. (2017). An improved criterion to select dominant modes from dynamic mode decomposition. *European Journal of Mechanics - B/Fluids*, **62**, 109–129. 76

Krug, D., Holzner, M., Lüthi, B., Wolf, M., Kinzelbach, W. & Tsinober, A. (2013). Experimental study of entrainment and interface dynamics in a gravity current. *Experiments in Fluids*, **54**, 1530. 2, 18, 19, 25

Krug, D., Holzner, M., Lüthi, B., Wolf, M., Kinzelbach, W. & Tsinober, A. (2015). The turbulent/non-turbulent interface in an inclined dense gravity current. *Journal of Fluid Mechanics*, **765**, 303–324. 2, 16, 17, 18, 19, 25, 29, 87

Kumar, R. & Dewan, A. (2016). A study of LES–SGS closure models applied to a square buoyant cavity. *International Journal of Heat and Mass Transfer*, **98**, 164–175. 49

Langham, J., Eaves, T.S. & Kerswell, R.R. (2020). Stably stratified exact coherent structures in shear flow: the effect of Prandtl number. *Journal of Fluid Mechanics*, **882**. 2, 10, 113

Lefauve, A., Partridge, J.L., Zhou, Q., Dalziel, S.B., Caulfield, C.P. & Linden, P.F. (2018). The structure and origin of confined Holmboe waves. *Journal of Fluid Mechanics*, **848**, 508–544. 2, 7, 19, 64, 87

Legg, S., Briegleb, B., Chang, Y., Chassignet, E.P., Danabasoglu, G., Ezer, T., Gordon, A.L., Griffies, S., Hallberg, R., Jackson, L., Large, W., Özgökmen, T.M., Peters, H., Price, J., Riemenschneider, U., Wu, W., Xu, X. & Yang, J. (2009). Improving Oceanic Overflow Representation in Climate Models: The Gravity Current Entrainment Climate Process Team. *Bulletin of the American Meteorological Society*, **90**, 657–670. 84

LeVeque, R.J. (2007). *Finite Difference Methods for Ordinary and Partial Differential Equations: Steady-State and Time-Dependent Problems*. Society for Industrial and Applied Mathematics. 51

Lipatnikov, A. (2012). *Fundamentals of Premixed Turbulent Combustion*. CRC Press. 56

Liu, G.R. & Quek, S.S. (2013). *The Finite Element Method: A Practical Course*. Butterworth-Heinemann. 51

Lombardi, V., Adduce, C., Sciortino, G. & La Rocca, M. (2015). Gravity currents flowing upslope: Laboratory experiments and shallow-water simulations. *Physics of Fluids*, **27**, 016602. 25

Lotfi, M. & Alipanah, A. (2019). Legendre spectral element method for solving sine-Gordon equation. *Advances in Difference Equations*, **2019**, 113. xi, 53, 54

Lowe, R.J., Linden, P.F. & Rottman, J.W. (2002). A laboratory study of the velocity structure in an intrusive gravity current. *Journal of Fluid Mechanics*, **456**, 33. 86

Magoulès, F. (2011). *Computational Fluid Dynamics*. CRC Press. 50, 61

Malm, J. (2011). *Spectral-element simulations of turbulent wall-bounded flows including transition and separation*. Ph.D. thesis, KTH Royal Institute of Technology. 53

Martin, J.E. & García, M.H. (2009). Combined PIV/PLIF measurements of a steady density current front. *Experiments in Fluids*, **46**, 265–276. 10, 11, 18, 25, 27

MASLOWE, S.A. (1986). Critical Layers in Shear Flows. *Annual Review of Fluid Mechanics*, **18**, 405–432. 14, 81, 83, 84, 152

MATLAB (2020). *9.8.0.1396136 (R2020a)*. The MathWorks Inc., Natick, Massachusetts. 73, 75, 76, 78, 100, 143

MAXWORTHY, T. (1984). The dynamics of a high-speed Jovian jet. *Planetary and Space Science*, **32**, 1053–1058. 81

MEIBURG, E. & KNELLER, B. (2010). Turbidity Currents and Their Deposits. *Annual Review of Fluid Mechanics*, **42**, 135–156. 19, 20, 49, 132

MEIBURG, E., RADHAKRISHNAN, S. & NASR-AZADANI, M. (2015). Modeling Gravity and Turbidity Currents: Computational Approaches and Challenges. *Applied Mechanics Reviews*, **67**, 040802. 2, 11, 49, 50, 57, 63, 85, 86, 92, 110, 112, 113, 114, 122, 132

MENDES, N., CHHAY, M., BERGER, J. & DUTYKH, D. (2019). *Numerical Methods for Diffusion Phenomena in Building Physics: A Practical Introduction*. Springer. 52, 53

MICHAELIS, D., NEAL, D.R. & WIENEKE, B. (2016). Peak-locking reduction for particle image velocimetry. *Measurement Science and Technology*, **27**, 104005. 35

MIDDLETON, G.V. (1966). Experiments on Density and Turbidity Currents: I. Motion of the Head. *Canadian Journal of Earth Sciences*, **3**, 523–546. 2, 6, 10, 18, 27, 63, 85

MILLER, P.L. (1991). *Mixing in high Schmidt number turbulent jets*. Ph.D. thesis, California Institute of Technology. 10, 113

MOIN, P. & MAHESH, K. (1998). Direct Numerical Simulation: A Tool in Turbulence Research. *Annual Review of Fluid Mechanics*, **30**, 539–578. 46

MOODIE, T.B. (2002). Gravity currents. *Journal of Computational and Applied Mathematics*, **144**, 49–83. 84, 152

MORTON, K.W. & MAYERS, D.F. (2005). *Numerical Solution of Partial Differential Equations: An Introduction*. Cambridge University Press. 55, 56

MUSUMECI, R.E., VIVIANO, A. & FOTI, E. (2017). Influence of Regular Surface Waves on the Propagation of Gravity Currents: Experimental and Numerical Modeling. *Journal of Hydraulic Engineering*, **143**, 04017022. 26

NASR-AZADANI, M.M. & MEIBURG, E. (2014). Turbidity currents interacting with three-dimensional seafloor topography. *Journal of Fluid Mechanics*, **745**, 409. 86

NEAMTU-HALIC, M.M., KRUG, D., HALLER, G. & HOLZNER, M. (2019). Lagrangian coherent structures and entrainment near the turbulent/non-turbulent interface of a gravity current. *Journal of Fluid Mechanics*, **877**, 824–843. 13, 19, 87

NECKER, F., HÄRTEL, C., KLEISER, L. & MEIBURG, E. (2002). High-resolution simulations of particle-driven gravity currents. *International Journal of Multiphase Flow*, **28**, 279–300. 2, 19, 20, 21, 47, 61, 114, 132

NECKER, F., HÄRTEL, C., KLEISER, L. & MEIBURG, E. (2005). Mixing and dissipation in particle-driven gravity currents. *Journal of Fluid Mechanics*, **545**, 339. 20, 21, 113

NEGRETTI, M.E., FLÓR, J.B. & HOPFINGER, E.J. (2017). Development of gravity currents on rapidly changing slopes. *Journal of Fluid Mechanics*, **833**, 70–97. 7

NEK5000 (2015). Nek5000 user guide. `https://nek5000.mcs.anl.gov/files/2015/09/NEK_doc.pdf`, accessed: 2017-11-29. 53

NEK5000 (2017). Nek5000 website. https://nek5000.mcs.anl.gov/, accessed: 2017-11-29. 46

NOGUEIRA, H.I.S., ADDUCE, C., ALVES, E. & FRANCA, M.J. (2013). Analysis of lock-exchange gravity currents over smooth and rough beds. *Journal of Hydraulic Research*, **51**, 417–431. 25

NOGUEIRA, H.I.S., ADDUCE, C., ALVES, E. & FRANCA, M.J. (2014). Dynamics of the head of gravity currents. *Environmental Fluid Mechanics*, **14**, 519–540. 2, 5, 8, 10, 18, 25, 27, 63

NORCONK, M.P. (2011). *Comprehensive review and application of particle image velocimetry*. Master's thesis, Michigan Technological University. 24, 29

NOVARA, M., SCHANZ, D., GESEMANN, S., LYNCH, K. & SCHRÖDER, A. (2016). Lagrangian 3D particle tracking for multi-pulse systems: performance assessment and application of Shake-The-Box. In *18th International Symposium on the Application of Laser and Imaging Techniques to Fluid Mechanics*. 36, 37, 42, 44

ODIER, P., CHEN, J., RIVERA, M.K. & ECKE, R.E. (2009). Fluid Mixing in Stratified Gravity Currents: The Prandtl Mixing Length. *Physical Review Letters*, **102**, 134504. 2, 9, 16, 18

ODIER, P., CHEN, J. & ECKE, R.E. (2012). Understanding and modeling turbulent fluxes and entrainment in a gravity current. *Physica D: Nonlinear Phenomena*, **241**, 260–268. 2, 15, 18, 25, 29

Ooi, S.K., Constantinescu, G. & Weber, L.J. (2007). 2D Large-Eddy Simulation of Lock-Exchange Gravity Current Flows at High Grashof Numbers. *Journal of Hydraulic Engineering*, **133**, 1037–1047. 20, 21

Ooi, S.K., Constantinescu, G. & Weber, L. (2009). Numerical simulations of lock-exchange compositional gravity current. *Journal of Fluid Mechanics*, **635**, 361. 2, 19, 20

Ottolenghi, L., Adduce, C., Inghilesi, R., Armenio, V. & Roman, F. (2016a). Entrainment and mixing in unsteady gravity currents. *Journal of Hydraulic Research*, **54**, 541–557. 5

Ottolenghi, L., Adduce, C., Inghilesi, R., Roman, F. & Armenio, V. (2016b). Mixing in lock-release gravity currents propagating up a slope. *Physics of Fluids*, **28**, 056604. 47

Özgökmen, T.M. & Chassignet, E.P. (2002). Dynamics of Two-Dimensional Turbulent Bottom Gravity Currents. *Journal of Physical Oceanography*, **32**, 1460–1478. 47

Özgökmen, T.M., Fischer, P.F., Duan, J. & Iliescu, T. (2004). Three-Dimensional Turbulent Bottom Density Currents from a High-Order Nonhydrostatic Spectral Element Model. *Journal of Physical Oceanography*, **34**, 2006–2026. 2, 20, 21, 47, 53, 63, 112, 113, 114

Özgökmen, T.M., Fischer, P.F. & Johns, W.E. (2006). Product water mass formation by turbulent density currents from a high-order nonhydrostatic spectral element model. *Ocean Modelling*, **12**, 237–267. 2, 19, 21

Özsoy, E., Di Iorio, D., Gregg, M.C. & Backhaus, J.O. (2001). Mixing in the Bosphorus Strait and the Black Sea continental shelf: observations and a model of the dense water outflow. *Journal of Marine Systems*, **31**, 99–135. 63, 85

Paik, J., Eghbalzadeh, A. & Sotiropoulos, F. (2009). Three-Dimensional Unsteady RANS Modeling of Discontinuous Gravity Currents in Rectangular Domains. *Journal of Hydraulic Engineering*, **135**, 505–521. 86, 114

Parsons, J.D. & García, M.H. (1995). *Flow Structure and Mixing Characteristics in Saline Gravity Current Fronts (HES 45)*. Ph.D. thesis, University of Illinois at Urbana-Champaign. 10, 26

Parsons, J.D. & García, M.H. (1998). Similarity of gravity current fronts. *Physics of Fluids*, **10**, 3209–3213. 8, 10, 18, 62, 113

Parsons, J.D., Friedrichs, C.T., Traykovski, P.A., Mohrig, D., Imran, J., Syvitski, J.P.M., Parker, G., Puig, P., Buttles, J.L. & García, M.H. (2007). The Mechanics of Marine Sediment Gravity Flows. In C.A. Nittrouer, J.A. Austin, M.E. Field, J.H. Kravitz, J.P.M. Syvitski & P.L. Wiberg, eds., *Continental Margin Sedimentation: From Sediment Transport to Sequence Stratigraphy*, 275–333, Blackwell, Oxford, UK. 63, 86

Patterson, M.D., Simpson, J.E., Dalziel, S.B. & van Heijst, G.J.F. (2006). Vortical motion in the head of an axisymmetric gravity current. *Physics of Fluids*, **18**, 046601. 25

Peakall, J. & Sumner, E.J. (2015). Submarine channel flow processes and deposits: A process-product perspective. *Geomorphology*, **244**, 95–120. 7, 17, 63, 86, 110

Peakall, J., Felix, M., McCaffrey, B. & Kneller, B. (2001). Particulate Gravity Currents: Perspectives. In W. McCaffrey, B. Kneller & J. Peakall, eds., *Particulate Gravity Currents*, 1–8, Wiley. 2, 6

Peakall, J., Best, J., Baas, J.H., Hodgson, D.M., Clare, M.A., Talling, P.J., Dorrell, R.M. & Lee, D.R. (2020). An integrated process-based model of flutes and tool marks in deep-water environments: Implications for palaeohydraulics, the bouma sequence and hybrid event beds. *Sedimentology*, **67**, 1601–1666. 135

Pelmard, J., Norris, S. & Friedrich, H. (2020). Statistical characterisation of turbulence for an unsteady gravity current. *Journal of Fluid Mechanics*, **901**, A7. 2, 12, 15, 16, 17, 19, 20, 21, 86, 134

Penney, J. (2017). *Direct Numerical Simulation of Salt Fingering Gravity Currents and Double-Diffusive Rayleigh-Taylor Instabilities*. Ph.D. thesis, University of Waterloo. 48

Pope, S.B. (2001). *Turbulent Flows*. IOP Publishing. xi, 19, 20, 49, 55, 56, 60, 61

Raffel, M., Willert, C.E., Scarano, F., Kähler, C.J., Wereley, S.T. & Kompenhans, J. (2018). *Particle Image Velocimetry: A Practical Guide*. Springer. 23, 30, 31, 36, 66

Rahmani, M., Seymour, B.R. & Lawrence, G.A. (2016). The effect of Prandtl number on mixing in low Reynolds number Kelvin-Helmholtz billows. *Physics of Fluids*, **28**, 054107. 2, 10, 113

Reynolds, A.J. (1974). *Turbulent Flows in Engineering*. Wiley. 10, 57, 113

Richecoeur, F., Hakim, L., Renaud, A. & Zimmer, L. (2012). DMD algorithms for experimental data processing in combustion. In *Proceedings of the Summer Program 2012*, 459–468, Center for Turbulence Research, Stanford University. 76

ROSSBY, T. & ZHANG, H.M. (2001). The near-surface velocity and potential vorticity structure of the Gulf Stream. *Journal of Marine Research*, **59**, 949–975. 81

RUBINATO, M. (2015). *Physical Scale Modelling of Urban Flood Systems*. Ph.D. thesis, University of Sheffield. 19, 24

RUD, M.A. (2016). *Application of Nek5000 to dispersion simulations*. Master's thesis, NTNU. xi, 53, 54

SADOWSKY, J. (1994). The Continuous Wavelet Transform: A Tool for Signal Investigation and Understanding. *Johns Hopkins APL Technical Digest*, **15**, 306–306. 74

SAMOTHRAKIS, P. & COTEL, A.J. (2006). Propagation of a gravity current in a two-layer stratified environment. *Journal of Geophysical Research: Oceans*, **111**. 25

SARKAR, S. & SCOTTI, A. (2017). From Topographic Internal Gravity Waves to Turbulence. *Annual Review of Fluid Mechanics*, **49**, 195–220. 84

SCARANO, F. (2012). Tomographic PIV: principles and practice. *Measurement Science and Technology*, **24**, 012001. 36

SCARANO, F., GHAEMI, S., CARIDI, G.C.A., BOSBACH, J., DIERKSHEIDE, U. & SCIACCHITANO, A. (2015). On the use of helium-filled soap bubbles for large-scale tomographic PIV in wind tunnel experiments. *Experiments in Fluids*, **56**, 42. 38

SCHANZ, D., GESEMANN, S., SCHRÖDER, A., WIENEKE, B. & NOVARA, M. (2012). Non-uniform optical transfer functions in particle imaging: calibration and application to tomographic reconstruction. *Measurement Science and Technology*, **24**, 024009. 41, 42

SCHANZ, D., SCHRÖDER, A., GESEMANN, S., MICHAELIS, D. & WIENEKE, B. (2013). 'Shake The Box': A highly efficient and accurate Tomographic Particle Tracking Velocimetry (TOMO-PTV) method using prediction of particle positions. In *10th International Symposium on Particle Image Velocimetry*. 36, 37, 41, 42, 44

SCHANZ, D., SCHRÖDER, A. & GESEMANN, S. (2014). 'Shake The Box' - a 4D PTV algorithm: Accurate and ghostless reconstruction of Lagrangian tracks in densely seeded flows. In *17th International Symposium on Applications of Laser Techniques to Fluid Mechanics*. 36, 37, 38, 42, 44

SCHANZ, D., SCHRÖDER, A., GESEMANN, S. & WIENEKE, B. (2015). 'Shake the box': Lagrangian particle tracking in densely seeded flows at high spatial resolution. In *9th International Symposium On Turbulence and Shear Flow Phenomena*. 36, 38

SCHANZ, D., GESEMANN, S. & SCHRÖDER, A. (2016). Shake-The-Box: Lagrangian particle tracking at high particle image densities. *Experiments in Fluids*, **57**, 70. 36, 37, 42, 43, 44, 45, 89

SCHMID, P.J. (2010). Dynamic mode decomposition of numerical and experimental data. *Journal of Fluid Mechanics*, **656**, 5–28. 76

SCHMID, P.J. (2011). Application of the dynamic mode decomposition to experimental data. *Experiments in Fluids*, **50**, 1123–1130. 76

SCHRÖDER, A., SCHANZ, D., MICHAELIS, D., CIERPKA, C., SCHARNOWSKI, S. & KÄHLER, C.J. (2015). Advances of PIV and 4D-PTV "Shake-The-Box" for Turbulent Flow Analysis – the Flow Over Periodic Hills. *Flow, Turbulence and Combustion*, **95**, 193–209. 41

SCHRÖDER, A., SCHANZ, D., GEISLER, R. & GESEMANN, S. (2016). Investigations of coherent structures in near-wall turbulence and large wall-shear stress events using Shake-The-Box. In *18th International Symposium on the Application of Laser and Imaging Techniques to Fluid Mechanics*. 37

SEQUEIROS, O.E., SPINEWINE, B., BEAUBOUEF, R.T., SUN, T., GARCÍA, M.H. & PARKER, G. (2010). Characteristics of Velocity and Excess Density Profiles of Saline Underflows and Turbidity Currents Flowing over a Mobile Bed. *Journal of Hydraulic Engineering*, **136**, 412–433. ix, xi, 7, 11, 12, 64, 65, 86

SHENG, J., MENG, H. & FOX, R.O. (2000). A large eddy PIV method for turbulence dissipation rate estimation. *Chemical Engineering Science*, **55**, 4423–4434. 56

SHER, D. & WOODS, A.W. (2015). Gravity currents: entrainment, stratification and self-similarity. *Journal of Fluid Mechanics*, **784**, 130–162. 2, 10, 11, 13, 18, 27

SHER, D. & WOODS, A.W. (2017). Mixing in continuous gravity currents. *Journal of Fluid Mechanics*, **818**. ix, 6, 11, 13, 18, 27

SIMPSON, J.E. (1969). A comparison between laboratory and atmospheric density currents. *Quarterly Journal of the Royal Meteorological Society*, **95**, 758–765. 2, 8, 10, 18

SIMPSON, J.E. (1997). *Gravity Currents: In the Environment and the Laboratory*. Cambridge University Press. ix, 1, 2, 5, 7, 8, 10, 11, 17, 62, 63, 85, 86, 92, 112, 113, 122, 132

SIMPSON, J.E. & BRITTER, R.E. (1979). The dynamics of the head of a gravity current advancing over a horizontal surface. *Journal of Fluid Mechanics*, **94**, 477–495. 10, 18, 46, 132

Stacey, M.W. & Bowen, A.J. (1988). The vertical structure of density and turbidity currents: Theory and observations. *Journal of Geophysical Research: Oceans*, **93**, 3528–3542. 7, 63, 84, 112, 113, 152

Stancanelli, L.M., Musumeci, R.E. & Foti, E. (2018). Computational Fluid Dynamics for Modeling Gravity Currents in the Presence of Oscillatory Ambient Flow. *Water*, **10**, 635. 114

Staquet, C. & Sommeria, J. (2002). Internal Gravity Waves: From Instabilities to Turbulence. *Annual Review of Fluid Mechanics*, **34**, 559–593. 84, 152

Steinmann, T., Casas, J., Braud, P. & David, L. (2019). Tomo-PTV measurement of a drop impact at air-water interface. In *13th International Symposium on Particle Image Velocimetry*. 37

Sumner, E.J., Peakall, J., Parsons, D.R., Wynn, R.B., Darby, S.E., Dorrell, R.M., McPhail, S.D., Perrett, J., Webb, A. & White, D. (2013). First direct measurements of hydraulic jumps in an active submarine density current. *Geophysical Research Letters*, **40**, 5904–5908. 9, 13, 17

Sumner, E.J., Peakall, J., Dorrell, R.M., Parsons, D.R., Darby, S.E., Wynn, R.B., McPhail, S.D., Perrett, J., Webb, A. & White, D. (2014). Driven around the bend: Spatial evolution and controls on the orientation of helical bend flow in a natural submarine gravity current. *Journal of Geophysical Research: Oceans*, **119**, 898–913. 63, 86

Sutherland, B.R. (1999). Propagation and reflection of internal waves. *Physics of Fluids*, **11**, 1081–1090. 80

Sutherland, B.R. (2010). *Internal Gravity Waves*. Cambridge University Press. 80

Talling, P.J. (2014). On the triggers, resulting flow types and frequencies of subaqueous sediment density flows in different settings. *Marine Geology*, **352**, 155–182. 62, 63, 112

Tan, S., Salibindla, A., Masuk, A.U.M. & Ni, R. (2019). An open-source Shake-the-Box method and its performance evaluation. In *13th International Symposium on Particle Image Velocimetry*. 36

Thomas, L.P., Dalziel, S.B. & Marino, B.M. (2003). The structure of the head of an inertial gravity current determined by particle-tracking velocimetry. *Experiments in Fluids*, **34**, 708–716. 2, 10, 11, 18, 27

Thorpe, S.A. (1975). The excitation, dissipation, and interaction of internal waves in the deep ocean. *Journal of Geophysical Research*, **80**, 328–338. 83

Torrence, C. & Compo, G.P. (1998). A practical guide to wavelet analysis. *Bulletin of the American Meteorological Society*, **79**, 61–78. 75

Tu, J., Yeoh, G.H. & Liu, C. (2018). *Computational Fluid Dynamics: A Practical Approach*. Butterworth-Heinemann, 2nd edn. 50, 51

Tu, J.H., Rowley, C.W., Luchtenburg, D.M., Brunton, S.L. & Kutz, J.N. (2014). On dynamic mode decomposition: Theory and applications. *Journal of Computational Dynamics*, **1**, 391–421. 76

Ungarish, M. (2009). *An Introduction to Gravity Currents and Intrusions*. Chapman and Hall/CRC. 62, 63, 85, 112

Unsworth, C.A. (2015). Section 3.3.4: Particle Imaging Velocimetry. In S. Cook, L. Clarke & J. Nield, eds., *Geomorphological Techniques (Online Edition)*, British Society for Geomorphology; London, UK, ISSN: 2047-0371. 24, 29, 33

Usherwood, J.R., Cheney, J.A., Song, J., Windsor, S.P., Stevenson, J.P.J., Dierksheide, U., Nila, A. & Bomphrey, R.J. (2020). High aerodynamic lift from the tail reduces drag in gliding raptors. *Journal of Experimental Biology*, **223**. 37

Vallis, G.K. (2017). *Atmospheric and Oceanic Fluid Dynamics*. Cambridge University Press, 2nd edn. 15

van Kan, J., Segal, A. & Vermolen, F. (2005). *Numerical Methods in Scientific Computing*. VSSD. 50, 51

Viviano, A., Musumeci, R.E. & Foti, E. (2018). Interaction between waves and gravity currents: description of turbulence in a simple numerical model. *Environmental Fluid Mechanics*, **18**, 117–148. 26

Wang, Z.J., Fidkowski, K., Abgrall, R., Bassi, F., Caraeni, D., Cary, A., Deconinck, H., Hartmann, R., Hillewaert, K., Huynh, H.T., Kroll, N., May, G., Persson, P.O., van Leer, B. & Visbal, M. (2013). High-order CFD methods: current status and perspective. *International Journal for Numerical Methods in Fluids*, **72**, 811–845. 53

Wells, M.G. & Dorrell, R.M. (2021). Turbulence Processes Within Turbidity Currents. *Annual Review of Fluid Mechanics*, **53**, 59–83. ix, 8, 9, 11, 14, 17, 63, 84, 85, 86, 152, 153

Wieneke, B. (2012). Iterative reconstruction of volumetric particle distribution. *Measurement Science and Technology*, **24**, 024008. 42, 43, 44, 89

WIENEKE, B. (2017). *PIV Uncertainty Quantification and Beyond*. Ph.D. thesis, Delft University of Technology. 30

WIENEKE, B. (2018). Improvements for volume self-calibration. *Measurement Science and Technology*, **29**, 084002. 41, 42

WILCOX, D.C. (2006). *Turbulence Modeling for CFD*. DCW Industries, 3rd edn. 19, 20, 49, 61

WILLERT, C.E. & GHARIB, M. (1991). Digital particle image velocimetry. *Experiments in Fluids*, **10**, 181–193. 33

YUAN, Y. & HORNER-DEVINE, A.R. (2017). Experimental investigation of large-scale vortices in a freely spreading gravity current. *Physics of Fluids*, **29**, 106603. 25

ZGHEIB, N., BONOMETTI, T. & BALACHANDAR, S. (2015). Direct numerical simulation of cylindrical particle-laden gravity currents. *Computers & Fluids*, **123**, 23–31. 47

ZHOU, J., ADRIAN, R.J., BALACHANDAR, S. & KENDALL, T.M. (1999). Mechanisms for generating coherent packets of hairpin vortices in channel flow. *Journal of Fluid Mechanics*, **387**, 353–396. x, 21, 100, 124

ZHU, J.B., LEE, C.B., CHEN, G.Q. & LEE, J.H.W. (2006). PIV observation of instantaneous velocity structure of lock release gravity currents in the slumping phase. *Communications in Nonlinear Science and Numerical Simulation*, **11**, 262–270. 25

ZOHURI, B. (2015). *Dimensional Analysis and Self-Similarity Methods for Engineers and Scientists*. Springer. 26

ZONTA, F. & SOLDATI, A. (2018). Stably stratified wall-bounded turbulence. *Applied Mechanics Reviews*, **70**. 109